UNIVERSITY OF OKLAHOMA

GRADUATE COLLEGE

MOISTURE AND THERMAL CHARACTERISTICS OF SOUTHERN PLAINS ICE STORMS: INSIGHTS FROM A REGIONAL CLIMATOLOGY AND HIGH-RESOLUTION WRF-ARW SENSITVITY STUDY

A DISSERTATION

SUBMITTED TO THE GRADUATE FACULTY

in partial fulfillment of the requirements for the

Degree of

DOCTOR OF PHILOSOPHY

By

ESTHER DANIELLE MULLENS
Norman, Oklahoma
2014

MOISTURE AND THERMAL CHARACTERISTICS OF SOUTHERN PLAINS ICE STORMS: INSIGHTS FROM A REGIONAL CLIMATOLOGY AND HIGH-RESOLUTION WRF-ARW SENSITIVITY STUDY

A DISSERTATION APPROVED FOR THE
SCHOOL OF METEOROLOGY

BY

_____
Dr. Lance Leslie, Chair

_____
Dr. Michael Richman

_____
Dr. David Parsons

_____
Dr. David Stensrud

_____
Dr. May Yuan

Acknowledgements

My time at OU has been enormously challenging, but greatly rewarding, and I have many people to thank. Firstly, Dr Peter Lamb, my co-Chair, who sadly passed away just a couple of months prior to the conclusion of this work. Pete created the OU-Reading (UK) exchange program that established my interest in studying abroad. I will always be immensely grateful for the opportunity he gave me, and the skills I have accumulated under his mentorship. Pete was a hands-off Advisor, he emphasized a self-teaching approach to problem solving, including developing the research focus, tools and implementation of a doctoral project. As I look back upon my time here, I can see the benefits this approach has provided me, and feel equipped to translate the successes and mistakes of the past several years to inform all that I do from now on. I also am extremely appreciative of co-Chair Lance Leslie, who has been very approachable, tremendously supportive and helpful in the science and technical aspects of this work. Dr Dave Stensrud was invaluable in helping me understand and build competence in WRF, and set me on the right path following errors encountered in the earlier stages of this research. Dr Mike Richman is a statistics guru and I appreciate his patience in helping me build a skill set in this area, especially as I'm not a natural! Thanks also to May Yuan for her efforts, and Dr Dave Parsons, who served on the committee last minute and has provided some constructive comments that served to strengthen this work. Additional appreciation to Zewdu Segele for getting me started on the WRF and sharing his codes. I have had many good years in Oklahoma, and have developed a wonderful community. In terms of moral support, thank you to Rebekah LaBar, Jeff Makowski, my roommates Rachel Riley and Becky Cintineo and the wonderful Masters

class of 2010/2011 who shared joys and pains of the coursework element of this degree. My UK friends have lifted my spirits through skype dates and a good catch up whenever I'm back in the country. My husband Stephen Mullens has often been more confident of me than I have been, and his love has sustained me. Thanks to my wonderful family, separated by many thousands of miles but with me always in spirit, to my new US Family, who have cheered me on, both literally and figuratively, and to my Church family, who have provided wisdom, encouragement and perspective.

The smooth running of this project would not have been possible without the dedication and expertise of the OCSER supercomputing team who has helped me out with many a problem I couldn't understand. The NCAR-NCL site has also been very useful in forming the programs used for data analysis. Thanks to the many scientists from which this work is built upon. I'd also like to acknowledge the use of the SPIA© index in this work, created by Sydney Sperry and Steven Piltz.

Finally, thank you God and my savior Jesus Christ for creating a world that is complex yet observable. The Earth is a beautiful home and has been entrusted to us to protect.

Trust in the Lord with all your heart

And do not lean on your own understanding.

In all your ways acknowledge him.

And he will make your path straight.

--- Proverbs 3 v 5-6

Table of Contents

List of Tables

List of Figures

Abstract

Winter storms, including snowstorms and ice storms, are infrequent in the Southern Great Plains of the United States (SGP), but can produce significant hazard and socioeconomic disruption. During 2000-2010, several severe ice storms impacted the region. These events combined resulted in nearly $800 million in damages, over 30 fatalities, and power disruption to over 3 million homes and businesses. Hitherto, basic climatological information for winter storms in this region remain understudied. This dissertation examines the characteristics of freezing precipitation events for the SGP by developing a regional spatial and synoptic climatology (1993-2011). Thermal profiles conducive to winter precipitation of varying types and intensities are also examined and compared with past literature. A combination of sounding analysis, and Principal Component (PC)/composite techniques are used to derive this climatology. Results identified that the SGP experiences freezing precipitation of varying intensity, but that ice storms to the region are notable for their large above-freezing inversion layer ('warm layer') temperatures/depths and mixing ratio. Freezing precipitation occurs most often over the central and eastern domain during December-February, while snowfall maximizes northwest of this zone with broader seasonal occurrence. The synoptic analysis showed that patterns conductive to storms with a pronounced mixed-phase region typically involved topographically aided ageostropic down-gradient advection of cold stable air in the lee of the Rocky Mountains, with an arctic high pressure over the northern/central Great Plains. A mid-level trough and low-level warm air advection provided ascent, and anomalously warm air to the south provided sufficient support for a warm layer. Long-duration ice storms were observed with a slow-moving high-

amplitude western trough, direct moisture transport from the Gulf of Mexico, and a ridge over the southeastern U.S.

Based on the climatology and past literature, a hypothesis is proposed that the Gulf of Mexico, as the proximal basin and major moisture source, may impact ice storm severity by modulation of the warm layer profile associated with strongly positive or negative SST anomalies. This hypothesis is tested using high-resolution nested WRF-ARW sensitivity studies with six representations of SST, including the 30-year climatology, a uniform ±2 degrees K perturbation to the control, and a physical upper and lower limit using the SST field for the warmest and coolest basin-average anomalies 1981-2011. Two case studies were utilized corresponding to different synoptic types.

The simulations revealed discernable influence of SST on freezing precipitation, including its temporal evolution and intensity. For the December 9-11 2007 case study, the warm layer formed well prior to the event, associated with persistent southerly flow and a warm anomaly over the southern U.S. The impact of SST on the warm layer intensity was weak in comparison to its existing magnitude, however the atmospheric stability profile was altered such that strongly negative SST produced stabilization above the maximum inversion temperature and markedly reduced precipitation on the first day of the ice storm. A dynamical weakening of the low-level jet and moisture transport in the strongly positive SST case counteracted observed increases in mixing ratio to yield weaker accumulation differences during the second precipitation episode.

For the January 28-30 2010 case study, the impact of SST was more pronounced on the warm layer, which had formed in association with return flow from the Gulf.

Warmer SST, especially strongly positive localized anomalies within the fetch of the impacted area, lead to both a moisture induced intensification of precipitation, and increased peak warm layer temperature, leading to changes in the location of freezing precipitation versus rain/snow, especially for Arkansas. Dynamical intensification (weakening) of precipitation occurred as increased (decreased) baroclinicity, warm air advection and latent heat release promoted a stronger geopotential low at 850 hPa, and a strengthened (weakened) low-level jet yielding greater (less) moisture transport.

Despite the differing thermal and dynamical responses, both case studies displayed potential for enhanced icing conditions with warmer SST, while cooler SST produced a marked reduction in severity. The January 2010 event showed greater sensitivity in the location and amount of icing due to the warm layer evolution being more directly connected to diabatic processes over the Gulf of Mexico 24-48 hours prior. Results showed discernable impact even with comparatively small SST perturbations (e.g., climatology versus control) indicating that winter precipitation is sensitive to basin SST anomalies. This work may be of use to forecasters and regional climatologists in gaining situational awareness and recognizing the role of both large-scale synoptic and regional thermodynamic drivers of phase type and intensity. Furthermore, given the observed increases in SST resulting from global climate change, this work provides physical understanding of processes that may impact ice storm evolutions in a warming climate, particularly with respect to the warm layer.

Chapter 1: Literature Context

1.1 Introduction and Research Statement

Winter precipitation type depends on the complex interplay between atmospheric dynamics, mesoscale and microscale processes, and the vertical thermal profile. The United States experiences numerous precipitation types, including snowfall, freezing rain and ice pellets. While all produce socio-economic hazard, arguably one of the most severe forms of winter weather is freezing rain, or 'ice storms'. An ice storm is the National Weather Service designation for a freezing rain event producing glaze (ice) accumulation in excess of 0.25 inch (Grout et al. 2012). Detrimental impacts include widespread shutdown of transport and infrastructure, ice loading on power-lines and trees, and heightened risk of personal injury. Cited causes of injury and death include automobile accidents, falling branches or trees, and occasionally carbon monoxide poisoning from faulty backup generators (National Climatic Data Center, *Storm Data*). Freezing rain strongly impacts forest ecology, including damage and tree mortality throughout impacted temperate hardwood forests (e.g., Olthof et al. 2004, Bragg et al. 2003, Hauer et al. 1994). Economic loss can result from interruption in timber production (e.g., Warrillow and Mou, 1999) and other commodities or produce (the 1998 northeast ice storm lead to loss of maple trees and thus maple syrup – a major economic contributor in eastern Canada, according to Kidon et al. 2001). Other adverse impacts include damage and loss of revenue to recreational areas, wildlife refuges, and private land, among others (Warrillow and Mau, 1999).

Compared to other regions of the contiguous U.S and Canada, winter storms are relatively uncommon in the Southern Plains states, with typically only a few events

annually (e.g., Houston and Changnon, 2007, Changnon and Karl 2003). It is their infrequency that may potentially increase adverse effects due to a lack of preparedness and adaptive capacity. Regional forecasters also have less opportunity to accrue experience in their prediction (Lackmann 2011, p221). Winter weather forecasting remains an operational challenge due to the multi-scale dynamic and thermodynamic processes that impact precipitation type (Castellano, 2012). Call (2009) polled 15 warning coordination Meteorologists in the Eastern region, noting that issuing a winter weather (e.g., ice storm) watch was much more common than issuing warnings more than 24-hours ahead of an event. Numerical model guidance has been known to struggle with mixed phase winter weather, such as microphysics, and the depth/southward extent of cold air (e.g., Ikeda et al. 2013, Leatham et al. 2010, Lackmann et al. 2002).

During 2000-2010, the Southern Plains experienced seven major ice storms. These events combined resulted in nearly $1bn dollars in damage[1], at least 35 directly attributable fatalities, numerous injuries, and power disruption to over 3 million homes and businesses (average > 100,000 per storm). This frequency and magnitude was considered somewhat unprecedented in recent memory for Oklahoma (Grout et al. 2012, Oklahoma Climatological Survey, Personal Comm.), with Oklahoma leading the nation in the number of winter weather-related major federal disaster declarations, particularly for ice storms (e.g., Grout et al. 2012). Additionally, the southeast regional climate center, encompassing the southern Appalachians (Fuhrmann and Konrad, 2009 http://erh.noaa.gov/ilm/ClimateConference/20.ppt) reported high variability in annual trends but also evidenced a recent increase in intense freezing rain events (1990-2007),

[1] Estimates compiled from NCDC Storm Event Database. Note however, that these values are expressed for guidance purposes, and may not represent a conclusive quantitative value, see Branick, 1997.

linked to a positive Atlantic Multidecadel Oscillation (AMO). There are no clear present or historical trends in freezing precipitation occurrence (Kunkel et al. 2013), and available information supports high interannual-decadal variability (e.g., Changnon and Karl 2003). However Call (2010) suggests that the increased dependence on electrical power has strained resources and exacerbated power outages and negative societal impacts during recent ice storms. The susceptibility of U.S sub-regions to financial damage from freezing precipitation was also investigated by Changnon (2003). South central states ranked fourth in total damage losses (1949-2000), but first in the ratio of number of freezing rain days to significant financial loss (roughly 3.5 freezing rain days to $1 million damage). The result was attributed to higher observed ice accumulations, potentially resulting from longer single-duration events and greater moisture availability leading to comparatively more damaging individual events.

This dissertation provides a detailed meteorological analysis of winter storms, with focus on ice storms, for the U.S Southern Great Plains (SGP). The spatial extent of the SGP domain is shown in chapter 2, and includes Oklahoma, portions of Texas, Kansas, Arkansas, Missouri and Louisiana. This research intends to improve understanding of the regional nature of freezing precipitation events, especially with regard to temperature and moisture profile characteristics. In particular, we consider the question of *what factors control or influence the severity of freezing precipitation?* The study has two components: The first is a climatological analysis of the thermal profile and synoptic scale evolution, based on a manually compiled dataset 1993-2011 (chapter 2 & 3). The second uses the Weather Research and Forecasting Model (WRF-ARW, Skamarock et al. 2008) to perform a suite of high-resolution sensitivity simulations

evaluating possible connections between sea surface temperature anomalies in the Gulf of Mexico with the thermodynamics of freezing precipitation, a hypothesis based on the developed climatology and past literature (chapters 4-7). The simulations use two recent case studies with different synoptic evolutions. Since to date limited research exists for the region, this dissertation work stands to make an important contribution. Further literature background[2] on freezing precipitation research is now presented. Later chapters provide further contextual literature as needed.

1.2 History and Definitions

According to Robbins and Cortinas (2002) freezing precipitation was reportedly first identified during an ice storm in central Germany, October 1898. It was observed from measurements taken from a nearby mountain that a near saturated region of above freezing temperature was present throughout the event in the lower troposphere, with sub-freezing air at the surface. Later case studies of ice storms in the United States by Frankenfield (1915) and Meisinger (1920) noted a similar vertical thermal profile. Reihl et al. (1952) advanced understanding of the larger-scale environment by identifying two common synoptic patterns associated with freezing precipitation in Illinois. In 1959, Bennett published a study that built upon this work, providing further synoptic contexts (see section 1.4).

In the late 1980s-1990s a surge of papers sought to better characterize the microphysical complexity of freezing precipitation, in relation to the evolution of the thermodynamic profile (e.g., Stewart 1987, Hoffman and Norman 1988, Czys 1996,

[2] Although important, the ecological literature on freezing precipitation is not further considered.

Zerr 1997). These studies heavily drew upon radiosonde data, and more recently remote sensing (e.g., Zhang et al. 2010). Given the forecasting challenges associated with correctly delineating precipitation phase type, interest lay in finding empirical distinctions between them. Whilst the specific details are complex and can vary for individual regions (described in section 1.5), this work improved understanding of the thermal profiles more associated to ice pellets, versus freezing rain. Figure 1.1 schematically illustrates conceptual temperature profiles for all winter precipitation types.

Rain (Panel A): Liquid precipitation that occurs in a near saturated environment with a vertical thermal profile characterized by above freezing surface temperatures and a general decrease in temperature with height (low level inversion layers sometimes present).

Freezing Rain (panel B): Supercooled liquid precipitation classically associated with a (near) saturated above freezing inversion layer, known as the 'warm layer' 'warm nose' or 'melting layer'. Here we apply the term 'warm layer'. Precipitation generated above this layer descends into the above freezing inversion and melts to form a liquid raindrop. These drops then pass through a subfreezing layer near the surface, which if sufficiently shallow and saturated, prevents precipitation from refreezing until it impacts a surface. Hoffman and Norman (1988) identified another microphysical path associated with the collision and coalescence of supercooled droplets in an environment characterized by a completely sub-zero vertical thermal profile. In most cases, a substantial dry layer was present in the mid-troposphere- the region associated with efficient growth of snowflakes (the 'dendritic grown zone' with temperatures typically -

12 to -17^{o}C). The lack of ice crystals, which would tend to encourage rapid glaciation within the cloud, allows the maintenance of distinct supercooled layers. Rauber et al. (2000) determined that this 'supercooled warm rain' process was most commonly associated with freezing drizzle. This dissertation focuses on the classic warm layer profile.

Ice Pellets (panel C): Partially frozen precipitation that has the characteristics of small hail or graupel. In the U.S definition 'sleet' is interchangeable with ice pellets. However internationally the definition of sleet varies, therefore 'ice pellets' is the preferred designation. The primary mechanism by which ice pellets form is similar to that of freezing rain and can be co-located with freezing rain. Some observed distinctions include cooler/shallower warm layers and/or deeper refreezing surface layers. This thermal profile can result in insufficient melting and/or partial refreezing (Stewart and King, 1987, Zerr 1997).

Snow (subzero profile: panel D): The classic snow profile is entirely subfreezing. Ingredients for the formation of heavy snowfall commonly include rising motion near a saturated or saturated isothermal layer near -15^{o}C, where growth by deposition and aggregation is particularly efficient. In many cases a deep saturated layer at any level supports snowfall generation, as deposition, riming and aggregation occur throughout the profile (e.g., Pruppacher and Klett 1981, Schultz et al. 2001).

Snow (above zero near surface profile: panel E): Snowfall may occur in temperatures exceeding 0^{o}C if the low level airmass is sub-saturated. There are a couple of mechanisms that may occur in these cases: The first is the evaporation and subsequent cooling of the airmass, especially during heavy precipitation. Lab

experiments by Matuso and Sasyo (1981, a,b) demonstrate that snow can occur in relative humidities of 40% with temperatures as high as 7°C (Schultz et al. 2001). The second mechanism occurs when snowflakes melt as they descend into the near surface above freezing environment. This can cool the airmass through diabatic cooling (e.g. Bosart and Sanders 1991, Kain et al. 2000, Fuhrmann 2011), and typically occurs in a more humid environment.

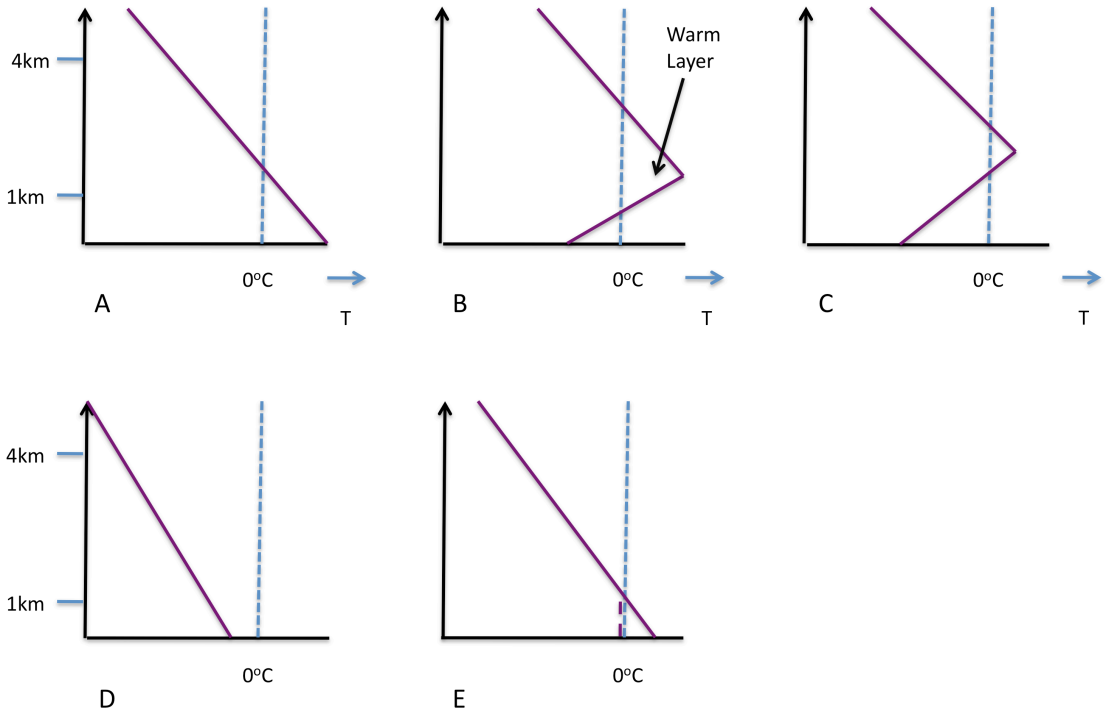

Figure 1.1: Conceptual representation of vertical thermal profiles associated with precipitation phase (A) rain, (B) freezing rain, (C) ice pellets, (D) snow and (E) snow with an initial surface temperature greater than 0°C, under the influence of diabatic cooling (as in Fuhrmann 2011). The Vertical dashed is the 0°C isotherm, while the purple solid line is the idealized environmental temperature profile.

1.3 Geographic Distribution of Winter Precipitation

National freezing precipitation climatologies (e.g., freezing rain and drizzle, ice pellets, hereafter FZPCP) across the contiguous U.S and Canada have been constructed

by Bennett (1959), Baldwin (1973), Bernstein and Brown (1997), Branick (1997), Bernstein (2000), Cortinas (2000), Rauber et al. (2000, 2001), Robbins and Cortinas (2002), Houston and Changnon (2007). Most indicate a broad zone of increased FZPCP frequency along an axis from the Texas Panhandle, north and east through Michigan and New England where a maximum is observed. Another maximum extends much of the length of the Appalachians southward to South Carolina. FZPCP is uncommon in intermountain regions west of the Rockies (except Washington), and subtropical southern states. The spatial climatology of Changnon and Karl (2003) is shown in Figure 1.2. This distribution reflects perhaps a number of features including the frequency of surface cold airmassess, availability and transport of moisture, and the occurrence of sufficient lifting mechanisms for the generation of precipitation (e.g., cyclones, storm tracks, topography). In contrast, the climatological distribution of snowfall, as derived by Changnon et al. (2006) for events exceeding 15.2 cm (6 inches) showed strong latitudinal dependence over the Great Plains. In the western, northern and eastern U.S, topography and water sources (notably the great lakes) appear to drive the frequency distribution (Figure 1.3).

FZPCP temporal distribution was examined by Cortinas et al. (2004) and Changnon and Karl (2003), among others. The majority occurs during the winter months of December, January and February, especially December and January (Changnon and Karl, 2003). There is an apparent seasonal dependence with latitude, and to a lesser extent longitude (e.g., Stuart and Issac, 1999). Snowfall events revealed broader seasonal range, particularly for the intermountain west. In the Great Plains and eastern U.S, snowstorms occur between October-April, with latitudinal dependence for

peak month(s). Changnon et al. (2006) showed peak months of January and February for the Southern Plains. Studies considering sub-daily records have noted that FZPCP is more frequent overnight and during the morning hours (e.g., Strapp et al. 1996, Cortinas et al. 2004) and often of short duration (e.g., mean 4.3 hours at Quebec, CA, Ressler et al. 2012).

1.4 Synoptic-Dynamic Evolution

Early analysis into synoptic conditions producing FZPCP was by Reihl et al (1952) who identified two leading patterns of freezing rain formation for winter storms in Illinois. One was associated with a surface cyclone, with observations of freezing rain about 50 miles north of a warm front in the northern sector of the system. This zone was narrow, bounded by snow to the north in the deeper cold airmass, and rain near the warm front. The other was characterized by a surface stationary front with a shallow arctic airmass to the north, and ascent of warm southwesterly flow over the cold air. Freezing rain in this latter case was often widespread, lighter, but of longer duration than the former (see also Robbins and Cortinas 2002, Ressler et al. 2012). Bennett (1959) suggested that the arctic airmass can be classified as polar continental, while the low-level warm airmass typically has its origins from the low latitudes (e.g., tropical maritime). Favorable conditions for freezing rain occur when the polar continental airmass is modified through low level moistening, preferentially occurring in proximity to large water bodies (e.g., Bernstein et al. 1998).

Rauber et al. (2001) developed a set of archetypal surface synoptic patterns common to FZPCP in the contiguous U.S east of the Rocky Mountains using nearly

1000 soundings over 24 years. This comprehensive assessment formed seven synoptic archetypes, three of which related to Appalachian topography (e.g., cold air damning). The four remaining patterns are shown in Figure 1.4. The most common archetype, 'Pattern A' (31% frequency) was associated with an arctic quasi-stationary front. Rauber et al. (2001) note that FZPCP fell near and just north of the surface 0^{o}C isotherm. The longer duration of these events also supported the earlier findings of Reihl et al. (1952) and recent work by Ressler et al. (2012), who compartmentalized 46 ice storm events into three categories based on the location and orientation of the 500 hPa trough. A western trough, accompanied by a persistent arctic anticyclone, yielded longer duration freezing precipitation but weakened forcing for ascent. Arctic anticyclones translating over the U.S during the winter can produce a proportionately large swath of FZPCP near their southern boundary (e.g., Bernstein et al, 1998). Pattern B was also earlier identified by Mesinger (1920) and Reihl et al. (1952) and occurs with the passage of a surface cyclone. FZPCP forms in a narrow band north of the warm front near the 0^{o}C isotherm as warm air ascents over the frontal boundary. Rauber et al. (2001) note that this pattern was less common (about 14% of events) and associated with short-lived FZPCP, usually due to thermal transitions associated with the faster system progression. Pattern C was a combination of patterns A and B, and was associated with strong surface winds produced from pressure gradient between the cyclone and anticyclone centers (e.g. Bennett, 1959). This pattern contributed to 19% of all events, and was second to pattern A in duration. Pattern D (10% frequency) developed FZPCP in the western quadrant of a surface anticyclone. In this case surface winds can have southerly component, implying warm advection in the refreezing layer

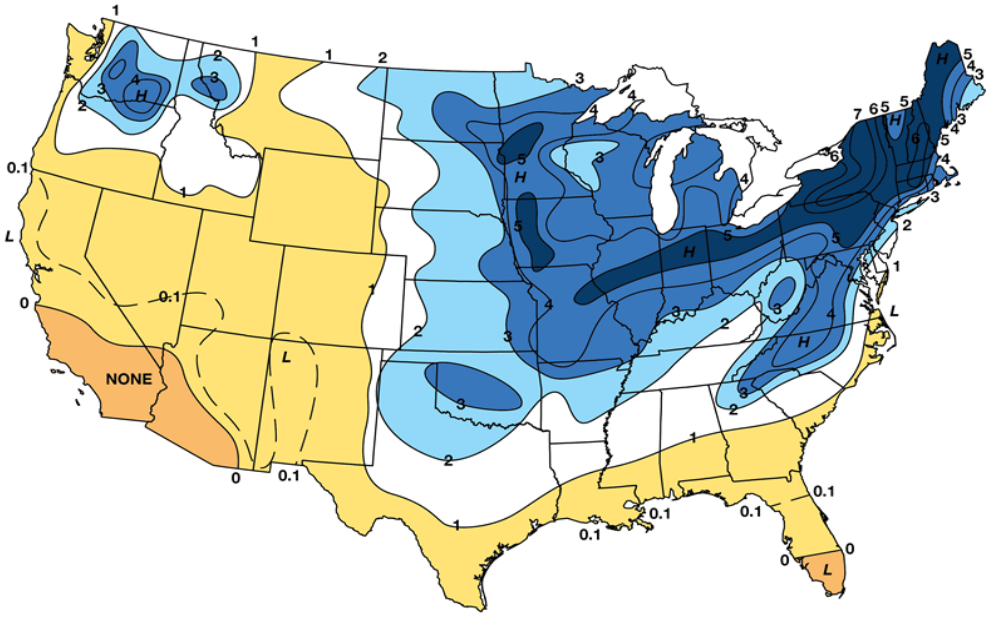

Figure 1.2: Distribution of freezing precipitation events by average number of days per year 1949-2000. From Changnon and Karl (2003), available at: http://mrcc.isws.illinois.edu/living_wx/icestorms/index.html#frequency

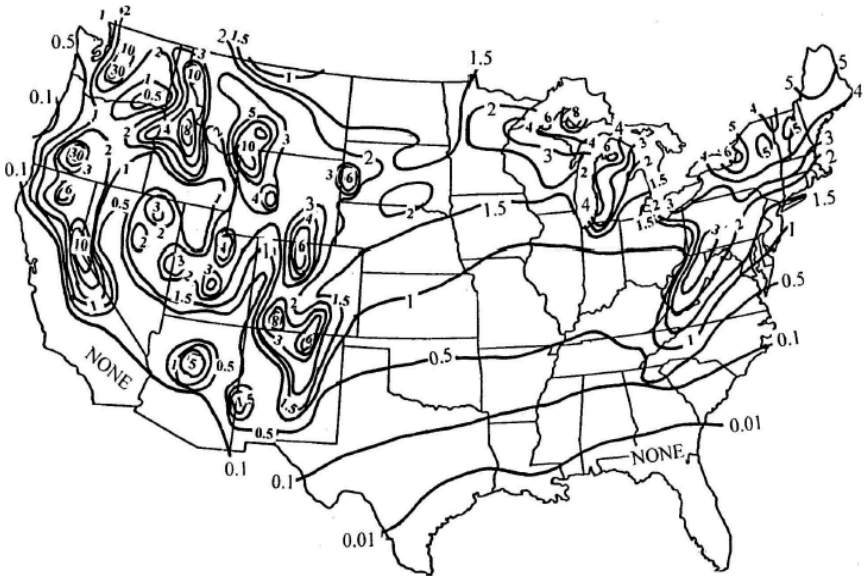

Figure 1.3: Annual average number of snowstorms 1901-2001, based on accumulation > 6 inch. From Changnon et al. (2006), their Fig. 2.

(excluding frictional effects). Depending on the characteristics of the surface airmass, and in the absence of reinforcing arctic air, winter precipitation accompanying this pattern was generally of short duration.

While the presence and maintenance of a shallow subfreezing surface airmass is essential for FZPCP, the low-level warm layer inversion (typically considered to be in the vicinity of 850 hPa, ~1km above ground) must be present and sustained in order for such precipitation to persist. Warm air advection (WAA) was demonstrated in the literature to be important to maintaining this layer against cooling associated with precipitation phase changes and vertical motion (e.g., Zerr, 1997, Rauber et al. 2001, Robbins and Cortinas 2002). Low-level veering of winds from northerly/northeasterly to south/southwesterly around 850 hPa is common. Robbins and Cortinas (2002) evaluate quasi-geostrophic (QG) advection and vorticity, finding that WAA tends to dominate at low levels (~850 hPa) in FZPCP north of stationary fronts, while differential vorticity advection becomes important as forcing for ascent in well-developed cyclonic systems. The temporal persistence of WAA relates to the synoptic-dynamic evolution of the system. Persistent freezing rain events over the U.S (e.g., Rauber et al. 1994, Gyakum and Roebber 2001) and elsewhere, including the prolonged damaging Chinese ice storm (e.g., Bao et al. 2010, Sun and Zhou. 2010) have noted pronounced circulation anomalies, including slow moving strong southwesterly flow and moisture advection from the subtropics, propagating disturbances promoting ascent, and continual replenishment of surface cold air through mesoscale (e.g., ice melting and sublimation regarding warm front northerly movement, Rauber et al. 1994), and

synoptic processes (e.g., persistent northerly component winds, slow moving or blocked flow promoting quasi-stationary arctic airmass and baroclinic zone).

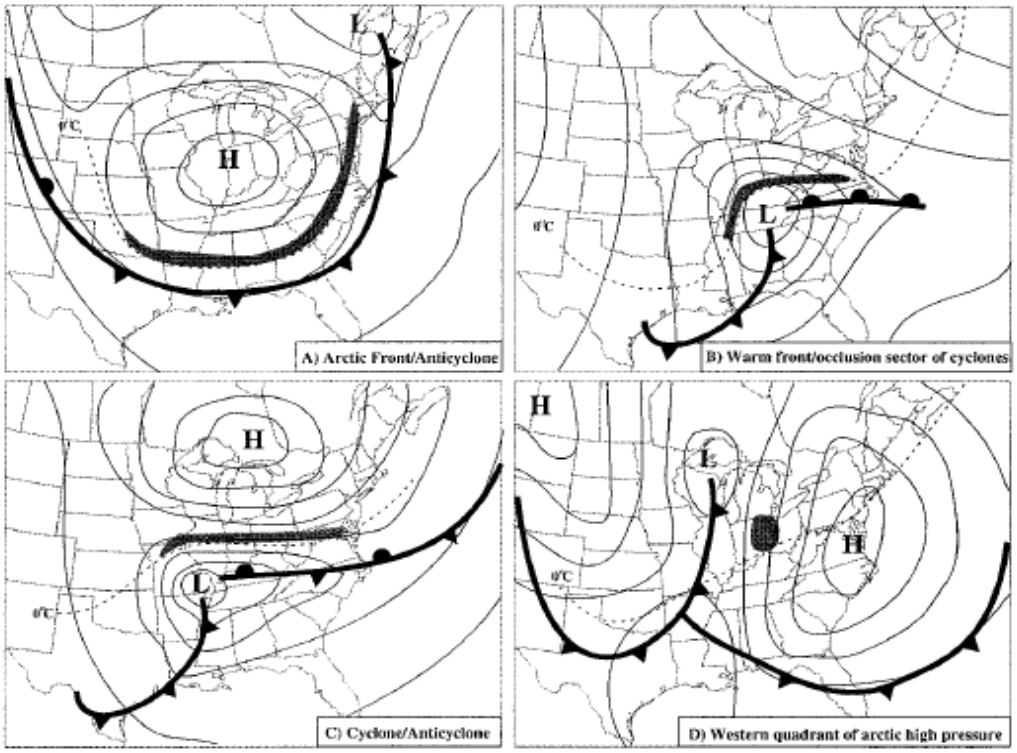

Figure 1.4: Non-terrain surface synoptic archetypes for freezing precipitation, from Rauber et al. (2001), their Fig. 2. Shaded area indicates region where freezing precipitation was observed. Archetypes manually identified from sounding analysis.

1.5 Thermal Features of Freezing Precipitation

An introduction to general properties of freezing and frozen precipitation was given in section 1.2. However, the evolution of each mixed phase winter storm tends to be different with regard to the placement of key thermodynamic parameters as mesoscale and microscale processes heavily influence the amount and duration of a given precipitation phase. A goal of past research has been to distinguish thermodynamic properties of ice pellets from freezing rain. Freezing rain can lead to

destructive ice accretion, whereas ice pellets largely accumulate at the surface, posing less threat to elevated structures (Lackmann 2011 p225). It is well known that the characteristics of the warm layer (depth, maximum temperature, saturation) are important to the formation of both hydrometeor types (Stewart and King 1987, Martner et al. 1993, Zerr 1997). Climatological studies by Rauber et al. (2001), Robbins and Cortinas (2002) have identified typical bounds on warm and refreezing layers associated with freezing rain. For example, Rauber et al. (2001) find that when a warm layer is present, 80% of freezing rain cases exceed +2^{o}C, 50% exceed +4^{o}C, and 30% exceed +6^{o}C, with a mean (mode) of +5^{o}C (+3^{o}). Studies have also identified a strong statistical relationship between warm layer depth and its maximum temperature. For example, Zerr (1997) analyzed 34 freezing precipitation case studies and found a correlation of 0.71. Rauber et al. (2001) obtain a similar result (0.8) using a far larger dataset (820 soundings). They suggest that this relationship is a natural result of the fact that a dry-adiabatic lapse rate must be supported above the inversion, and thus a greater central temperature implies greater layer depth exceeding 0^{o}C.

For the surface subfreezing layer, Rauber et al. (2001) report 84% of events with temperature < -2^{o}C, 53% of events < 4^{o}C, and 22% of events < -6^{o}C, with a mean and mode of -5^{o}C and -3^{o}C respectively (implying national average warm and refreezing layer temperatures roughly symmetric around 0^{o}C). Robbins and Cortinas (2002) find a median minimum refreezing layer temperature of -2.9^{o}C, where the minimum temperature was located on average a few hundred meters above ground level. Layer depths average around 600-800m, with a range of 400-1100m. Unlike the warm layer,

there is no clear linear relationship between refreezing layer depth and its minimum temperature (e.g., Rauber et al. 2001, Zerr 1997).

Zerr (1997) applied a theoretical melting and freezing heat transfer model, using observed FZPCP thermodynamic profiles, and assuming different particle mass sizes. His results demonstrated (i) a size dependence of the warm (refreezing) layer temperature required to completely melt (freeze) a falling hydrometeor, (ii) A cooler refreezing layer promotes refreezing of the particle (ice pellets), especially if the warm layer was not sufficient to completely melt it. Figure 1.5 shows Zerr's plot of particle mass against temperature for both layers. This conceptual study was highly idealized, considering a single hydrometeor with constant vertical velocity, irrespective of phase changes, and a relative humidity of 100%. The initial particle was also assumed to be a dendritic snowflake as in Mitra et al (1990). It was recognized that all of these factors can have a large impact on precipitation type. For example, a subsaturated profile introduces evaporative cooling, increasing (decreasing) the distances required for complete melting (freezing). Multiple falling hydrometeors introduce added complexity as they interact with one another, increase sensible and latent heat transport, assume a spectrum of different sizes, and thus the potential for mixed phases. The introduction of ice nuclei within the refreezing layer may also support partial refreezing of hydrometeors. Furthermore, not all FZPCP scenarios start with spherical particles aloft. Zhang et al (2010) used remote sensing techniques to evaluate particle shapes and size distributions within Southern Plains winter storms, identifying a high degree of variability. In many cases weak vertical motion and ample moisture provide an environment that is conducive to the formation of highly non-spherical aggregates.

The microphysical complexity of FZPCP is the fundamental reason for a relative lack of success in creating nationally consistent algorithms to enable forecasters to distinguish between freezing rain and ice pellets. Early algorithms evaluated low-mid atmospheric thickness (e.g., 1000-500 hPa) and empirically derived thresholds to distinguish rain from snow, and eventually freezing rain and ice pellets, using thickness measures in the lower atmosphere (e.g. 1000-900 hPa, 850-700 hPa). More recently, the entire thermodynamic profile has been evaluated to determine precipitation phase (e.g., Ramer 1993, Baldwin et al 1994, Bourgouin 2000). Czys et al. (1996), in an approach similar to Zerr (1997), modeled a single ice sphere's descent through a given thermodynamic profile. The final phase of the sphere was diagnosed from the ratio of the time the sphere is present in the warm layer, and the theoretical time for complete melting. Cortinas et al. (2000,2002) advocate that using a selection of algorithms to diagnose precipitation type from model output may be more beneficial than a single approach. This probabilistic assessment can be used to determine a 'most likely' precipitation phase for a given situation, methodology that accounts for inherent uncertainty in the simplifying assumptions for each.

1.6 Regional Analyses

Regional analyses of FZPCP have included the Canadian Arctic (Roberts and Stewart 2007), central and eastern Canada (McKay and Thompson 1969, Strapp et al 1996, Laflame and Periard 1998, Stewart and Issac 1999, Ressler et al. 2012), the northeast U.S (Castellano 2012, DeGaetano 2000, Gyakum and Roebber 2001), east coast/mid Atlantic (Forbes et al. 1987), southeast (Gay and Davis 1993, Ramos DeSilva

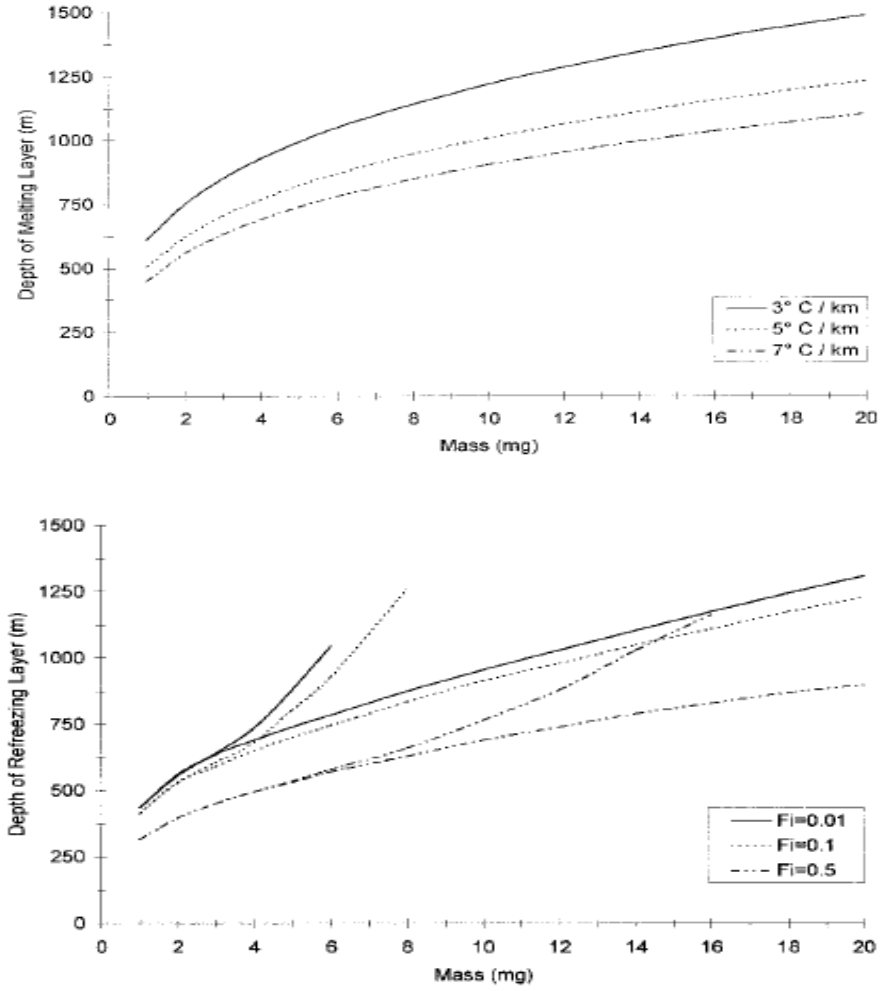

Figure 1.5: Top: Hydrometeor mass versus depth of warm layer required to melt 99% of this mass. Each curve represents a different lapse rate. Bottom: Mass versus depth of a layer required to refreeze a hydrometeor with initial fractions of ice between 0.01 and 0.5 for lapse rates of -5 K/km and -10 K/km. From Zerr (1997), his Fig 13 and 14.

et al. 2006, Fuhrmann and Konrad 2013), the Midwest (Riehl et al. 1952, Rauber et al. 1994), and the Great Lakes (Cortinas 2000). At least a couple of studies examined radiosonde profiles at multiple locations in order to point out regional variability in thermodynamic structure (e.g., Bernstein 2000, Robbins and Cortinas 2002). Further regional research is ongoing, with initiatives in the Northeastern US (e.g., Castellano,

Bosart and Keyser, Suny-Albany), and the Southern Plains (this Dissertation, Oklahoma Climatological Survey/Southern Climate Impacts Planning Program).

The results of these studies show a high degree of variability of features ranging from synoptic to micro-scale. Bernstein et al (2004) posits that variability results from the position of a region with respect to storm tracks, large bodies of water, and topography. For example areas of topography, especially N-S orientated mountain chains, were favored locales for FZPCP due to cold air that can become trapped at low levels through ageostropic pressure gradient flow (e.g., Forbes et al. 1987, Roebber and Gyakum 2003). The proximity of a given domain to a large water source, such as an ocean, influence the magnitude of the warm layer and the availability of moisture. In Bernstein's (2000) analysis, warm layers, along with increasing amounts of freezing rain and ice pellets relative to freezing drizzle, appeared more prevalent in locations including Pennsylvania, central North Carolina and Maine. As well as favorable topography, these sites were all proximate to the Atlantic Ocean, and so Bernstein, and later Gyakum and Roebber (2001), Robbins and Cortinas (2002), Fuhrmann and Konrad (2013) have attributed the generation and maintenance of the warm layer to low-level advection of moist subtropical maritime air. Bernstein considered two other locations within close proximity to water, one in the Pacific Northwest. In this case, observed warm layers were shallow and had temperatures only slightly above 0^{o}C, which Bernstein linked to cooler sea surface temperatures (SST) of the northern Pacific. The second location, in northern Wisconsin (Green Bay), was adjacent but west-southwest of the Great Lakes, and tended to experience a much greater proportion of freezing drizzle, especially when winds had a long fetch over the lakes. The propensity for

freezing drizzle over freezing rain is likely synoptically driven, with large-scale weak ascent over stationary fronts being the primary mechanism for the former.

The synoptic pattern that generates FZPCP was seen to vary markedly with location. For example, in the eastern U.S, many events are associated with the passage of a surface cyclone to the south/southeast, and in some cases, the development of a secondary cyclone (e.g., Robbins and Cortinas 2002, Cortinas et al. 2004). Further west within the Great Plains, FZPCP may be more frequent with arctic anticyclones (e.g., Rauber et al. 2001, pattern A), however a unified region-by-region synoptic classification remains to be evaluated. We can surmise, based on these studies, that FZPCP frequency, type, and severity is regionally determined. Figure 1.6 demonstrates an example of regional thermodynamic variation from Robbins and Cortinas (2002). In general:

(i) Proximity to warm oceans is associated with higher moisture content and greater warm layer temperature/depth.

(ii) Freezing drizzle may be more common further north, and is frequently associated with arctic anticyclones.

(iii) The synoptic pattern that contributes the most FZPCP varies with location.

(iv) Southern latitudes experience less frequent winter storms, but a greater proportion of these are mixed phase. Cortinas et al (2004) hypothesize that this is due to preponderance of shallow cold air on the leading edge of Arctic airmasses, better sustaining a mixed phase thermodynamic profile.

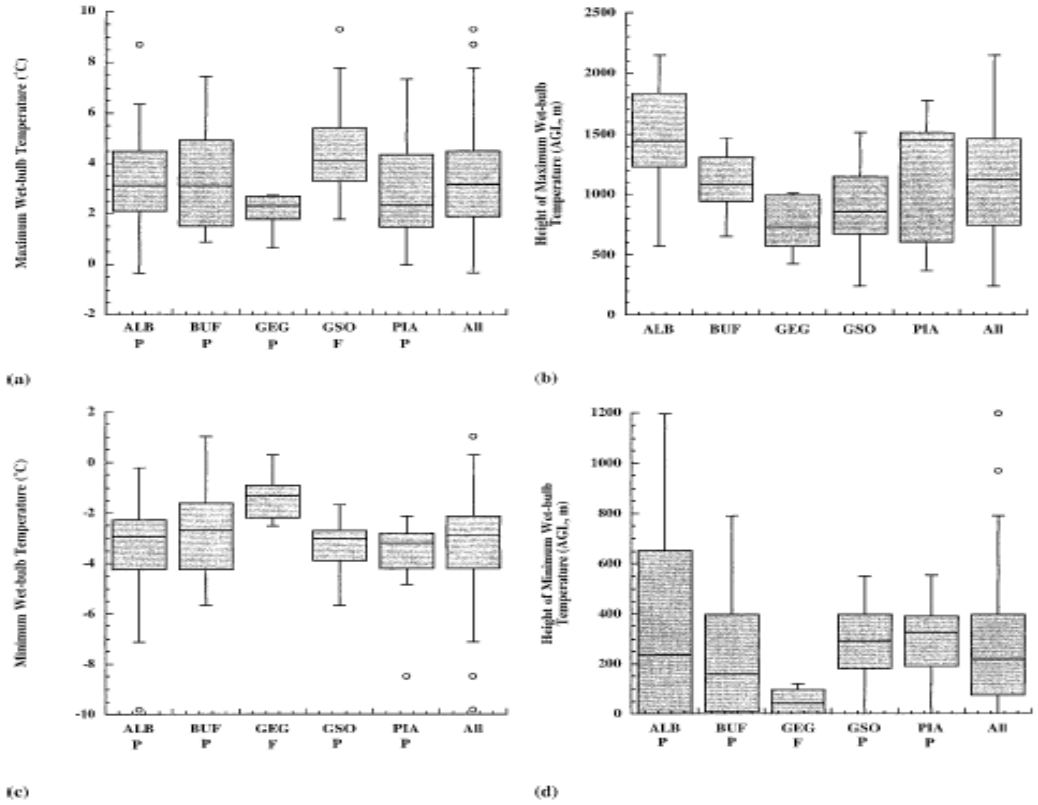

Figure 1.6: (a) Maximum wetbulb temperature (^{o}C); (b) of max wetbulb temperature; (c) low-level minimum wetbulb temperature; (d) height of low-level minimum for all cases in the dataset. Each box encloses 50% of the data. ALB = Albany NY, BUF = Buffalo NY, GSO = Greensboro NC, GEG = Spokane WA, PIA = Peoria IL, All = All soundings. Note the distinctive differences in the median and spread of each variable with location. From Robbins and Cortinas (2002).

1.7 Large Scale Dynamics

An aim of this dissertation is to relate the evolution and precipitation characteristics (e.g., intensity, phase), to the larger scale environment. Determining links with global circulation anomalies including atmospheric teleconnections is outside the scope of this work. Focus in instead on the concept that '*the sensible weather that results from a particular circulation pattern is highly dependent on details of the airflow'* (Roebber and Bosart 1998, Fuhrmann 2011). In other words, the intensity and precipitation phase of a given winter storm is a function of the characteristics of the

regional environment and the air masses ingested into the system. A lagrangian method for examining airflow is through calculation of air parcel trajectories. Gyakum and Roebber (2001), Fuhrmann (2011), Fuhrmann and Konrad (2013) examined back-trajectories (a trajectory integrated back in time from a point and time of interest) for several winter storms. Gyakum and Roebber (2001) computed 3-week trajectories incident to heavy freezing rain within the severe 1998 northeast ice storm. Low-level air parcels spent considerable time near the surface over the subtropical Atlantic Ocean. Diabatic heating and moistening advected very high values of equivalent potential temperature (θ_e ~330K) into the precipitation region. Five synoptic analogues for this event all showed differing θ_e evolutions, related to their path and altitude above the marine boundary layer, implying that despite similar synoptic features (e.g., location of pressure systems, trough), the evolution of event-specific air masses may be distinctly different.

Fuhrmann and Konrad (2013) examined trajectories for near surface, warm layer, and dendritic growth zone within snowstorms and ice storms in central North Carolina. They also observed that the establishing of the warm layer was the result of diabatic processes accumulating heat and moisture along the trajectory path, thermodynamic characteristics of the source region, and/or the region over which the air parcel spends much of its time. Like Gyakum and Roebber (2001), Furhmann and Konrad (2013) identified that air parcels residing for long durations in the marine boundary layer (PBL) of the subtropical Atlantic were associated with warmer, moister warm layers, which is illustrated in Figure 1.7. Snowstorms typically had more northerly trajectories and/or air parcels remaining aloft of the marine PBL.

By focusing on the generation and maintenance of the warm layer, the above results place considerable emphasis on the role of adjacent oceans. Only one paper by Ramos De Silva et al. (2006) attempted to directly relate ocean SST to the evolution of FZPCP. In that study, uniform Atlantic SST anomalies (SSTA) of ±2°C, ±4°C were imposed within a regional domain of the RAMS numerical weather prediction model (Pielke et al. 1992, Walko and Tremback 2001), and the thermodynamic and precipitation response examined for an ice storm in the southeastern U.S. The results supported a significant relationship between SSTA and the depth and magnitude of the warm layer for the analyzed case study. A more positive SSTA produced a moister, warmer inversion, shown in Figure 1.8, and a greater proportion of freezing rain. Negative SSTA was associated with a weaker warm layer, and relative increases in ice pellets and snow. This result was further supported by a linear regression between observed warm layer properties and weekly mean SST during FZPCP. The SST perturbation magnitude primarily evaluated in this work was beyond physical limits, largely to promote trend identification. As an extension to the above, and recognizing the repetition of this research question in the literature (e.g., mentioned by Castellano 2012, and Fuhrmann 2011 as a topic for further study) we apply a more nuanced set of perturbations based on realistic fields to produce a more physically constrained assessment of the magnitude of association between SSTA and warm layer evolution.

For the SGP, the Gulf of Mexico (GOM) is the closest ocean basin by distance, and is also well known to influence sensible weather over the domain. The GOM primarily influences SGP meteorology through the advection of moisture. Wintertime interior SST is typically on the order of 20-25°C, which yields ample moisture given

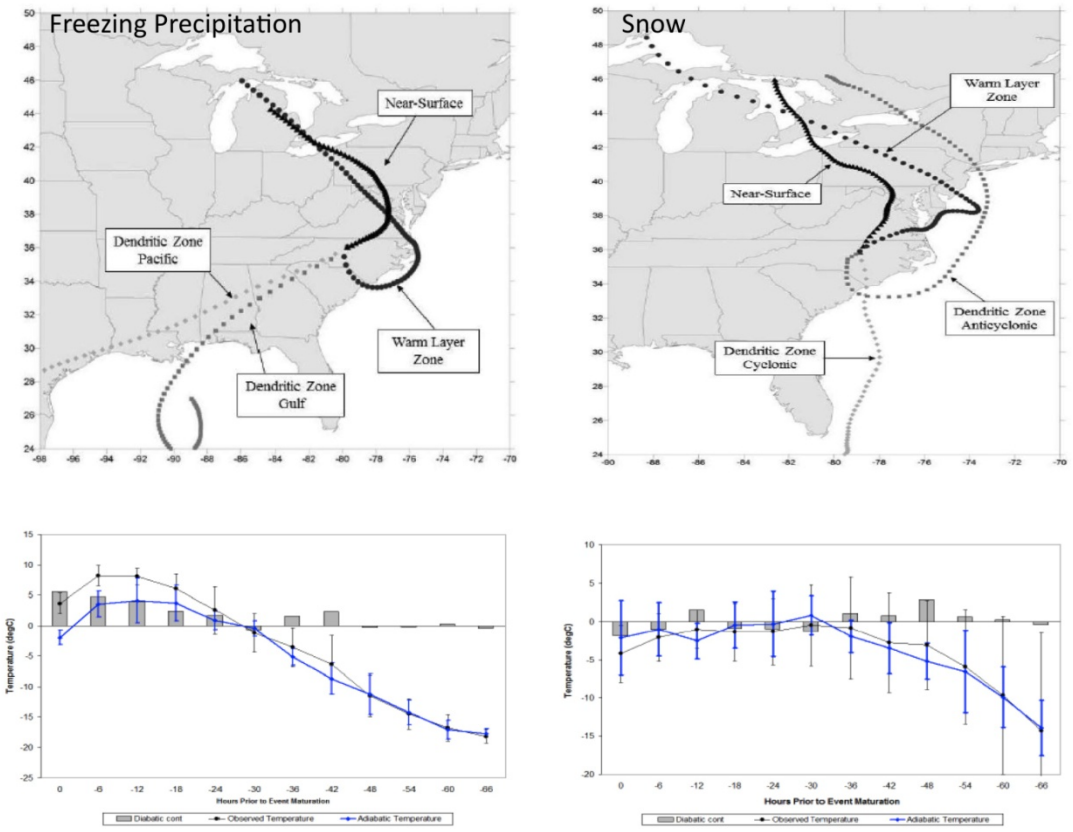

Figure 1.7: Top: Airmass trajectories (calculated using NOAA HYSPLIT model) for ice storms (left), and snowstorms (right) in central North Carolina. Bottom: Adiabatic and diabatic contributions to temperature variations within the low level warm layer for a subset of ice storms (left) and snowstorms (right). From Fuhrmann (2011).

appropriate atmospheric conditions. The role of SST in the thermodynamic evolution of winter precipitation is hypothesized to be important to the evolution and regulation of precipitation phase – and thus the severity of SGP ice storms. Further literature discussion of GOM SST variability is presented in chapter 4.

1.8 Dissertation Content

This dissertation content is outlined below by chapter. This work incorporates a broad set of topics, including synoptic-dynamic meteorology, climatology, numerical

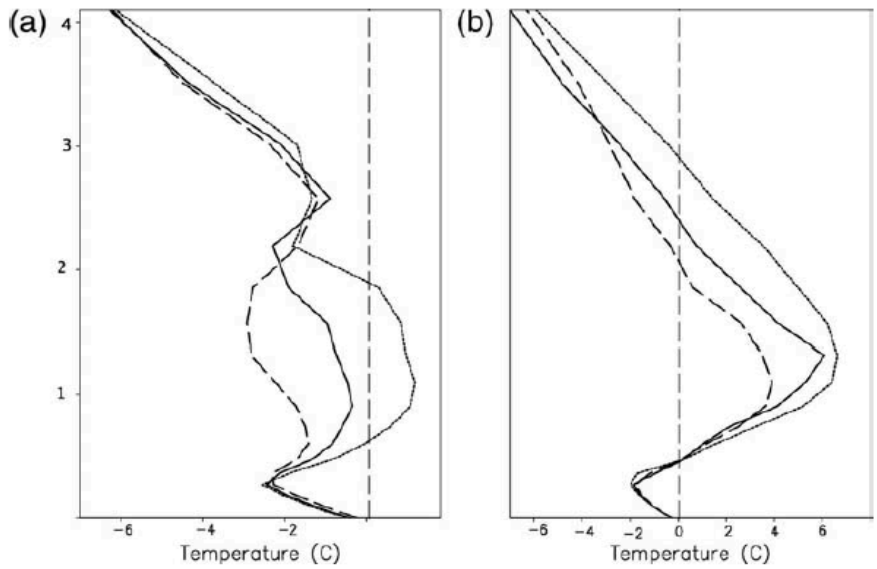

Figure 1.8: Air temperature profiles (^{o}C) for control (black line) and perturbed Atlantic SST simulations (-4 ^{o}C = dashed line, +4 ^{o}C = dotted line) near Greensboro, NC at two times during an ice storm (a) 2100 UTC 4th Dec 2002, (b) 0400 UTC 5th Dec 2002. From Ramos De Silva et al (2006), their Fig. 7.

modeling, lagrangian airflow characteristics, microphysics and large-scale climate, all within the context of understanding SGP freezing precipitation. This research should hopefully be useful to forecasters, climatologists and modelers, and the preliminary nature of some of our results sets up a platform for future regional analyses/extension. Chapter contents include:

Chapter 2: *A Regional Climatology of Winter Precipitation over the Southern Great Plains:* Background and methodology are presented on the manual compilation of a database of winter weather for the study domain 1993-2011. Using this database, spatial and temporal distribution of freezing and frozen precipitation are analyzed for the region. Using upper air data, the thermodynamic characteristics of freezing precipitation within the domain are examined, and placed into a national context, including comparison with prior studies.

Chapter 3: A Synoptic Climatology of Southern Great Plains Winter Storms: 1993-2011: This chapter provides a preliminary synoptic climatology for winter storms within the domain, with an emphasis on elucidating features between snowfall events, and those with a distinct freezing precipitation component. Using principal component (EOF) and composite analysis, and considering a suite of variables from the North American Regional Reanalysis (NARR), common synoptic flow patterns are shown, and their specific characteristics described.

Chapter 4: Development of a WRF-ARW Sea Surface Temperature Sensitivity Study: Based on earlier results, and a brief summary of air parcel trajectories incident to the warm layer during freezing precipitation, a hypothesis regarding the relationship between sea surface temperature (SST) and the thermal/moisture structure of the warm layer is presented. In order to test this, a set of SST anomaly fields for the GOM is required. Background literature is considered on the nature of SST variability in the GOM, and the types of SST anomaly perturbations that can be utilized. The final set of SST anomaly fields for two ice storm case studies are presented and justified. Furthermore the observed evolutions of both cases are discussed.

Chapter 5: Configuration of the WRF-ARW: Validation of Control Simulations: In order to conduct a sensitivity study truthful to a given event, a reliable simulation of the actual unperturbed event must be obtained. Here we discuss the WRF setup, including the choice of physical parameterization schemes. Simulations of the December 9-11 2007 ice storm, varying two PBL and 4 microphysical schemes, are validated against a suite of observations, including the Atmospheric Radiation Measurement (ARM)

central facility, Oklahoma Mesonet, and NCEP Stage IV precipitation, in order to obtain the 'best' configuration. Model biases and uncertainties are summarized.

Chapter 6: Results of SST sensitivity study: December 9-11 2007: The results of the SST study are presented for the first case study. Four key variables and their evolutions are investigated. These variables include: precipitation, thermal profile, synoptic and mesoscale features (fronts, forcing for ascent, moisture transport), and cloud cover/radiation. The impacts of the SST perturbations are compared relative to the 'REAL' or control scenario. The chapter concludes with an estimate of the change in ice storm severity resulting from SST perturbations, where the amount of freezing rain and ice pellets is assessed using a basic algorithm developed by Bourgouin et al. (2000).

Chapter 7: Results of SST Sensitivity Study: January 28-30 2010: This case study had a markedly different synoptic evolution to the former, which yields some comparisons that can be made between them regarding the impact of SST perturbations versus the impact of the synoptic 'type' (see Chapter 3) on the warm layer. The outline of this chapter is essentially the same as above.

Chapter 8: Conclusions and Further Work: This summary chapter reiterates our key results and provides a deeper comparison between the two case studies used and their response to the SST perturbations. Further research questions and opportunities are described.

Chapter 2: Developing a Thermodynamic Climatology of Freezing Precipitation and Snow for the Southern Great Plains 1993-2011

2.1 Introduction

Chapter 1 provided literature background and context for this dissertation research. In this chapter, and chapter 3, techniques and insight from prior literature, notably Rauber et al. (2000,2001), Robbins and Cortinas (2002), Zerr (1997), are used to develop a regional climatology of winter storm events, and their synoptic and thermodynamic characteristics for the U.S Southern Great Plains (SGP). Readers should be aware that the geographical definition of SGP varies in the literature (e.g., compare this analysis to Lamb et al. 2012), so our domain may not necessarily correspond with other studies. Possibly due to event infrequency, winter storm climatologies, particularly for freezing precipitation (FZPCP), have not been attempted comprehensively for the region. This work aims to address this dearth of knowledge in a preliminary sense, and promote further research. Aims of this present chapter include:

i. Development of a winter storm database for the SGP domain 1993-2011 (Sec. 2.1).

ii. Evaluation of spatial and temporal distribution for freezing and frozen precipitation (Sec. 2.2).

iii. Examination of domain wide thermodynamic characteristics of freezing precipitation (freezing rain, drizzle, ice pellets) using upper-air profiles from several stations (Sec 2.3).

iv. Scientific and regional context of results through comparison with prior studies.

2.2 Spatial Analysis

2.2.1 Development of winter storm database

The SGP study region is shown in Figure 2.1. It encompasses 10 (8) degrees of longitude (latitude), including portions of Arkansas, Louisiana, Kansas, Missouri, Oklahoma and Texas. The domain is further subdivided into four equally spaced quadrants, created primarily to aid initial selection of winter precipitation events for inclusion to the database. Since each precipitation episode impacted a different portion of the domain, the quadrants provided a first order measure of location(s) of greatest impact. As spatial coverage of most winter storm events was typically large, it was not necessary to further subdivide the region at this stage.

Winter weather events encompassing ice storms, freezing precipitation, snowstorms and winter storms, between January 1993 and February 2011, were obtained using NOAA's National Climatic Data Center Center (NCDC) *Storm Event* database (http://www.ncdc.noaa.gov/stormevents/). A decision flowchart, shown in Fig. 2.2, illustrates the process by which the database was developed. *Storm Event* archives notable weather events by county, state, and approximate duration, providing brief descriptions of salient features. The designation of event type (e.g., 'ice storm', 'winter storm', 'winter weather', 'glaze') in some cases was inconsistent with the magnitude and/or type of the resulting event. For example, a 'winter storm' accompanied by significant icing, or a 'winter weather' event reaching the storm criteria established

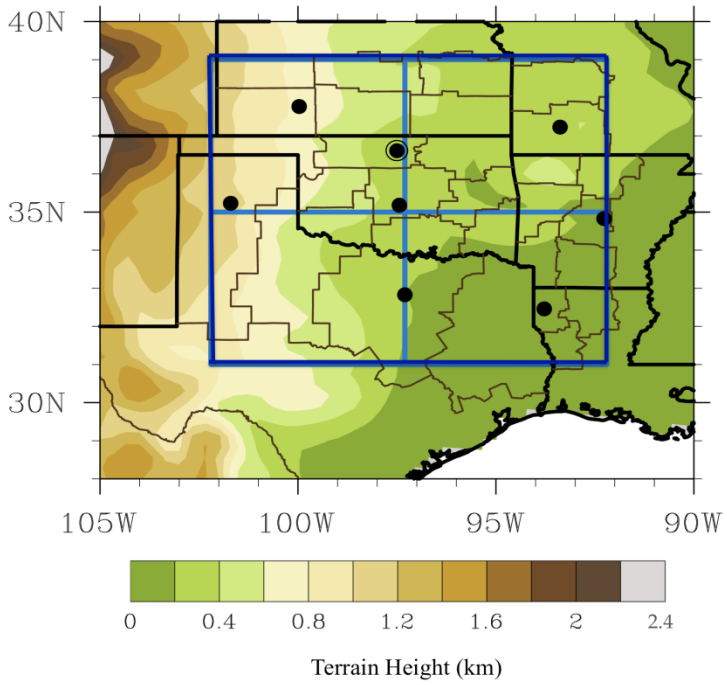

Figure 2.1: Map of the Southern Great Plains domain, including study region (dark blue box) and its quadrants (thin blue lines), NOAA climate divisions used (thin black lines), rawinsonde stations (black dots) with the ACRF Lamont site circled, and elevation above sea level (shaded, in km). Other rawinsonde stations are (from west-to-east) Amarillo (TX), Dodge City (KS), Oklahoma City (OK), Dallas-Ft Worth (TX), Shreveport (LA), Springfield (MO), and Little Rock (AR).

for this dissertation (see below). The text description was generally the most important aspect for event screening, providing more detail into socioeconomic disruption, location, and often maxima in ice/snow accumulations.

The first year (1993) for the present analysis was chosen to coincide with the start year of the online record when this research was initiated in 2010. Information of winter storm type, i.e., ice storm, freezing rain or drizzle, ice pellets and snow, were gathered separately for each state, and manually combined to form a database denoting the date, duration, quadrant locations and phase type(s) of each event traversing the

SGP[3]. A temporal gap of 48-hours (2-days) at a given location was required to class an event as a separate storm. As the *Storm Event* archive (and its corresponding *Storm Data* publication) provide brief quantitative estimate of precipitation accumulation, approximations for event impact were ascertained. Included cases typically had reported accumulation at any location ≥ 3 (trace to 0.1 in) inches of snow (freezing rain).

Given the qualitative nature of *Storm Event* archive/*Storm Data*, locations of precipitation and its attendant phase type were further appraised from NCDC surface analysis charts at 3-hour intervals. (http://nomads.ncdc.noaa.gov/ncep/NCEP), or from local station climate summaries for Oklahoma City (OK), Tulsa (OK), Wichita (KS), Dodge City (KS), Amarillo (TX), Dallas (TX), Little Rock (AR) and Springfield (MO), sourced from http://www.ncdc.noaa.gov/IPS/lcd/lcd.html. Events after 2005 were also documented using regional surface analysis at 2-hour intervals, available from the *Meteorological Case Study Selection* database (http://locust.mmm.ucar.edu/). This process of selection yielded nearly 160 individual winter storm events included to the dataset.

Unfortunately, no direct measurements of freezing precipitation (notably spatial extent) were readily available from the aforementioned sources, and this analysis was not restricted to a point location (e.g., compare Ressler et al. 2012, who evaluated a single site). Some past studies have utilized Automated Surface Observing Data (ASOS, e.g., Jones et al. 2004, DeGaetano, 2000) to consider sub- daily freezing precipitation, including time series and accumulation. The use of this dataset was outside the scope of this work, especially given the volume of data that would have been necessary to subset

[3] The *Storm Data* publication extends back to ~1950, however temporal considerations precluded development of a longer dataset at this stage.

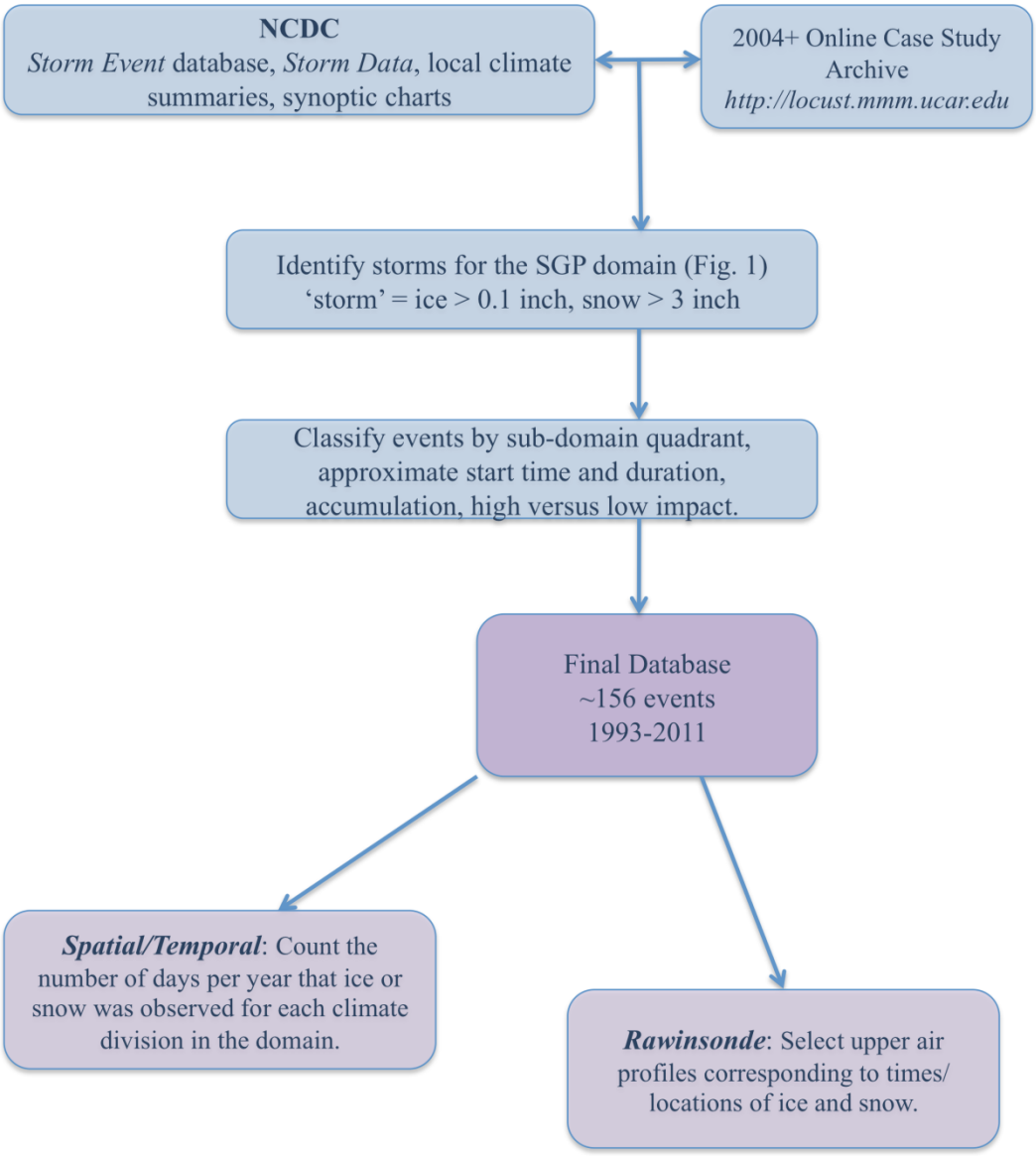

Figure 2.2: Flowchart summarizing the collection, criteria, and decision process for the spatial and sounding-based regional climatology described in section 2.2.1. The dissertation appendix, section 2, further documents this methodology.

and analyze. Freezing precipitation can be estimated from liquid equivalent precipitation, but this method struggles to accurately quantify individual phase proportions to the total accumulation during winter storms with rapid transition. One additional source of information used here to assess spatial extent and phase of

precipitation was obtained from the North American Regional Reanalysis (NARR, Meisinger et al. 2006, see chapter 3 for a description of this dataset), which includes variables that estimate the daily fractional coverage of a particular phase type (snow, freezing rain, ice pellets) based on the Eta model and using an algorithm based on Baldwin and Contorno (1993). Unpublished work by Blunden and Arndt (2011) used NARR data to construct climatologies for several station sites over Oklahoma, Arkansas. NARR captured the number of FZRA days and monthly trends for each station site, with inter-station uncertainties but no apparent secular bias.

From the information gathered from these sources, freezing (ice) and frozen (snow) precipitation events can be matched to NOAA climate divisions (CDs) over the domain (see appendix, sec 2 for example). The CDs used are shown in Fig. 2.1. Much of this investigation was manually intensive; fairly consistent with some prior methodologies utilized in the literature (e.g., Zerr 1997, Rauber et al. 2001, Ressler et al. 2012). Using the database, the number of days per calendar year that either freezing precipitation/ice or snow (freezing rain, drizzle and ice pellets are included in the definition of ice) were recorded to have been falling e.g. both a 1-hour or 12-hour precipitation episode would be given equal weight (1-day).

The spatial distribution of precipitation was evaluated by CD, subsequently normalized by CD area using a weighting factor (see appendix, section 2), and expressed as a frequency (days per year). *Storm Event* does provide some information on counties impacted, however, it was occasionally intermittent - available for some case studies and not others. The compromise was to evaluate over the broader spatial extent of the CDs instead (see appendix). This removes the potential for higher

resolution detail, but captures the gross nature of the ice and snow climatology of the region. It is likely that the values in this climatology may be underestimated, particularly as light, short lived and/or highly localized winter precipitation may not always be reported to the database. Future research could further develop this work by examining surface METAR/ASOS, Cooperative Observer and radar data. One might then be able to construct a higher resolution spatial analysis from more quantitative sources.

One additional caveat of particular note for *Storm Events/Storm Data* relates to the potential for reporting inconsistencies. Unpublished work by Kovacik et al. (2010) identified some abrupt changes in spatial ice storm frequency (2000-2009) between National Weather Service County Warning Areas (CWA) that indicated differing practices of local forecast offices regarding the designation of winter precipitation systems, particularly in terminology (e.g., 'ice storm' versus 'winter storm'). Given that our study is performed over less than 6 CWAs, along with use of multiple sources, and careful examination of event descriptions regardless of terminology, we hope to have minimized errors associated with reporting.

2.2.2 Spatial and temporal winter precipitation distribution

Figure 2.3 (a) and (b) display the spatial distribution of snow and ice by frequency of occurrence per CD, while the rightmost plot (c) expresses these as a ratio of ice to snow days (18-year mean). The distribution suggests a higher number of freezing precipitation events in the central and northeastern SGP, with some evidence of a southwest to northeast zone of higher frequency, noted previously by Kovacik et al.

(2010) and Grout et al (2012). Snowfall was more frequent in western and northern sub-sections, along with regions of elevated terrain in the east (Ozarks of northwest Arkansas). The elevated terrain (approx 1 km increase from east to west) of the western sub-region and upslope ascent may aid in winter precipitation development. This region is also potentially more remote with respect to low-level warm moist air conductive to a warm layer.

The ratio of ice events to snow events showed a northwest to southeast increase. This implies a higher proportion of winter storms with freezing (frozen) precipitation to the southeast (northwest). The lack of smooth transitions between CDs may reflect both their differing areas, relatively small sample, discrepancies in reporting frequency, possible human error (e.g., Branick 1997). Further work would be required to establish this conclusively. In addition, winter weather events can be localized, particularly freezing rain and drizzle, which can occur in narrow bands associated with the position of the 0^{o}C isotherm. Topographic variation (e.g., aforementioned Ozarks) likely promoted localized changes to event frequency.

Figure 2.4 shows the average annual distribution of events for each domain quadrant for the winter months of November through March. The overall frequency of winter weather increased south to north. Freezing precipitation is primarily confined to November-February, with peak frequencies in December and January. Snow events evidence broader seasonal distribution, especially in the western sub-domain, with a secondary peak in March. The unique ingredients that combine to create a suitable environment for freezing precipitation may control its seasonal distribution, specifically in the requirement of a shallow surface subfreezing layer. Rauber et al. (2001) suggest

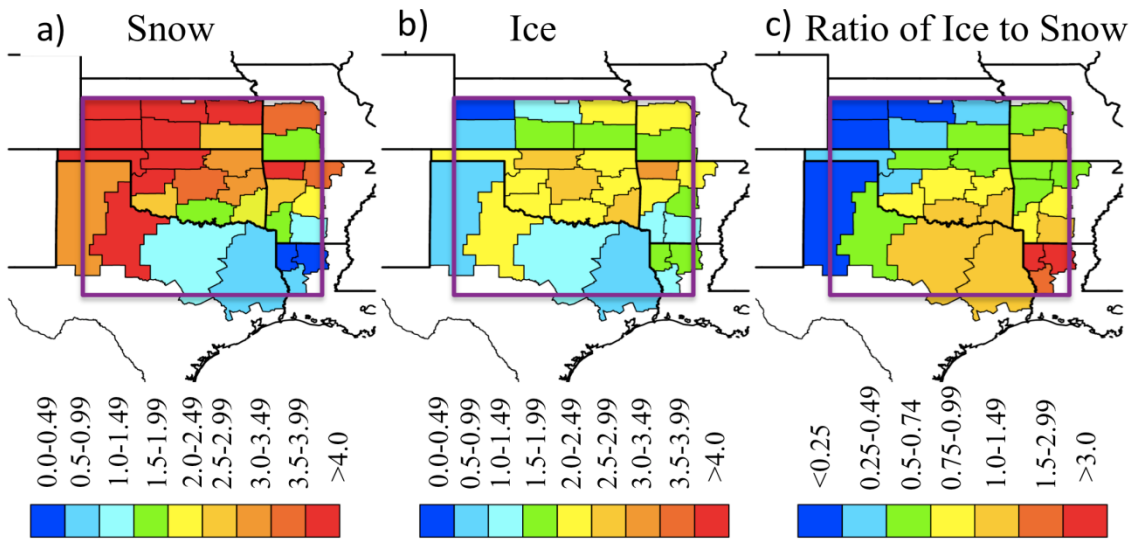

Figure 2.3: Spatial distribution of ice and snow events, expressed as average number of days per year, normalized by the total mean CD area to account for their differing size. (a) Snow (b) freezing precipitation (ice), (c) ratio of freezing precipitation to snowfall (days per year). Study region is enclosed in purple box.

that this commonly occurs along the leading edge and within a cold anticyclone. These airmasses are typically shallow, commonly developing over snow-covered regions of the Canadian arctic (e.g., Wang et al. 1995). This is due principally to the high albedo of snow, which induces radiative cooling of the overlying air (Namias 1962). High latitude snow cover tends to reach its maximum extent and depth during mid-winter, and thus the frequency of these airmasses may increase during this time. The seasonal pattern for freezing precipitation was similar to Changnon and Karl (2003). Nonetheless, we confirm the low overall frequency of winter precipitation, typically impacting less than 4 days per year (based on derived median).

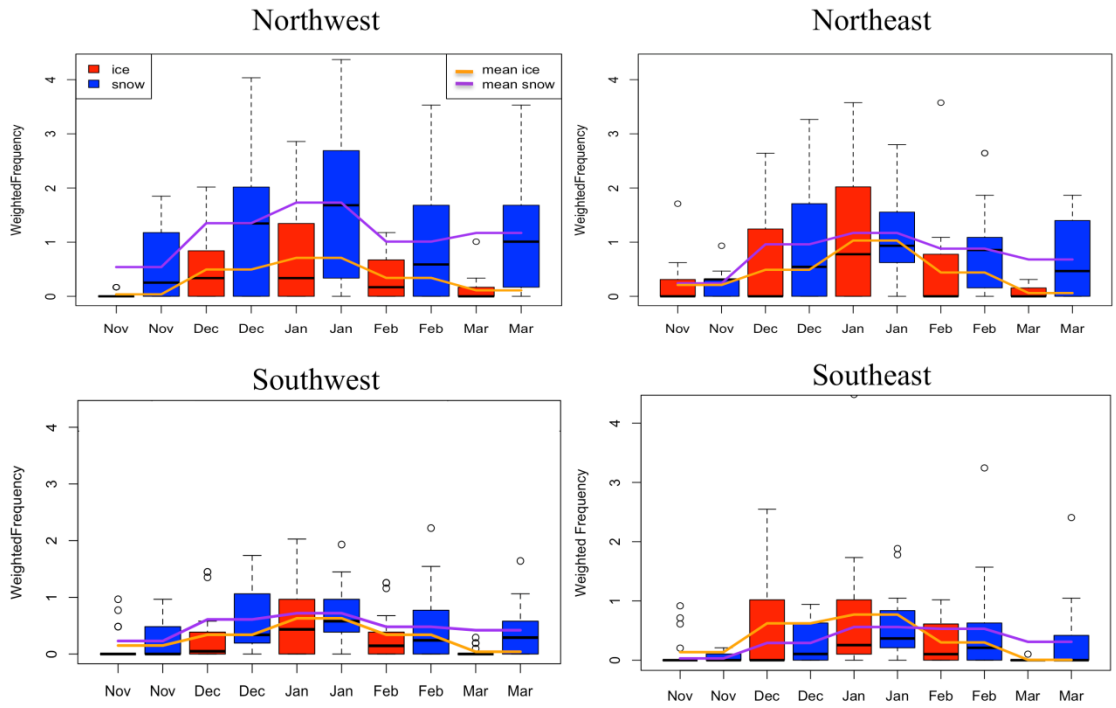

Figure 2.4: Average monthly variation of ice and snow events by quadrant during November-March. Frequency is number of days per month, normalized by CD mean area, with each CD assigned quadrants in which ≥ 50% of CD area resides. Box and whisker diagram shows the median (thick black line), interquartile range (colored box), 10th and 90th percentiles (horizontal bar) and extreme values (>90%, <10%, circles) for each month, valid 1993-2011. Lines give the monthly average normalized frequency for ice and snow.

2.3 Sounding Analysis

2.3.1 Methodology

The second stage of our regional climatology was to examine the vertical atmospheric profile characteristics of SGP winter storms. Given its thermal dependence and complexity, the focus was on freezing precipitation and its hydrometeor categories (freezing rain, FZRA; drizzle, FZDR; ice pellets, IP), however, a non-exhaustive small subset of snowfall (SN) events were examined for comparison. For this study, sounding profiles from eight locations were used (shown in Figure 2.1). Seven are National Weather Service operated, providing upper air profiles at 12-hour intervals for 00 and

12 UTC (06, 18 CST). Occasionally, extra soundings, typically at 06 or 18 UTC, are launched in advance or during significant weather. The final location is operated by the Department of Energy Atmospheric Radiation Measurement (ARM) program, located at their central facility (ACRF, Stokes and Schwartz 1993, Ackerman and Stokes 2003), generating higher vertical resolution research soundings every 6 hours (00, 06, 12, 18 UTC). The NWS soundings were obtained from the University of Wyoming online sounding archive, and the ACRF soundings from their archive (http://www.arm.gov/)

Winter storm precipitation soundings were identified from the aforementioned developed database. Soundings launched within 1-hour of a precipitation observation at or near the site were considered. 'Near' was difficult to define objectively, but typically referred to an adjacent observation or set of observations to the sounding site. A total of 97 (24) vertical profiles were obtained for freezing precipitation (snow). The freezing precipitation soundings were subdivided into categories including FZRA (light and heavy, 57), FZDR (21), IP (19), heavy FZRA associated with significant icing events (station site 24 hr or storm accumulations > 0.25 inch, 25), and light FZRA associated with weak icing (station site 24-hr or storm accumulations ≤ 0.25 in., 32).

The combination of limited domain, and limited temporal/spatial co-location of precipitation type produces a relatively small sample size for each category, particularly IP, FZDR and SN. Since the dataset was manually compiled and analyzed, it did take time to evaluate variables from each profile. A greater sample size could be generated by (i) evaluating cases prior to 1993, and (ii) reviewing the database and adding additional profiles that may have been missed. These results should be interpreted with the caveat that a larger dataset may alter the range and average magnitude of the

variables considered. In addition, the low sample size precludes the use of robust statistical evaluation. Despite these limitations, insight may be gathered from this study, which remains to be expanded upon.

The techniques used here are subject to the same limitations as previous sounding based analyses. A key uncertainty is the fact that surface observations and sounding data may not exactly coincide in time and space. Another is the likely underrepresentation of brief localized winter precipitation. Rauber et al. (2001) suggest that these caveats do not significantly bias their results. In most cases, nearby stations reported the same precipitation type, reducing the impact from non co-located information. Here, visual examination of surface observations temporally co-incident with the included sounding profiles yields conclusions consistent with Rauber et al's. (2001) assertions, with the possible exception of IP where nearby stations reported FZRA or FZDR (not shown), highlighting problems with delineating between phase in cases of rapid transition. With the expansion of dual-polarimetric radar though the NWS and SGP ACRF it may soon be possible to examine thermodynamic and microphysical environments associated with ice and mixed phase precipitation in much finer detail and exactly coincident in space and time.

From each sounding, variables relevant to the thermal, dynamic, cloud and microphysical characteristics of FZRA, FZDR, IP and SN were utilized. Thermal quantities include maximum and minimum wetbulb temperatures (T_w in the warm layer if present, and refreezing surface layer respectively), warm and refreezing layer depths (WLD, FLD), surface temperature, mixing ratio, height of maximum and minimum wetbulb temperatures (H_{max}) above ground level (AGL), and environmental melting

(EMP) and refreezing parameters (EFP). The EMP and EFP, developed by Robbins and Cortinas (2002), and derived from Pruppacher and Klett (1980), represent the effects of the environmental thermal profile on the melting and refreezing of ice particles. The form of EMP and EFP used are shown in Eq. 2.1 and 2.2.

$$EMP = \int_{zm_{base}}^{zm_{top}} -(T_0 - T_w)dz \qquad (2.1)$$

$$EFP = \int_{zf_{base}}^{zf_{top}} (T_0 - T_w)dz \qquad (2.2)$$

Where $T_0 = 0^oC$, and zm_{top} (zf_{top}) and zm_{base} (zf_{base}) warm (refreezing) layer top and base respectively.

Dynamic variables include wind speed, wind direction, speed and directional differences across the warm layer, or surface to 700 hPa layer if none was present. These choices were motivated by the observed importance of low-level WAA in developing and maintaining the warm layer (Zerr 1997, Stewart et al. 1995, Rauber et al. 2000, Robbins and Cortinas 2002). In addition, near-surface wind conditions can influence the severity of icing impacts, and the advection of surface cold and/or dry air, and thus the thermal profile of the refreezing layer.

Variables that describe cloud characteristics include cloud top temperature (CTT), cloud depth, cloud base height, number of cloud layers and the existence of convective potential instability (CI), as in Rauber et al. (2001). Cloud layers were identified from a sounding using profiles of relative humidity (RH), dewpoint depression and air temperature. Cloud base was defined as the first level at which temperature increases with height, coincident with near saturated conditions (RH>95%) or an increase in relative humidity to near saturation (Chernykh and Eskridge 1996).

The fraction of cloud aloft is considered a function of temperature and dewpoint depression, as in Arabey (1975), who noted that at least partial cloud coverage can still be present aloft ($T < -50^{o}C$) in relative humidities as low as 55%. However, the precipitation generation region within the cloud is typically defined as the highest layer with dewpoint depressions less than 2-3^{o}C (Rauber et al. 2000). In this study a threshold of 2.5^{o}C was used. Since the precipitating portion of the cloud is of primary interest, 'cloud top' is defined as the highest level with 2.5^{o}C sub-saturation (RH~84%). Cloud depths are the vertical depth over which this threshold is met, although layers less than 1 km deep with lower relative humidities may still be considered within the same cloud. Soundings with distinct and deep dry layers between near-saturated regions were assumed to possess more than one cloud layer.

The temperature at the top of the precipitation generation region (CTT) provides an indication of initial precipitation phase. For example, temperatures less than -10^{o}C imply the presence of ice nuclei and cold rain processes (Pruppacher and Klett 1997). Between -10^{o}C and 0^{o}C, Rauber et al. (2000) suggest that warm rain (collision-coalescence) processes operate, but the extent of this is unclear. Precipitation generation in this temperature range may be expected to contain lower concentrations of ice nuclei and higher concentrations of supercooled water. In some cases, the entire cloud may be located within the warm layer (CTT>0^{o}C). In others, freezing precipitation has been observed without a warm layer (Huffman and Norman 1988).

Sources of uncertainty related to the estimation of the aforementioned variables can include missing data, erroneous readings, rounding/interpolation errors in the calculation of thermodynamic metrics, such as layer depths bounded by the 0^{o}C

isotherm (which does not necessarily fall neatly on a measurement level). For ARM-SGP soundings, the vertical resolution was ultra-high at ~2 hPa, contrasted with NWS at ~25-30 hPa, Therefore errors in the former were negligible as the resolution was sufficient to resolve 0^{o}C levels bounding the warm layer. For the latter, sharp temperature changes between adjacent levels were observed at the warm layer intersection. Interpolation of the 0^{o}C height involved a simple linear procedure shown by equation A2.1 (appendix) that may depart from the 'true' layer height, but not by a large degree. In addition, the instrument has small measurement errors for each variable. A representative error for temperature, relative humidity and wind within the troposphere is around 0.2-0.5K, 5% and 3-5 ms^{-1} respectively (e.g. WMO 1996, McGrath et al. 2006). McGrath et al. (2006) note that an ascending radiosonde is steered by in-situ flow such that it may drift from its original location by as much as 200 km. Thus, it is conceivable that the soundings considered remain *within the synoptic storm system* but drift out of the location of freezing precipitation aloft. A comparison of cloud height data from the ACRF site, versus sounding derived cloud information (Figure 2.5), showed some distinct differences in the mid-upper troposphere. The ACRF cloud fraction data was radar/profiler derived and a measure of cloud directly above that location. Despite the advantage of the ACRF suite of cloud measurements, the radiosonde derived cloud cover was used for the sake of consistency with other domain station sites.

Missing data was not a significant problem as any affected variable was simply removed. Examination of each profile revealed no erroneous readings within the lower troposphere. An infrequent type of error aloft was a rapid drop in relative humidity,

possibly associated with the radiosonde exiting a cloud layer and encountering rapid drying (e.g., WMO 1996). One final caveat of note was the fact that, due to the limited number of case studies, the 97 sounding profiles are obtained from approximately 36 events of varied duration. Though no soundings were duplicated in location, soundings at the *same time* were evaluated at *different sites*. It is anticipated that processes on the meso- and micro-scale should vary to the extent that no two soundings will be precisely alike. It is expected that freezing precipitation soundings are biased toward longer duration, significant freezing precipitation, which produce the majority of observed icing to the SGP (Changnon 2003).

2.3.2 Thermal characteristics

Table 2.1 (a) and (b) summarize important thermal features associated with freezing and frozen precipitation respectively. The tables express these in terms of the *proportion of soundings;* a percentage of the total number of soundings in each category corresponding to the variable description (leftmost column). The table structure is similar to that of Rauber et al. (2000). Table 2.1(a) indicates that SGP FZRA can be highly variable in their vertical thermal structure, but were often distinct from IP. Our results were also generally consistent with prior sounding analyses discussed in chapter 1. Based on this sample, freezing precipitation in the region typically involved a warm layer, pronounced for FZRA during ice storms, where the majority (92%) of profiles exhibited maximum inversion temperature $\geq 5^{o}$C. Conversely, FZRA associated with light icing, FZDR and IP all indicated cooler warm layers (63%-73% with maximum $T_w \leq 5^{o}$C). This may reflect the possibility that such events contain a mixture of FZRA

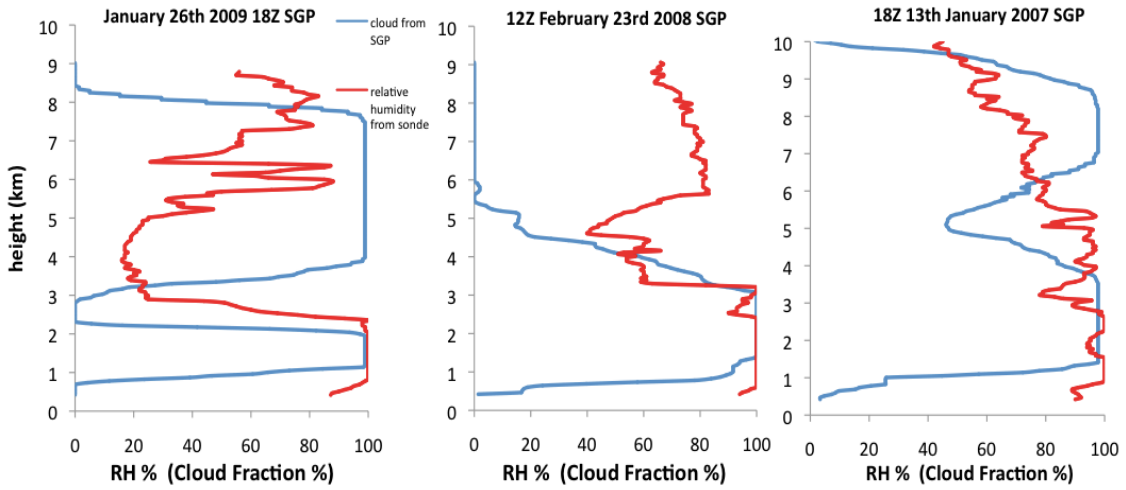

Figure 2.5: Vertical profile of cloud fraction (blue, %), derived from the ARM Southern Great Plains field site vertically pointing cloud radar and ARSCL products, contrasted with radiosonde-estimated relative humidity (red, %) for 3 separate freezing rain events. The drifting of the sounding with altitude likely contributed to the discrepancies at mid/upper levels of the atmosphere.

and IP, lowering the proportion of ice accumulation.

The elevation and depth of the warm and refreezing layers were determined from the WLD/FLD and heights of the maximum and minimum T_w. Deep (shallow) warm (refreezing) layers are found to be conducive to the complete melting of a falling hydrometeor, and subsequent supercooling, rather than refreezing. (Robbins and Cortinas 2002). Warm layer depth exceeded 2 km in approximately 47% of FZRA profiles. The majority of these high-depth cases affiliate with ice storms (84%). Conversely, light FZRA, and FZDR WLDs were typically shallower (21, 33% > 2 km respectively). IP in particular was infrequently associated with WLD > 2 km (16%). Given that WLD is significantly correlated to maximum T_w (Zerr 1997, Rauber et al. 2001), these results are consistent with expectations.

Only 4 of 97 profiles indicated no above-freezing inversion layer, 3 FZDR and 1

FZRA. The vertical profile of these cases (see composite sounding, section 2.3.5) was analogous to that identified by Rauber et al. (2000). The low number of observations may be both a factor of this phase type typically occurring for short durations, and often concurrently with light snowfall, or conditions where weak ascent, coupled with dry air aloft in the crystal growth zones promotes supercooled water. However, Rauber et al. (2000) did suggest that the spatial distribution of subfreezing-profile freezing precipitation showed a marked decrease in frequency with decreasing latitude. Additionally, Bernstein (2000), Robbins and Cortinas (2002) show FZDR maxima typically located over the northern half of the contiguous U.S, and immediately east of the Rocky mountains, the latter case often associated with weak saturated upslope flow (e.g., Bernstein 2000).

While warm layer characteristics of IP were not distinct from FZDR and light FZRA, IP evidenced a tendency to deep refreezing layers with nearly 53% of profiles exceeding 1 km FLD (compared to 21%, 24% and 28% for FZRA, FZDR and light FZRA respectively). Heavy FZRA only had 8% of events with FLD ≥ 1 km, and 36% ≤ 500 m. Refreezing layer temperature is also important in predicting hydrometeor phase as lower temperatures (≤ -5^{o}C) may support ice nuclei. Houze (1993), Wallace and Hobbs (1977) estimate ice nuclei concentration increases by a factor of ten for every 4^{o}C temperature decrease below freezing. IP had the coolest median minimum T_w (-7.5^{o}C, not shown), while FZDR also evidenced profiles with comparatively low T_w (median temperature -6.5^{o}C, not shown). The average FZRA profile showed a near 50/50 split between categories, with a median value of -5^{o}C (not shown). These aforementioned thermal results are further encapsulated in the EMP/EFP ratio. A

Table 2.1a: Thermal categories for SGP freezing rain, drizzle and ice pellet events. Hydrometeor sub-categories were defined in the text. Values expressed as the % of soundings that agree with the parameter/range. Shaded values indicate the greatest % agreement.

Parameter/Range	All	FZRA	FZDR	IP	Heavy (Ice Storm) FZRA	Light FZRA
Number of Rawinsonde Soundings	97	57	21	19	25	53
Maximum $T_w < 5^oC$	52.6	43.9	63.6	63.2	8.0	73.1
Maximum $T_w > 5^oC$	47.4	56.1	36.4	36.8	92.0	26.9
Max. T_w height < 1km	35.1	40.4	42.9	10.5	44.0	40.4
Max. T_w height 1-2 km	57.7	57.9	42.9	73.7	56.0	51.9
Max. T_w height > 2 km	7.2	1.8	14.3	15.8	0.0	7.7
WLD 1-2 km	37.1	33.3	33.3	52.6	16.0	44.2
WLD > 2 km	38.2	47.4	33.3	15.8	84.0	21.2
FLD 1-2 km	24.8	21.1	19.0	42.1	8.0	26.9
FLD > 2 km	3.1	0.0	4.8	10.5	0.0	1.9
FLD < 500 m	23.7	35.1	9.5	5.3	36.0	26.9
Minimum $T_w > -5^oC$	38.1	49.1	23.8	21.1	56.0	36.5
Minimum $T_w < -5^oC$	61.9	50.9	76.2	78.9	44.0	63.5
Ratio EMP/EFP < 1	49.0	42.1	40.9	78.9	8.0	59.6
Ratio EMP/EFP of 2-5	11.2	14.0	9.1	5.3	24.0	7.7
Ratio EMP/EFP > 5	23.6	33.3	13.6	5.3	56.0	11.5
Warm layer mixing ratio < 5 gkg^{-1}	28.5	28.1	40.9	15.8	12.0	42.3
Warm layer mixing ratio 5-7 gkg^{-1}	52.2	50.9	31.8	78.9	40.0	57.7
Warm layer mixing ratio > 7 gkg^{-1}	15.4	21.1	9.1	5.3	48.0	0
No Warm layer	4.2	1.8	14.3	0.0	0.0	5.8

notably high ratio was found for heavy (ice storm) FZRA, associated with the higher magnitude warm layer. Figure 2.6 shows the EFP and EMP associated with the freezing precipitation subcategories. The key result is that *the defining difference between severe and non-severe FZRA, assuming an adequate and comparable lifting mechanism for precipitation, is with the characteristics of the warm layer.* A pronounced deep and warm inversion also contain increased moisture (mixing ratio), with 88% of ice storm

Table 2.1b: As Table 2.1a but for a subset of snowfall events. Variables related to the warm layer are removed.

Parameter/Range	SN	Light SN	Heavy SN
Number of Rawinsonde Soundings	24	15	9
Maximum $T_w < 0^oC$	91.7	86.7	100.0
Maximum $T_w > 0^oC$	8.3	13.3	0.0
Max. T_w height < 1km	58.3	53.3	66.7
Max. T_w height 1-2 km	29.2	26.7	33.3
Max. T_w height > 2 km	12.5	20.0	0.0
Max T_w height at surface	54.2	53.3	55.6
Minimum $T_w > -5^oC$	12.5	13.3	11.1
Minimum $T_w < -5^oC$	88.5	86.7	88.9
900-800hPa mixing ratio < 2 gkg^{-1}	4.2	6.7	0.0
900-800hPa mixing ratio 2-5 gkg^{-1}	95.8	93.3	100.0
900-800hPa mixing ratio > 5 gkg^{-1}	0.0	0.0	0.0

FZRA exceeding 5 gkg^{-1}. IP also possessed on average a deep moist layer, but maximized between 5-7 gkg^{-1}, compared to ≥ 7 gkg^{-1} in the former case.

The thermal profile for SN events (stratified into heavy and light based on station site accumulation) are included for brief comparison. As anticipated, SN was favored when the vertical temperature profile is sub-freezing, with 87% (100%) of light (heavy) SN with maximum $T_w < 0^oC$. In two cases of light SN, $T_w > 0^oC$, one with maximum temperature at the surface, and the other aloft near 1700 m AGL. In neither case did this maximum exceed 1^oC. In 58% of events, the height of maximum T_w was in the lowest 1 km, with 54% at the surface. The remainder of cases; 47% (33%) light (heavy), had weak sub-zero inversion layers above 1 km. Temperatures near the surface were typically colder than most freezing precipitation profiles, with nearly 89% of events $< -5^oC$.

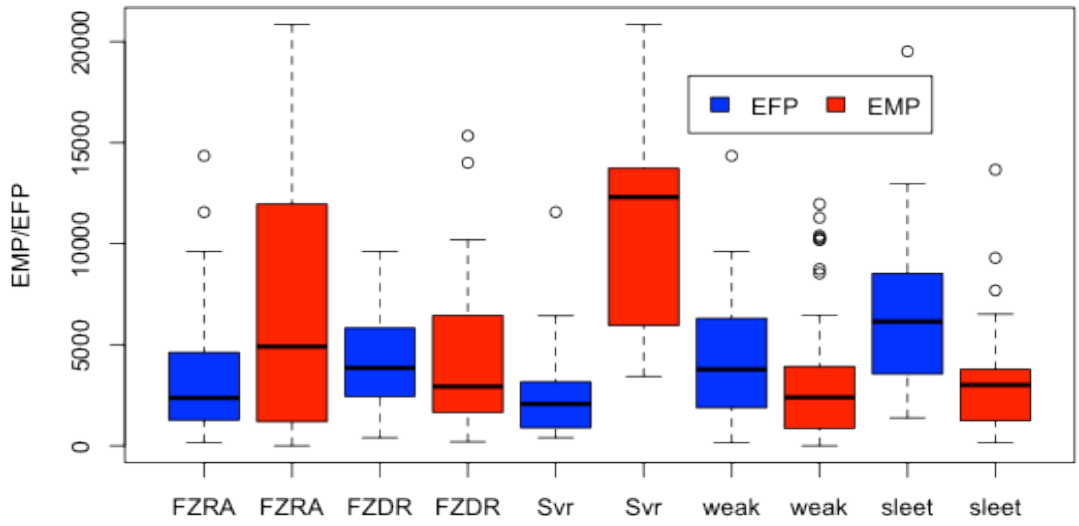

Figure 2.6: Environmental melting and freezing potentials for each freezing precipitation category. EMP/EFP are expressed as ^{o}Cm. 'Svr' indicates ice storm freezing rain, while 'weak' indicates lower accumulation or mixed phase freezing rain.

2.3.3 Wind characteristics

Wind speed and direction statistics are useful in elucidating information regarding air-mass sources, and inferring presence of warm and/or cold air advection (WAA and CAA respectively). The results of this analysis are shown in Table 2 (a) and (b) for freezing and frozen precipitation respectively. Additionally, Figure 2.7 displays wind roses for each hydrometeor type at the surface and 850 hPa. For all SGP freezing precipitation surface wind direction at the sounding location was typically north-northeasterly (62% IP to 72% FZRA), with southwesterly flow within/aloft of the warm layer (e.g., 180-270^{o}, 63% IP to 76% FZDR and heavy FZRA). IP was associated with slightly higher proportions of northwesterly (southeasterly) surface (850 hPa layer) flow. Northwesterly (300-360^{o}) surface winds were most common for SN (Table 2b, Fig. 2.8), presumably advecting cold air behind and to the north of a surface cold front.

In addition, winds during SN had a greater frequency of northerly component flow at low-levels (e.g., 50% at 330-90^{o} for the surface-700 hPa layer).

Approximation for the presence of WAA/CAA was ascertained from the speed and directional shear *across the warm layer* (roughly 900-700 hPa, or 850-700 hPa layer for snow). Light FZRA, FZDR events typically showed a lower magnitude change in wind speed and direction, or even a weakening of wind speed (29% of FZDR cases with change in wind speed < 0 kt). Speed shear of > 20 kt was most common for heavy FZRA (56%), which also experienced substantial veering in direction (52%, 60-200^{o}). While frictional effects near the surface may contaminate some of the signal, this implied low-level WAA aids to maintain the existence of the warm layer against cooling associated with melting hydrometeors, also promoting vertical motion and additional precipitation. The remaining freezing precipitation categories peaked in a more moderate speed shear range (0-20 kt), however directional veering was generally most frequent for all categories in the 60-200^{o} range. IP was associated with a slightly greater proportion of backed (negative) directional shear (26%, versus 8-15% for the other categories). This result may imply a transition to CAA at low-levels. SN events generally indicated stronger winds at the surface and aloft, especially the few heavy snow samples (67% with speeds > 15 kt at the surface, and 78% above 20 kt (850 hPa). Directional shear (850-700 hPa) indicated higher frequency of low-level backed flow (50%).

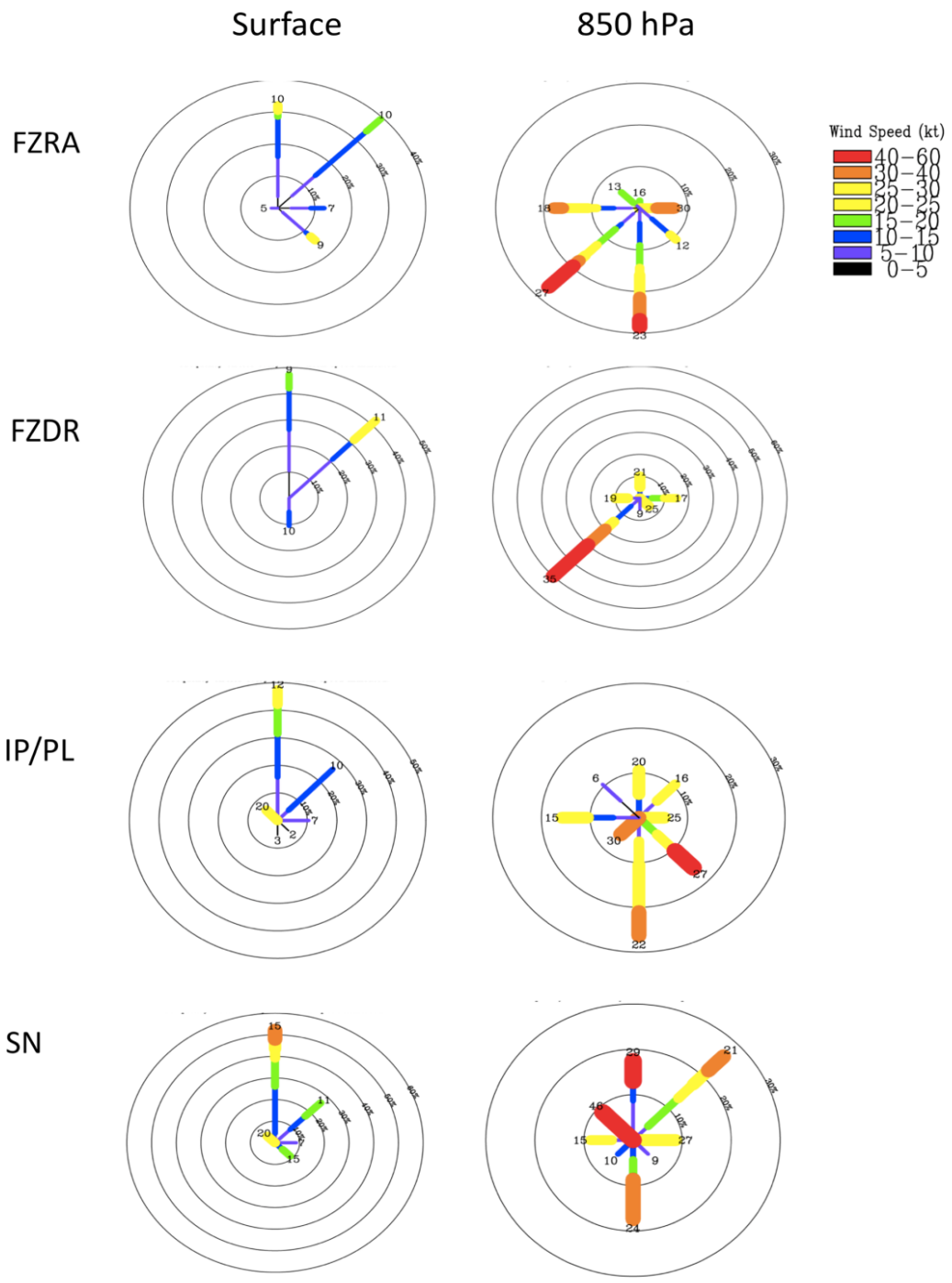

Figure 2.7: Wind roses for freezing rain, freezing drizzle, ice pellets and snow at the surface (left) and 850 hPa layer (right). Directions follow standard compass. Concentric rings indicate frequency increments of 10%, while shading is wind speed in knots. Values are binned into 8 directional bounds, N, NE, E etc.

Table 2.2a: Wind profile characteristics for SGP freezing precipitation. Table structure described in caption to Table 2.1a.

Parameter/Range	All	FZRA	FZDR	IP	Heavy FZRA	Light FZRA
Number of Rawinsonde Soundings	97	57	21	19	25	53
Wind Dir at surface 300-360^o	13.4	8.8	19.0	21.1	16.0	7.7
Wind Dir at surface 0-90^o	69.1	70.2	71.4	63.2	72.0	69.2
Wind Dir at maximum T_w 100 -179^o	18.6	21.1	4.8	26.3	8.0	21.2
Wind Dir at maximum T_w 180 - 270^o	66.0	63.2	76.2	63.2	76.0	61.5
Speed change (top-bottom) over warm layer 0-20 kt	51.7	47.4	52.4	63.2	40.0	50.0
Speed change over warm layer > 20 kt	33.0	38.6	23.8	26.3	56.0	25.0
Speed change over warm layer < 0 kt	19.6	14.0	28.6	15.8	4.0	25.0
Directional change (top-bottom) over warm layer 0-50^o	31.0	35.1	28.6	21.1	24.0	40.4
Directional change over warm layer 60-200^o	41.3	43.9	33.3	42.1	52.0	34.6
Directional change over warm layer < 0^o	14.4	10.5	14.3	26.3	8.0	15.4

Table 2.2b: Wind profile characteristics for a subset of snowfall events. Low-level directional changes estimated over the surface-700 hPa layer in lieu of no warm layer.

Parameter/Range	SN	Light SN	Heavy SN
Number of Rawinsonde Soundings	24	15	9
Wind Dir at surface 300-360^o	25.0	20.0	33.3
Wind Dir at surface 0-90^o	54.2	66.7	44.4
Wind Dir at 850 hPa100 -179^o	16.7	20.0	11.1
Wind Dir at 850 hPa 180-270^o	12.5	6.7	22.2
Wind Dir at 850 hPa 330-90^o	50.0	46.7	55.6
Wind Speed at surface < 10 kt	25.0	40.0	22.2
Wind Speed at surface >15 kt	37.5	20.0	66.7
Wind Speed at 850hPa <20 kt	50.0	66.7	22.2
Wind Speed at 850hPa > 20 kt	50.0	33.3	77.8
Directional change (top-bottom) over 850-700hPa 0-50^o	25.0	13.3	44.4
Directional change over 850-700hPa 60-200^o	20.8	20.0	22.2
Directional change over 850-700hPa = negative	50.0	60.0	33.3

2.3.4 Cloud characteristics

Inferences to cloud microphysics may be made simply by examining the thermal profile of a cloud resolved through a sounding profile. This analysis is similar to that of Rauber et al. (2000) who inferred cloud properties from freezing precipitation soundings over the contiguous U.S. Table 2.3 (a) and (b) shows the results for the SGP, using the definitions described earlier. Note that these definitions are merely *approximations of cloud cover*, uncertainties include aforementioned radiosonde drift, and precise levels for cloud base/top, e.g., pronounced near saturated surface layer and inversion complicating classical methods for obtaining cloud base (LCL). The region exhibits a range of CTT (RH ≥84%) related largely to the intensity of precipitation at the sounding location. FZDR for example had over 60% of events with CTT > -5^{o}C, while FZRA and IP have 68-88% with CTT <-10^{o}C. IP in particular evidences low CTT, with 50% less than -20^{o}C. Low cloud entirely embedded within a warm layer and/or shallow supercooled cloud layer were most associated with FZDR, with cloud depths typically ≤ 2 km - well documented by the aforementioned studies. FZDR soundings also had a greater proportion of cloud layers aloft, (43%), generally in the mid-troposphere (78% with upper CTT > -40^{o}C). It was not clear whether a seeder-feeder process was at work in some of these events, as a substantial dry air mass was observed to separate layers aloft. FZRA (including ice storms) also had nearly 40% of cases with more than one cloud layer, however the lowest precipitating cloud layer was notably deeper, and the upper cloud layer displaced further aloft (44% with CTT < -40^{o}C). No sounding produced a sub-saturated depth sufficient to qualify as a separate cloud layer for IP, however, caution should be implied when interpreting this result

physically due to the low sample size. Nonetheless, heavy FZRA and IP are associated with deep cloud layers and cloud top temperatures sustaining ice processes. In conjunction with their varied intensities and moisture availability (see also Table 2.1a, the depth of the near saturated (RH>95%) cloud layer was greater for IP and heavy FZRA (60-63%) than the other categories.

The cloud characteristics of snowfall (Table 2.3b) are also related to precipitation intensity. Heavier SN events have a vertical cloud profile similar to IP with typically a single deep cloud layer, and cold cloud top temperatures (100% CTT < -10^{o}C). Light snow has a more varied range of CTT (60% < -10^{o}C), with evidence of multiple cloud layers (40%). Typically for SN, the atmosphere is moist, with near saturated cloud depths exceeding 2.5 km in 38% of cases. Both light and heavy SN have cloud depths extending to 4 km, and 46% beyond 5 km. Temperatures within the uppermost near saturated layer were in the -12 to -19^{o}C range in 29% of cases (56% for heavy SN). Houze (1993) explains that the ambient supersaturation between ice and water is greatest in this temperature range, which increases the surface-to-volume ratio of the ice crystal. The primary habit of ice in this range is dendrites and sector plates. The structure of dendritic snow crystals promotes aggregation at -10 to -16^{o}C, as observations suggest the arms of the dendrites become entangled, resulting in enhancement of snowfall rates. For FZRA/FZDR where cloud top temperatures are warmer, the dominant precipitation growth mechanisms may take a variety of forms depending on the specific temperature and humidity structure.

Motivated by the conclusions of Rauber et al. (2001) and Robbins (1998), the potential for upright elevated convection was briefly assessed by evaluating temperature

Table 2.3a: Cloud properties of freezing precipitation in the SGP. See Table 2.1a for description of table structure. CTT estimated for all profile-estimated cloud layers.

Parameter/Range	All	FZRA	FZDR	IP	Heavy FZRA	Light FZRA
Number of Rawinsonde Soundings	97	57	21	19	25	53
Lowest layer cloud depth < 1km	9.3	7.0	23.8	0.0	4.0	15.4
Lowest layer cloud depth 1.01 – 4.99 km	44.3	38.6	76.2	26.3	36.0	53.8
Lowest cloud layer depth > 5 km	45.4	54.4	0.0	68.4	60.0	30.8
> 1 Cloud Layer	28.5	32.7	42.9	0.0	39.1	32.7
CTT > 0°C	19.8	12.7	57.1	0.0	13.0	28.9
CTT < 0°C (below warm layer)	1.0	0.0	4.8	0.0	0.0	1.9
CTT -5°C to 0°C	9.5	5.5	23.8	5.6	8.7	11.5
CTT -10°C to <-5°C	11.8	12.9	14.3	5.6	8.7	13.5
CTT -20°C to <-10°C	31.1	38.2	4.8	38.9	52.2	21.2
CTT < -20°C	28.0	30.9	0.0	50.0	17.4	25.0
Depth of near saturated cloud layer (RH ≥ 95%) < 500 m	7.2	7.0	14.3	0.0	8.0	9.6
Depth of RH ≥ 95% cloud layer 500 m to < 1.5 km	22.7	22.8	38.1	5.3	12.0	34.6
Depth of RH ≥ 95% cloud layer > 2.5 km	45.3	49.1	19.0	63.2	60.0	32.7
Temperature of uppermost RH ≥ 95% layer (°C) -18 to -12	1.7	5.7	0.0	0.0	12.0	0.0
Temp of uppermost RH ≥ 95% layer -10 to 0	56.6	59.6	42.9	63.2	44.0	63.5
Temp of uppermost RH ≥ 95% layer > 0	32.6	31.6	38.1	31.6	44.0	26.4
Combined depth of upper cloud layers < 2 km	37.0	38.9	33.3	0.0	55.6	29.4
Combined depth of upper cloud layers > 2 km	62.9	61.1	66.6	0.0	44.4	70.6
CTT of deepest upper cloud layer > -40°C	63.0	55.6	77.8	0.0	66.6	64.7
CTT of deepest upper cloud layer < -40°C	37.0	44.4	22.2	0.0	33.3	35.3
Presence of Convective instability	34.3	40.0	18.2	36.8	52.0	21.2

.

Table 2.3b: As Table 2.3a but for the snowfall subset. Dashed line (--) indicates missing or non-applicable information.

Parameter/Range	SN	Light SN	Heavy SN
Number of Rawinsonde Soundings	24	15	9
Lowest layer cloud depth < 1km	8.3	13.3	0.0
Lowest layer cloud depth 1.01 – 4.99 km	41.7	46.7	44.4
Lowest cloud layer depth > 5 km	45.8	40.0	55.6
> 1 Cloud Layer	25.0	40.0	0.0
CTT > 0°C	0.0	0.0	0.0
CTT < 0°C (below warm layer)	0.0	0.0	0.0
CTT -5°C to 0°C	8.3	13.3	0.0
CTT -10°C to <-5°C	16.7	26.7	0.0
CTT -20°C to <-10°C	33.3	20.0	55.6
CTT < -20°C	33.3	40.0	33.3
Depth of near saturated cloud layer (RH > 95%) < 500 m	8.3	13.3	0.0
Depth of RH ≥ 95% layer 500 m to < 1.5 km	25.0	26.7	0.0
Depth of RH ≥ 95% layer > 2.5 km	37.5	33.3	44.4
Temperature of uppermost RH ≥ 95% layer (°C) =-19 to -12	29.2	20.0	55.6
Temp of uppermost RH ≥ 95% layer = -10 to 0	25.0	40.0	0.0
Temp of uppermost RH ≥ 95% layer > 0	0.0	0.0	0.0
Combined depth of upper cloud layers < 2 km	8.3	13.3	0.0
Combined depth of upper cloud layers > 2 km	16.7	26.7	0.0
CTT of deepest upper cloud layer > -40°C	8.3	13.3	0.0
CTT of deepest upper cloud layer < -40°C	16.7	26.7	0.0
Presence of Convective instability within or above cloud layer	--	--	--

and pressure excess from the saturated adiabat, associated with lifting of an air parcel above the maximum warm layer wetbulb temperature for each vertical profile. Slantwise convective potential was not considered. The two aforementioned studies had concluded that precipitation in winter storms is generally non-convective. Rauber et al. (2001) had found the potential for convective instability in 12.5% of their sounding database, with only 0.8% exhibiting deep convective potential (defined as ≥ 300 hPa ascent). In this smaller regional analysis, the proportion of soundings possessing

instability, weak or strong, was much higher, approximately 34%. This proportion was highest for FZRA (particularly ice storms), and IP. Out of these soundings, only 25.7% (~9% total) possessed the potential for deep convection, with these profiles restricted to just 4 winter storms.

Table 2.4 considers the relationship between the maximum warm layer temperature and the presence of convection by way of a contingency table. The resulting values suggest that convective instability above the warm layer was more common with higher warm layer temperatures ($T>5^{o}C$). This may result from (i) increased lapse rate above the inversion, and (ii) warmer antecedent environment and/or stronger WAA and isentropic ascent. The presence of convection within winter storms complicates precipitation type forecasting, as higher vertical velocities in convective cells favor increased condensation rates of supercooled water, collected by ice particles to form graupel (Houze 1993). Graupel has a higher fall speed than snowflakes and aggregates (~0.5-1.5 ms^{-1}); observations suggest velocities of 1-3 ms^{-1}, increasing sharply with graupel diameter. Physically based precipitation type algorithms (e.g., Czys 1996) have traditionally assumed an approximately spherical snow aggregate as the initial hydrometeor type above the warm layer. In convection, this produces a potential overestimate of freezing rain if graupel is present. The enhanced precipitation rates that may be associated with hydrometeors in convective cells, along with downdraft cooling of the warm layer, mean that convective freezing rain can be brief, and often mixed with ice pellets. The observed connection between convective potential, and warm layer maximum temperature most likely is representative of the fact that *the freezing rain thermal profile can typically only be sustained during convection*

by high maximum warm layer temperatures.

Table 2.4: Contingency table demonstrating the relationship between observed maximum T_w (^oC) in the warm layer, and the presence of convection for freezing precipitation soundings.

Max T in the Warm Layer	Presence of Convection: Yes	No
Greater than 5^{o}C	20	19
Less than 5^{o}C	7	42

2.3.5 Composite precipitation type profiles and comparison to prior studies

The above results have demonstrated preliminary key characteristics of SGP FZPCP. As an additional summary, composite vertical profiles were constructed for each hydrometeor category using a subset of 10 randomly selected profiles (4 for no-warm layer FZDR, 9 for heavy SN), displayed in Figure 2.8 and Fig. 2.9 for FZPCP and snow respectively. The aforementioned notable differences between subcategories (Tables 2.1-2.3) were confirmed, most especially in the magnitude and depth of the warm layer, and the increase in moisture depth for heavy FZRA and IP events. Furthermore, the composite profile for FZDR further demonstrates the tendency for warm CTTs. Rauber et al. (2000) find that this profile is common to FZDR in the Southern U.S (their figure 3c). Cases with no warm layer appear to be associated with light drizzle, evidenced by very shallow cloud layers. This profile differs from light snow in that the near saturated region is shallower with a pronounced dry layer in the mid-troposphere near the dendritic growth region. Light snow profiles typically exhibit a deeper layer of higher relative humidity, with average CTT closer to -15^{o}C favoring the development of snowflakes/aggregates over supercooled droplets.

The composite profile for IP in Fig. 2.8 revealed that, on average, much of the low-level profile is sub-saturated (typically ≥10%). This can produce additional cooling of the ambient atmosphere through evaporation, and according to Zerr (1997), and Mitra et al. (1990), a drop in RH by 10% increases the total distance for complete melting by 100 m. When the refreezing layer is cold and sub-saturated, the additional evaporative cooling may be sufficient to refreeze a partially melted hydrometeor. Tables 2.1-2.3 demonstrated some spread in the temperature and moisture of IP profiles, such that more than one thermodynamic evolution emerged. The first is arguably the 'classic' profile – a weak elevated warm layer and deep refreezing layer with a deep near-saturated cloud layer (Fig. 2.8). An additional profile for the SGP suggested a deep warm layer (e.g., WLD > 2 km, $T_w > 5^oC$), but a comparatively deep (≥ 1 km) and cold ($<-5^oC$) refreezing layer. The primary mechanism for the generation of IP in this case appeared to be associated with low temperatures within the refreezing layer, as complete melting for a range of hydrometeor sizes would be anticipated in the warm layer. Of the 19 IP profiles in this dataset, 7 had maximum T_w exceeding 5^oC.

Table 2.5 summarizes key thermodynamic observations for different regions across the U.S derived from a selection of past literature, providing inter-regional context for our results. As discussed in chapter 1, freezing precipitation shows high regional variability. In some locations FZDR is favored over FZRA. For example, Albany, NY, Spokane, WA and Green Bay, WI on average exhibit shallower, cooler warm layers. Greensboro, North Carolina shows a thermal range similar to the SGP. Freezing precipitation in central North Carolina occurs frequently with winter cold air damming along the Appalachian mountain chain (Furhmann 2011). The predominant

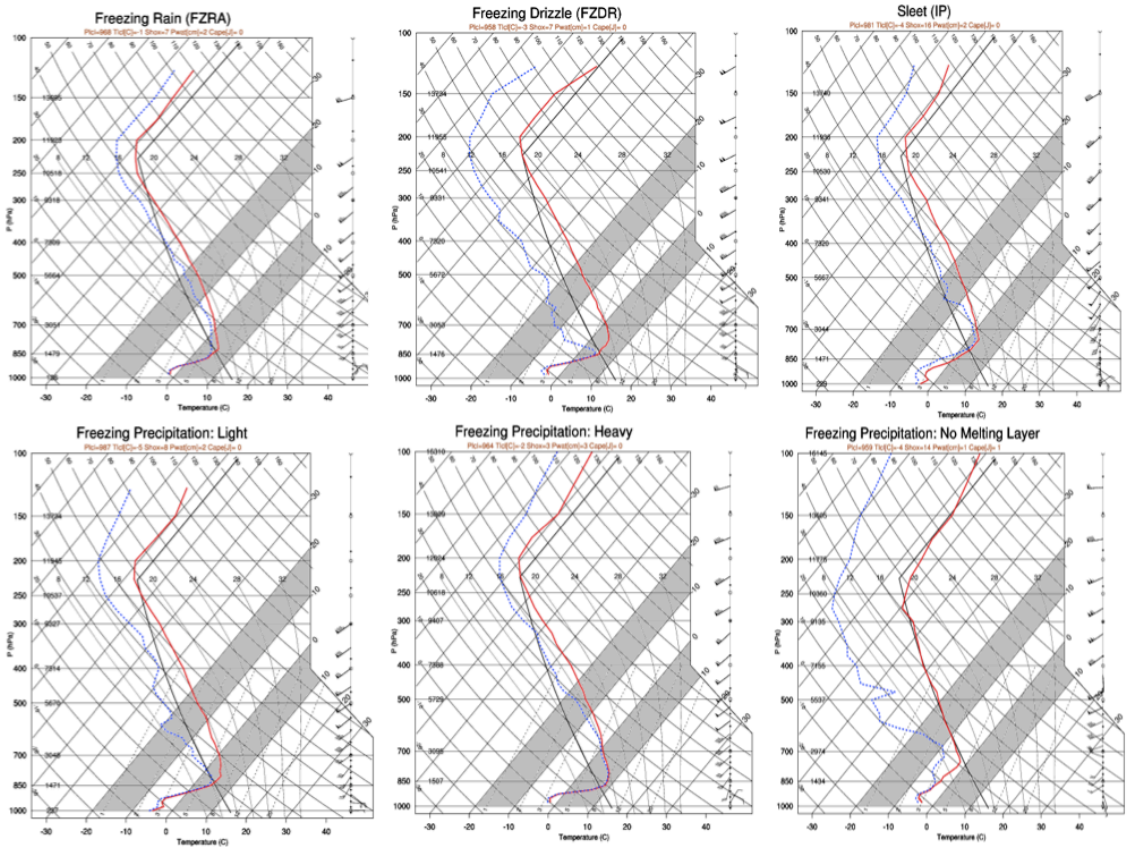

Figure 2.8: Schematic composite soundings for all categories of freezing precipitation, based on 10 vertical profiles (4 for freezing drizzle without a warm layer). Temperature ranges between 0°C -10°C, and -10°C to -20°C are shaded to indicate the warm layer inversion and dendritic growth layers respectively**.** Black line is temperature profile for a standard atmosphere.

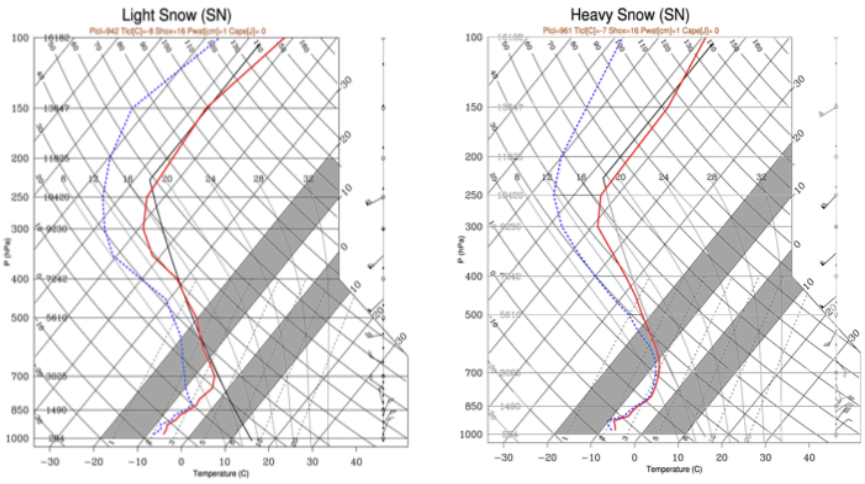

Figure 2.9: Composite soundings for light snow (left), and heavy snow (right). Aforementioned shaded regions from Fig. 2.8 are also applied here.

synoptic patterns conductive to freezing precipitation also vary by region, and although North Carolina and the SGP have similar thermal profiles, their wind profiles differ. In the former case, freezing precipitation is common to cyclonic low-pressure systems advecting warm-moist air from the southeast. In the Plains states and elsewhere, most events exhibit low-level southwesterly flow. Aloft (above 700 hPa, ~3 km), southwesterly flow is ubiquitous. In terms of cloud profiles, which also reflect the dominant precipitation type, within the contiguous U.S away from oceanic moisture sources, most freezing precipitation is light and associated with shallow (< 4 km) cloud layers. Both Greensboro, NC and the SGP evidence higher average cloud depths and lower CTT, potentially associated with a larger proportion of events in the FZRA and IP categories.

The fact that the SGP exhibits thermodynamic profile supportive of heavy freezing precipitation may result from its geographic location, alluded to by past studies including Robbins and Cortinas (2002) and Changnon (2003) but not studied in depth. Robbins and Cortinas (2002), in their analysis of the Spokane, WA area, identify a plausible connection between the temperature of a nearby oceanic moisture source (northern Pacific), and the maximum temperature achievable in the warm layer. They suggested, *"the maximum wet-bulb temperature of the warm (melting) layer can be determined by calculating the wet-bulb potential temperature of the source region air."* In this particular case, the cool sea surface temperatures (SST) associated with the adjacent ocean (~8-10^{o}C), produced maximum warm layer temperatures on the order of 2^{o}C, accounting for adiabatic cooling of the ascending air parcel. Fuhrmann (2011), Fuhrmann and Konrad (2013) demonstrated the key role of the subtropical Atlantic in

moderating air parcels ingested into winter storm systems. During boreal winter, average SST in the western subtropical Atlantic are 20-23^{o}C (based on data from NCEP-NCAR Reanalysis, not shown). When lifted to 850hPa, and assuming no dynamic and diabatic processes, the resulting warm layer maximum temperatures are approximately 7-10^{o}C. For the SGP, the Gulf of Mexico (GOM) moisture source is important in regional precipitation and severe weather. In addition, the region experiences a regular topographically forced southerly low-level jet (e.g., Maddox 1983, Stensrud 1996, Higgins et al. 1997). Wintertime GOM temperatures are similar to the sub-tropical Atlantic. Therefore, assuming that the sub-tropical maritime GOM airmass is the primary airmass associated with a warm layer, the range of maximum temperatures is potentially similar, supporting the results of this present analysis. We suggest that the favorable thermal profiles for freezing precipitation, particularly freezing rain, is supported in the SGP by virtue of its *proximity to the Gulf of Mexico and the subtropics, associated with warmer and deeper warm layers and greater moisture availability*. Note however, that not all events necessarily derive their warm layer characteristics from the GOM. In some situations, attendant synoptic and mesoscale circulation promote alternative moisture source regions and/or indirect transportation of GOM moisture (chapter 3,4).

TABLE 2.5: Comparison of selected results of this analysis against previous literature for national and regional freezing precipitation. Author shown in red: B = Bernstein (2000), R&C = Robbins and Cortinas (2002), R00/01 = Rauber et al. (2000, or 2001), F= Fuhrmann et al. (2008). Precipitation types shown in gray: ZR = freezing rain, ZL = drizzle, IP = ice pellets, GZR = heavy freezing rain.

Variable	Northwest		Northeast		Northern	Southeast	Midwest	National	Southern Plains
Sounding Location	**Spokane, WA *(B, R&C)***	**Albany, NY *(R&C)***	**Portland, ME *(B)***	**Pittsburg, PA *(B)***	**Green Bay, WI *(B)***	**Greensboro, NC *(B, R&C, F)***	**Peoria, IL *(R&C)***	**Various *(R00/01, Z, R&C)***	**Various**
Maximum T or T_w (°C) Mean (A)/median (M)/ mode (MO)/ range (S)	1-3 (ZR, *B, S*) 2.3 (M, *R&C*)	3.1 (M)	0-9 (ZR) 0-4 (ZR/IP) 0-7 (IP)	2-6 (ZR mix) 3 (ZR) 0-4 (ZR/IP)	2-4 (ZR) 0-2 (ZR/IP)	4-10 (ZR, *B, S*), 0-8 (ZR/IP, *B, S*), 0-3 (IP, *B, S*), 4.1 (M, *R&C*). 71% ZR events: 4-11 *(F)*	2.3 (M)	5 (A, *R01*) 3 (MO, *R01*)	5.6 (ZR, M), 4 (ZL M) 4.5 (IP, M), 9.4 (HZR, M) 0-12 (S)
Minimum T or T_w (°C) (as above)	-3 to -1 (ZR, *B*) -10 to -2 (ZL, *B*) -1.3 (M, *R&C*)	-2.9 (M)	-7 to -1 (ZR) -14 to -4 (ZR/IP) -11 to -2 (IP)	-7 to -2 (ZR mix) -4 (ZR) -7 to -3 (ZR/IP)	-5 to -1 (ZR) -10 to -6 (ZR/IP)	-6 to -1 (ZR, *B, S*), -8 to -2 (ZR/IP, *B, S*), -12 to -2 (IP, *B, S*), -3 (M, *R&C*). 51% ZR events: -6 to 0 *(F)*	-3.2 (M)	-5 (A, *R01*) -3 (MO, *R01*)	-5 (ZR, M), -6.9 (ZL, M) -7.5 (IP, M), -4.6 (HZR, M), -12 to -0.7 (S)
Melting Layer Depth (m)	500-1400 (ZR, *B, S*) 1001 (M, *R&C*)	1394 (M)	800-2800 (ZR) 0-1500 (ZR/IP)	1300-2000 (ZR mix) 1100 (ZR) 200-1300 (ZR/IP)	1200-1400 (ZR) 400-700 (ZR/IP)	1200-2700 (ZR, *B, S*), 400-2600 (ZR/IP, *B, S*), 500-1400 (IP, *B, S*), 1663 (M, *R&C*). 69% ZR events 1200-2700 *(F)*	1236 (M)	---	1985 (ZR, M), 1807 (ZL, M), 1279 (IP, M) 2322 (HZR, M), 60-3051 (S)
Freezing Layer Depth (m)	100-700 (ZR, *B, S*) 251 (M, *R&C*)	1000 (M)	200-1300 (ZR) 500-1800 (ZR/IP)	200-1000 (ZR mix) 300 (ZR) 500-2100 (ZR/IP)	300-1000 (ZR) 1600-2200 (ZR/IP)	300-900 (ZR, *B, S*), 300-1400 (ZR/IP, *B, S*), 600-1800 (IP, *B, S*), 503 (M, *R&C*), 90% ZR events 200-900 *(F)*	815 (M)	---	599 (ZR, M), 734 (ZL, M), 1130 (IP, M), 539 (HZR, M), 130-1760 (S)
EMP (°Cm)	1407 (M, *R&C*) 141-2251 (S)	2513 (M) 0-10668 (S)	---	---	---	3950 (M, *R&C*) 601-13311 (S) (ZR only)	1947 (M) 0-7009 (S)	2411 (M, *R&C*) 0-13311 (S)	4907 (ZR, M), 2931 (ZL, M), 3010 (IP, M), 12305 (HZR, M), 0-20851 (S)
EFP (°Cm)	200 (M, *R&C*) 0-1057 (S)	1655 (M) 5-22178 (S)	---	---	---	1111 (M, *R&C*) 251-3127 (S) (ZR only)	1422 (M) 419-18660 (S)	1247 (M, *R&C*) 0-22178 (S)	2370 (ZR, M), 3856 (ZL, M), 6152 (IP, M) 2071 (HZR M), 165-14349 (S)
Wind direction at surface (compass or degrees)	NE ~ 50 *(B)*	---	NW-NE, peak N (ZR) N-E (IP)	WNW/NE (ZL) NE-SE (ZR/IP)	NNE/NE	NE *(B)*	---	NW-NE *(R01)*	NE (~40)
Wind direction 850 hPa (compass, or degrees)	---	SW	SE	---	---	S *(R&C)* 43% ZR events: SW 34% ZR events: SE *(F)*	SW	SW: 230 (MO, *R01*)	SW 210 (ZR, M), S 180 (FR, MO), SW 210 (ZL), S 175 (IP, M)
Wind speed at 850 (ms^{-1})	< 5 *(B)*	---	---	---	---	---	---	12 (A, *R01*)	9.3 (ZR, M), 12.9 (ZL, M), 10.3 (IP, M) 0-30.9 (S)
Wind speed/direction aloft	W/SW *(R&C)*	SW	SW-SE	---	---	86% ZR events: SW *(F)*	SW ---	SW *(R01)*	SW
No melting layer: proportion (%)	86 (ZL)	---	Uncommon	100 (ZL) 0 (ZR/IP)	71 (ZL) 0 (ZR/IP)	22 (ZL) 0 (ZL/IP)		16.1 *(R00)* (of this 95 (ZL), 5 (ZR))	4.1 (all) 18.1 (ZL), 0 (ZR/IP)
Cloud top temperature (average/range /frequency)	-7 to 1 (ZL) <-15 – 0 (ZR)	---	-10 to 0 (ZL) < -10 (ZR/IP)	---	---	-6 to 4 (ZL) 82% events < -15 (ZL/IP)	---	> 0 (72% ZL, 27% ZR) -5 to 0 (62% ZL) < -10, (79% ZR) *(R00)*	-40 to 6 (M=-16) (ZR) -15 to 6 (M=1.2) (ZL) -35 to -4 (M=-21) (IP)
Convective instability? (%)	---	---	---	---	---	---	---	12.5 *(R01)*	34.3
Number of soundings/data used	22 (*B*)=14 ZL, 6 ZR, 1 IP. 6 *(R&C)*	18 *(R&C)*	34 *(B)* = 9 ZL, 6 ZR, 5 IP, 5 ZR/IP and 9 ZR mix.	21 *(B)* = 7 ZL, 1 ZR, 8 ZR/IP	15 *(B)* = 7 ZL, 4 ZR, 3 ZR/IP mix	57 *(B)*= 9 ZL, 11 ZR 5 IP with 15 ZR mix and 17 ZR/IP mix. 18 *(R&C)* 35 *(F)*	10 *(R&C)*	34 *(Z)*, 972 *(R00, R01)*, 68 *(R&C)*	97 total: 25 HZR 21 ZL, 57 ZR, 19 IP

Chapter 3: Preliminary Synoptic Climatology of SGP Winter Storms

3.1 Introduction

In this chapter our climatology is extended by examining synoptic evolutions common to winter storms for the region. The 18-year period of study means that this investigation is preliminary and based on limited sample size. Given the lack of information to date, even preliminary work was an opportunity to contribute some original insight, which could hopefully be of use to SGP forecasters in recognizing common evolution, and for prediction of precipitation type. Research aims of this chapter included:

(i) Ascertaining the nature and distinctions for synoptic patterns containing a broad mixed phase/freezing precipitation zone (hereafter 'ice'), versus those dominated by snow over the SGP.

(ii) Investigating common locations for winter precipitation for each derived pattern.

(iii) Obtaining distinguishing thermodynamic characteristics of synoptic type, and between ice and snow.

The content of this chapter forms a forthcoming article by Mullens et al.

3.2 Methodology

3.2.1 Selection of cases, and rationale for technique

Chapter 2 (sec. 2.1, 2.2) provided details on the study domain and database development. The events used in this work were drawn from that database. Figure 3.1

illustrates criteria used to select events forming the datasets used here. A key objective of this particular work was to differentiate the evolution of SGP winter storms that produced a broad region of freezing precipitation, from those primarily producing snowfall with no well-defined transition zone. To facilitate this, events were subjectively (manually) categorized as 'ice' or 'snow' depending on whether or not they exhibited this transition zone, also with regard to the socioeconomic impact of each phase type. Snow events were classified as winter storms with snowfall typically exceeding 3 inches, and freezing precipitation (primarily freezing rain) of short duration *and* low intensity (< 0.1 inch). Ice pellet accumulations above 0.1 inch were permitted, as presence/absence of freezing rain was of primary interest. For 'ice' events, a broad zone of freezing precipitation (freezing rain) should be observed, even if snowfall accompanied the system. The lower limit for accumulation was 0.1 inch, provided the event had a broad impact region and duration ≥ 6 hours. NCDC *Storm Data* publication was used to scan through all qualitative information for each event, including accumulation estimates. Additional data sources described in chapter 2 were further perused.

The temporal evolution of synoptic conditions accompanying winter precipitation was examined by defining an approximate onset time, T_0. This time was based on first observations of a given precipitation type from a representative station and/or *Storm Data* in the impacted sub-region. Since the majority of our data sources were of 3-hour resolution or lower, there was some uncertainty in demarking T_0. For the composite analysis (sec 3.2.4, 3.3, 3.4) various meteorological parameters of note were examined 24-hours prior to, and after T_0 (T_{-24}, T_{+24} respectively) to extract

information on duration and persistence of key features. Criteria for selection of events included (Figure 3.1):

(i) Precipitation category as previously described. Events were assigned as either 'ice' or 'snow', thus forming two separate datasets.

(ii) To prevent overly biasing results to a specific sub-region of the domain, only events impacting at least two of the four quadrants (Fig. 2.1) were used.

(iii) An exception to the dominant precipitation definition was made in cases where an event was displaying heavy ice and snow accumulations over the domain at T_0, resulting in estimated > 6 (>0.25) in snow (ice) over more than 2 domain quadrants. Although the dominant precipitation phase was ambiguous the event was likely high-impact, so inclusion to the dataset(s) was desired. Five events meeting these criteria were identified and assigned to both datasets[4].

(iv) Events of a temporal duration less than 6 hours, provided only small accumulation of either phase, were not included.

By performing the selection criteria (i)-(iv) on the database, 42 snowfall events, and 33 ice events were retained, forming the datasets used in this chapter. The dataset primary variable was the 500 hPa geopotential height (gpm), for approximate precipitation onset time, T_0. The list of case studies used is provided in appendix Tables A3.1 and A3.2 for ice and snow respectively. The choice of the mid-tropospheric height field as the primary variable in the initial identification of common synoptic flow was motivated by its extensive use in the literature to classify weather regimes (e.g., Casola

[4] Two ice events meeting this threshold criterion for snowfall may have been erroneously left out from inclusion to the snow database, but their absence was unlikely to have drastically changed the synoptic patterns derived here.

and Wallace 2007, Horel 1981, Blackmon 1976). Flow at this level strongly influences weather system movement and surface pressure evolution.

The next stage was to identify an appropriate objective technique for simplifying the information within the two datasets to a set of common 500 hPa flow patterns for ice and snow[5]. A method was desired that would generally retain a height field visually comparable to those observed during actual events. Given the relatively small number of case studies, it was possible to individually plot the T_0 geopotential heights for each event, along with their standardized anomalies (relative to the mean and standard deviation calculated from all events within the desired dataset, not shown). A couple of common techniques for pattern identification include cluster techniques and principal component analysis (PCA). Both are high-level statistical methods to convert a complex dataset to one of reduced dimensionality, where underlying simplifying structures may be revealed. For the atmospheric sciences, examples include establishing common flow fields and variable interrelationships (e.g., pressure, height, precipitation), or atmospheric teleconnections that explain a large proportion of the variability of a given parameter. Our dataset sample size is limited to the extent that only a comparatively simple analysis to group events using just the height field was performed. The method of choice was PCA (sec. 3.2.3).

The 500 hPa height data used was from North American Regional Reanalysis (NARR, Mesinger et al. 2006). The NARR dataset is a higher resolution extension of NCEP-NCAR Global Reanalysis (Kalnay et al. 1996), for North America, developed

[5] Manual techniques e.g., pseudo-subjective clustering based on trough axis location (e.g., Ressler et al. 2012), or surface features (e.g., Rauber et al, 2001, Castellano 2012) are alternative methods that tackle a similar problem.

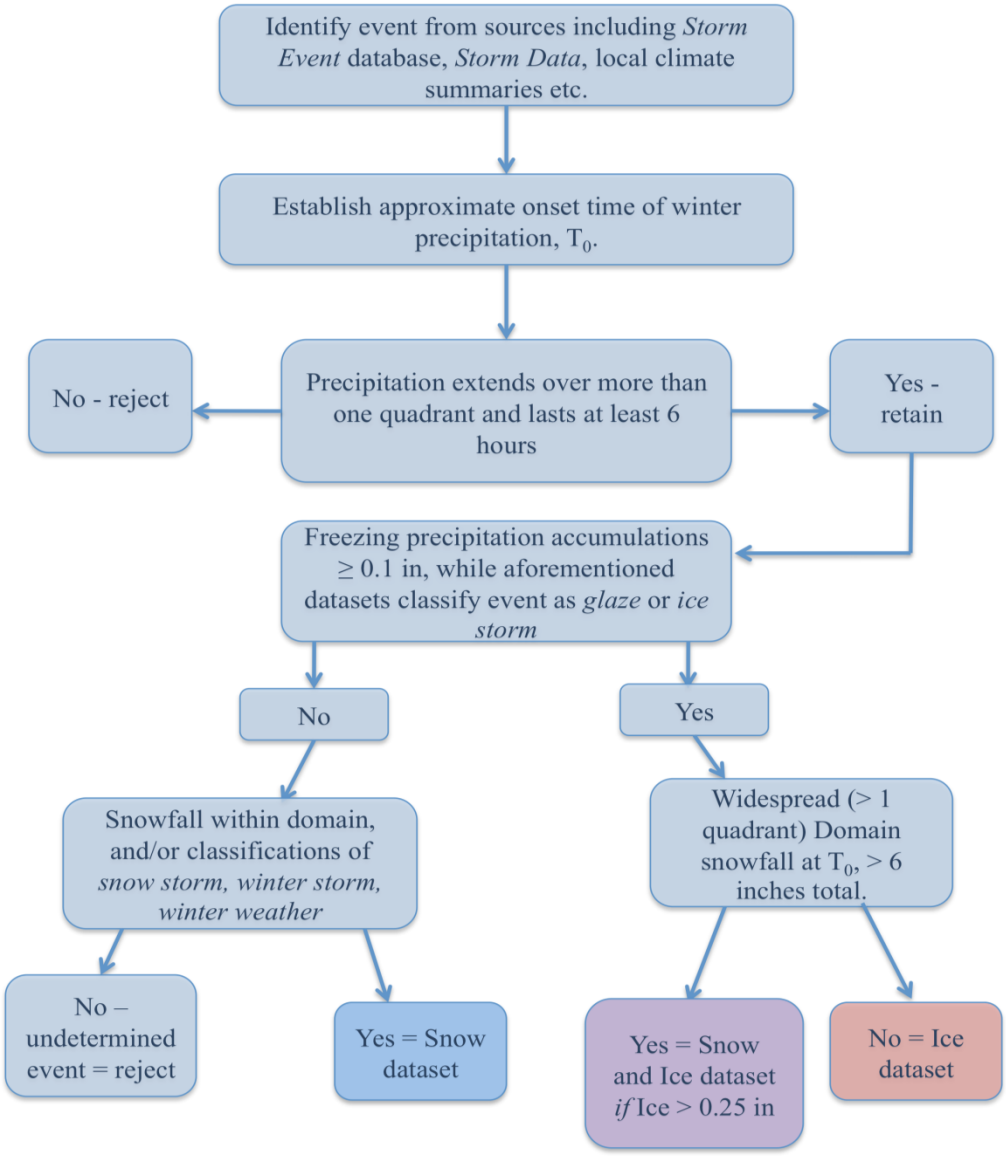

Figure 3.1: Flowchart depicting the sequence of decisions used to select snow and ice case study events for each dataset.

using a 32km grid size NCEP Eta model with the Regional Data Assimilation system (RDAS). For computational efficiency, NARR fields were interpolated to 1^{o}x1^{o} horizontal resolution, with 29 vertical levels. Geopotential height was evaluated over much of the contiguous U.S and eastern Pacific (20-50^{o}N, 220-280^{o}W), and converted to standardized anomalies for the ice and snow datasets separately (based on the mean

and standard deviation of each). Due to the large latitudinal extent of the domain a simple and common technique to adjust for the change in latitude-longitude grid area toward the poles was used, which weights the height field by the square root of the cosine of latitude. This avoids overrepresentation of variance from higher latitudes.

3.2.2 Accuracy of NARR data against in-situ observations

The NARR dataset is a 33-year (1979-2012)[6], gridded dataset, with numerous variable options, making it attractive for regional, climatological and case study work. Nonetheless, despite its high resolution and sophisticated data assimilation techniques it is wise to evaluate briefly NARR performance against in-situ observations. Oklahoma in particular is a heavily instrumented state. Surface temperature data from the Oklahoma Mesonet (Brock et al. 1996, McPherson et al. 2007) and upper air data from the ACRF-SGP in Lamont, Oklahoma were compared against equivalent NARR variables for two case studies, one freezing rain event between December 9 and 11 2007, and a snowfall event during December 22-23 2004. Vertical profiles of NARR zonal and meridional winds (not shown), specific humidity and air temperature (Figure 3.2) above the surface agreed well, in a smoothed sense, with ACRF sounding observations, but with peak magnitudes typically underestimated. The greatest discrepancy was for near surface (below 900 hPa) air temperatures, for which NARR values almost always were warmer than observations. Comparisons of ACRF and NARR surface temperatures for both events are given in Table 3.1, which indicate that NARR relative warmth included a distinct diurnal maximum around noon CST (1800

[6] At the time of this dissertation research.

UTC).

This warm NARR surface temperature bias also was suggested by spatial comparison with interpolated Mesonet observations (for method uncertainty estimates, see appendix section 5) across Oklahoma, shown in Figure 3.3 (a,b). Importantly, those comparisons revealed slower southward progression of the NARR surface 0^{o}C. This isotherm remained north of its observed location, especially in the ice storm case, this difference maximizing between 100^{o}W and 96^{o}W (~80 km), with an erroneously zonal orientation. The snow case study also exhibited northward error but by a lesser amount (~30 km). These results suggest that NARR data may not correctly represent shallow cold arctic airmasses common in SGP winter storms, possibly resulting from inadequate treatment by the Eta model's planetary boundary layer and radiation schemes. Kennedy et al (2011) noted large positive bias in downward shortwave (solar) radiation with NARR reanalysis. They attributed this finding to an erroneous lack of low cloud cover, and insufficient absorption by aerosols and water vapor in the Eta model. Our analysis produced composited representations of the surface 0^{o}C isotherm (section 3.2.4), requiring an accounting for surface warm bias. Median NARR minus ACRF/Mesonet surface temperature difference was about +1.7^{o}C. Therefore the composites use the +1^{o}C isotherm in place of 0^{o}C to approximate the freezing line. It should be noted that during severe ice storms Mesonet stations encounter power disruption, resulting in loss of data (which was the case at 18 UTC for December 9 2007, chapter 5), and erroneous readings resulting from iced instruments, particularly rain gauges and anenometers. Fortunately, for this work neither instrument was required, and the temperature data was consistent with the progression of the event.

Table 3.1: NARR versus ACRF-SGP air temperature at the surface for (a) ice storm (December 9-11 2007) (b) snowfall event (December 22-23 2004).

(a)

Time/Day (UTC)	ACRF Air Temperature (^{o}C)	NARR Air Temperature (^{o}C)	Difference NARR minus ACRF (^{o}C)
1200/9	-5.67	-3.34	+2.33
1800/9	-4.49	-0.49	+4.00
0000/10	-4.28	-3.12	+1.10
0600/10	-4.90	-5.81	-0.91
1200/10	-4.42	-3.45	+0.97
1800/10	-2.73	+1.59	+4.32

(b)

Time/Day (UTC)	ACRF Air Temperature (^{o}C)	NARR Air Temperature (^{o}C)	Difference NARR minus ACRF (^{o}C)
0000/22	+3.65	+3.32	-0.33
0600/22	+0.15	+0.45	+0.30
1200/22	-2.75	-1.85	+0.90
1800/22	-6.50	+1.50	+8.00
0000/23	-6.30	-2.33	+3.97

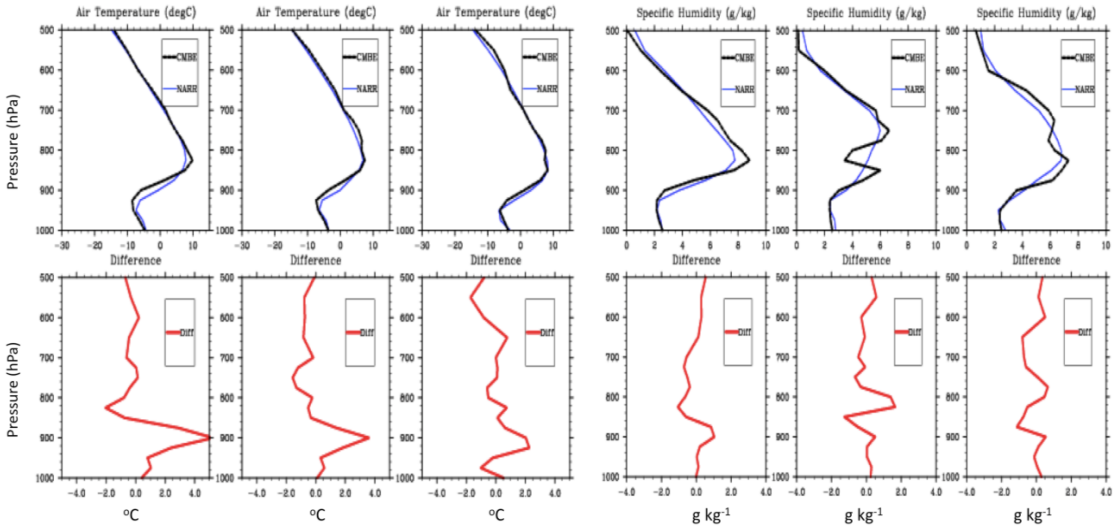

Figure 3.2: Vertical profile plots between 1000-500 hPa for NARR (blue) and ACRF (black) air temperature at 12 UTC 9, 00 UTC 10 and 12 UTC 10 (left), and specific humidity for the same times (right). Bottom panels show the corresponding difference values for NARR minus ACRF (red lines).

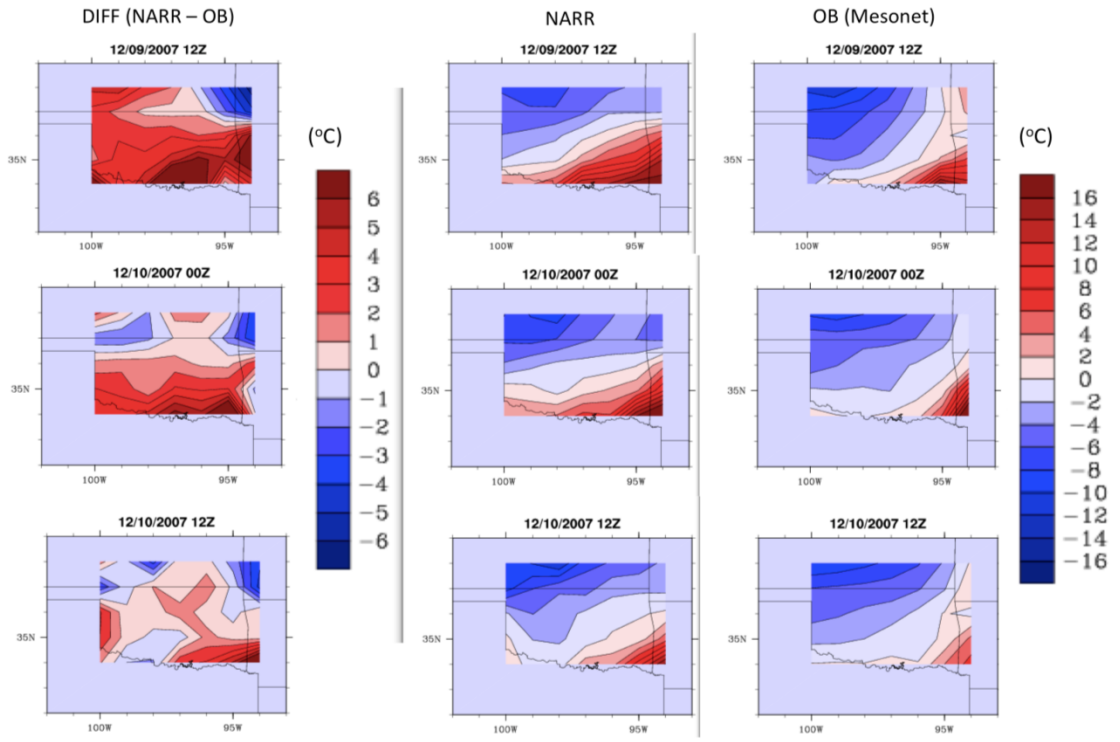

Figure 3.3a: NARR versus Mesonet observations for Oklahoma at 12 UTC 9 (top), 00 UTC 10 (middle), and 12 UTC 10 (bottom) December 2007. Mesonet surface temperatures (^{o}C) interpolated to NARR 1^{o}x1^{o} lat/lon grid. Leftmost panel displays NARR minus Mesonet difference, while right two panels show NARR and Mesonet temperature distributions respectively.

3.2.3 Rotated Empirical Orthogonal Function (EOF) analysis

EOF (PC) analysis is a technique to relate a correlation (covariance) dispersion matrix for a given dataset to computed eigenvectors, to determine an optimal number of eigenmodes to retain. Ideally, those retained explain a large variance of the desired variable, with modes of variability being well separated from one another. This allows the user to extract physically meaningful information regarding atmospheric behavior (e.g., Richman 1986). Richman (1986) details some of the benefits of rotated EOF/PCA over unrotated solutions for meteorological applications. The goal of rotation is to further analyze PCs to retrieve clearer and more separated loading patterns, while

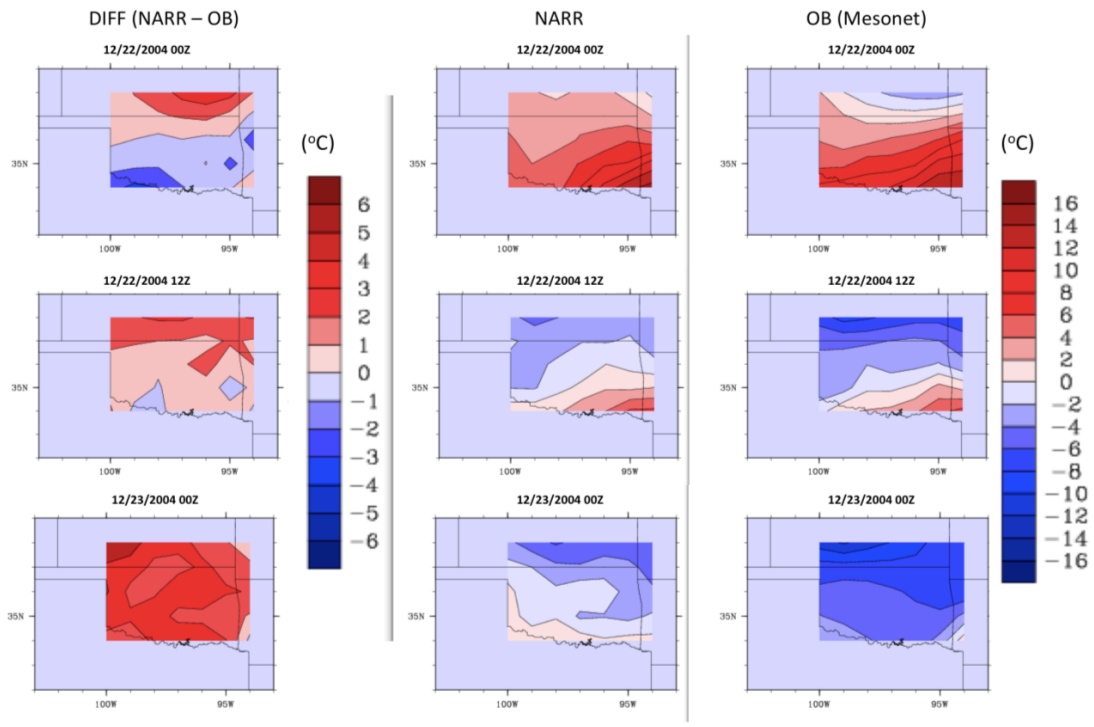

Figure 3.3b: In the style of Fig. 3.3(a) but for a snowfall event on December 22-23 2004. Left column: 00 UTC 22, center: 12 UTC 22, right: 00 UTC 23.

maximizing simple structure. Rotation adds complexity to a solution, and is sensitive to the number of retained PCs, however it is insensitive to domain shape, does not suffer from large sampling errors from poorly separated eigenvalues, and may in many cases yields physically more meaningful results. Two main types of rotation include *orthogonal* and *oblique.* An orthogonal rotation (e.g., Varimax) assumes that factors in the analysis are not correlated, while an oblique rotation (e.g., Promax) makes no such assumption.

Two common approaches to PCA include spatial (S) mode and temporal (T) mode (Richman 1986). In S-mode, time series of a variable are constructed at each domain grid-point, and the correlation between adjacent grid-point time series are examined to identify sub-regions with similar patterns. For T-mode, correlations

between the overall spatial distribution of a variable at each time are examined, identifying subgroups of times with similar spatial patterns. S-mode analysis is often used in the study of atmospheric teleconnections, while T-mode examines atmospheric flow fields. For this work each time-point represents a discrete 500 hPa height field associated with a winter storm event. Given that the intention is to resolve common flow patterns, a T-mode analysis seemed intuitively more appropriate in this context.

In order to evaluate a suitable rotation technique for this work, both Promax and Varimax rotations were performed on the ice dataset, and plots of rotated PC (RPC) loadings inspected to determine the degree of simple structure. Strong simple structure should show most loadings within the hyper-plane and along or near the (x,y) axis, with increasing departure from the axis in all directions for moderate and weak simple structure (e.g., Richman 1986). Figure 3.4 shows the eigenvalues for the ice dataset, while Figure 3.5 and 3.6 show pairwise plots of RPC loadings for the initially retained RPCs for Varimax and Promax k=2 respectively. Promax k=3 and 4 were also considered but yielded evidence of less simple structure compared to k=2 (based on pair-wise plots of PC loadings, not shown) Based on this information, Promax k=2 was used here.

The Promax RPC (PRPC) analysis was performed using the statistical software program “R”. R possesses a simple user interface and has a number of powerful statistical routines. The calculation of PRPCs for the snow and ice datasets were as follows:

(i) Eigenvalues were computed from a correlation matrix of the 500 hPa standardized height anomalies and the separation between them examined visually (Figure 3.4).

(ii) Unrotated PC loadings were calculated from the eigenvalues. Rotated PCs were then formed from a subset of the initial unrotated PCs. The number to retain was determined by the plot of eigenvalues. All eigenvalues were included in the PRPC until their separation was approximately even, and the gradient of the eigenvalues approaches zero. In practice, 10 PCs were initially rotated for both ice and snow.

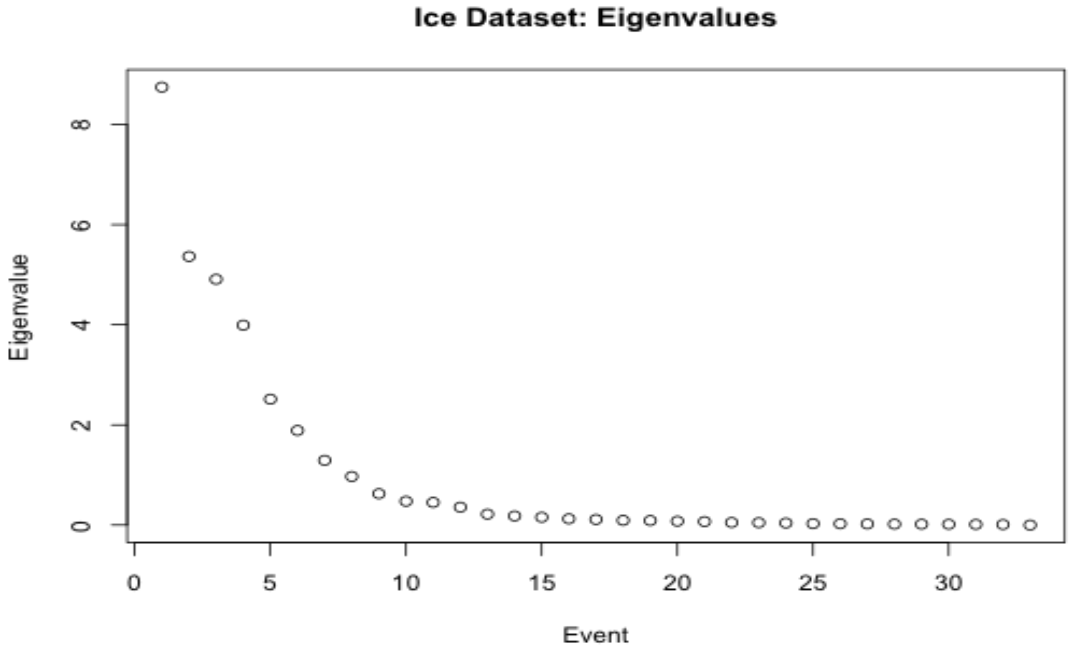

Figure 3.4: Eigenvalues (y-axis) associated with 33 ice events (x-axis).

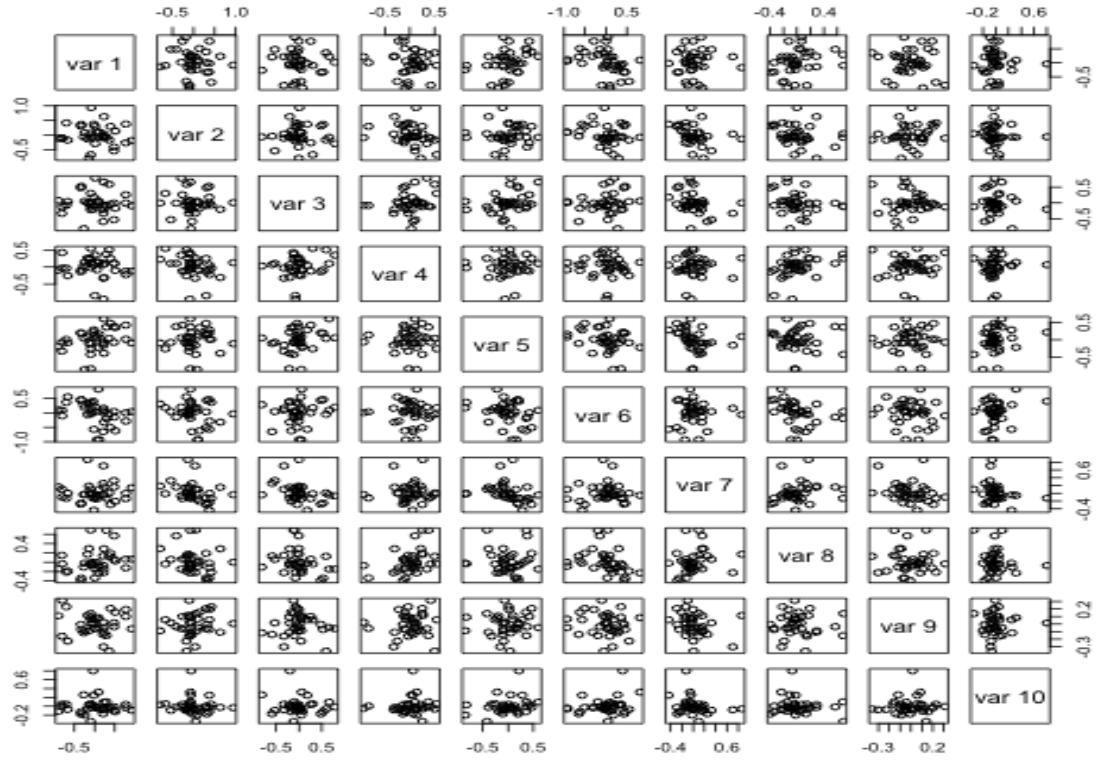

Figure 3.5: Pair-wise plots of rotated PC loadings for Varimax rotation. Simple structure is indicated when loadings cluster near the center of the axis, or along the hyperplanes (~±0.1) of the EOF-x and y axis.

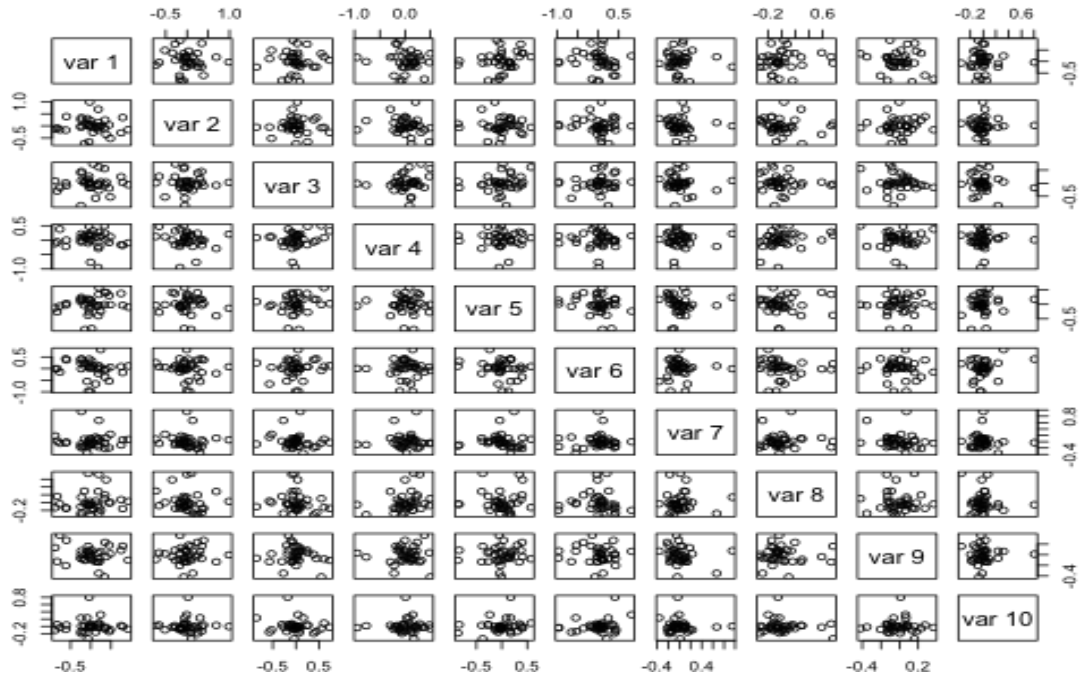

Figure 3.6: As Fig. 3.5 but for Promax (k=2) rotation.

(iii) Since the initial number of rotated loadings may not be optimal, the number of PRPCs to eventually retain was determined via an analysis of congruence between each PC loading vector, and the correlation matrix of the original standardized height field. The equation for congruence is displayed in equation 3.1 below, and was previously given by Harman (1976), and Richman (1986). Table 3.2 illustrates the process to reduce the number of PRPCs for the ice dataset. A congruence of less than |0.68| was considered to have little to no match to the original data, while greater than |0.92| is considered a good match, and above |0.98| an excellent match. The average value of congruence across loadings was assessed, and the number of retained loadings exhibited both maximum number of PRPCs with congruence > 0.9, and the highest average congruence across all PRPCs. For ice and snow, the total number retained was 4 and 3 respectively.

$$C_{ab} = \frac{\sum_{j=1}^{n} e_{ja} e_{jb}}{[(\sum_{j=1}^{n} e_{ja}^2)(\sum_{j=1}^{n} e_{jb}^2)]^{1/2}} \tag{3.1}$$

Where C_{ab} is congruence, e_{ja} the PC loading vector, and e_{jb} the correlation matrix.

(iv) Once the desired number of PRPCs had been retained, scores were calculated. For every score one can resolve two possible meteorological fields, the additive inverse of the score, and the score itself. Equation 3.2 may be used to subsequently resolve the height field from the scores directly, however, it was decided instead to composites (sec. 3.2.4) to resolve the height field.

$$x = \pm Z\sigma + \overline{X} \qquad (3.2)$$

Where x is the resolved height field (m), Z the PRPC score, σ the standard deviation, and $\overline{X}$ the mean of all height fields in the dataset (m).

Once PRPC scores were calculated, the constituent events within the datasets for ice and snow were binned into groups based on their scores. The technique in this case was to use the standardized anomalies for each event, and evaluate the magnitude of the loading correlation against each PRPC score, using a threshold value of |0.45| to include or reject. In a previous iteration (not shown) a threshold value of |0.6| was used. Unfortunately, given the low sample size, this threshold reduced the number of events in each pattern. The subsequent choice of threshold was chosen to balance the need to have a sufficient number of events per pattern to generate suitably representative

Table 3.2: Example of the method to derive the most suitable number of retained PRPCs. The table shows congruence coefficients between correlation matrix (col) and PC loadings (row) for 10 to 2 rotated PCs for the ice dataset. The final number retained was 4, shown in bold, which represented the greatest number of RPCs with high congruence values.

	1	**2**	**3**	**4**	**5**	**6**	**7**	**8**	**9**	**10**
10 RPC	-0.961	0.973	-0.853	-0.942	0.881	-0.94	0.772	0.842	-0.699	-0.22
9 RPC	-0.961	0.972	0.855	-0.940	0.883	-0.943	0.760	0.839	-0.211	
8 RPC	-0.963	0.972	0.859	-0.937	0.883	-0.943	0.784	0.840		
7 RPC	-0.964	0.970	0.865	-0.928	0.850	-0.980	0.779			
6 RPC	0.971	0.936	0.870	-0.908	0.870	-0.945				
5 RPC	-0.984	0.926	0.926	0.942	0.600					
4 RPC	**-0.974**	**0.951**	**0.925**	**0.950**						
3 RPC	0.952	-0.848	0.950							
2 RPC	0.932	-0.957								

composite evolutions with the necessity to retain separated 500 hPa height fields. Even so, the threshold was low enough such that several cases in each dataset correlated to more than one score (e.g., Tables A3.1, A3.2), indicative of weak simple structure and 'blending' of flow fields. During grouping, each event 500 hPa height field was visually examined and compared with the results of the PRPCA (not shown). This was an available option for this sample, but far less practical with a larger dataset.

3.2.4 Composites

Once events were partitioned into appropriate pattern groups, composites of atmospheric variables were constructed. Composites are a highly utilized basic statistical method, which evaluates the spatial average of a given field over a domain. The intention of this work was to consider some distinguishing features of the dynamics, thermal and moisture properties of each pattern type for ice and snow respectively at T_{-24}, T_0 and T_{+24} hours. Furthermore, perhaps ambitiously for the sample size, we attempt to derive *specific* patterns physically observed in nature, rather than utilizing more general techniques that tend to smooth over a greater range of trough characteristics (amplitude, location), but have the benefit of greater sample size (e.g., Ressler et al. 2012). Variables composited (using NARR data) include precipitable water vapor, vector winds near the surface and aloft, air temperature, and sea level pressure. In addition, the composite 500 hPa height field was displayed for each pattern type. In order to account for uncertainty in T_0, time T_0, T_{-24}, T_{+24} ± 3 hours are included in the composite. For example, a composite with n=6 events would have 6x3 (18) composited times.

3.2.5 Caveats

The above methodology was subject to uncertainty, as were the patterns revealed by the analysis. Arguably the most significant concern was the small (temporal) sample size. More events should be obtained and added to the dataset(s) in order to make robust assertions regarding the prevalence and structure of resolved pattern types. At this time the manually intensive nature of the project made obtaining a larger sample prohibitive. It is hoped that significant extension to this work can be completed in the future. Additional caveats included:

(i) While based on objective criteria, selection of the final number of retained PRPCs was quasi-subjective, especially when congruence coefficients were similar. In some cases, the choice of the number of PRPCs to keep will change the pattern structure of the resulting scores.

(ii) Each event in the dataset had a different domain distribution of freezing and/or frozen precipitation. Unlike many studies, the analysis was not performed with reference to a specific station site. To do so would have likely reduced the number of cases within the dataset. Whether specific patterns tend to impact specific regions within the domain was also a research question, and is briefly addressed in sections 3.3 and 3.4.

(iii) This analysis was not concerned with the variance explained by each pattern, the major test of the methodology was in its ability to resolve physically realistic patterns. The relative frequency of these patterns over the period of study was assessed by counting the number of events within each pattern

group. However, event frequency is likely to change with a larger dataset, as is the potential number of resolved pattern types.

(iv) The PRPC domain may play a non-trivial role in the resultant grouping of events. It was noted in a few cases that height fields disagreeing visually in the location/amplitude of the trough axis were placed in the same groups. It may be that a portion of the domain less pivotal for the development of precipitation (e.g., structure of the eastern ridge) may have accounted for this correlation. Future work should examine potential impacts of a varying domain size.

3.3 Results: Synoptic Patterns for Freezing Precipitation (Ice)

From the analysis described in section 3.2, four PRPCs were retained from the ice dataset, with produced eight height fields, using the described logic. In this section particular attention is paid to the 'leading' five pattern types, while an appendix (section 3) outlines the basic evolution of some remaining types. These five patterns were identified and ranked from three criteria: (i) number of events per group (n); (ii) magnitude of the average correlation between PRPC loading and event standardized height field and; (iii) number of events not also correlated to another pattern type (using the threshold discussed previously). The same methodology was used for snow PRPC scores and their subsequent flow patterns (section 3.4).

In this and the following section, composite progression of each pattern between T_{-24} and T_{+24} hours were evaluated. In reality the evolution of the upper level trough, thermodynamics, surface pressure, wind fields and precipitation will differ with each

storm system. The variables must also be considered to be intrinsically related, especially for freezing precipitation, where the thermal and pressure fields accompanying the upper level flow pattern are essential components to the analysis. In other words, winter weather requires a specific set of ingredients that cannot be identified through mid-tropospheric flow alone. These composites are a guide to *one possible sequence of evolution*, with respect to duration, precipitation magnitude, location, and phase type. Note that the five patterns shown for freezing precipitation incorporate 70% of the dataset. The number of events per composite are: *Ice Pattern 1* (6), *Ice Pattern 2* (5), *Ice Pattern 3* (5), *Ice Pattern 4* (5) and *Ice Pattern 5* (4), with two events overlapping two pattern types (see Table A3.1). These patterns regionally extend the work of Rauber et al. (2001) by concentrating on the holistic evolution of each type with respect to multiple parameters, but also by using the geopotential height field as the typing variable, rather than surface features.

Figures 3.7, 3.8, 3.9, 3.10 and 3.11 are multi-panel plots displaying key aspects of the composite average circulation for *Ice Patterns 1-5* respectively. The top panel shows NARR constituent event precipitation (fractional coverage of precipitation type > 20%); panel (a) displays 500 hPa geopotential height and 250 hPa winds; panel (b) sea level pressure and 975 hPa vector winds; panel (c) standardized 850 hPa temperature anomalies and location of surface and 850 hPa freezing line isotherms in purple and blue respectively; and panel (d) precipitable water vapor (PWV) standardized PWV anomalies (> 1.5σ, stippled) and 850 hPa vector winds for patterns 1-5 (T_{-24} to T_{+24}) respectively. Standardized anomalies were calculated relative to a 1979-2012 mean and standard deviation and expressed relative to 1 standard deviation (1σ).

Ice Pattern 1 (Fig. 3.7) shows a positively tilted trough south of a zone of northwesterly flow over the northern U.S (a). The northwesterly flow corresponds to the southeastward movement of a cooler airmass (c), indicated by the high sea level pressure at T_{-24} (b). As the trough moves eastward over the ensuing 24-hours, low-level southerly winds increase to 15-25 knots, implying moisture advection from the Gulf of Mexico (GOM) (d). In addition, 850hPa temperatures increase under southerly flow (c), and sustain an above-freezing inversion layer above the cool surface airmass associated with the arctic high centered over the Northern Plains (b). Colder air filters into the domain on the western edge of the mid-level low (c). At time T_0, the composite trough axis is just west of the domain, with quasi-geostrophic height falls promoting ascent, and adequate moisture (~+1.5σ, d). The composite depicts the domain under the left exit/right entrance region of two upper jet streaks, indicating divergence at this level.

The composite storm suggests a favorable region for freezing precipitation over western, through central and northeastern sections of the domain at T_0 (region bounded by the zero-degree surface and 850 hPa isotherms). For individual events freezing precipitation locations are determined primarily by the southward extent of the surface arctic airmass. Additionally, subtle changes in the magnitude of the low-level temperature inversion, moisture, wind fields and trough axis, as well as mesoscale focuses for ascent (fronts, WAA maxima) can alter the mixed phase region. This pattern type suggests high variability between constituent events, likely for the above reasons. This composite also indicates the later formation of a weak low-pressure system along the coastal Gulf (b, T_{+24}).

At T_{+24}, the mid-level trough axis resides over the domain. Colder air aloft behind the trough deepens into the region (c), gradually limiting the potential for sustained freezing precipitation. Snowfall may occur with suitable moisture and lift, and multiple phase types have been observed for the domain with this pattern. Recent examples of winter storms in this category include the Christmas storm of 2000 (December 24-26), which produced heavy icing (~ 1 in) over southern Oklahoma into Arkansas, and ice pellets and snow further north, and January 28-29 2010, where several hours of freezing rain and ice pellets, followed by snowfall over Oklahoma translated east into Arkansas on the 29th.

Ice Pattern 2 (Fig. 3.8) depicts a longwave positively tilted trough over the western U.S through Baja California at T_{-24} (a). Over the ensuing 48-hours the major trough axis does not progress much. A baroclinic zone, possibly associated with a quasi-stationary surface front (not shown), is present within the low-level troposphere, orientated southwest to northeast. A strong upper level jet streak (a) is promoted by the enhanced temperature gradient (c). Formation and orientation of the frontal zone is aided by apparent pressure gradient driven southward acceleration of an arctic airmass east of the Rocky Mountains (b, also evident from the inverted pressure trough). Composite sea level pressure at T_{-24} and T_0 show a pressure dipole across the Rockies. Such structures are commonly observed during cold air damming in the lee of the Appalachians. Lackmann (2011, p.196) describes the process as a westward deflection of northerly flow, leading to mass accumulation east of the mountain barrier and increased sea level pressure. Conversely, on the western slopes the Coriolis force

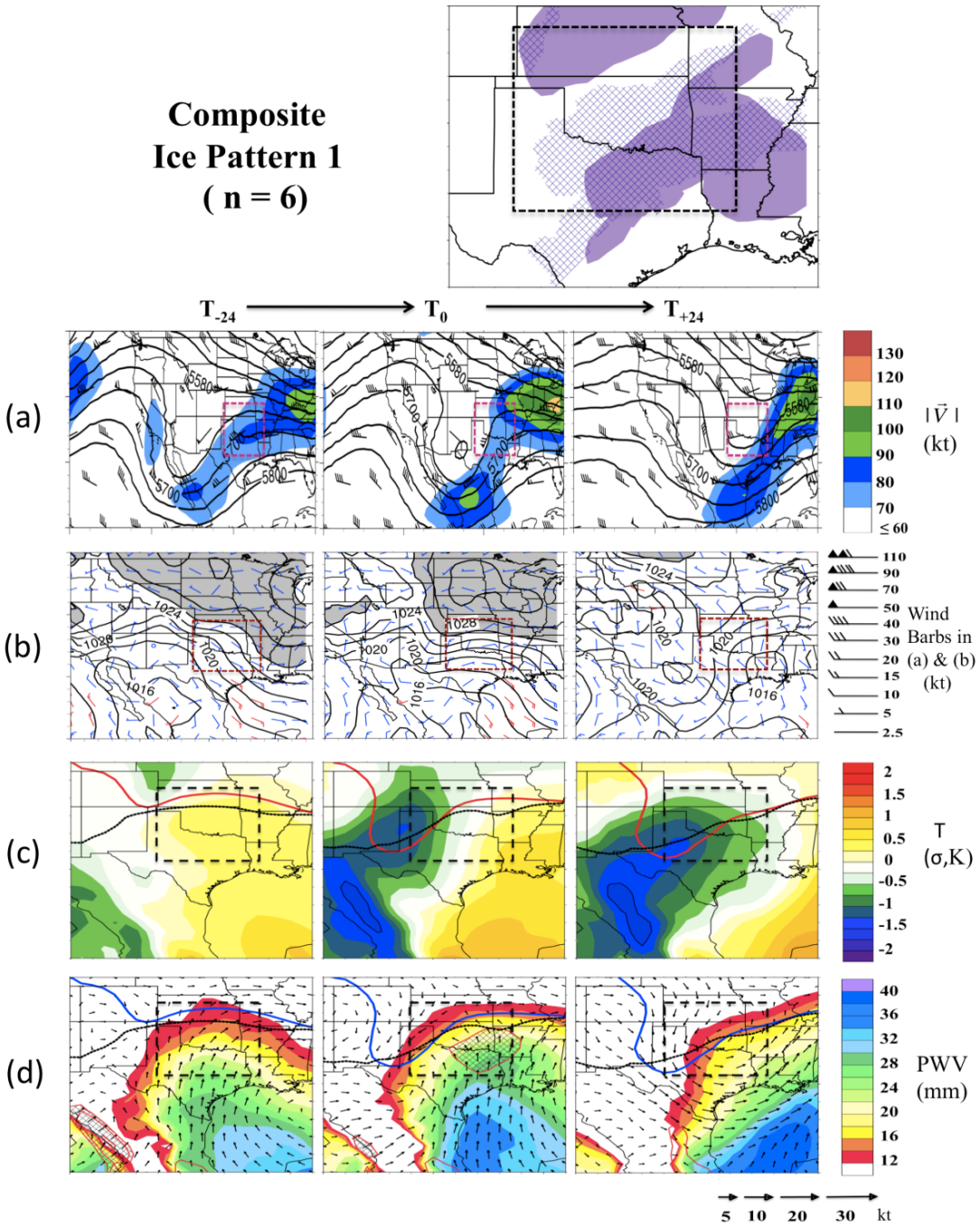

Figure 3.7: Multi-panel plot for composite *Ice Pattern 1*. The layout of this and subsequent figures was described in the text (section 3.3). The SGP domain is highlighted in each panel. Please note the different domains plotted. Additionally, panel (b) displays 975 hPa winds> 15 kt in red, and SLP > 1026 hPa in light grey. Panel (c) shows 850 hpa (surface) zero (1^{o}C) isotherms in red (black), while panel (d) displays the same isotherms in blue (black). For the top panel, locations of NARR derived categorical freezing rain (ice pellets) are displayed in solid (stippled) purple.

deflection draws mass away from the barrier promoting lower surface pressure. A weakening of this dipole might be observed associated with pressure falls promoted by the approaching trough. Standardized temperature anomalies by T_0 within the arctic airmass range from -1 to -1.75σ (c), a notable departure from the 1979-2012 average, while air to the south remains above climatology, between +0.5 and +1.25σ. The pronounced broad anticyclone over the southeastern U.S promotes suggests sustained low-level WAA, evidenced by increased 850 hPa temperatures by T_0. Anticyclonic flow also advects moisture from the western GOM. Panel (d) shows 25-30kt southwesterly wind at 850hPa, and a region of positive PWV anomalies exceeding +1.5σ southwest to northeast over the domain. Moisture trajectories at this level derive from the GOM, but also the Mexican Plateau and eastern subtropical Pacific. The composite average potential freezing precipitation zone is north of the surface front and parallel to the jet axis.

There is less spread in the location of freezing precipitation with this pattern type (top panel), with locations generally extending from Oklahoma northeastward. Examples of recent events include January 26-28 2009, which produced a swath of freezing drizzle followed by ice pellets over central Oklahoma, with more substantial freezing rain over eastern portions of the state into Arkansas. Since the longwave trough remains anchored in the west during the initiation of freezing precipitation, mechanisms for ascent may involve shortwave troughs ejected ahead of the long-wave, and persistent isentropic ascent over a quasi-stationary frontal boundary.

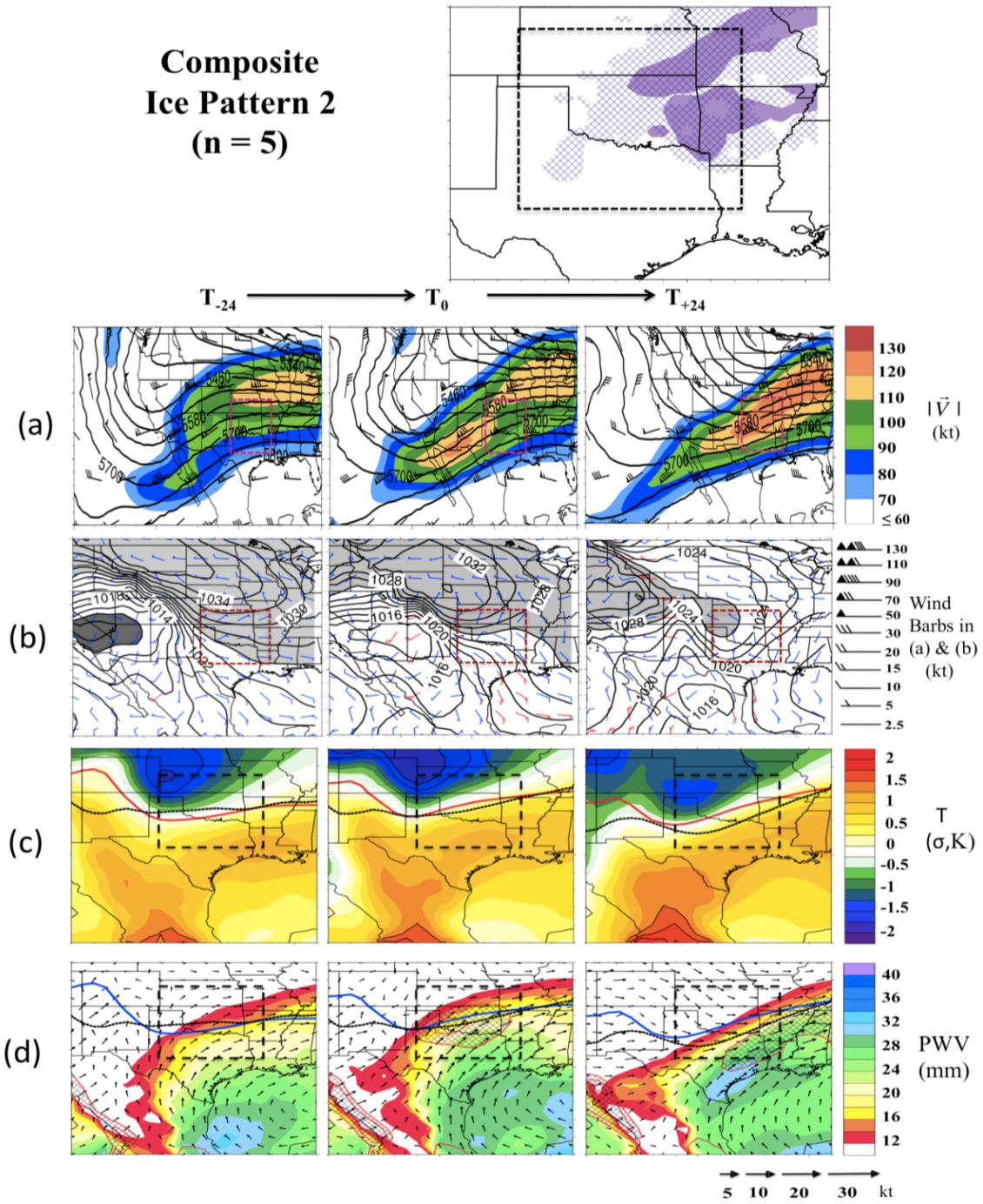

Figure 3.8: As Fig. 3.7 but for *Ice Pattern 2*. For panel (b), SLP < 1012 hPa is shaded in dark grey.

Ice Pattern 3 (Fig. 3.9) shows amplification of certain features associated with *Ice Pattern 2*, notably in the amplitude of the western trough (a), and the magnitude of

temperature and moisture anomalies. At T_{-24}, 850 hPa temperatures are particularly warm over the domain (c), while composite SLP (b) shows an arctic high over the northern high plains, translating south and east with time. The SLP pattern suggests topographical damming, and the airmass by T_0 shows negative anomalies near -1.5 to -2σ over the western high plains, which weaken by T_{+24}. A strong jet streak (~100 + kt) extends from the subtropical Pacific through to the northeast U.S (a).

By T_0 the trough axis has not advanced significantly, but has expanded meridionally. WAA ahead of the trough over the domain keeps low-level temperatures notably warmer than climatology over the southeastern U.S (> +1.5σ). The composite location of potential freezing precipitation is located to the north of that in *Ice Pattern 2*, and broader due to the higher 850 hPa temperatures (c,d). There is also more agreement in the location of freezing precipitation for each constituent event, shown in the top panel. This consistency may serve to compound the magnitude of anomalies (e.g., c, d) relative to the other pattern types. Freezing precipitation aligns with the upper jet, and surface zero degree isotherm, along an axis from southwest to northeast. Precipitable water vapor exceeds +2σ over a broad region, and +3σ over much of the domain. This increase over *Ice Pattern 2* may in part result from more direct moisture transport from the Gulf of Mexico (d). Between T_0 and T_{+24} eastward movement of the trough is slow, retaining favorable conditions for precipitation (assuming sustained ascent). With this pattern type snow over the domain is uncommon (unless the cold air is deeper and/or the trough more progressive), and freezing precipitation concludes either through erosion of the freezing layer by warming (e.g., latent heat release from refreezing precipitation, and/or WAA), or southward movement and deepening of the arctic

airmass. A notable event in this category was an ice storm on December 9-11 2007 over the central domain. Isentropic ascent, WAA and convective instability above a particularly pronounced warm layer produced icing locally exceeding 1 inch. Rates of accumulation were large due to the preponderance of training cellular convection (chapter 4).

Ice Pattern 3 can be associated with significant icing, with four long duration severe events since 2000 corresponding to this type. Factors contributing to potential severity include: (i) the quasi-stationary frontal boundary, strong WAA with slow moving upper level flow; (ii) direct Gulf moisture transport with large positive precipitable water anomalies; (iii) upper level steering flow parallel to the front; (iv) high temperatures in the warm layer sustaining freezing rain at higher precipitation rates.

Ice Pattern 4 (Fig. 3.10) depicts a progressive composite trough. At T_{-24}, high SLP moves southward from Canada, in the wake of a low-pressure system over the Great Lakes (b). Winds are down-gradient, but the temperature profile does not suggest that on average this airmass is particularly cold (c), showing weak negative anomalies over the high plains, and positive anomalies over the southern and eastern CONUS. Positive anomalies are second only to *Pattern 3* in magnitude. The location of the surface and 850 hPa freezing isotherms suggest a composite region of freezing precipitation focused over the northern half of the domain since cool surface airmass is more aggressively modified further south. As the trough axis amplifies the zero degree isotherms orientate parallel to this axis and the upper jet. Moisture is also significant

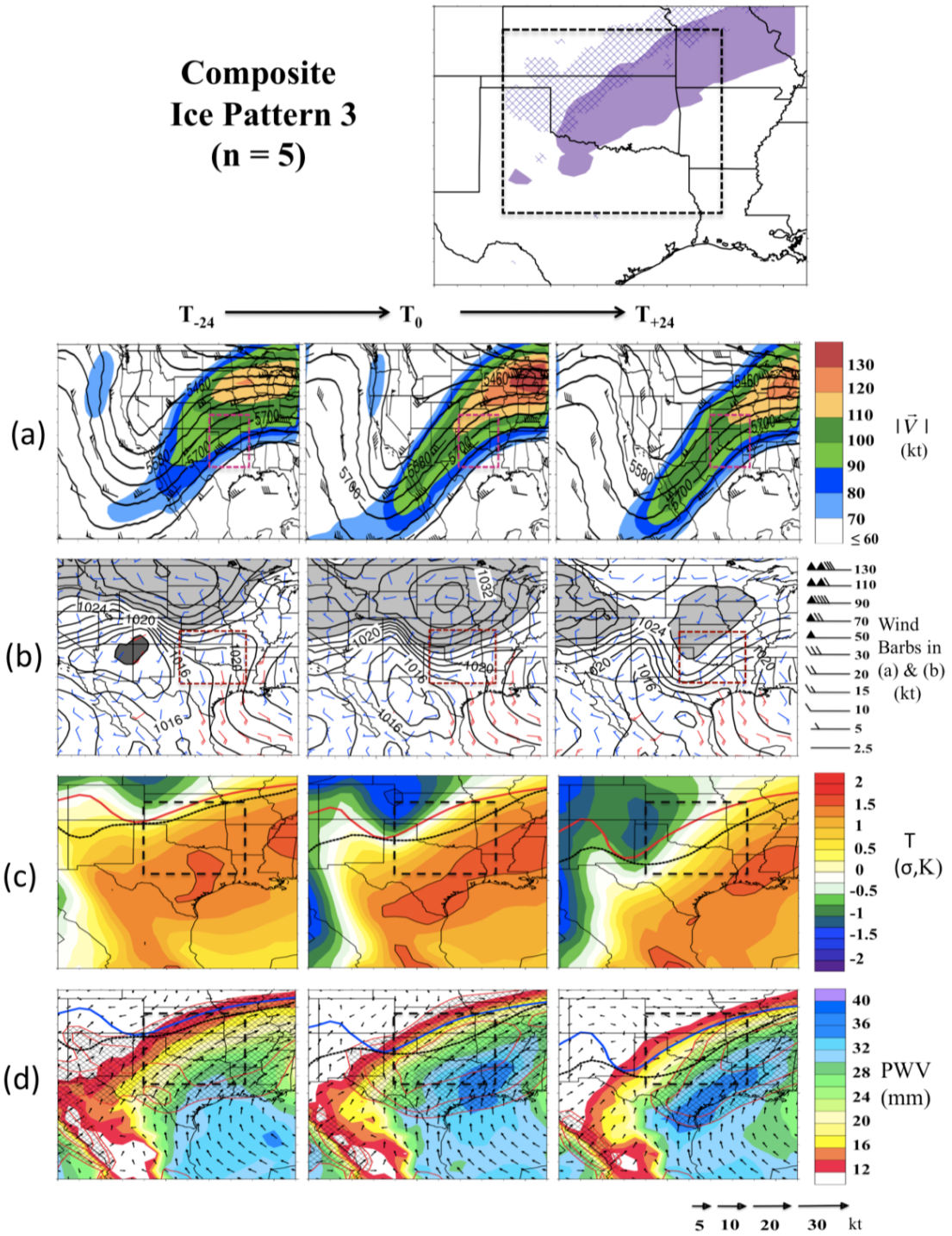

Figure 3.9: As Fig. 3.7/3.8 but for *Ice Pattern 3*.

over the domain by T_0, derived largely from the GOM for the warm layer (d). As freezing precipitation evolves, the high surface pressure weakens, associated with height falls ahead of the upper trough. Behind the trough, cooler and drier air advects into the SGP (c,d).

Fig. 3.10 shows that the regions experiencing freezing precipitation in *Ice Pattern 4* include the northern and western domain extending northeast. Freezing precipitation is typically of shorter duration than *Patterns 2 and 3*. An event of note for this pattern was a winter storm during January 4 1998 (a day prior to the long duration northeast U.S/Canada Ice Storm). The event was short lived and largely restricted to the morning hours, but associated with rapid accumulations over southeastern Kansas to 0.5 inch (along with > 1 inch of ice pellets) during elevated thunderstorms, while north-central, and western and Panhandle Oklahoma experienced several hours of moderate-intensity precipitation with 0.25-0.5 inch of ice on elevated surfaces. To the south flash flooding was observed in many locations over Oklahoma, Missouri, Arkansas and Texas.

Ice Pattern 5 (3.11) shows a long-wave trough axis over the far western U.S at T_{-24} that moves eastwards and amplifies west of the domain over southwest Texas and New Mexico at T_0 (a). The more zonal nature of the trough with respect to the other patterns may result from the expansive area of particularly cold low-level air across the northern half of the U.S prior to winter storm development (b,c). The resulting temperature gradient promotes a strong west-southwesterly jet by T_0, with the domain located in the composite right entrance region, favorable for upper level divergence

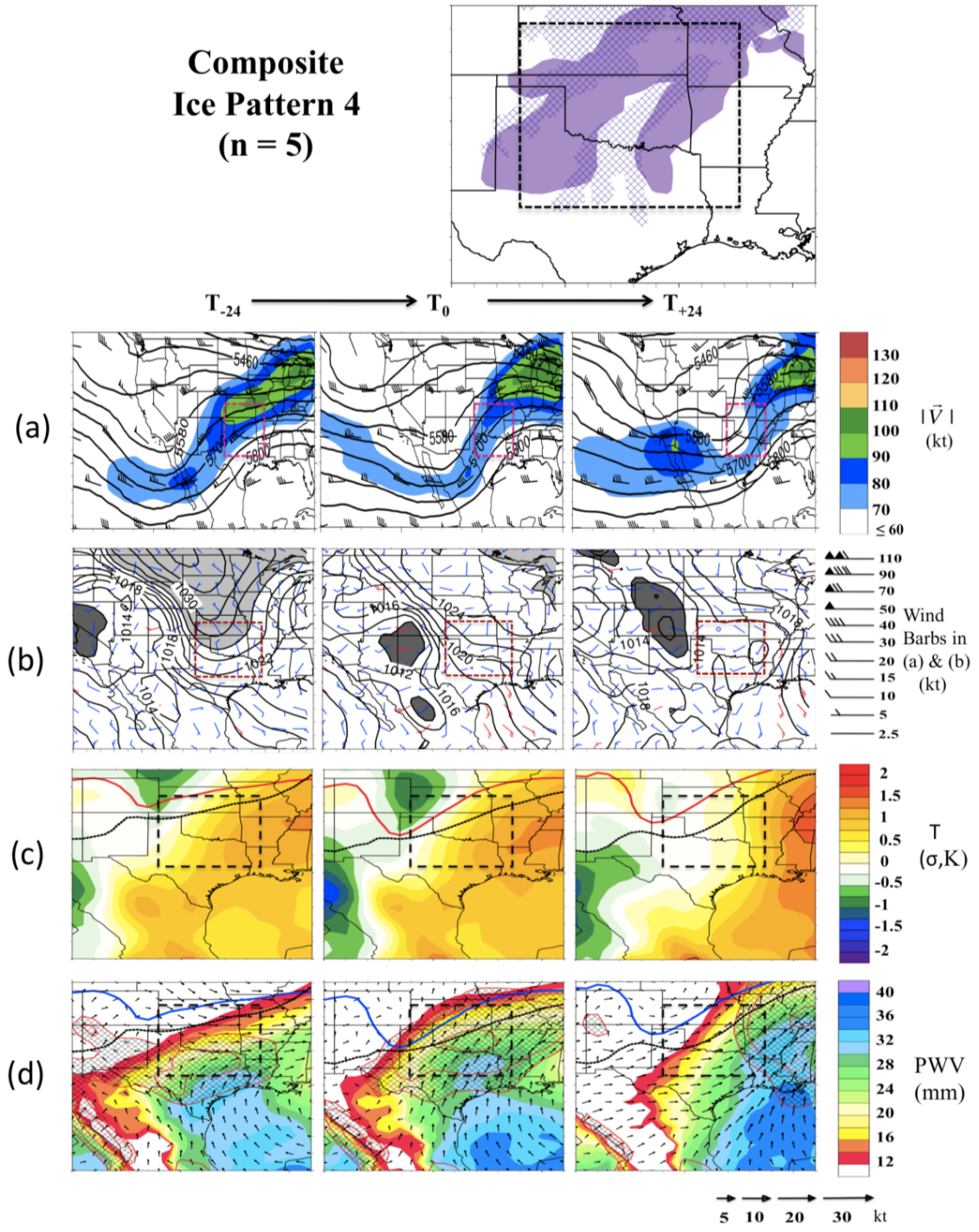

Figure 3.10: As Fig. 3.7/3.8 but for *Ice Pattern 4*.

and ascent. SLP at T_{-24} (b) suggests that the cold airmass penetrates almost to the Gulf of Mexico. Nonetheless, warm low-level temperatures persist in the far southern U.S (>+0.5σ, c).

By T_0, low-level southerly flow east of the trough axis warms the low-levels, and promotes broadening of an above 0^oC temperature inversion over southern portions of the domain. The 850 hPa wind trajectories also become more favorable for moisture advection into the region, particularly to eastern portions (d), where PWV anomalies exceed +1.5σ. Freezing precipitation was primarily generated to the northeast of the mid-level trough at T_0 in conjunction with height falls and WAA. By T_{+24}, the upper trough has moved to the east, and colder air from the northwest moves aloft into the domain, shifting the warmer airmass south and east (c).

Ice Pattern 5 is another pattern type favorable for multiple phases of winter precipitation, which often occur simultaneously over the domain. An example includes 12-13 December 2000, which produced heavy snow over Oklahoma and points north, with ice pellets and ice accumulation over north Texas into southern/western Arkansas. Fig 3.11 demonstrates the locations of freezing precipitation for the events in this pattern, indicating a preference to the south and east.

The five patterns described represent a large subset of cases within our small ice dataset. Nonetheless, they are not exhaustive. Some key observations based on this preliminary work include:

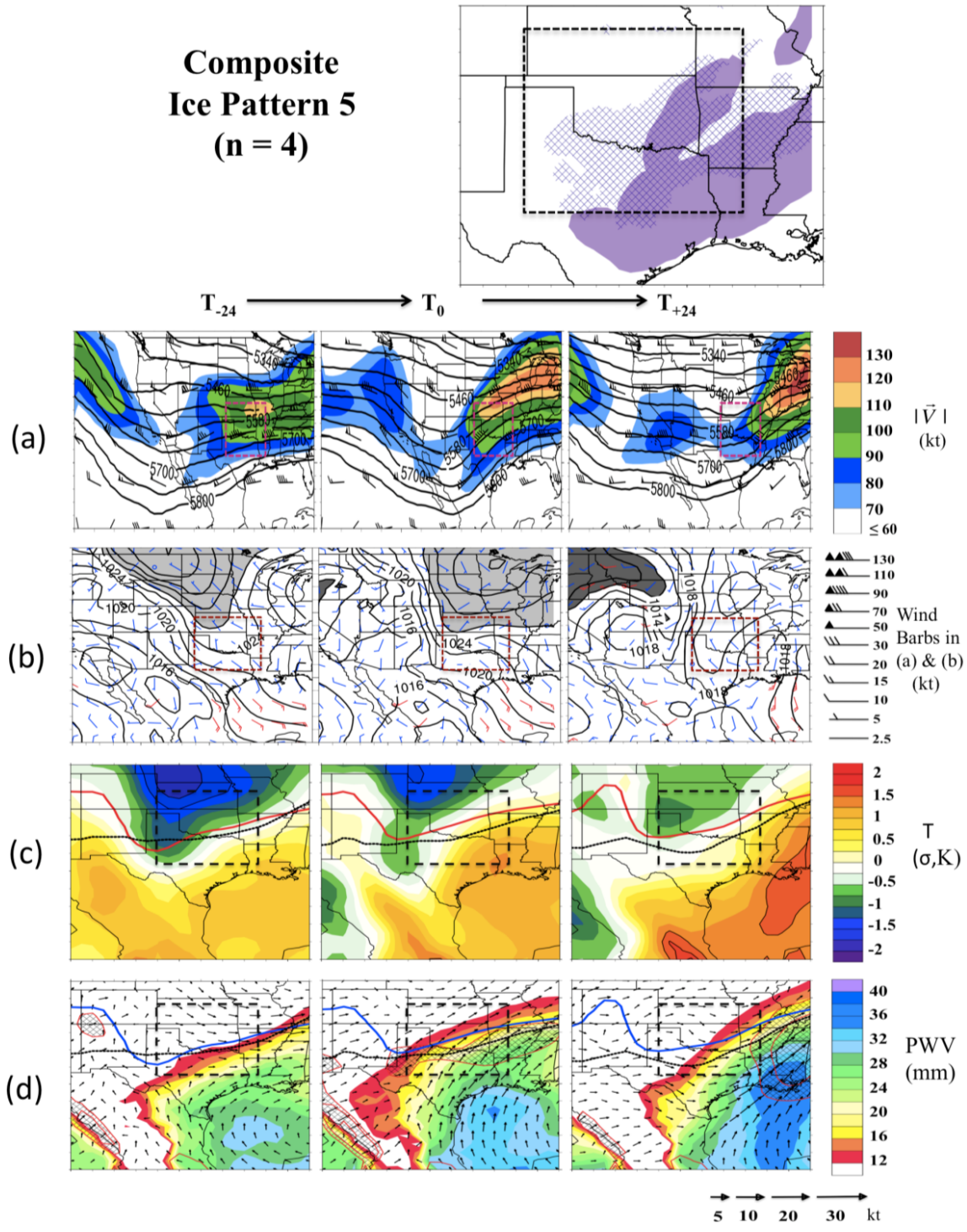

Figure 3.11: As Fig. 3.7/3.8 but for *Ice Pattern 5*.

(i) A tendency for a slower-moving western trough (*Ice Pattern 2, 3)*, producing weaker large-scale dynamics over the domain but the possibility of multiple propagating shortwaves as focus for ascent (see also Sanders et al. 2013). Isentropic ascent and WAA north of a quasi-stationary front demarking the boundary between the arctic and subtropical airmass appears common.

(ii) High sea level pressure over the northern tier of the U.S, and in some cases, a pressure dipole across the Rocky Mountains reminiscent of cold air damming. This high SLP was almost always present preceding SGP freezing precipitation.

(iii) Warm air at low levels (approximate level of warm layer inversion) over the southern U.S. Notably, severe icing events for the central domain typically corresponded with larger positive departures from climatology.

(iv) Moisture transport from the Gulf of Mexico, or the eastern Pacific, with the more significant events possessing greater precipitable water content, and direct Gulf moisture transport of longer duration.

(v) Weak or absent surface cyclone development, even with a proximal trough axis. Surface low-pressure occasionally forms by T_{+24} and as a result is largely unrelated to freezing precipitation for the region.

3.4 Synoptic Patterns for Snowfall and Comparison to Section 3.3

In order to better understand evolution of freezing precipitation, it was helpful to provide a contrast with events that produced a weak or absent transition zone. Below

are descriptions of the five leading patterns from the retained three PREOFs for snowfall. These five patterns describe 71% of all cases in the dataset. The number of events per composite are: *Snow Pattern 1 (9), Snow Pattern 2 (6), Snow Pattern 3 (7), Snow Pattern 4 (6), Snow Pattern 5 (6)*. Figures 3.12-3.16 are formatted in the same fashion as Fig. 3.7-3.11 for Snow Patterns 1-5 respectively.

Composite *Snow Pattern 1* (Fig. 3.12) is associated with development of a broad, low amplitude trough in the south, and west-northwesterly flow over much of the northern states (a). This airmass is particularly cold, similar to *Ice Pattern* 2 and 5 (Fig. 3.8, 3.11), while the airmass to the south is close to the 1979-2012 mean (c). SLP at T_{-24} and T_0 (b) shows southeastward movement of arctic high pressure over this period, similar to that observed for ice. At T_{-24} northwesterly near-surface flow over the plains and Midwest is evident, appearing to be in the wake of a low-pressure system situated east of the Great Lakes, at the periphery of the figure. By T_0, pressure has increased over the Northern Plains, associated with further cold air advection and airmass deepening. Cold anomalies exceed -1.5σ over a broad area (c). The increasing temperature gradient over the southern U.S may contribute to strengthen the jet aloft over the ensuing 48-hours (a).

From the SLP and height fields, forcing for precipitation is possibly associated with mid-level short-waves and isentropic ascent. The location of snowfall associated with constituent events tends to northern portions of the domain, however exact locations will depend on moisture availability, focus for ascent, and location of surface front, among others. An example of an event in this category was a snowstorm during

February 15th-16th 1993, which produced widespread and locally heavy snowfall (~12 in) over the northern domain.

The height field of *Snow Pattern 1* is most visually comparable to *Ice Pattern 5*. However, the *Snow* composite does not reveal a region suitable for sustained freezing precipitation (850 hPa freezing isotherm is further south that its surface counterpart, c, d versus Fig. 3.11 c, d). Comparison of SLP and 975 hPa wind vectors for the two patterns (b, versus Fig. 3.11b) indicates persistent and stronger northwesterly flow into the SGP for *Snow,* at T_{-24}, with a long fetch extending into Canada. Conversely at the same time for *Ice*, flow over the northern tier has backed to the west, and the area of high pressure in the central plains appears to weaken, implying modification of the arctic airmass. In the former case, strong northwesterly flow at 850 hPa well into the domain evidences a deeper layer of cold air (c, d), while to the south *Snow* composite standardized temperature anomalies are less pronounced. Partially as a consequence of the lack of warm air aloft, moisture into the domain is less for *Snow Pattern 1*, with PWV on the order of 14mm or less at T_0 (d, versus Fig. 3.11d).

Snow Pattern 2 (Fig. 3.13) depicts a trough over the western U.S at T_{-24}, amplifying by T_0, with an axis through west-central portions of the domain (a). A weak jet streak at trough base intensifies after T_0 and propagates the trough axis eastward. The domain low-level airmass (c) is warmer than climatology (+0.5 to +1σ) , extending into the central and eastern U.S at T_{-24}. In the absence of a shallow cold surface layer, the vertical temperature profile decreases with height (c, d). As the upper level trough moves east, southern Rocky Mountain lee troughing intensifies, and coupled with the

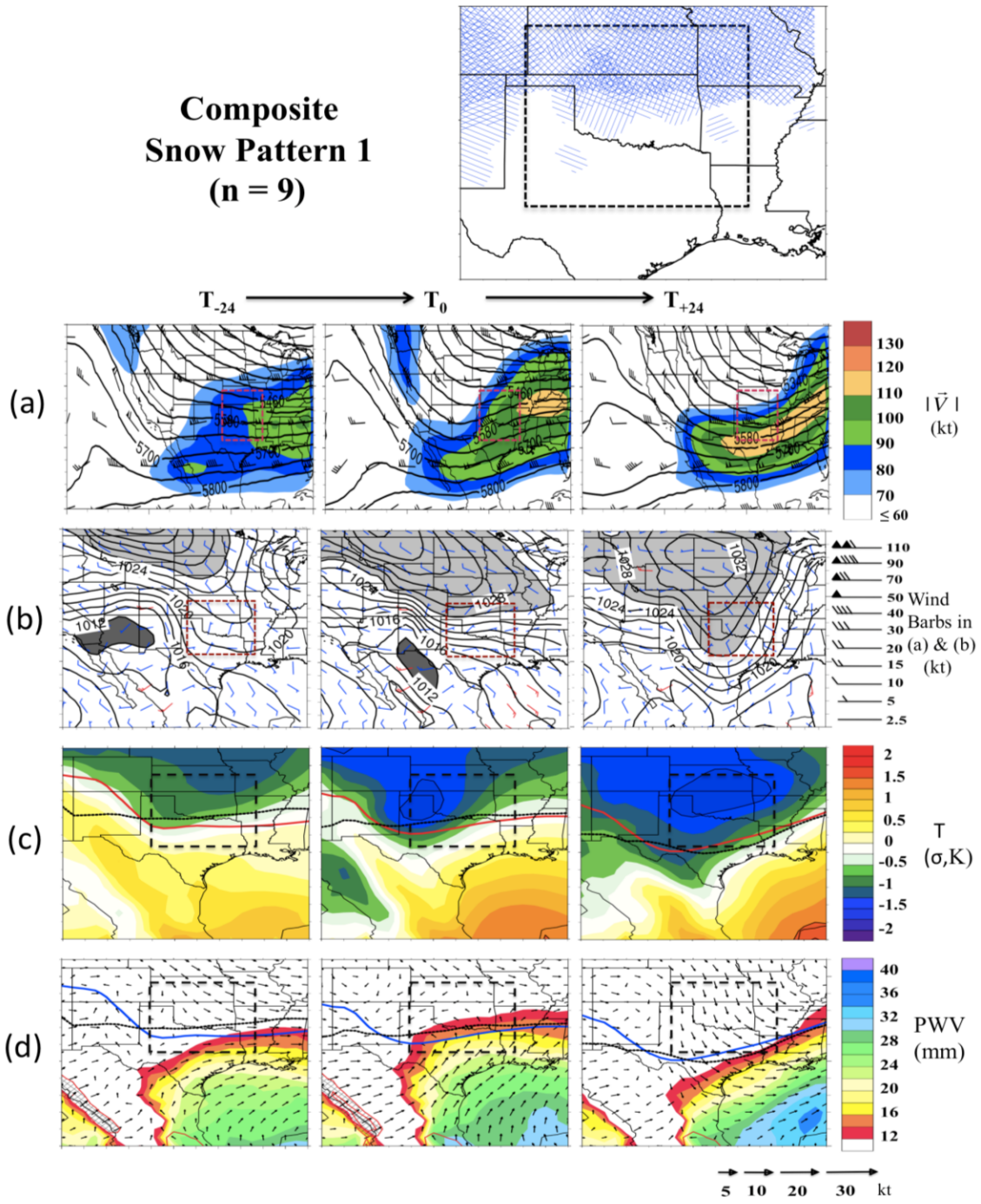

Figure 3.12: As Fig. 3.7/3.8 but for *Snow Pattern 1*. Note that the top panel now displays categorical snowfall (20% coverage contour), with blue stippling for each constituent event, providing a measure of common location.

warmer and presumably lower static stability airmass (e.g., compare Fig. 3.7c, 3.13c), promotes cyclogenesis, occurring at T_{-24} over northern Mexico east of the base of the upper trough (b). By T_0, the center of low pressure is located in the vicinity of eastern Texas and the Gulf coast. Behind the surface cyclone, much cooler air advects into the region via deep column northwesterly flow (c, d). Within the warm sector of the cyclone, moisture is accelerated northwards via strong southerly flow, producing PWV anomalies of +1.5 to +2σ (d). Snowfall occurs north and northwest of the cyclone center, north of the warm sector (top panel).

Snow pattern 2 is one of two snow patterns that associated with a well-developed surface cyclone as the focus for precipitation. According to Fig 3.13, snowfall can occur anywhere within the domain, with increased frequency northwestward. The location of snowfall is tied to the track of the surface low. An example of an event in this category is a late season snowstorm on March 12 1999, which brought heavy snow (locally ~10 in) to southwestern Kansas, northwestern Oklahoma, and eventually lesser amounts to northern Oklahoma and Arkansas.

The evolution of *Snow Pattern 2* can be compared to that of *Ice Pattern 1* (Fig. 3.7). A notable distinction between them is the SLP field (b), where surface high pressure dominates the ice pattern, indicative of a shallow cold airmass over the domain prior to the arrival of the mid-level trough. Surface cyclone development in the latter case may be tempered by the higher static stability of the surface airmass and near surface cold air advection, which weakens amplification of the upper trough, and surface cyclogenesis through differential thermal advection in the lower levels that promotes descent (Bluestein, 1993, p169). The presence of an apparently stronger jet

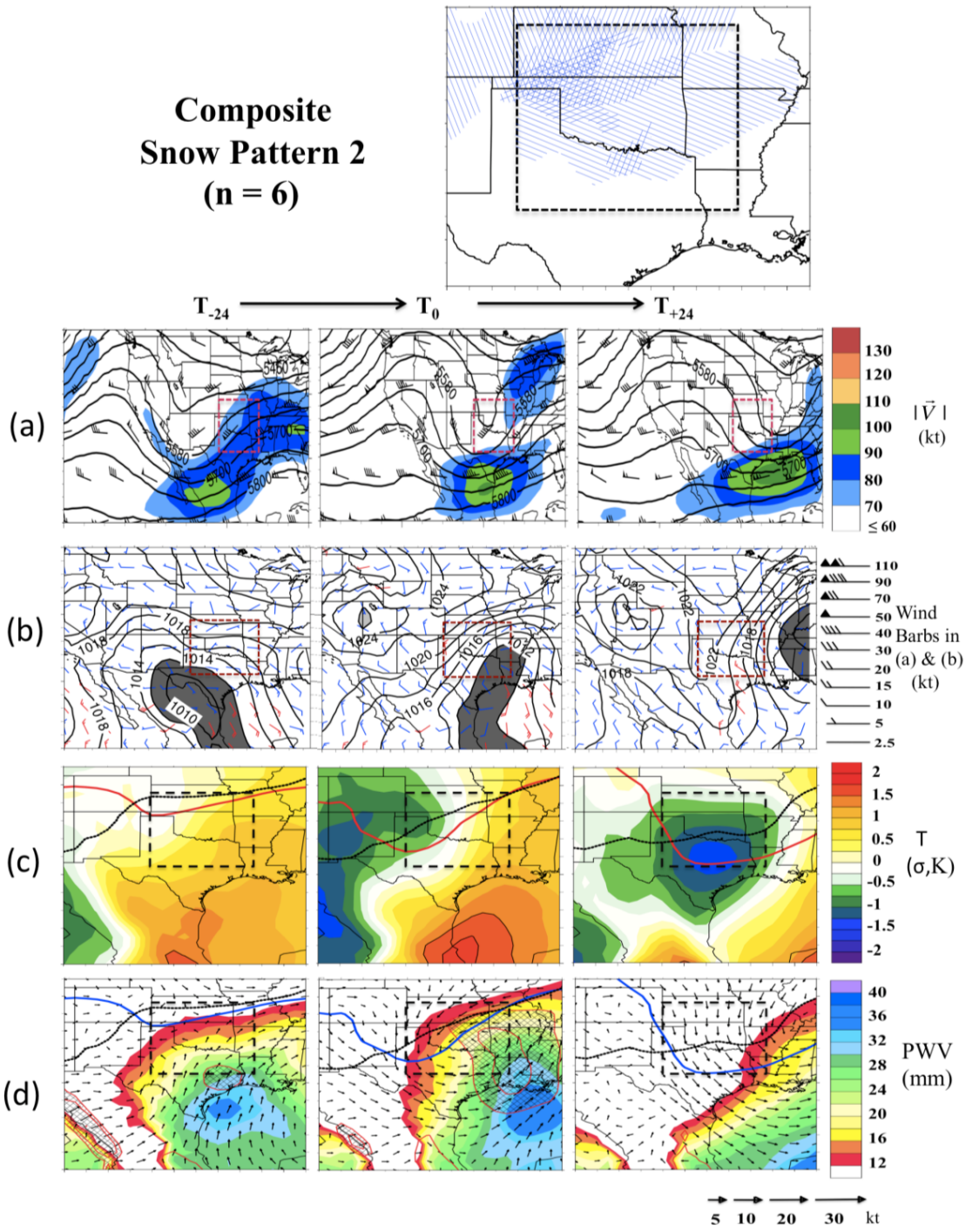

Figure 3.13: As Fig. 3.7/3.8, 3.12 but for *Snow Pattern 2*.

streak at the base of the trough axis may imply faster system progression, but further work and a larger sample would be required to support this.

Snow Pattern 3 (Fig. 3.14) is another pattern with largely zonal mid-level flow (e.g., compare with *Snow Pattern 1*, and *Ice Pattern 5*). A notable feature of the composite height field is a trough over the northwestern U.S that remains largely stationary over the 48-hour period. To the south, a shortwave ejects west of the domain by T_{-24} to reside over the domain at T_0 (a). The strongest upper level flow is located just to the south (a). SLP and near surface winds (b) indicate a broad arctic airmass over the eastern half of the U.S, moving south and east with time. The wind field is variable, with predominantly domain-northeasterly flow. Low-level temperature anomalies (c) also do not reveal substantial departures from climatology until T_{+24}, when reinforcing cooler air is transported to the rear of the mid-level trough and/or weak low. Moisture availability is adequate, with departures in PWV of near or above $+1\sigma$ at T_0, despite little evidence in the composite of sustained southerly flow (d). The weak and variable low-level wind flow may be a factor in creating a less favorable environment for ice, despite the existence of an apparent shallow arctic airmass. It may well be that any low-level inversion that exists is either not sufficiently warm to support freezing precipitation or is quickly eroded. An example of a pattern 3 event is January 9-10 1993 where a wide swath of snowfall exceeding 6 inches was produced through northern Oklahoma and Kansas, accompanied by a brief nocturnal episode of freezing drizzle and ice pellets.

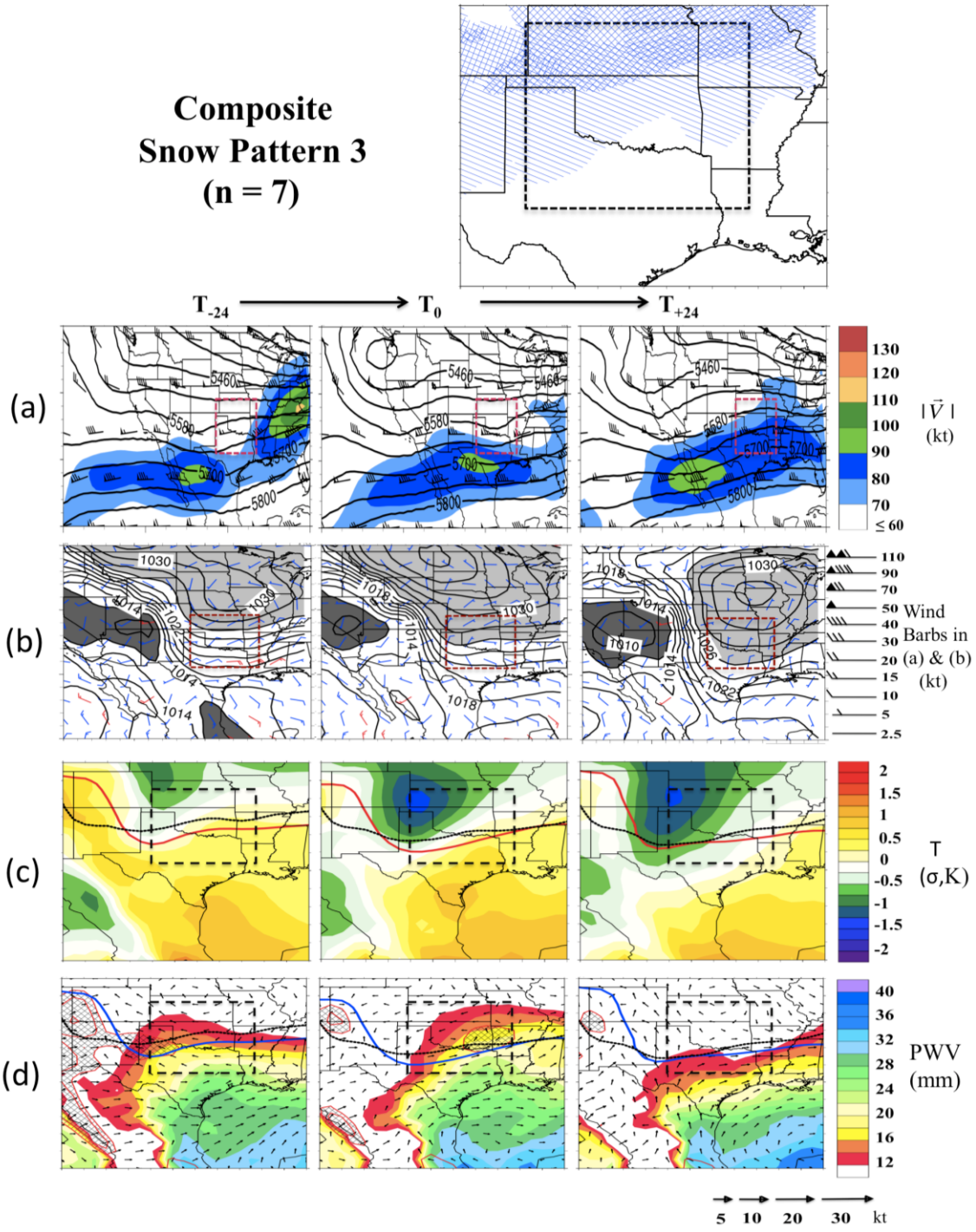

Figure 3.14: As Fig. 3.7/3.8, 3.12 but for *Snow Pattern 3*.

Snow Pattern 4 (Fig. 3.15) is the second example of snowfall associated with a surface cyclone. In this case, a positively tilted trough west of the domain at T_{-24} amplifies by T_0, aided by a 100 kt jet streak upstream of the axis. At T_0 the meridional extent of the trough extends from Canada to Mexico (a). By T_{+24} the trough axis is east of the domain, and substantially colder air on its western side intensifies an upper level jet streak over the southeastern U.S. The evolution of low-level temperature and moisture is similar to *Snow Pattern 2* (Fig. 3.15), however, due to the more developed circulation, moisture is advected further north over the Midwest (d). The 850 hPa, 975 hPa vector winds and SLP are reflective of a stronger circulation, as is the notably cold, dry air on the western edge, suggesting strong subsidence (c, d). Additionally, the composite average minimum pressure of the cyclone is lower for *Pattern 4* (b). If the air north of the developing cyclone is sufficiently cold, freezing precipitation could occur for a brief time, however, strong ascent and heavy precipitation might produce a faster erosion of any warm layer inversion present.

The location of snowfall for this pattern appears to favor the eastern domain (top panel). The more intense surface cyclone, (b) and rapid cooling and drying west of its center (c, d) do not promote a wide snowfall shield on its western edge. In addition, the average duration of snowfall is likely to be less in any given location, but the rate of snowfall potentially greater than *Snow Pattern 2* (not shown). A recent event in this category is the Oklahoma Christmas eve blizzard of 2009, which was notable for its high winds, leading to significant drifting of snow. Approximately one foot of snow accumulated in portions of Oklahoma, with the worst conditions occurring during the evening rush hour.

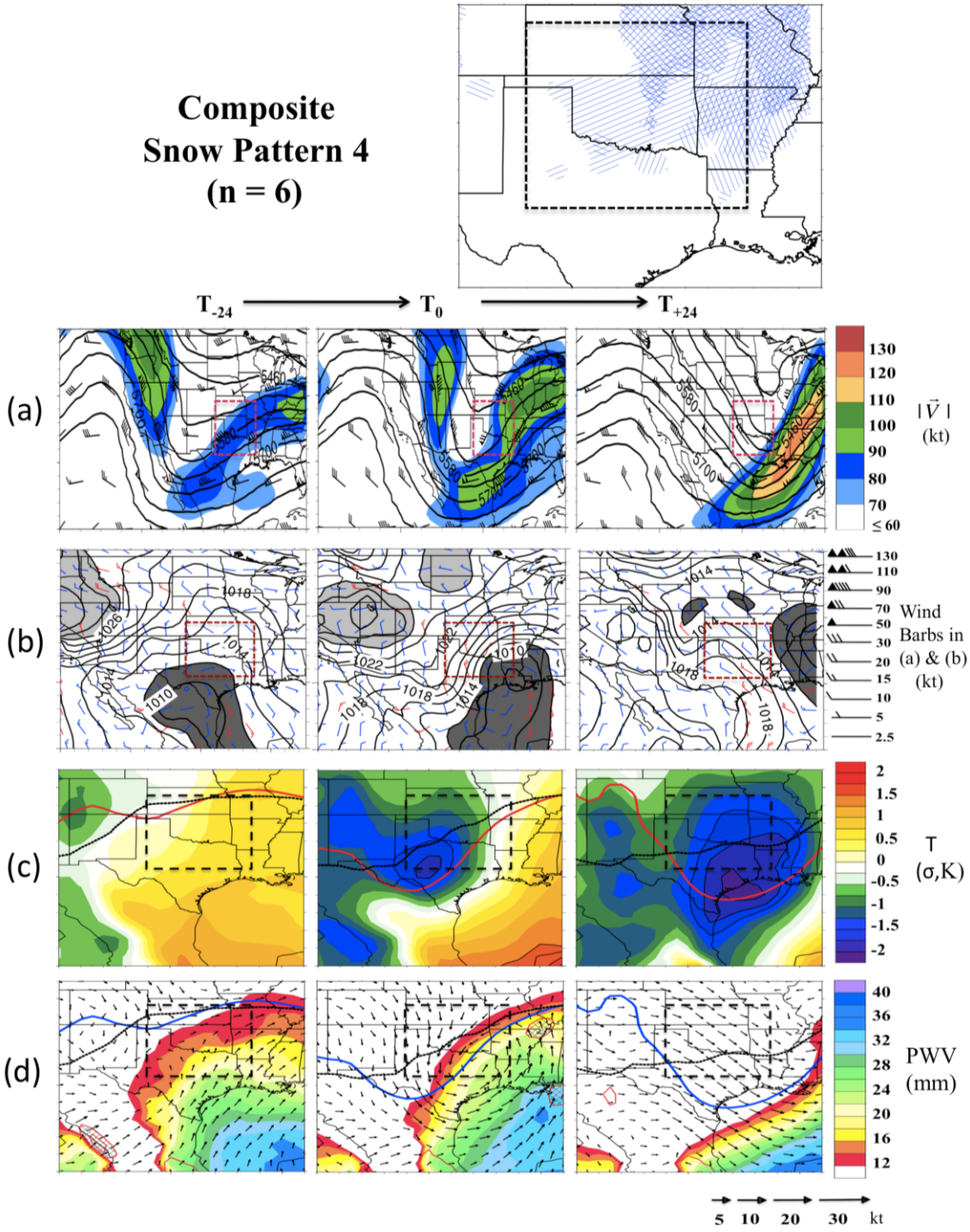

Figure 3.15: As Fig. 3.7/3.8, 3.12 but for *Snow Pattern 4*. Note that the NARR categorical snowfall was not well resolved for at least one event in this category (December 24-25 2009), despite the observation of heavy snowfall.

Snow Pattern 5 (Fig. 3.16) depicts a trough over the far southwest U.S, with a zone of northwesterly flow to the northeast at T_{-24} (a, b). By T_0, a split flow pattern emerges, with a weaker shortwave over the northwestern U.S, while the main driver of winter storm development in the Plains is associated with the eastward progression of the southern trough. At the surface, a well-developed cyclone is centered over the Great Lakes at T_{-24}, while higher pressure, and cooler northwesterly flow dominates the Great Plains (b). The airmass does not appear to be exceptional with respect to climatology (c, d), but cooler air advances almost to the Gulf of Mexico. Much like *Snow Pattern 1*, this results in cool domain 850 hPa low-level temperatures (c, d). As the upper trough approaches the composite does not show cyclogenesis (b). Cooler air to the west of the trough reinforces the cold airmass in place. As a result of strong southerly flow from the Gulf of Mexico, PWV anomalies exceed $+1\sigma$ over most of the domain, while 850 hPa trajectories indicate WAA into the low levels at T_0.

Locations of snowfall for the constituent events extend throughout the northern region, and much of the remainder of the domain bar the far south and southeast (top panel). A notable event includes December 23-24 2002, which impacted northern Oklahoma, southern Kansas and northern Arkansas/southern Missouri. Accumulations ranged from 3-8 inches, locally 10 inches in Kansas.

3.5 Summary of Key Differences

Sections 3.3 and 3.4 detail the evolution of each composite winter storm for Ice and Snow categories respectively. Similarities were found for attendant height and pressure fields for within and between ice/snow patterns. Nonetheless, this work has

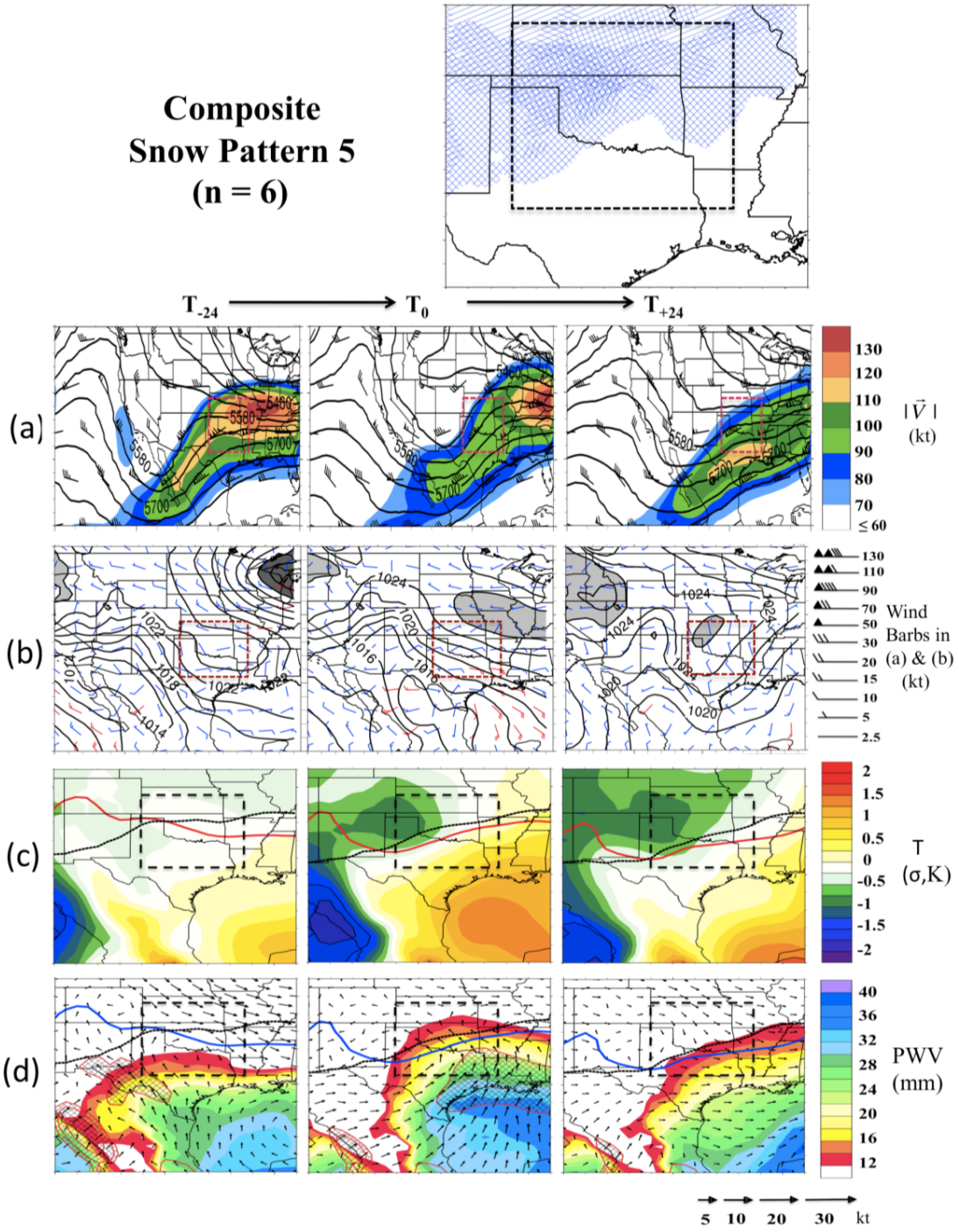

Figure 3.16: As Fig. 3.7/3.8, 3.12 but for *Snow Pattern 5*.

revealed some important distinctions that could be of value to regional Forecasters, as well as providing specific composite evolutions aiding pattern recognition.

3.5.1: Sea level pressure

Our results showed that all ice composites, and two snow were accompanied by high SLP over much of the central and northern U.S prior and during precipitation onset (T_{-24}, T_0). This is indicative of an arctic or 'cold' anticyclone. Such airmasses are typically shallow, especially at their southern periphery, as they undercut subtropical air to the south, creating conditions favorable a warm layer inversion. The southward movement of cold air was in conjunction with an inverted trough east of the Rocky Mountains. This topographically promoted 'cold surge' is highly ageostrophic (perpendicular to the isobars and down the gradient of pressure; e.g. Bell and Bosart, 1988). Colle and Mass (1995) observed that cold surges over the Southern Plains are wider than their Appalachian counterparts. As cold air damming structures require a topographical barrier to inhibit geostrophic flow, cold surges are most effective immediately east of the barrier, with geostrophy resuming ~ 500 km from the boundary (the approximate Rossby radius of deformation). However, the gently sloping terrain of the high Plains may extend their effective radius by additional small scale damming of air parcels with a westerly component. The development of a warm layer associated with these conditions is displayed schematically in Figure 3.17.

As cold air damming results from a pressure gradient, the magnitude of the pressure gradient over the Southern Plains may moderate speed and southward extent of the cold air. In addition, higher static stability airmasses are trapped against the barrier more effectively (Forbes et al., 1987). In the cases where these structures were observed prior to snowfall events there was evidence of cooler air south of the front, potentially producing weaker low-level WAA, and negating a substantial warm layer. We

investigated this quantitatively by first grouping pattern types by proximity and amplitude of the major trough axis, and presence of surface cyclone versus prominent baroclinic frontal boundary, yielding subgroups of (I1) *Ice Pattern 1,* 4 (n=11), (I2) *Ice Pattern 2, 3,* 5 (n=13), (S1) *Snow Pattern 2, 4, 5* (n=18), (S2) *Snow Pattern 1, 3* (n=15). Average 850 hPa temperatures above and below freezing were evaluated for a domain encompassing the SGP extended north (south) to $42^{o}(28^{o})$ and east to 90^{o}W. The mean was bootstrapped using 1000 replications in each case for T_{-24} and T_{0}. I2 domain temperatures above freezing were significantly higher (95% CI) than all other sub-groups for both times, while the 24-hour coverage of above freezing temperatures increased 4.5%. I1, S1 and S2 did not evidence significant differences. For below freezing domain temperatures, S2 was statistically lower than I1 and S1, but not against I2. S1 showed the largest 24-hr positive expansion of sub-freezing air (14.1%).

A Student's 2-tailed T-test was performed for SLP at T_{-24} for the ice and snow events from table A3.1, A3.2, using NCAR Command Language (NCL). Temporal means and variances were calculated, along with equivalent sample size (number of statistically independent samples). The difference variances for ice and snow were accounted for by using the Welch's T-test. The result, shown in Fig. 3.18, suggested a significant difference between T_{-24} ice and snow throughout the Great Plains and Southeast/Gulf of Mexico, with the former yielding higher SLP. Averaging over each event for each grid point and evaluating regional SLP spread (boxplots, Fig. 3.18) for the Northern and Southern Plains also corroborated this finding. The higher pressure over the GOM associated with ice events may also indicate the prevalence of concurrent anticyclonic flow due to the westward extension of the Atlantic subtropical high.

3.5.2: Mid-level trough and surface cyclone

Another distinction between ice and snow composites was the location of the trough axis with respect to the domain, particularly as precipitation was developing (T_0). Caveats regarding onset time aside, ice events in this sample often were associated with a more western trough axis at T_0 (~59%, versus 27% for snow with major trough axis base west of AZ/NM border). Such conditions potentially allow longer duration WAA over the domain, while stronger upper level forcing (e.g., via vorticity advection) remains west of the region initially. This set-up is not favorable for cyclone development, but can prolong precipitation associated with isentropic ascent and warm air advection. Ressler et al. (2012) note that freezing rain associated with trough axes well to the west of their study site produced longer duration precipitation, but on average weaker precipitation rates. To some extent this was also observed here (*Ice Pattern 2*), however, in cases of enhanced ascent from short-wave perturbations, or from potential instability aloft associated with a deep moist warm layer, conditions may favor more intense precipitation *(Ice Pattern 3)*.

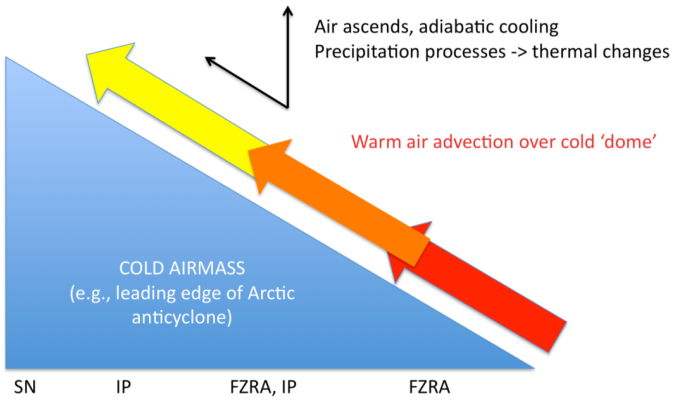

Figure 3.17: Schematic depicting the precipitation types accompanying 'cold surge' events in the SGP.

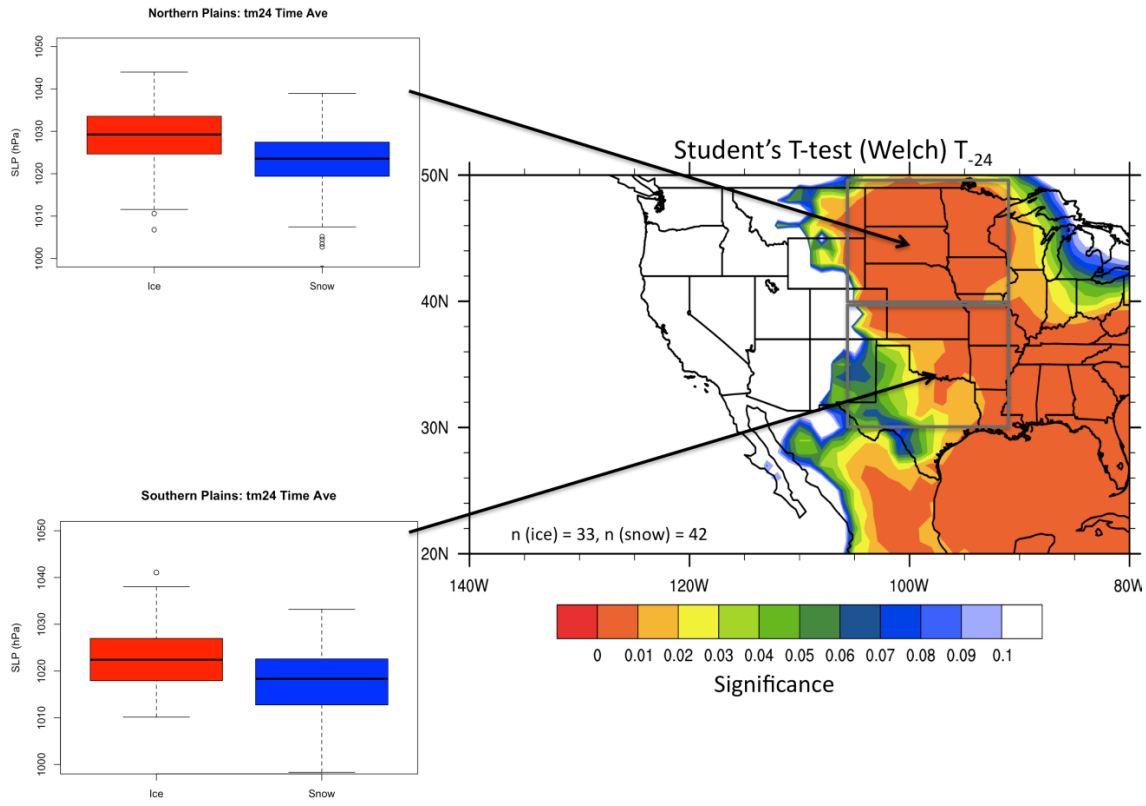

Figure 3.18: Student's (2-tailed) t-test for ice events against snow events SLP at T_{-24} (left). Number of events per dataset shown by text in main figure. Only statistical significance ≤ 10% shown, with values < 5% more a more robust indication of significance. Temporally averaged grid point distributions of SLP for ice and snow shown by boxplots for the Northern and Southern Plains, defined 40-50°N, 90-105°W, and 30-40°N, 90-105°W respectively. Calculations using NCL 'ttest' function. Caution should be applied when interpreting t-test due to low sample, and the possibility of non-normal distributions, albeit test is generally insensitive unless non-normality is large.

When a trough axis was proximal to the domain *(e.g, Ice Pattern 1, Snow Pattern 2, 4)*, snow events indicate enhanced cyclogenesis relative to ice. A proximal amplified trough enhances upper level support for a deep column of rising motion. However, the higher static stability surface airmass associated with ice events may act to inhibit low-level ascent and retard cyclone development. For ice, cyclogenesis appears to occur most favorably once the arctic airmass has migrated south to the Gulf coast, where the resulting temperature contrast enhances baroclinicity. Nonetheless,

these systems do not evidence rapid development. The deeper surface low for snow produces high precipitation rates north of the cyclone center, and possibly rapid transitions between phase types (i.e., rain, mix, snow). Figure 3.19 shows schematically approximate centers of low pressure (based on local minimum) for snow and ice events and their track T_{-24} to T_{+24}. The figure confirms our assertions, demonstrating that ice events typically have a less well-defined center of low pressure, developing after the initiation of freezing precipitation over the domain, and generally not deepening during the analyzed time.

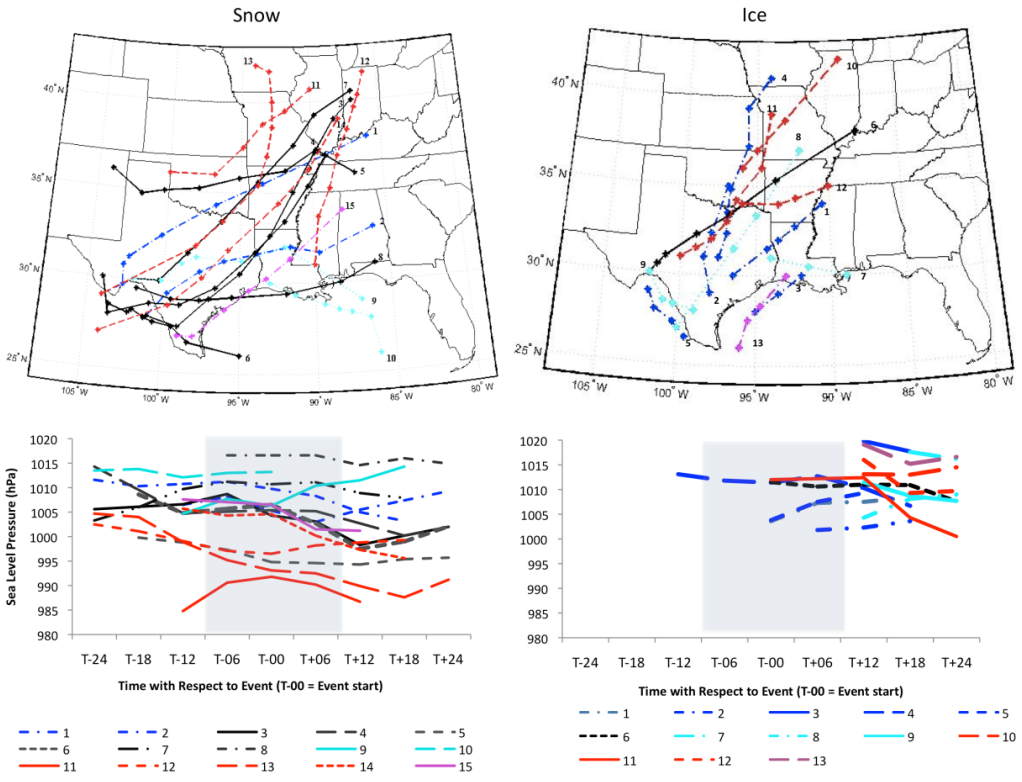

Figure 3.19: Approximate paths surface cyclones between T_{-24} and T_{+24} for snow (left) and ice (right). These tracks were based on calculation of local minima, and manual removal of stationary pressure signals (e.g., lee troughing), and cyclones not present over the southern U.S. The tracks are color coded by pattern type, pattern 1 = blue, 2 = black, 3 = cyan, 4= red, 5=purple. The corresponding SLP time series is marked by a number for each track, and displayed in the time series plots snow (bottom left), ice (bottom right). The period within 6-hours of T_0 is shaded in grey.

Chapter 4: Introduction to Case Studies, and Development of a WRF-ARW Sea Surface Temperature (SST) Sensitivity Study

4.1 Introduction

In chapters 2 and 3, a regional preliminary climatology of winter storms, with an emphasis on freezing precipitation (FZPCP), was performed for the SGP domain. Chapter 2 demonstrated that the region can develop pronounced warm layers associated with temperature and moisture advection from the subtropics, including the Gulf of Mexico (GOM). The results of chapter 3 revealed a subset of synoptic flow patterns producing FZPCP, and that the structure of this flow strongly determined the warm layer magnitude and location/intensity of FZPCP. In this chapter the physical basis for a sensitivity study is introduced that examines the role of SST in the GOM to the evolution of mixed-phase precipitation. The case studies used for this work are described and experimental methodology compiled.

4.2 Physical Basis

Chapter 1 introduced work by Gyakum and Roebber (2001), Fuhrmann and Konrad (2013). These studies indicated that moisture and temperature structure of the examined warm layer was influenced to some degree by the adjacent oceans (the Atlantic, in their case). Therefore, we may speculate that there could be a link between regional SST anomalies and the warm layer. Such a hypothesis had also been alluded to by Bernstein (2000), Robbins and Cortinas (2002) and Changnon and Karl (2003), but only examined in one peer-reviewed modeling study by Ramos De Silva et al. (2006).

This latter work was summarized in chapter 1, and suggested increased SST in the adjacent Atlantic did impact the magnitude of the warm layer for an ice storm over North Carolina, observing that is was both deeper, and earlier forming, leading to higher total precipitation in the form of freezing rain. The simulated locations of these precipitation phases (freezing rain, snow, ice pellets) was not found to change, neither did overall precipitation accumulation (all winter phases). This analysis, while insightful, only examined one case study. From the results of this dissertation work, different circulation fields resulting in freezing precipitation for the SGP have been identified that are likely primary drivers for the timing, duration, and magnitude of ice accumulation. An evaluation of more than one case study is desired to better characterize SST sensitivity for diverse winter storm systems.

For the SGP, the GOM basin is the region of investigation for reasons previously provided. However, in order to more fully identify to what extent SST variability in the basin is likely to be a factor in regional winter storms, a brief two-fold analysis is conducted that checks for a potential relationship, primarily between warm layer depth/temperature.

4.2.1: Check 1: Air mass trajectories

Trajectory modeling tracks the movement of air parcels or particles using a Lagrangian framework. Trajectories are typically calculated using gridded wind fields on pressure or height surfaces (e.g., Fuhrmann 2011). The basic equations used to evaluate air parcel trajectory are given in Stohl (1988), and Fuhrmann (2011), shown by Eqn. 4.1 and 4.2.

$$\frac{d\overline{X}}{dt} = X'[\overline{X}(t)] \tag{4.1}$$

$$\overline{X}_0(t = t_0) = \overline{X}_0(\overline{X}, t) \tag{4.2}$$

Where t is time, $\overline{X}$ is a position vector, and X' a velocity vector. Equation 4.2 is a rearrangement of Eqn. 4.1 for time, t_0, which gives the initial position of an air parcel. Trajectories may be evaluated both forward ($t_0 > 0$) and backward ($t_0 < 0$) in time. Back trajectories define a start time at the end-point location, and integrate backward to project the path of the air parcel into the region of interest. Applications have included dynamical processes and structure of extratropical cyclones (e.g., Uccellini et al. 1985, Mass and Schultz 1993), air quality (e.g., Hondoula et al. 2009), large-scale flow climatology (e.g., Strong et al. 2007), and source regions of water vapor during high impact precipitation events (e.g., Brimelow and Reuter 2005, Gustaffson et al. 2010).

In this brief investigation, the HYSPLIT (Hybrid Single Particle Lagrangian Integrated Trajectory) model (version 4.9, Draxler and Rolph 2011) was used to investigate air parcel trajectories incident to the warm layer (specifically, the level of maximum temperature, T_{max}) during FZPCP. Four-day (96-hour) back trajectories were calculated for 73 station-sounding based reports of FZPCP during 36-winter storms at six locations, including Dallas Ft Worth Texas (DFW), Norman Oklahoma (OUN), Lamont Oklahoma (LMT), Springfield Missouri (SGF), Little Rock Arkansas (LZK), and Amarillo/Dodge City (AMA/DDC, computed as the halfway point). Use of several locations within the domain, rather than attempting to define a 'representative' point, allows for possible sub-domain variability in airmass sources. Due to the overlap of

winter storm events, trajectories were sometimes evaluated for the same storm at different sites. While this may bias the data toward long-duration events, it is assumed that regional and temporal differences in the mesoscale circulation mean that no two trajectories within the same storm system are necessarily identical.

HYSPLIT computes the trajectory of a single air parcel using the 3D velocity field from gridded meteorological data. In this case, NARR was used as input at 6-hour intervals. The process by which trajectories are calculated was provided in more detail by Fuhrmann (2011). The model requires a wind field (**u**,**v**), interpolated to a terrain following (sigma) coordinate. Meteorological variables are linearly interpolated from the input data levels to the model levels. The model calculates layer heights (AGL) using the hypsometric equation based on layer average virtual temperature. Model vertical velocity can be evaluated using dataset vertical velocity, isobaric or isentropic coordinates. NARR data includes vertical velocity, which can be used directly by HYSPLIT. Due to improvements in model resolution and parameterization of physical processes, using the model vertical velocity field is considered as or more accurate now than storm relative isentropic techniques (e.g., Schultz 2001, Furhmann and Konrad 2013).

Like all numerical models, HYSPLIT suffers from inherent uncertainty related to both its architecture, and the user selected calculation methodologies. Fuhrmann (2011) provides examples some typical sources. Common computational uncertainties include integration errors, truncation (shortening of timesteps or number of grid cells used in the model), and resolution error. Resolution error impacts the interpolation of various parameters, and produces uncertainty in the trajectory position over time. Stohl

and Seibert (1997) use an earlier version of HYSPLIT to assess this, finding position errors of up to 20% for trajectories over 24 hours. The common way to test for and incorporate resolution uncertainty is to initiate multiple trajectories, offset by small increments in the horizontal and vertical, and monitor their divergence in time. Fuhrmann (2011) used this approach (based on Draxler 2003) to calculate ensemble trajectories for specific case studies. He found that the divergence of trajectory solutions is highly case-study dependant. Given that our experiment examines numerous events, it would be prohibitively time consuming to determine the ensemble spread for each of them. It is assumed that the calculated 'instantaneous' trajectories have inherent uncertainty, especially past 48-hours.

Figure 4.1 displays altitude and equivalent potential temperature (θ_e) at T_{max} for five source regions (defined as the area where the trajectory resides at t-96 hour) during FZPCP. The percentage contribution to the total dataset is also provided. Trajectories originating over the GOM are shown to be fairly frequent, accounting for just over 25% of the analyzed total. Furthermore, the air parcels also remain generally near or within the marine PBL, subsequently developing high values of θ_e (median ~320 K). Other source regions include the more remote Pacific, generally yielding less moisture to the domain (panels b and c). Air parcels originating in the southern or northern U.S typically remain near the surface, gradually accumulating heat and moisture as they modify through their local environment. In some cases, trajectories loop anticyclonically at low altitude over the GOM before entering the precipitation region. In these 'recurving' cases, it is anticipated that the diabatic heating mechanisms (e.g., Latent heat flux into the air parcel) may be particularly important. Twelve such

examples were included in the dataset (not shown), making the total number of trajectories with GOM influence nearly 42%.

Figure 4.2 evaluates warm layer trajectories for the top 6 events by precipitation accumulation (based on liquid precipitation equivalent over storm duration), corresponding roughly to the dataset top 10%. Approximate accumulation was gathered from NCDC climatological summaries for the relevant station site, with metrics per 24-hours. Total event accumulations ranged from 1.4-2.8 inches (35-70 mm) per day, however it was not possible to separate out relative contributions by phase type. The majority of cases exhibited air parcel trajectories at low altitude over the GOM basin at some point (a). A mixture of GOM and subtropical Pacific trajectories are shown for the same events near the top of the warm layer (b). We can therefore confirm from these results that the GOM is a common source of warm layer heat and moisture during FZPCP.

4.2.2: Check 2: Trends

Ramos De Silva et al. (2006), in addition to a sensitivity analysis, performed a linear regression of 68 winter storm events (28 ice storms), examining for a statistical relationship between warm layer depth (WLD) and SST anomaly (SSTA) in the subtropical Atlantic Ocean. The regression relationship was found to be statistically significant, (p-value< 0.04) despite concerns over 'measurement noise' (offsets between actual precipitation time/phase and sounding profile).

Based on this work, a similar analysis was performed for the SGP domain. Using the FZPCP thermodynamic profiles from chapter 2 for all hydrometeor categories

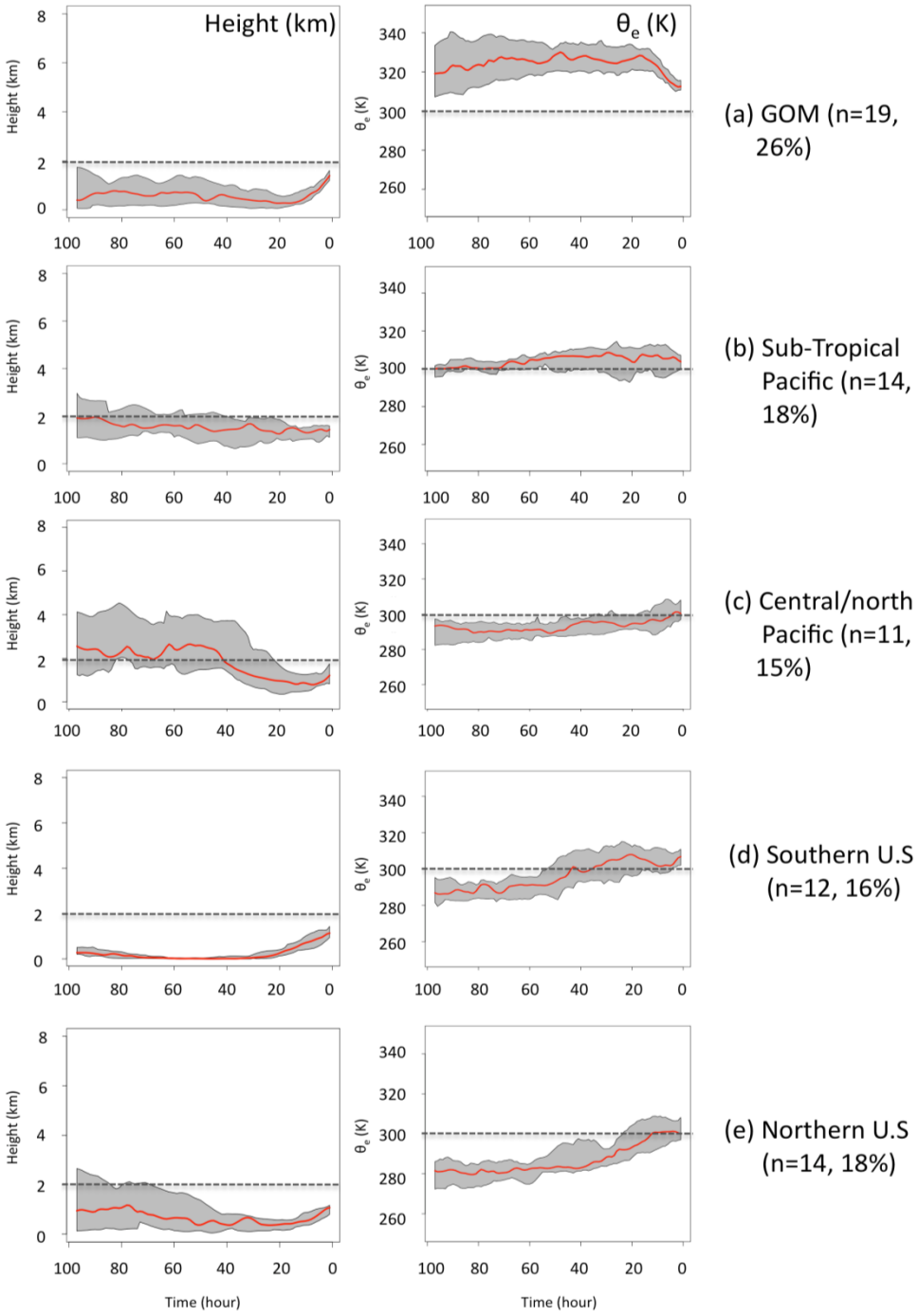

Figure 4.1: Trajectory profiles for different source regions (a-e, right), including height (left), and equivalent potential temperature (right). The median of the total number of profiles for each (n) is shown by the red line, while the interquartile range is shown by the gray shaded area. Each trajectory is integrated over 96-hours, with t-96 representing the source region, and t-0 (0 on the x-axis) the warm layer zone. Dashed horizontal lines present to aid visual interpretation**.**

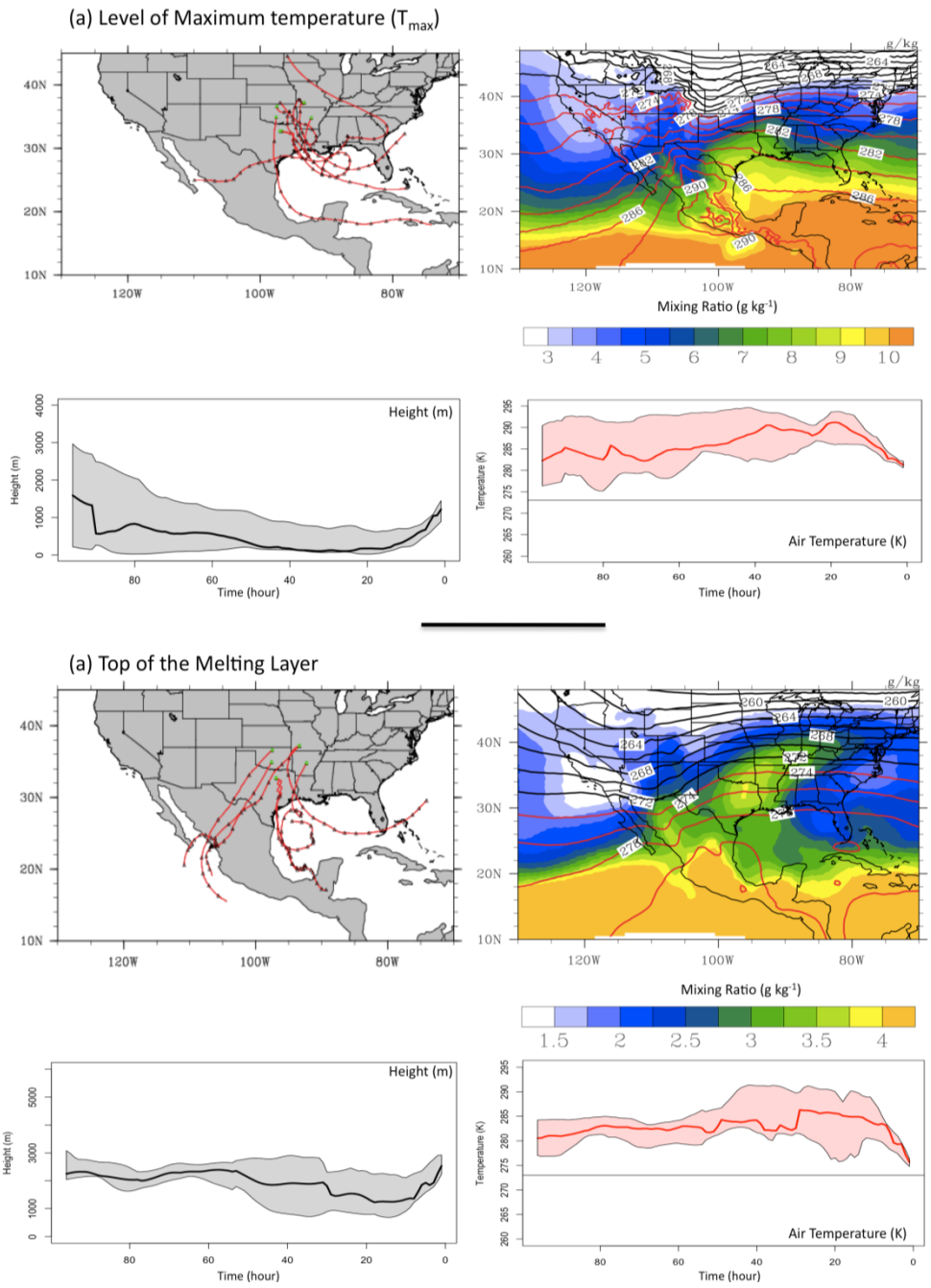

Figure 4.2: Multi-panel plot for (a) level of warm (melting) layer maximum temperature (b) top of warm layer. Back trajectories for the top 6 events by precipitation amount are displayed (top left), as is the average mixing ratio and air temperature for the 48-hours preceding trajectory end-point (top right). The bottom left and right time series show altitude and air temperature along the trajectory path respectively, with the median (inter-quartile range) shown by the solid line (shaded area). Gray thin line (273 K) on temperature time series present to aid interpretation.

bar drizzle (~75 soundings), corresponding SST data was obtained for each. In this case, blended satellite ('Advanced Very High resolution' Radiometer, or AVHRR) and in-situ (buoy, ship) data at a gridded horizontal resolution of 0.25 degree (~28 km) known as the 'Optimum Interpolation Version 2' (Reynolds et al. 2007, see section 4.4). SSTA were relative to 1971-2000 mean at daily time intervals. SSTA for three GOM sub-domains (Figure 4.3) were calculated for the days that freezing precipitation occurred, and for the week prior, expressed as a 'storm' (daily) or 'weekly' average respectively. Values of WLD, temperature, and EMP (chapter 2, eqn. 2.1) were derived for each profile (entirely sub-freezing profiles ignored). A linear regression using 'R' software was performed for each GOM sub-domain against EMP. Figure 4.4 shows the results of this regression. For each sub-domain, the storm average (daily) SSTA indicated a positive association with EMP. Unfortunately, the datasets did not yield similar variance (unless the EMP values were transformed by dividing by a factor of 10,000), indicating heteroscedasticity. While the slope of the regression line was significant according to linear regression using R (p-value <5%, R^2 values ~0.25-0.29, not shown), a heteroscedastic dataset means the degree of association may be overestimated. Nonetheless, based on these results we see a general trend for higher EMP during positive GOM SSTA. Furthermore, the categorization of profiles into IP, severe and light FZRA allowed for visual comparison of where these phases lie on the spectrum of SSTA/EMP.

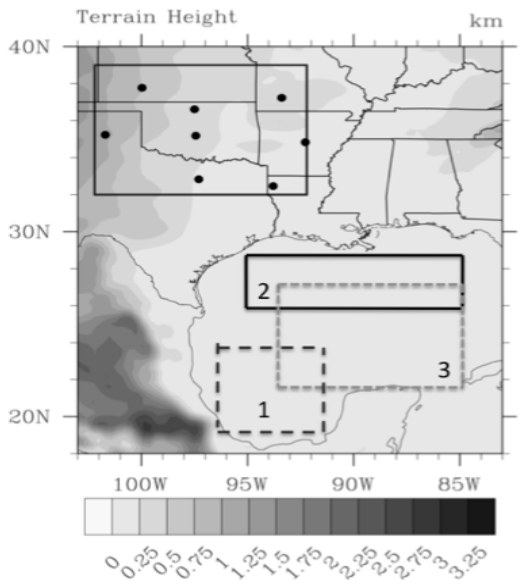

Figure 4.3: The GOM domains used in a linear regression against warm layer EMP. The SGP domain and sounding sites are also shown (see also chapter 2, Fig. 2.1). The domains were selected to provide good coverage over the interior basin (away from the northern and western continental shelf), while examining possible key sub-regions.

4.2.3 Research questions

The brief investigations of subsections 4.2.1, 4.2.2 confirmed the physical basis of this work, supporting the hypothesis of a relationship between SST and SGP warm layer characteristics. We speculate that a fetch from the GOM leads to the advection of warmer, moister (cooler, lower moisture) air in the positive (negative) SSTA case. This work seeks to expand on that of Ramos De Silva et al. (2006), using an advanced mesoscale model and a carefully constructed sensitivity analysis. In particular, although Ramos De Silva et al. (2006) showed evidence of strong sensitivity to large SST perturbations, here we intend to examine how storm dynamics, thermodynamics and FZPCP respond to more modest SSTA. This work is primarily intended to provide an assessment of the magnitude of the response to both uniform and physically-constrained

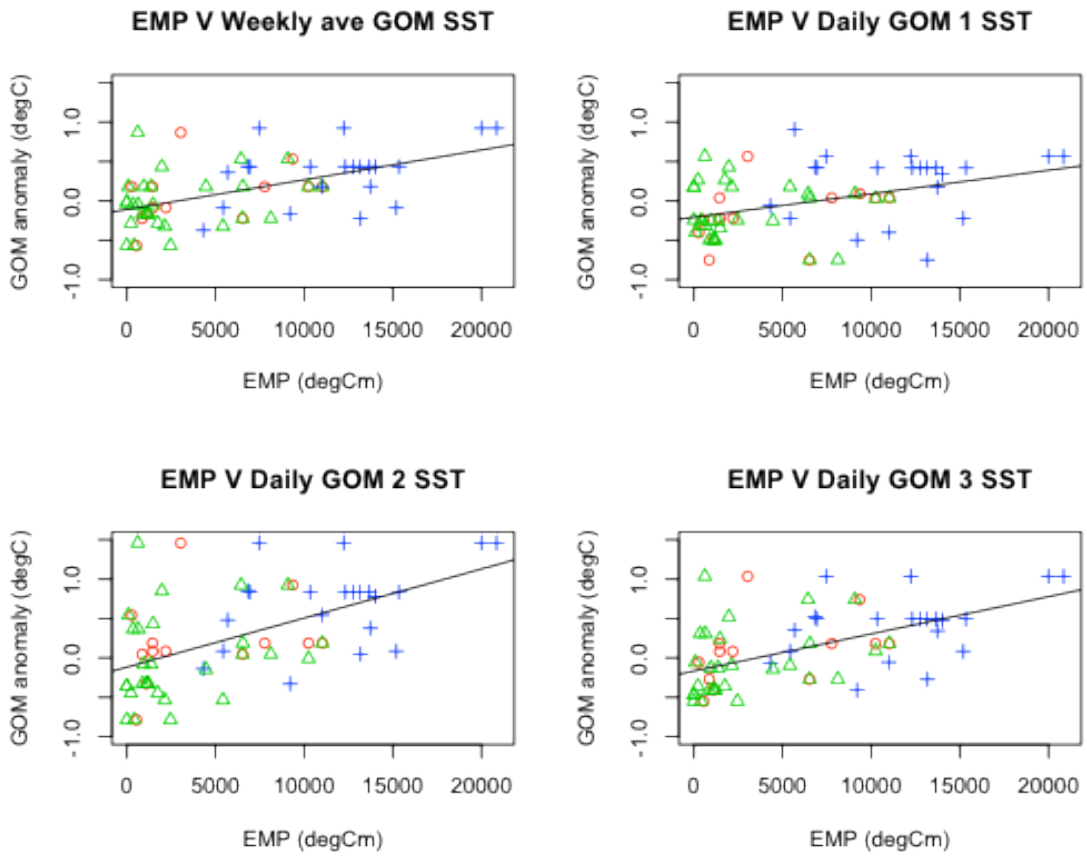

Figure 4.4: Results of linear regression of SST against EMP for basin average SST preceding each winter storm event (top left), storm averaged SST for region 1 (top right), region 2 (bottom left), and region 3 (bottom right). Heavy freezing rain (ice storm) profiles shown by the blue cross, ice pellets by the open red circles, and freezing rain by the green triangles.

SST fields, connecting potential relationships between basin anomalies (whole domain, and sub-domain) through the use of back-trajectory analysis as a tool to infer extent and timing of airmass modification, and examining how historical events might have been altered under alternate SST regimes. This information may be useful for medium-term prediction and situational awareness for systems developing in the presence/absence of strong GOM basin anomalies. Importantly, this work may also be applied in the context of assessing potential changes to such systems under a warmer future climate, given the

observed increase in global SST (although we admit in a warmer climate the whole vertical profile is likely to change, not just the low-level thermodynamics). Key research questions to be investigated from this chapter, through to chapter 7 include:

(i) How well can the WRF-ARW replicate the evolution of the selected winter storm case studies? (including evaluation of 'best' physics options for this application) – Chapter 5.

(ii) What are appropriate SST perturbations to apply? – Chapter 4, sec 4.4.

(iii) How do the SSTA change the evolution of the winter storm event? Special consideration is given to the timing of precipitation, and the approximate locations and accumulation of each hydrometeor phase (SN, FZRA, mix IP/FZRA, and rain) based on thermal and dynamical changes. Does this confirm the assertions of our hypothesis? – Chapter 6 and 7.

(iv) What regions of the GOM are important for the SGP, that is, what is the SSTA distribution in the GOM, and which locations potentially produce the largest impact on the winter storm? – Chapter 6 and 7.

4.3 Introduction to Case Studies

The case studies selected for this work are characteristic examples of two synoptic patterns common to the region; *Ice Pattern 1 and 3* (e.g., chapter 3). The ice storm of December 9-11 2007, an *Ice Pattern 3* event, was chosen because it produced significant regional impacts. The primary precipitation mode was elevated convection, a more unusual freezing rain event. The *Ice Pattern 1* event occurred on January 28-30 2010, and was associated with an arctic high to the north, and a deepening 850 hPa low

in association with a progressive mid-level trough. Multiple precipitation types occurred over the domain. This event was driven primarily by strong large scale forcing with both convective (in rain region) and stratiform precipitation. Details on the evolution of both case studies are described in the following subsections.

4.3.1 Case 1: December 9-11 2007

A long-duration freezing rain event occurred between December 9 and 11 2007. In the five days prior to the event, average low-level temperatures were anomalously warm over the southern/western states, with a collocated positive geopotential height anomaly (based on NARR data) shown in figure 4.5. Figure 4.6 is a surface synoptic analysis valid at 12 UTC on December 9. A surface arctic anticyclone extended over the north central U.S, with shallow subfreezing surface air filtering south over the Great Plains, associated with ageostropic down gradient flow, as described in chapter 3. A quasi-stationary front extended east-northeast from north-central Texas. To the south an unseasonably warm and moist airmass prevailed, with temperatures in excess of 290 K (18^{o}C). At this time, convective precipitation was ongoing over the SGP, extending northeastward parallel and north of the surface front, in a region of isentropic ascent and warm air advection (WAA, not shown). Figure 4.7 shows a vertical sounding valid 12 UTC 9 for Norman, Oklahoma, evidencing a deep layer of elevated convective instability. The Storm Prediction Center mesoscale discussion 193, valid near 16 UTC Dec 9 (http://http://www.spc.noaa.gov/products/md/2007/md2193.html) noted strong low- level WAA near 700-850 hPa, and MLCAPE values between 500 and 1000 JKg^{-1}, promoting the convective mode.

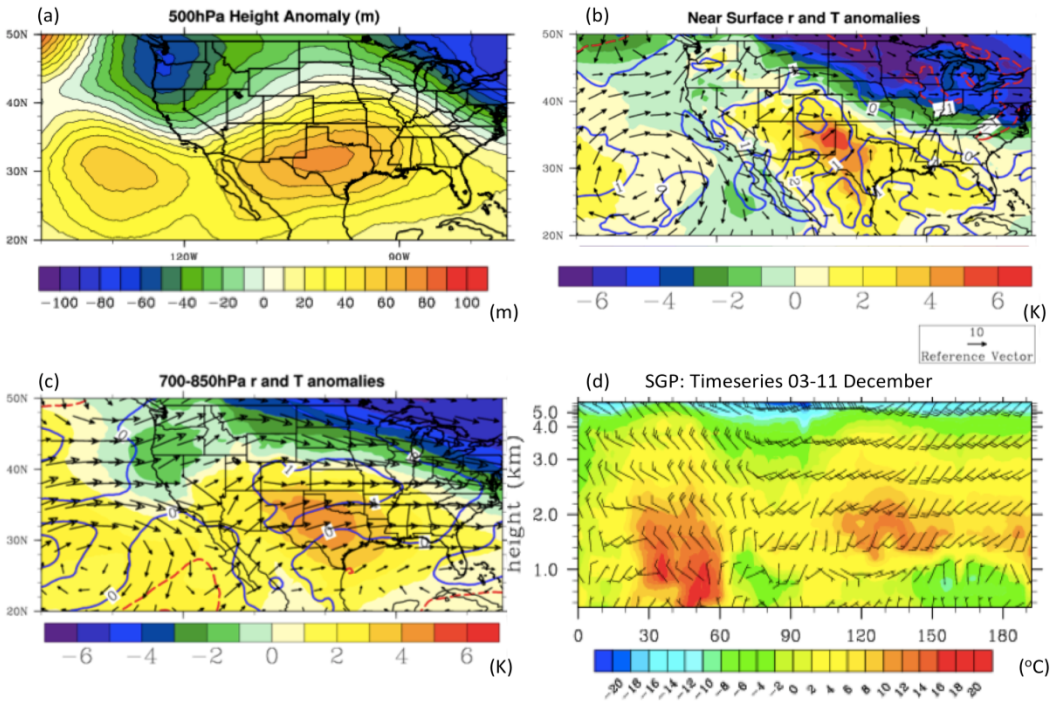

Figure 4.5: Multi-panel plot depicting the average meteorological conditions between December 3-11 2007. (a) Shows the geopotential height anomaly (relative to a 1971-2000 NARR climatology) in gpm, (b) shows 975 hPa temperature anomalies (shaded, K), vector wind anomalies (arrows), and mixing ratio anomalies (g kg^{-1}, blue contours), (c) shows the 850-700 hpa layer average anomalies as in panel (b), (d) is a time-height plot from 00 UTC December 3-00 UTC December 11 showing air temperature (shaded, ^{o}C), and vector winds (barbs, intervals of 5 knot) from 0-5 km AGL valid at the ARCF-SGP facility in Lamont, Oklahoma.

The axis of freezing precipitation remained largely unchanged for over 24 hours, with training convection primarily over the central SGP, extending southwest to northeast. The 500 hPa height field, shown in Fig. 4.8, valid 12 UTC December 9, depicts a broad amplified western trough with a strong mid-level jet transporting moisture into the region from the sub-tropical Pacific. Figure 4.9 shows the composite anomaly fields in relevant thermal fields, SLP, and 500 hPa height (NARR 1979-2001 mean), and anomaly correlations for these parameters between December 8-12. Anomaly correlations (AC) are a measure of the persistence of synoptic conditions,

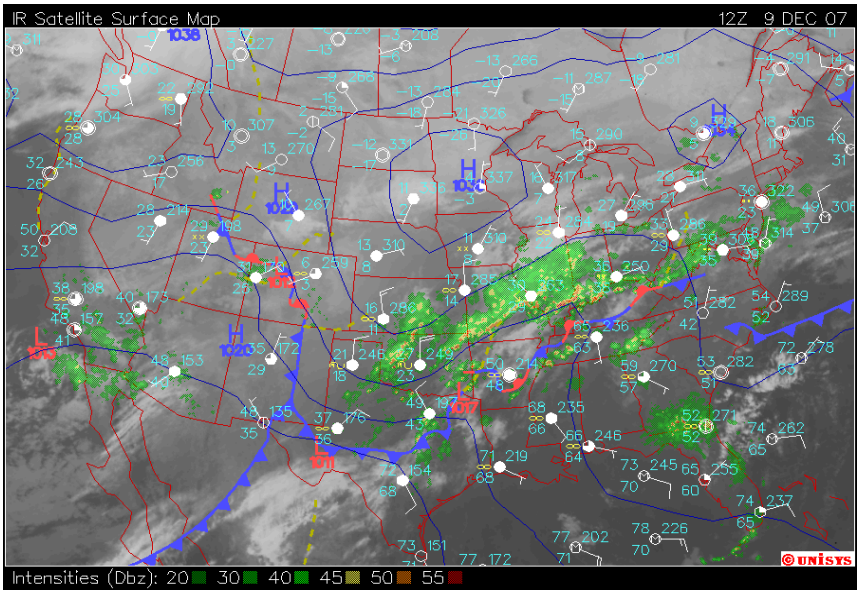

Figure 4.6: Synoptic chart valid 12 UTC December 9, depicting sea level pressure (blue solid contours, hPa), fronts, station weather and wind speed (intervals of 5 kt), infrared satellite, and composite radar reflectivity. Image courtesy of http://locust.mmm.ucar.edu and Unisys.

calculated based on the equation given by Gyakum and Roebber (2001), shown in Equation 4.3.

$$\mathrm{AC} = \frac{\sum_i \sum_j a(1)_{i,j} a(2)_{i,j}}{\sqrt{\sum_i \sum_j [a(1)_{i,j}]^2 \sum_i \sum_j [a(2)_{i,j}]^2}}, \qquad 4.3$$

Where *a(1)* and *a(2)* are anomaly fields at each gridpoint in x and y *(i,j)*. Anomalies were expressed relative to the composite anomaly field for the whole event, calculated at 6-hour intervals using NARR. The December 2007 ice storm conditions showed notable persistence, with high correlations (> 0.5) throughout the analyzed period. Slow eastward movement of the trough produced gradual decorrelation throughout the storm.

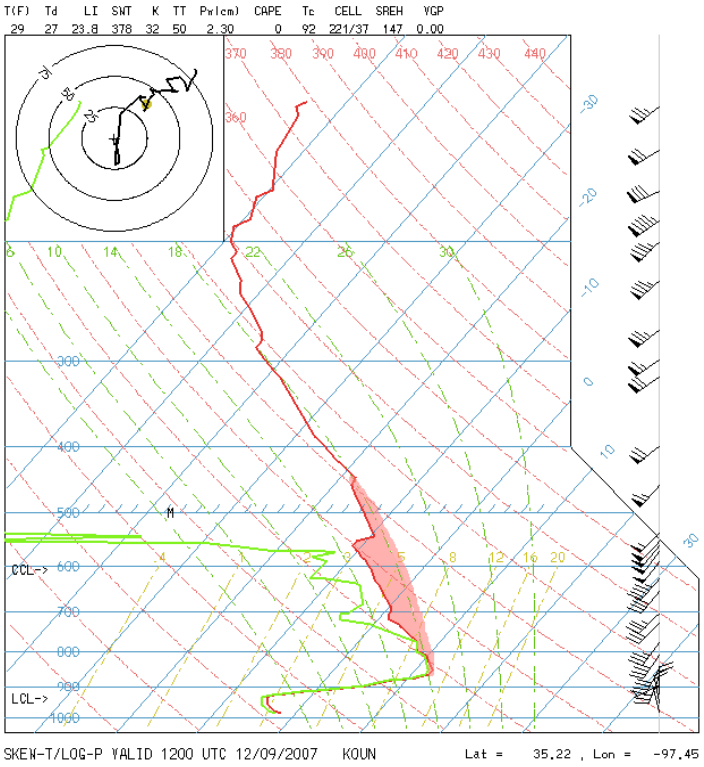

Figure 4.7: Thermodynamic sounding profile at Norman, Oklahoma (OUN) valid at 12 UTC December 9. Red (green) lines indicate air (dewpoint) temperature (^{o}C). The shaded region shows the elevated unstable layer from ~850 hPa to near 500 hPa. Sounding profile image courtesy of http://locust.mmm.ucar.edu.

Figure 4.10 shows accumulated precipitation for the SGP, and a precipitation time series valid for OUN, derived from NCEP Stage IV radar and rain gauge derived precipitation. A simple algorithm was used based on Bourgouin (2000) to separate constituent phases, described in chapter 6, sec 6.2. Primary domain phases were rain, and freezing precipitation (IP/FZRA). The particularly well-defined warm layer likely contributed to the largely freezing phase of precipitation, and compounded societal impacts. Accumulations exceeded 1 inch over a wide swath of the central SGP, with regions in excess of 2 inches also noted. Rain was located south of this zone over Arkansas through southern Illinois. The precipitation time series indicates heaviest

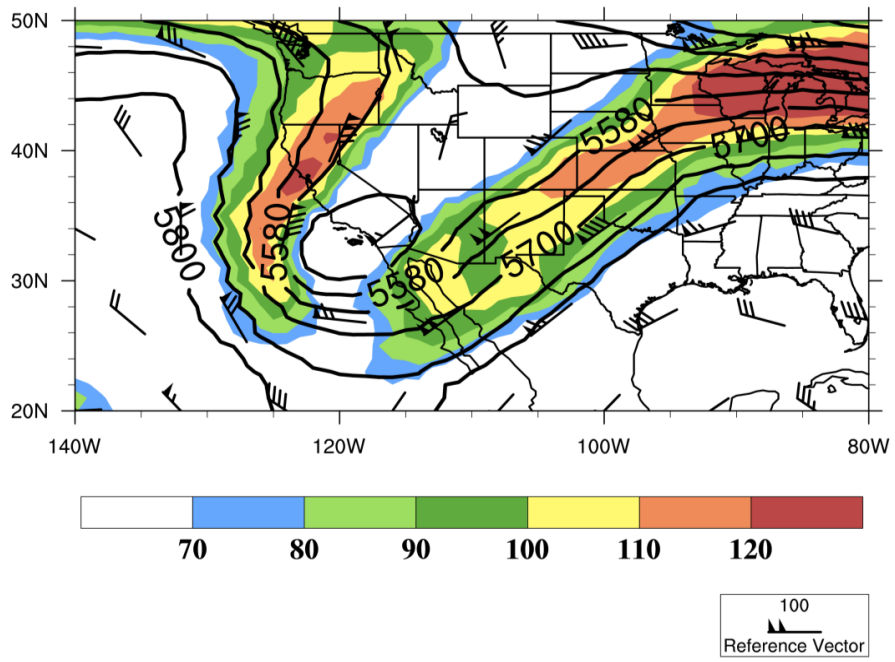

Figure 4.8: 500 hPa geopotential height field (gpm, black contours), and 250 hPa wind velocity (kts, barbs and shaded contours) valid at 12 UTC December 9.

precipitation rates occurred overnight (Fig. 4.11, shaded). Based on these peaks, we define two convective episodes, one for an 18-hour period from 06 UTC December 9, and the other from 06 UTC December 10, which are used to analyze the model representation of this event in chapter 6. The end of the ice storm for much of the SGP (bar the panhandle of Texas and southern KS) occurred toward the evening of December 10, when surface temperatures rose above 0^{o}C.

Figure 4.11 depicts 96-hour backward ensemble air parcel trajectories (using HYSPLIT), ending at OUN at 12 UTC 9, 00 UTC 10 and 12 UTC 10 for 850 hPa. The ensembles were generated by initiating trajectory calculations at small incremental offsets (0.01 km) in the horizontal and vertical plane. Red trajectories were members with mixing ratios into the freezing precipitation zone at/above 8 gKg^{-1}. The majority of

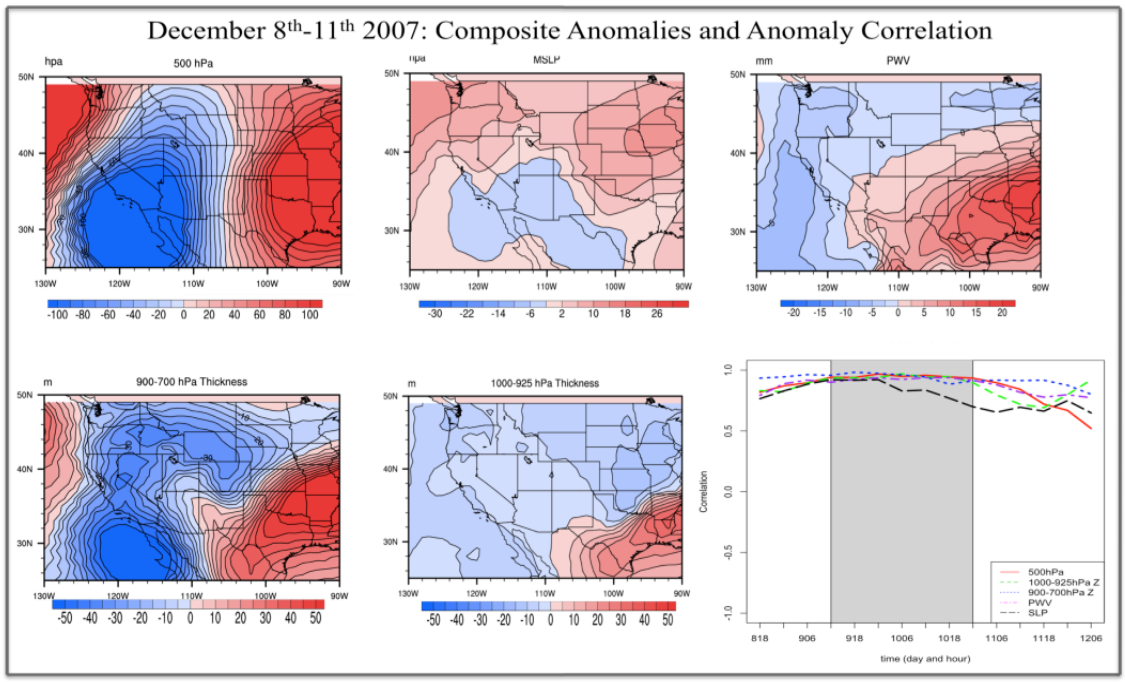

Figure 4.9: Composite anomalies of NARR geopotential height (gpm,, top left), sea level pressure (SLP, hPa, top center), precipitable water (PWV, mm, top right), 850-700 hPa thickness (m, bottom left), and 1000-925 hPa thickness (m, bottom center), valid from 12 UTC 9 – 00 UTC 11 December and relative to the NARR baseline 1979-2001 climatology. The bottom right panel shows the anomaly correlations for each 6-hour period from 18 UTC December 8 to 06 UTC December 12, while the grey shading is the approximate duration of freezing precipitation at OUN.

ensemble members move northward from the western GOM at 12 UTC 9, and 12 UTC 10, with a smaller land-based cluster. As previously observed, most trajectories members descended to the near surface over the ocean (~t-40 to t-10), before rapid ascent into the freezing precipitation region. This places the majority of air parcel paths near the surface over the northwestern GOM. At 00 UTC 10, most members apparently circulated around the SGP and southern U.S. At this time, the mixing ratio within the precipitation zone had decreased, especially relative to 12 UTC 10 when the approaching trough, and increased WAA enhanced mixing ratios and began to warm the

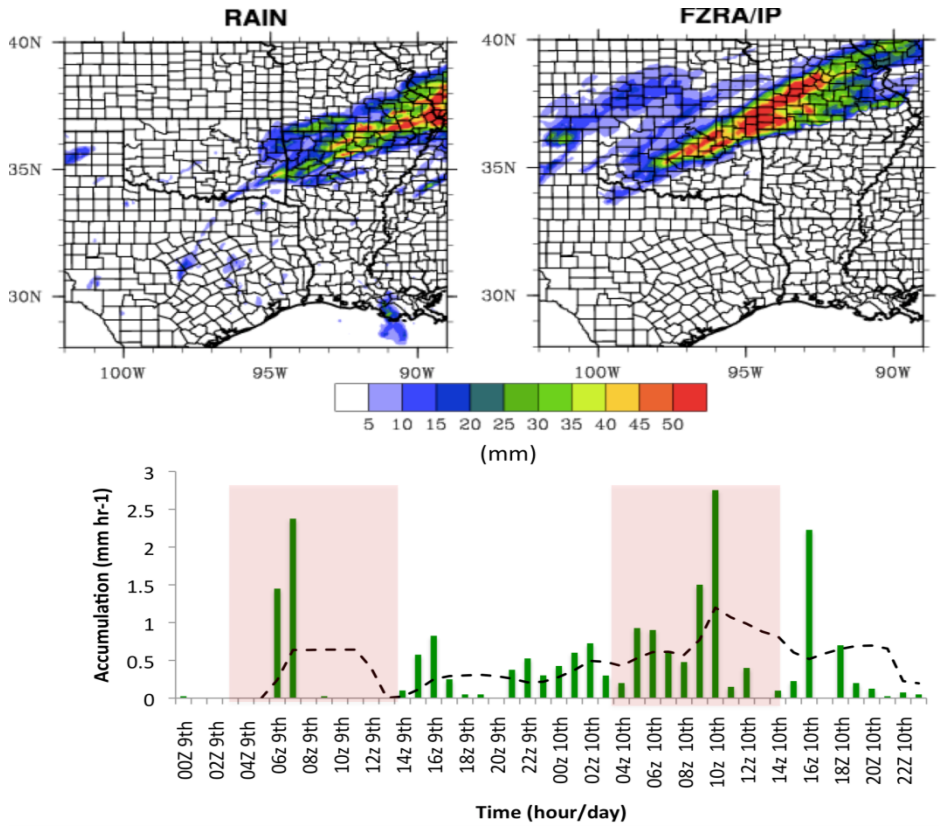

Figure 4.10: TOP: Accumulated 48-hour precipitation in liquid (rain), and freezing (IP/FZRA) phases ending at 00 UTC December 11. BOTTOM: Time-series of precipitation at 1-hour intervals for OUN. Dashed line is a running mean filter for every 5-th hour. Red shaded regions denote the two nocturnal episodes of convective precipitation. Data from NCEP Stage IV.

surface layer. It is interesting to note that GOM trajectories were prevalent during the overnight/early morning, while localized trajectories dominated mid-late afternoon. This may be related to the strengthening of the low-level flow overnight, possibly associated with a low level jet.

According to NCDC *Storm Data,* impacts were primarily felt within the populated I-44 corridor, producing one of the most costly ice storms in recent memory. Whilst relatively warm temperatures preceding the event limited ground accumulation, overlying surfaces such as trees and power-lines were heavily damaged. At the height of

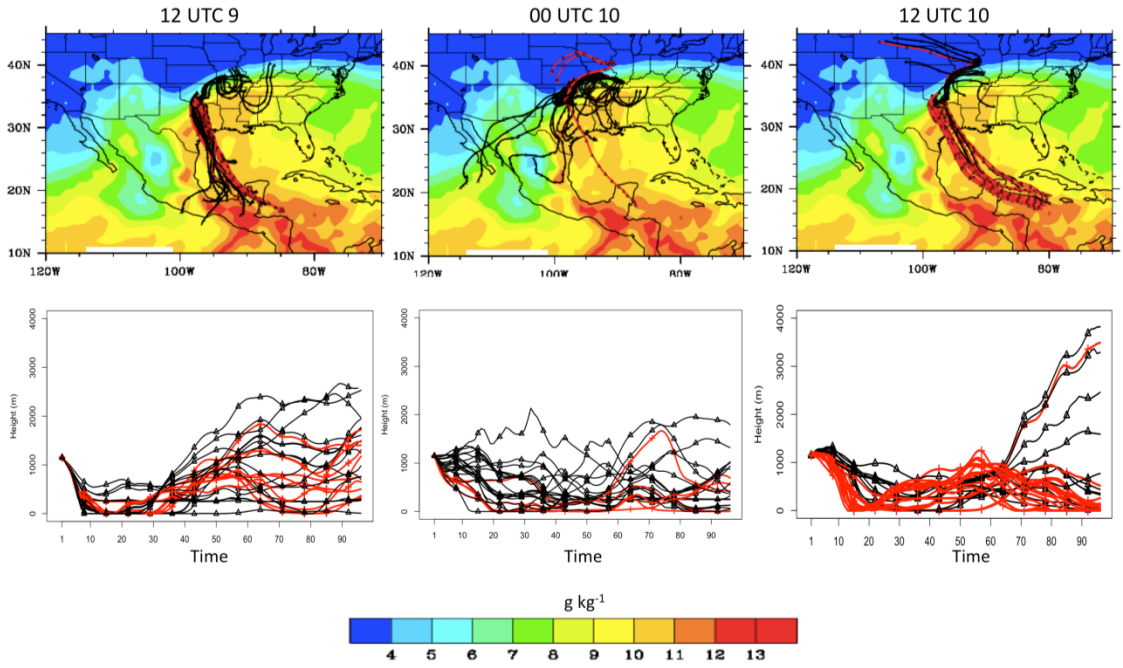

Figure 4.11: Four-day Ensemble HYSPLIT trajectories ending at OUN at 850 hPa for 12 UTC December 9 (top left), 00 UTC December 10 (top center), 12 UTC December 10 (top right). 48-hour average mixing ratios overlaid (g kg^{-1}, filled contours). Trajectory members with mixing ratios > 8 g kg^{-1} at T0 shown in red. Bottom panels show time series the altitudes of each trajectory (AGL, m) for the corresponding end-times.

the storm, an estimated one-third of the state's population lost power. A state of emergency was declared for all 77 OK counties. The economic cost exceeded $300 million in Oklahoma alone. Missouri and far southern Illinois were also impacted by between 0.25 and 2 inches of mixed FZPCP.

4.3.2 Case 2: January 28-30 2010

A winter storm impacted a broad swath of the southern U.S January 28-30 2010. In the seven-day period January 23-30, the region evidenced broad negative geopotential height anomalies, shown in Figure 4.12. This may evidence an active regime with successive troughing. Furthermore, negative low-level temperature

anomalies were prevalent over and west of the domain, while a time series of temperature versus height at the ACRF SGP site implied warm layer development during January 26-27. Prior to this, strong northwesterly flow had depleted the lower-levels of an inversion layer (panel d).

Over portions of the SGP, a number of precipitation phases were experienced as the upper trough approached. This progressive trough is shown in Figure 4.13. An ill-defined surface low-pressure over northeastern Mexico on January 28 moved eastward and became better defined along the Gulf Coast on the 29th. At the 850 hPa layer, a trough was evident on the 28, with a center passing over southern Oklahoma through eastern Texas. Cold air was present at the surface as freezing precipitation developed, associated with a broad arctic high over the central U.S.

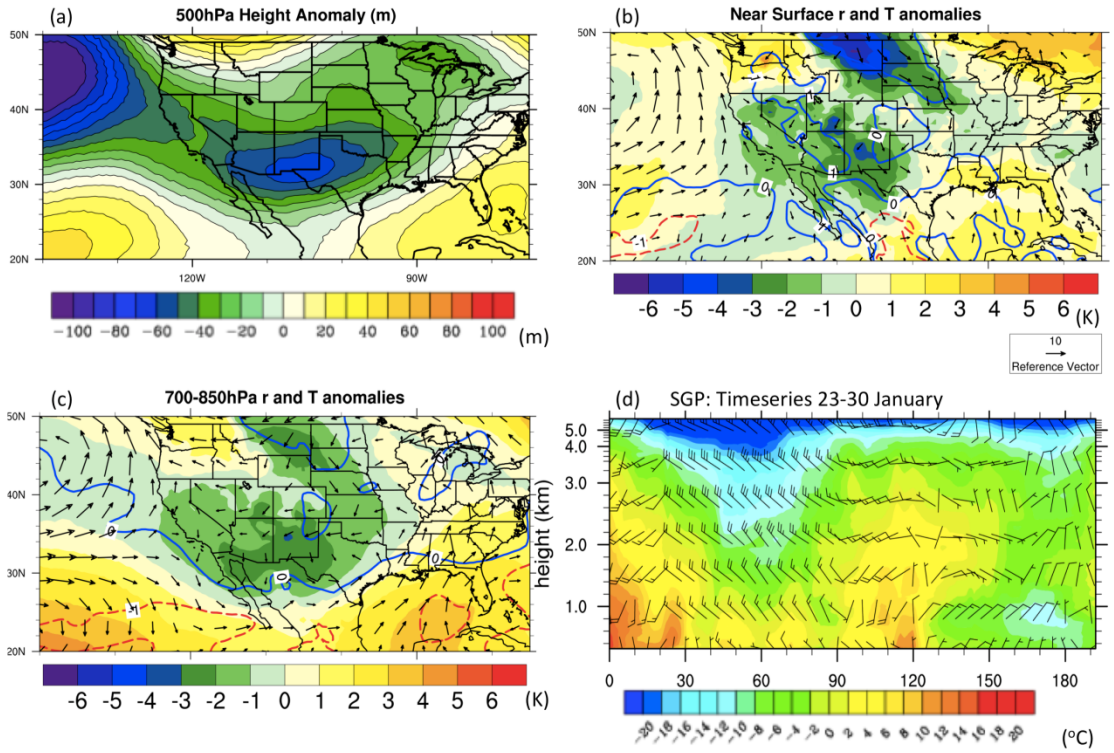

Figure 4.12: As Fig. 4.5 but for January 23-30 2010

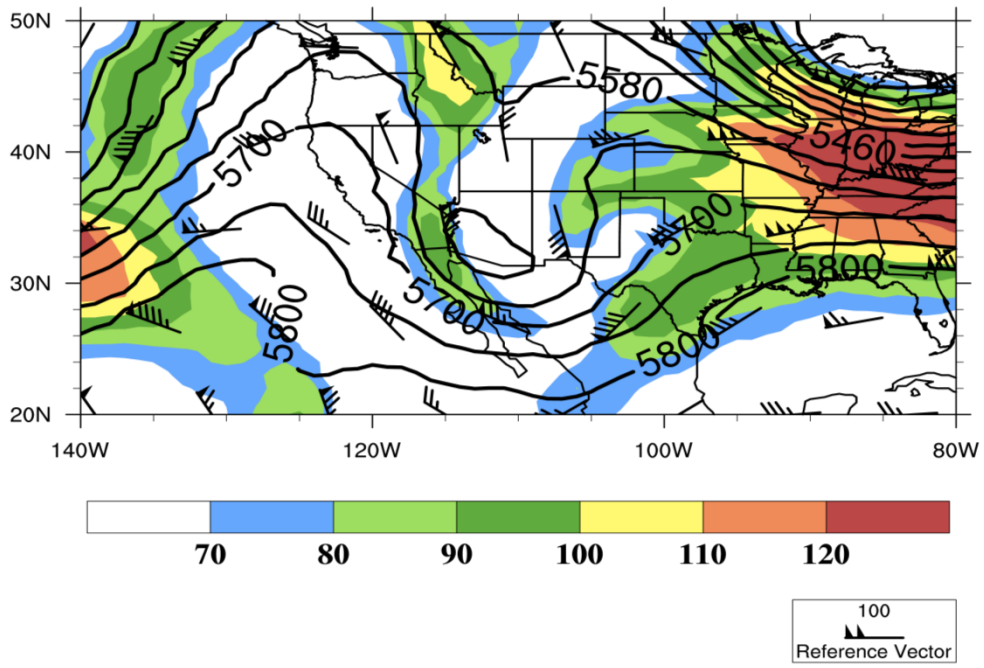

Figure 4.13: As Fig. 4.8 but for 12 UTC January 28 2010

Figure 4.14 shows the surface synoptic analysis valid 15:30 UTC on the 28th. South of the cold front temperatures over the southeastern U.S were relatively cool while over Texas temperatures between 283 and 288 K (10-15°C) were present. Over this latter region heavy convective precipitation was observed, which became vigorous enough to warrant a severe thunderstorm and tornado watch between San Antonio and Dallas (not shown). North of the surface front the refreezing layer developed around 12-15 UTC, with a mixture of FZRA and IP from southwestern OK, northeastern Texas, through central Oklahoma. Snowfall occurred later over northern Oklahoma as cold air deepened in association with the mid-level trough. Precipitation ended over Oklahoma on the 29th, with freezing and frozen precipitation at this stage over Arkansas. Also of note was a possible gravity wave on the afternoon of the 28th, which brought rapid advection of dry midlevel air into Oklahoma, ending precipitation for a time (Fig. 4.16).

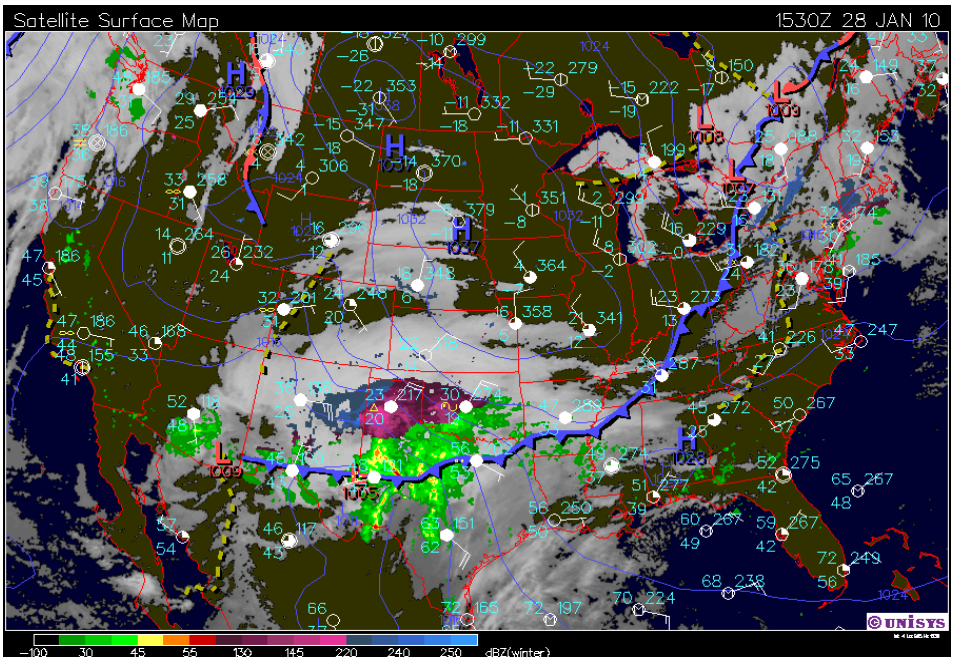

Figure 4.14: Synoptic analysis, valid 15:30 UTC January 28. Similar to that described in Figure 4.6 but with the addition of phase discrimination for radar derived precipitation, where green-yellow-red indicates rain, purple ice and blue snow. Image courtesy of http://locust.mmm.ucar.edu and Unisys.

Figure 4.15 reveals storm composite anomalies and anomaly correlations (see Eqn. 4.3). Notable de-correlation outside of the storm event evidences the progressive movement of the trough and associated temperature, SLP and moisture.

Precipitation accumulation and time series for OUN, shown in Figure 4.16, show heavy rainfall over the southern SGP, the main belt of freezing precipitation over the center, orientated east-west, and snowfall over the northern and central domain. Freezing precipitation was heaviest over southwestern Oklahoma, supported by storm reports of 0.25-1 inch of ice accumulation on the 28th, leading to numerous road incidents, and nearly 180,000 facilities losing power (*Storm Data*, NCDC). On the 29th, the heaviest freezing rain accumulated over central/south central Arkansas, leading to a reported 30,000 power outages. At OUN (time series), precipitation began as rain

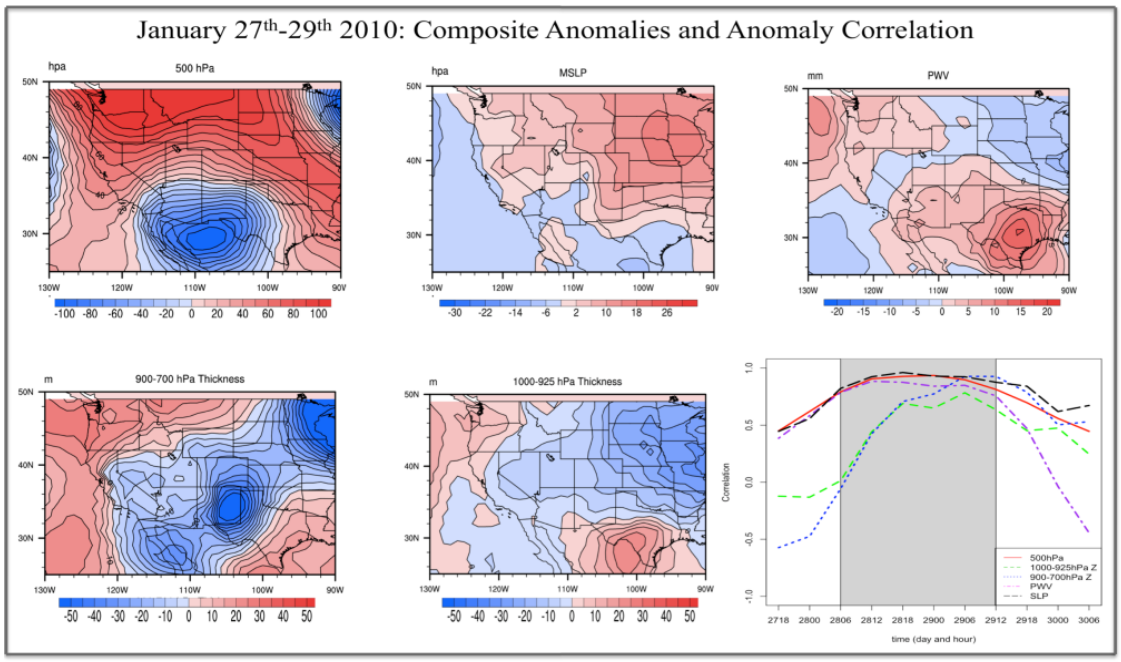

Figure 4.15: As Fig. 4.9 but for the January 28-30 winter storm. Anomalies calculated between 00 UTC 28 and 12 UTC 29, based on storm timing over Oklahoma. The gray shaded times on the lower panel denote the approximate duration of the winter storm over western and central Oklahoma**.**

early on the 28th, subsequently changing to FZRA near 15 UTC, and IP around 21 UTC. On the 29th, FZDR and light snowfall were the primary precipitation types as FZPCP moved east. Approximately 0.5 inch of FZRA accumulated at OUN.

Air parcel trajectories were computed in a similar fashion as before, based on FZPCP in the vicinity of OUN between 15 UTC January 28 and 00 UTC January 29, shown in Figure 4.17. The ensembles indicate some uncertainty in trajectory path. Air parcels generally originated (t-96) over the northern or western U.S, descended over the southern U.S or northern GOM and re-curved into the domain. This movement was indicative of a possible return flow event, marked by an initial intrusion of cold air into the southeastern U.S, and its subsequent warming and moistening and northward advection into the SGP ahead of the upper low. The moistest ensemble members (red,

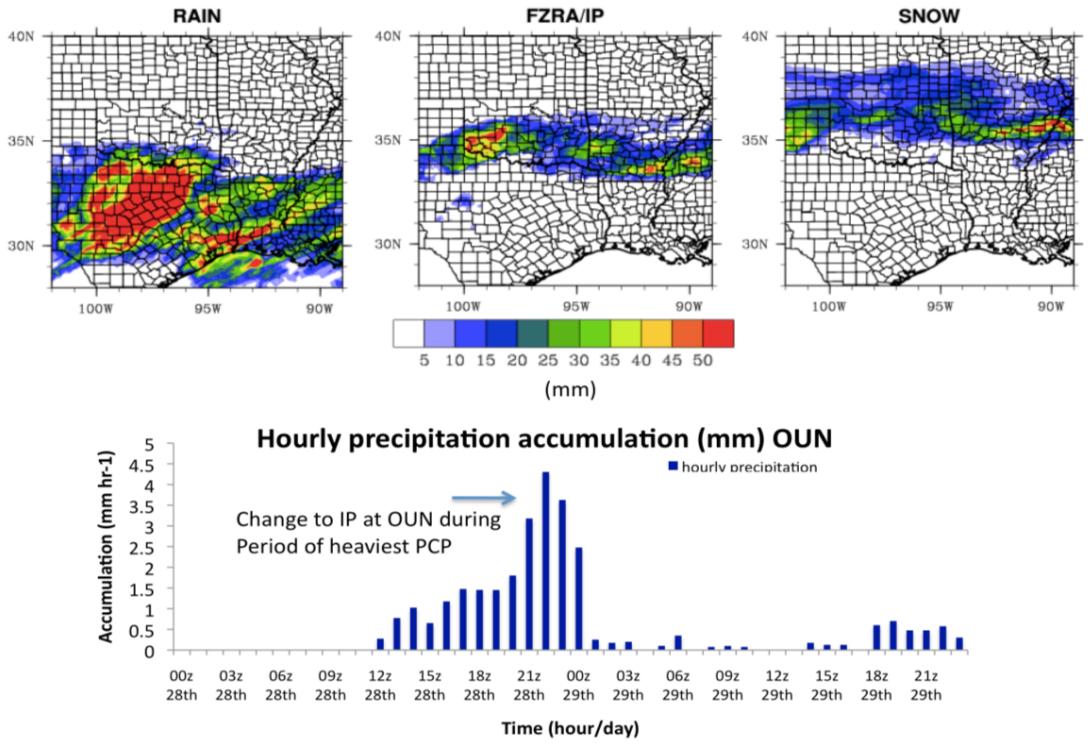

Figure 4.16: As Fig. 4.10 for January 28-30 2010, with the addition of the snow-phase (top right panel).

> 5.5 g kg^{-1}) typically moved further south and at lower-altitude over the GOM.

4.4 SST Sensitivity Study: Experiment Configuration

4.4.1 Rationale for imposed SST Anomalies (SSTA)

In order to apply a reasonable set of SST anomaly perturbations for our sensitivity analysis some understanding of the variability of GOM SST was desired. The prominent oceanic circulation within the GOM is the 'loop current' (LC). The LC transports warmer water from the Caribbean Sea into the basin via the Yucatan channel, supplying a significant fraction of source water to the Gulf Stream (Nowlin 1972). The current pushes northward into the GOM, sometimes into the north central basin before

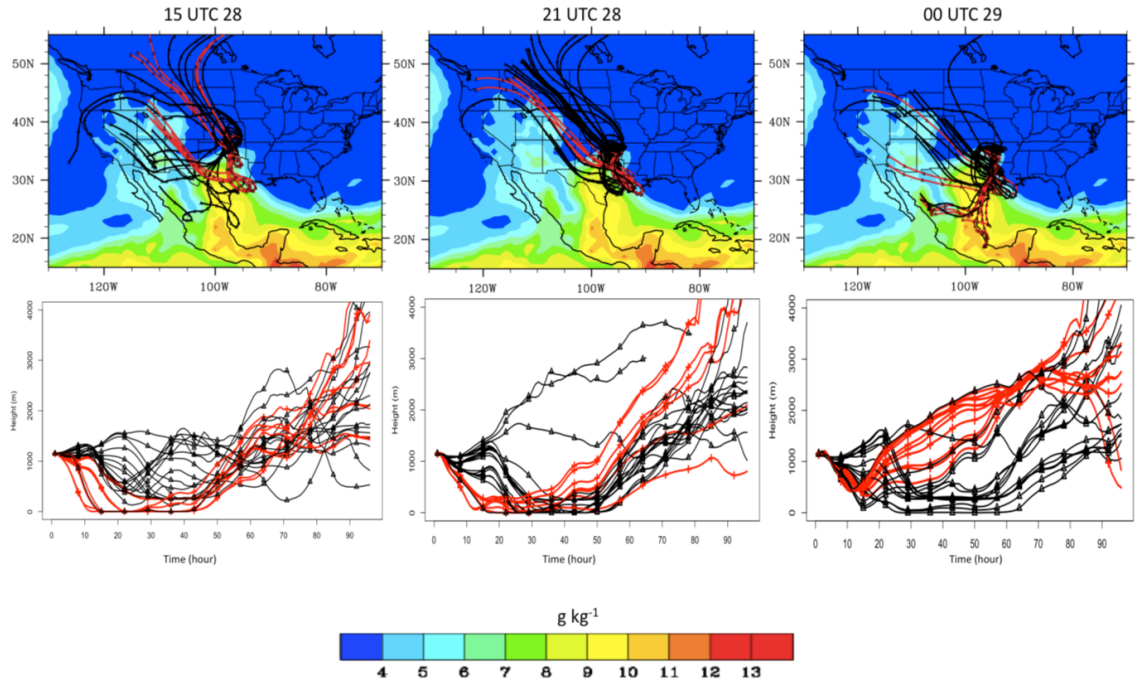

Figure 4.17: HYSPLIT ensemble trajectories, members with mixing ratios at T0 > 5.5 g kg^{-1} shown in red valid for times during freezing precipitation at OUN on January 28/29. Figure layout as in Fig. 4.11.

turning southward and exiting through the Florida Strait. Eddies of warm well-mixed water shed from the current episodically and move slowly westwards (~2.5 ms^{-1}, Elliott 1979), shown schematically in Figure 4.18. The LC is highly variable in its behavior (Hurlburt and Thompson 1980), and appears to be forced by a complex interplay of internal dynamics, basin topography and the overlying atmospheric wind flow (Sturges and Evans 1983). It is not agreed as to whether there is a seasonal cycle in the circulation (e.g., Cochrane 1972, Molinari 1978).

A recent study by Chang and Oey (2010) simulated the effects of persistent easterly flow over the basin (the dominant wind direction climatologically, especially in winter). Under these conditions they identified increased volume exchange between

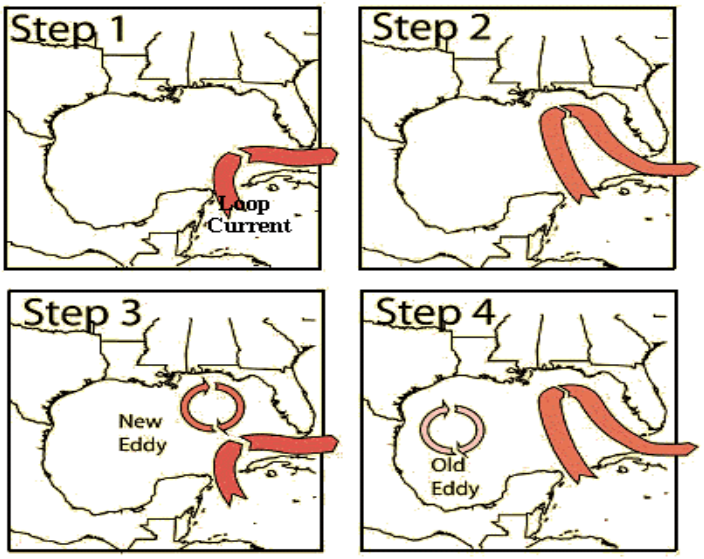

Figure 4.18: A schematic diagram illustrating the loop current circulation, including its northward push into the GOM, the shedding of eddies and their westward translation. Image courtesy of: http://www.wunderground.com/hurricane/loopcurrent.gif.

Caribbean and Gulf waters, leading to enhanced heat flux into the basin. Furthermore, wind induced currents along the northern and southern continental shelves promoted heat redistribution well into the western basin. The wind forcing allowed the LC to accumulate more mass, producing larger eddies once shed from the circulation. These effects ultimately resulted in greater oceanic heat content over the GOM basin (especially in the west, their Fig. 1). It is not clear how these results might translate into SST variability, however, ocean heat content is typically positively associated with SST. SST variability over the GOM basin is currently not well understood. It is known to be related to the LC, with anomaly structures potentially unconnected to any other basin (Anderson and Clark 2011). Cold air outbreaks over the continent during winter can produce negative SSTA along shallow continental shelf waters due to the loss of heat at the surface layer. Furthermore, the wintertime SST decrease is most marked in

these regions (e.g., Huh et al. 1978, Wang et al. 1998). Longer-term SSTA variability appears to be linked to the Atlantic Multidecadal Oscillation (AMO), while a historical signal for increasing average SST associated with global climate change is weak to absent for the wintertime basin (December-January-February), shown in Figure 4.19. Recent studies on ocean ecology have noted increased abundance of some types of subtropical herbivorous fish to the northern GOM, and 21st Century warming is expected to impact the basin (e.g., Vergés et al. 2014).

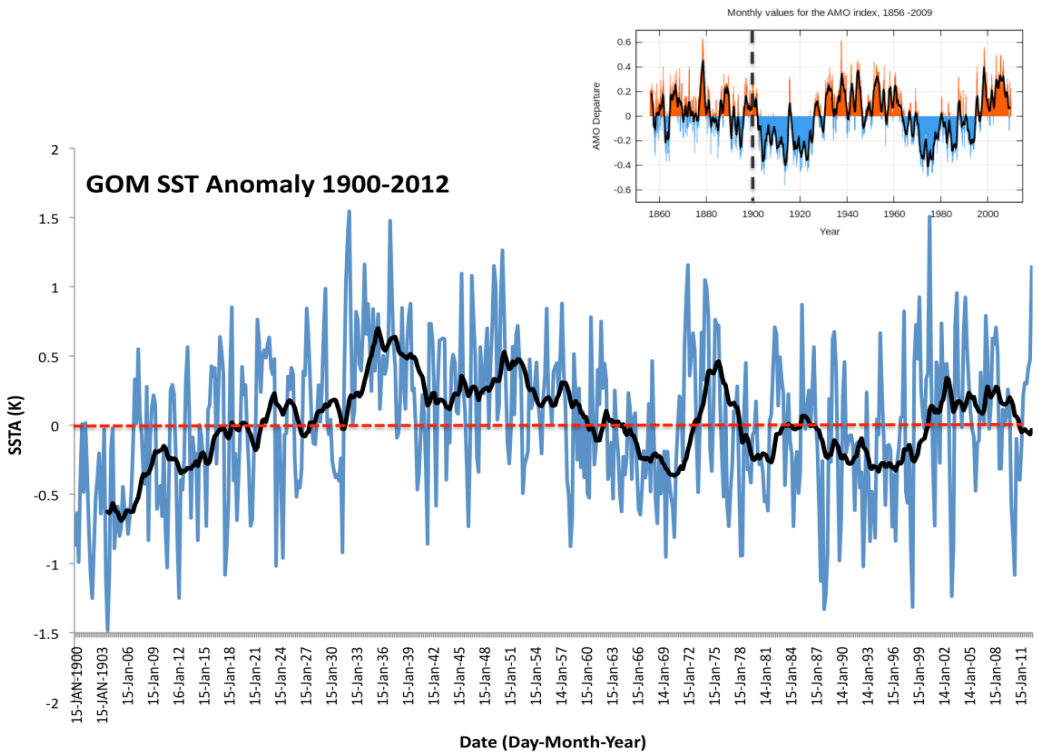

Figure 4.19: Main Panel: SST anomaly time series for the GOM basin, expressed as an average for the whole basin, and relative to the default 1971-2000 climatology in the ERSST (extended reconstructed) SST analysis for 1900-2012 November-March (blue lines). The black solid line is a 10-year moving average, and the red dashed line demarks a zero anomaly. The top panel inset shows the phase of the Atlantic Multidecadal Oscillation, with the corresponding times to the right of the black dashed line. Inset courtesy of http://eoearth.org.

Since there is limited literature on the subject of GOM SSTA, and a thorough statistical investigation into common modes of variability was beyond the scope of this work, a few options were available for the sensitivity study: (1) A uniform perturbation, which would shift the SST up or down by an integer value over the whole domain (e.g., Ramos de Silva et al. 2006, Ludwig et al. 2013); (2) a study that would take a portion of the SSTA field and perturb its gradient (e.g., Booth et al. 2012). Such a technique is often applied when evaluating the evolution of weather features directly over the SST region, e.g., tropical or extratropical cyclones; (3) A 'patch' method that would impose a single anomaly or series of anomalies in the background SST field that decay over a certain distance, typically using some Gaussian or cosine-squared function (e.g., Brayshaw 2006). This method is common for idealized studies, by imposing an artificial yet physically realistic anomaly distribution based on the SST variability of the basin in question.

For this work, option (1) is a basic method, but provides an upper estimate of sensitivity and is linear about a control. Since the only former paper on this topic used this technique, a similar method was advisable in order to be directly comparable. The use of (2) was considered, but it was ultimately difficult to determine where to impose a gradient anomaly. One option might have been along the continental shelf, or the loop current flow north of the Yucatan Strait. In the end, we assumed here that the basin-wide broad scale SST is more important to the evolution of inland precipitation through advection, so we do not pursue this option at this time. (3) Is a more rigorous technique, but with little knowledge of the GOM variability, SSTA blobs would essentially be

input at random without any particular justification for their physical realism. Consequently, only option (1) above was pursued for one set of perturbations.

An additional simple yet realistic perturbation option involves using known SSTA information to identify physically plausible maxima and minima. In this case, it was decided to concentrate on basin average anomalies, rather than any localized maxima/minima, though this could be the subject of future work. The procedure involved gathering SST information between 1981-2011, valid for the start date of the freezing precipitation event. This constrains the dataset to be an SST field observed at the same time of year as the case study in question. For this segment of the analysis, daily NCEP Optimum Interpolation (OI) version 2 (Reynolds et al. 2007) was employed and regridded from 0.25^{o} to 0.5^{o} horizontal grid spacing (see appendix, sec. 4 for assessment of interpolation uncertainty). The dataset was expressed as a SST anomaly field relative to a 1981-2011 mean for the day in question. This 31 years of SSTA data was then ranked based on the basin average anomaly, with the top and bottom year in question being retained and denoted 'HI' and "LO' respectively. Figure 4.20 displays SST anomaly structures for HI and LO for the December 2007 (top) and January 2010 (bottom) case studies.

4.4.2 Final configuration of SSTA, and datasets used

Based on aforementioned rationale a set of SST perturbations were generated for both case studies, described in Table 4.1. The control simulation, designated 'REAL' is the SST field observed during the event. A climatological field (1981-2010), or 'CLIM' was available at daily intervals at a high resolution of $1/12^{o}$, but interpolated (via a

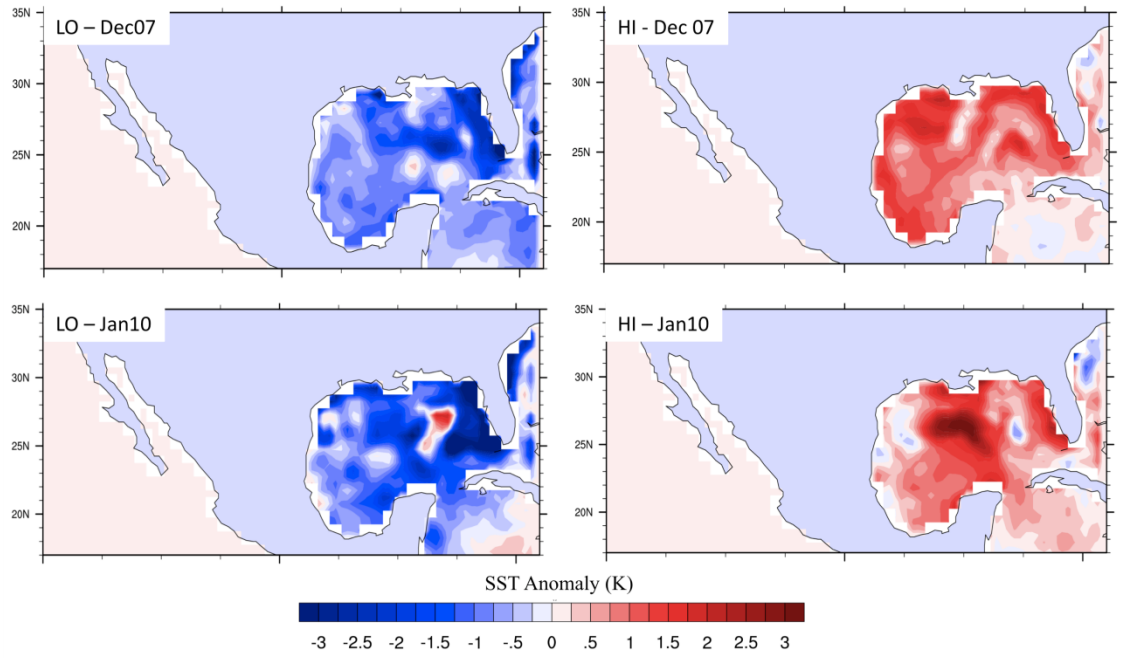

Figure 4.20: SSTA fields (in Kelvin) derived from a 31-year dataset valid for the week preceding the winter storm case study. TOP: lowest and highest basin average for the December 2007 event (corresponding to the years 2010, and 2004 respectively). BOTTOM: as TOP but for January 2010, corresponding to the years 2011 and 2002. Anomalies expressed relative to 1981-2010.

bilinear interpolation in NCL graphics software, appendix section 4) to 0.5^{o}. We use this field to reflect the climatological distribution of SST for each case study. Two uniform perturbations to the REAL field were applied everywhere over the GOM, representing the 'upper limits' in our analysis, these perturbations are +2 K and -2 K, referred to as 'P2' and 'M2' respectively. Finally, the aforementioned 'HI' and 'LO' SST fields were included as a physical assessment of upper and lower limits to basin-average SSTA. Perhaps as a caveat for interpretation, these latter perturbations were not equidistant in magnitude around either the control or climatology, but lay within the range of REAL to P2/M2. Advantageously however, the different spatial distribution of these anomalies allows later experimental work to examine the role of sub-basin SSTA. Pacific SSTs

were at all times fixed to the time of the event in question (i.e., REAL). The SST fields used for the WRF modeling study are shown for the December 2007 event in Fig. 4.21 and January 2010 in Fig. 4.22. A principal assumption for this work is that the *SST is independent of the overlying atmosphere*. In other words, SST anomalies are primarily the product of ocean variability, and are unconnected to synoptic conditions over the time scales of the simulations (~1 week).

SST used for the simulations was obtained from two datasets. The first was the 'Real Time Global' or RTG analyses, developed by the NCEP Marine Modeling and Analysis Branch (MMAB) (http://polar.ncep.noaa.gov/sst/rtg_low_res/). RTG is available at two resolutions, an ultra-high resolution $1/12^{th}$ degree, or a lower resolution 0.5 degree and was available daily. REAL, P2, M2 and CLIM used data from RTG at 0.5^{o} resolution[7]. It was anticipated that this grid spacing was sufficient for the purposes of this study. Higher resolution SST fields can resolve fine-scale structure and are generally more faithful to reality in regions of strong horizontal gradient, such as the Gulf Stream. For applications including tropical cyclone modeling, coastal meteorology and ocean meteorology, such information has been advantageous. We assume here that while good representation of the SST field is desired, the sensitivity analysis will not be significantly altered by the use of high-resolution fields. The broad scale magnitude of SST is believed to be most important to the thermodynamic changes through advection of temperature and moisture by the synoptic flow. Nonetheless, it could be useful to investigate this assumption through the replication of one or both case studies using

[7] The RTG dataset had already been run in WRF simulations prior to the development of the 'HI' and 'LO' perturbed fields. Ideally, a single dataset would have been used for all fields, but time factors prevented this. The 31-year analysis used to derive these fields was from OI V2 data. For consistencies sake, OI V2 was retained for HI/LO and interpolated to RTG grid spacing.

Table 4.1: Description of the SST anomalies used in the WRF-ARW sensitivity study. Columns 3 and 4 show the magnitude of each basin-average anomaly with respect to the 1981-2010 climatology (real) field in Kelvin for December 9 and January 28 respectively (based on OI V2). Each SST field has a daily temporal resolution, and 0.5° (~55 km) horizontal grid spacing.

Simulation	Perturbation	SSTA December 2007 CLIM (REAL)	SSTA January 2010 CLIM (REAL)	Description
REAL	None	+0.55 (0.0)	-0.85 (0.0)	Actual SST field, daily
CLIM	1981-2010 average (daily)	0.0 (-0.55)	0.0 (+0.85)	1981-2010 long-term average, daily
P2	Uniform +2 K	+2.55 (+2.0)	+1.16 (+2.0)	REAL + 2 K, whole basin, daily
M2	Uniform -2 K	-1.45 (-2.0)	-2.85 (-2.0)	REAL - 2 K, whole basin, daily
HI	Highest basin anomaly	+0.84 (+0.19)	+0.83 (+1.68)	Highest basin ave SST from the 1981-2011 period for week preceding/during event, daily.
LO	Lowest basin anomaly	-1.14 (-1.69)	-1.46 (-0.61)	Lowest basin ave SST from the 1981-2011 period for week preceding/during event, daily.

very high-resolution data.

The RTG dataset has been used extensively in numerical modeling. It is similar to Optimal (or optimum) Interpolation (OI) in that it uses the same satellite retrievals (AVHRR), corrections, ship and buoy data. The processing of this information to develop the gridded dataset is also the same. A full description of the techniques used are beyond the scope of this work. In general, ship and buoy data is regarded as the in-situ 'truth', and used as boundary conditions for a given domain. The satellite data are corrected relative to the in-situ information using a 'Poisson' technique described in Reynolds and Smith (1993). Firstly, preliminary in-situ and satellite data is calculated by using a spatial median filter to removes extremes at each gridpoint. Regions (gridpoints) where sufficient in-situ information is available do not require much further processing, while remaining SSTs are calculated from Poisson's equation (Reynolds and Smith 1993, p.942). In this technique, any biases in the satellite are adjusted against

the boundary conditions defined by the in-situ information. The primary difference between the OI dataset used here to extract HI and LO is in the initial resolution (0.25^{o}). Subsequent interpolation to RTG resolution (0.5^{o}) yielded similarities in distribution but differences in magnitude (locally up to 0.75 K) between the two datasets (not shown), contributing uncertainty to our representation of the actual SST fields in the model. Nonetheless, for reasons given earlier, this type of idealized study is expected to be less sensitive to such uncertainties.

The SST fields described in Table 4.1 and Fig. 4.21, 4.22 were converted to a format that can be read by WRF pre-processing software, and then run with this software to generate the initial and boundary conditions for the outermost model domain. The SST fields were initiated with the WRF, and updated in the model daily, allowing for the subtle changes in the field over the duration of the simulation. The perturbed SST fields, including anything other than REAL, were applied to the model in the same way. This meant that the model would have to adjust to the initial field as it integrated forward in time. In order to allow adjustment to the 'shock' of such perturbations, especially with regard to the low-level thermal and moisture profile, a seven day simulation length was chosen, initialized five days before the winter storm event. This duration was found to be of more than sufficient length for adjustment to occur (not shown). More discussion on WRF configuration is provided in chapter 5.

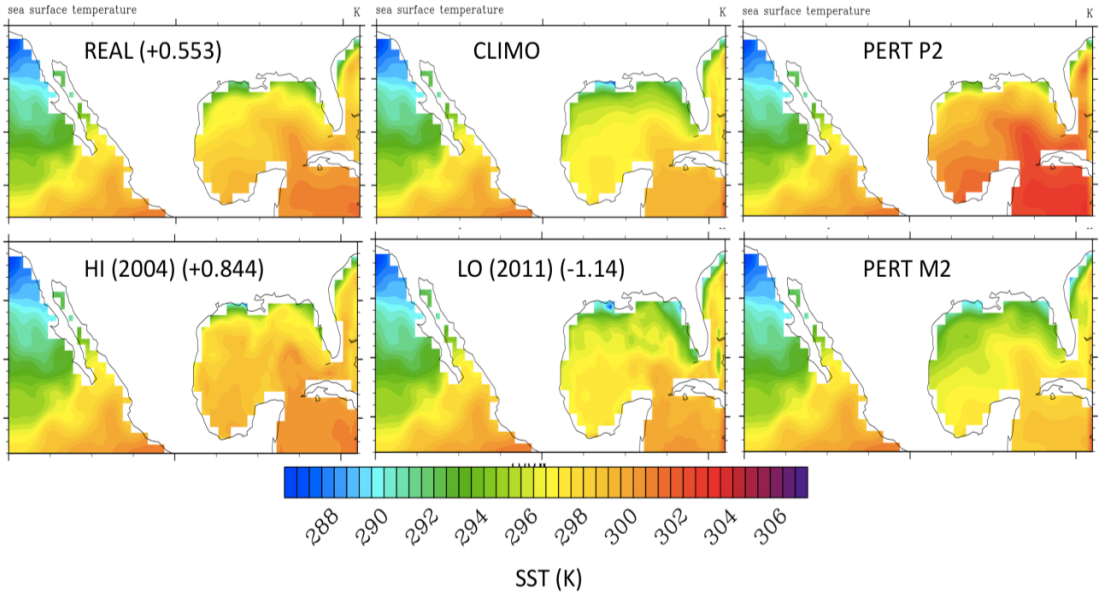

Figure 4.21: SST fields (in Kelvin) used as input to the WRF-ARW sensitivity study. These plots are valid for December 9.

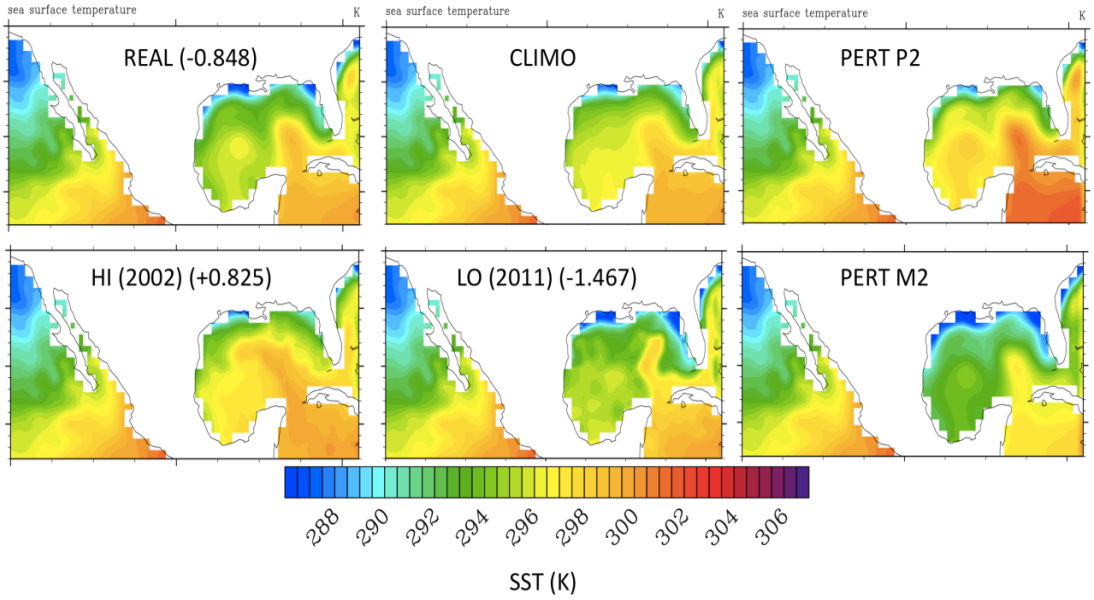

Figure 4.22: As Fig. 4.21 but for January 28. As a note to the reader, the unusual isolated positive SST anomaly and sharp gradient in the northeastern GOM in the 'LO' SST field for this case study was observed by multiple SST datasets, thus we do not have reason to suspect that this field is erroneous.

Chapter 5: Configuration and Validation of WRF Control Simulations

5.1 Introduction

Chapter 4 presented, background motivation and physical basis for a sensitivity study to examine the impact of Gulf of Mexico SST on the thermodynamic evolution of freezing precipitation for two case studies. The chosen events were described, and a set of six perturbed SST fields derived for each (see Table 4.1). This chapter details development of the WRF-ARW control ('REAL') configuration, including the choice of domains, resolution, and parameterization schemes. Simulations for both case studies are validated against a suite of observations in order to assess the model's ability to reproduce the major features of each.

5.2 WRF-ARW

5.2.1 Model overview

The WRF-ARW (Weather, Research and Forecasting Model – Advanced Research WRF, Skamarock et al. 2008, hereafter WRF) was the model utilized for this work. WRF is a mesoscale numerical weather prediction model designed for operational and research applications (http://wrf-model.org/index.php). Its creation was a collaborative effort between the National Center for Environmental Prediction (NCEP), National Center for Atmospheric Research (NCAR), the Forecast Systems Lab (FSL), Air Force Weather Agency (AFWA), and University of Oklahoma (OU), with contributions from many other University Scientists. WRF is updated roughly every 6

months, and is currently on version 3 of its architecture. Each update reflects growth in the state of knowledge of the physics, numerics, and data assimilation.

WRF has numerous functionalities, which make it a diverse and attractive model for research applications. Users may conduct idealized or real simulations of past or future weather events, evaluate forecast improvements through 3 or 4-dimensional variational data assimilation (VAR), conduct nested simulations (higher resolution sub-domains utilizing the coarser outer domain information as input and boundary conditions), or even experiment with regional climate applications. It is estimated that over 20,000 researchers use WRF in 130 countries.

The WRF has been implemented in prior case study based research pertaining to winter weather, (e.g., Thompson et al. 2004, Bernadet et al. 2009, Shi et al. 2010, Hosek et al. 2010, Wang et al. 2011, Gao et al. 2013) and extra-tropical weather systems (e.g., Otkin and Greenwald 2008, Booth et al. 2012). Nonetheless, its application specifically in the context of freezing precipitation remains limited. Hosek et al. (2010) used WRF (version 3.2) to simulate a heavy freezing rain event over Newfoundland to ascertain whether the model could provide accurate forecasts of ice accretion. A high resolution, nested regional simulation revealed that the model was able to replicate the freezing rain event with respect to the thermal profile and duration, albeit underestimating total accumulation and 'flattening' the spatial precipitation distribution (i.e., over-predicting in some regions, whilst under-predicting in others). Another study by Gao et al. (2013) simulated long duration freezing precipitation episode in China, comparing modeled cloud microphysical information to CloudSat observations. Their results suggested a good reproduction of the location and amount of precipitation, but over-prediction of

ice phase in simulated cloud, and liquid water phase near the surface. Given the lack of literature on the subject, our work provides a different and additional analysis of modeling freezing precipitation and its attendant thermodynamic evolution on a variety of scales.

5.2.2 Domain and Physics options

When this work was initiated in 2009, WRF 3.1 was the latest model update, and this version was utilized for the majority of the simulation development and physics configuration over the subsequent three years. Nonetheless, in 2012, the architecture was upgraded to version 3.4 in order to remain up to date with then-current improvements and research.

The first choice when configuring the model was the choice of domain and nesting options. Numerous exploratory experiments were conducted using ARW core 3.1 for a combination of nested domains, resolutions, durations, and input and boundary datasets in order to evaluate the 'best' set of choices. In addition, two-way nested simulations were tested for winter storm case studies including December 9-11 2007, and January 26-28 2009, also employing analysis and spectral nudging, and observational nudging of the near surface environment in order to reduce uncertainty in event evolution. Due to space constraints, very little of this work is summarized here. The key result of these investigative studies was the fact that notable errors in the timing of precipitation and the development of a near-surface refreezing layer occurred. These errors were generally only weakly influenced by physics and even input condition options, but were endemic to the model's representation of the synoptic scale

evolution. It was later identified that the culprit was the domain used for the outermost (parent) nest.

Figure 5.1 illustrates the growth of errors associated with the western boundary of the original parent domain (panel a). Although it included the majority of CONUS, the longwave trough located over Baja California intersected the western boundary. Such strong forcing at this boundary can produce spurious and fast propagating numerical inertia-gravity waves due to insufficient treatment of large accelerations and gradients 'cut off' at domain-edge. One option was to reduce the size of the parent nest so-as not to resolve the longwave trough at all, however, simulation of the synoptic scale evolution within the model was desired. The domain was thus expanded westward by several hundred kilometers in order to fully capture the trough.

Once the appropriate parent domain had been established, three nested domains (parent, and two additional) were chosen in order to yield a high-resolution simulation with explicit precipitation processes in the innermost nest, with horizontal grid spacing of 30 km, 10 km and 3.3 km respectively. Nesting is a useful and more computationally efficient alternative to one extensive high-resolution domain, allowing the user to 'focus in' on a region of interest. Figure. 5.2 shows the spatial extent of our nests. The initial choice of physics included RRTM (rapid-radiative transfer model) longwave, and Dudhia shortwave radiation, BMJ (Betts-Miller-Janjic) convective parameterization (applied to domains 1 and 2), Mellor-Yamada–Janjic (MYJ) planetary boundary layer (PBL) scheme and surface layer scheme, NOAH land surface model, and WSM6 (Hong et al. 2006) microphysics. This set-up is equivalent to the operational NSSL-WRF physics configuration minus the convective scheme. While the Kain-Fritsch (KF, Kain

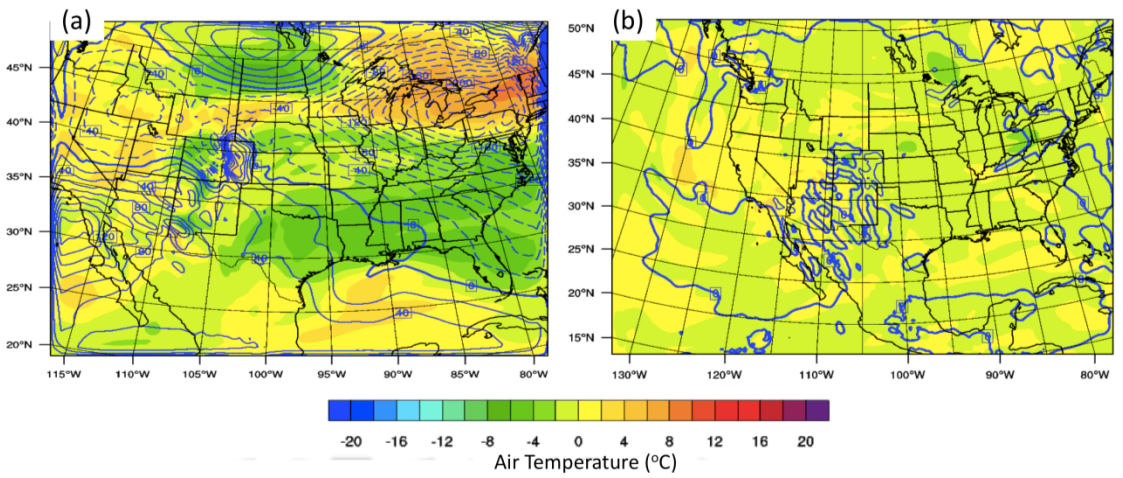

Figure 5.1: WRF-ARW simulated 200 hPa geopotential height (intervals of 20 gpm, blue contours, negative dashed) and air temperature (°C, color fill), expressed as a difference field relative to the NCEP/GFS Final Analysis at the corresponding time (00 UTC 8 December). Panel (a) shows the results for the original domain used, while (b) shows the final chosen domain.

et al. 2004) may be advantageous in a number of contexts, it is also more computationally expensive and was therefore not pursued. Given that the vertical thermal profile is highly important in the accurate simulation of mixed phase precipitation, 59 levels in the vertical were employed, staggered with 20 levels below 800 hPa to better resolve near-surface refreezing and warm inversions.

An additional consideration was whether or not to apply procedures to constrain errors over time, especially with the 7-day simulation (chapter 4, sec 4.4). Methods to reduce model uncertainties include data assimilation, observational nudging or analysis nudging. Data assimilation has been proven as an effective technique to reduce forecast uncertainty but was not applicable in this context where the meteorological environment requires the freedom to vary from the observed event. Similar issues likely apply to observational nudging. Grid (analysis) nudging seeks to constrain error by relaxing

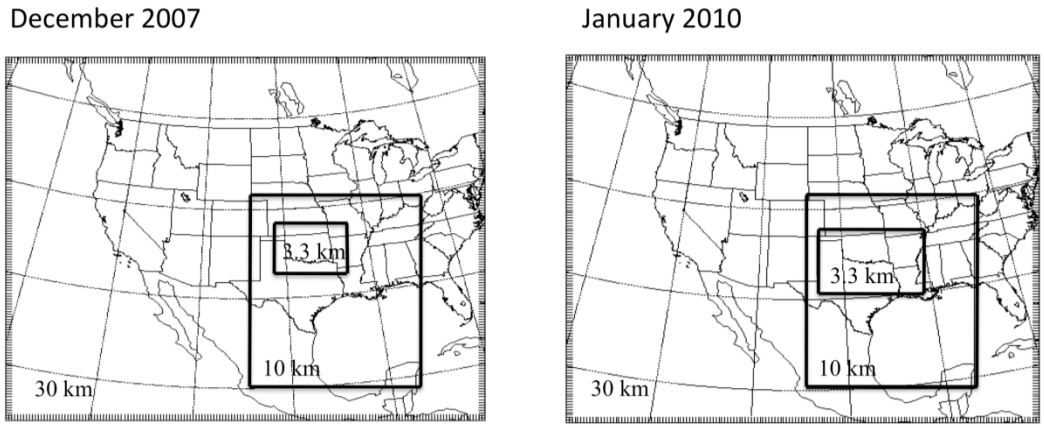

Figure 5.2: Domains selected for the 1-way nested simulations for (left) December 2007, and (right) January 2010.

model representation of a given variable or set of variables toward those of the input analysis (e.g., Stauffer et al. 2007a,b). It is often utilized for longer duration simulations where model error can grow with time. The choice of variables to nudge, as well as the strength of nudging and the layers over which to apply it are non-trivial choices and relate, among others, to the accuracy of the initial conditions, and their ability to resolve fine-scale phenomena. In this work, analysis nudging, based on 1^{o}x1^{o} GFS-NCEP final analysis (FNL) as input and boundary data (http://rda.ucar.edu/datasets/ds083.2), was applied in the parent domain at 6-hour intervals throughout the simulation, and only above the PBL for temperature and moisture. Furthermore, the nudging coefficient was reduced for moisture from the WRF default of 0.0003 s^{-1} by a factor of 6. To allow the inner two domains a greater ability to vary, one way nesting was used. In this case, results from the coarser domain were used as boundary conditions to the higher resolution domain, with no feedback from the higher resolution domain into the coarser domain. Similar methodology was employed for a sensitivity study examining the role

of SST anomalies on the intensification of a cyclone over the Kuroshio extension (Bond et al. 2010).

5.3 Configuration of Microphysics and Planetary Boundary Layer options

The initial configuration of physics options was described above. It is evident from perusing the literature that the various options and their interactions can yield very different model simulations. In addition, there is no consistent 'winner' in terms of accuracy amongst the various schemes, their efficacy largely related to the investigated meteorological environment. Given the large set of options in WRF, including > 4 convective schemes, over 10 microphysics options, several planetary boundary layer options, and so on, the set of potential combinations was far too great for complete treatment here. From earlier work (not shown), along with inferences from the literature (e.g., Hosek et al. 2010) it was determined that the physics options that potentially play the greatest role in the treatment of freezing precipitation include microphysics parameterization (MP) and planetary boundary layer (PBL)/surface layer schemes. We therefore performed a brief inter-comparison and evaluation of a subset of popular MP and PBL schemes available in WRF for a simulation of the December 2007 case study to identify the most suitable schemes for use in the sensitivity analysis.

5.3.1 Microphysics

Microphysical parameterization is necessary for representing important processes in cloud and precipitation development on the model grid scale (Straka 2009). MP schemes predicts the cloud and precipitation characteristics using equations that

calculate the drop size distributions and mixing ratios of a specified number of hydrometeor categories, which can include cloud water, ice, snow, graupel and hail. The MP representation ultimately affects the resultant precipitation accumulation, type, and atmospheric heat and moisture tendencies.

MPs available in WRF are 'bulk' parameterizations, which assume a functional form of the particle size distribution, usually based on empirical information for a given hydrometeor species (e.g., exponential, gamma). The distributions can be integrated over a large range of hydrometeor size to predict mixing ratio or occasionally number concentration (but not both) in a '1-moment' scheme, or both mixing ratio and number concentration in a '2-moment' scheme (Lackmann 2011, p260). It is generally regarded that 2-moment formulations, whilst being more computationally expensive, are more realistic due to more accurate estimate of size distribution (and its change with time), fall velocity, collection efficiency, and sedimentation rates. Many complex processes must be accounted for by a given MP, especially those resolving cold rain (ice) processes, including diffusional growth, aggregation (autoconversion, accretion), collection of rainwater by ice (riming), nucleation, melting and freezing, and sedimentation, whilst also attempting to in some limited fashion account for the wide variety and strong temperature dependence of ice crystal habits.

Since our research is focused on mixed phase precipitation, any choice of MP must necessarily include ice processes. Prediction of as many hydrometeor classes as possible was also desired, including graupel (for the representation of ice pellets), which yields at least a 6-class scheme. A further advantage would be if the scheme had been utilized or tested in winter precipitation conditions. Finally, two-moment microphysics

was preferred if it yielded discernable improvement over a single moment scheme. Based on these requirements, four MPs were chosen for evaluation:

WRF Single Moment 6-Class (Hong et al. 2006): Is a highly utilized one-moment scheme, which predicts the evolution of mixing ratio, and was initially based on the Lin et al (1983) and Rutledge and Hobbs (1983) equations, adding processes for cloud ice, such as number concentration, accretion and nucleation. The scheme uses an exponential size distribution for all hydrometeor classes.

Thompson et al. (2004, 2008): This form is single-moment for cloud water, rain, snow and graupel (i.e., predicts only mixing ratio), while also predicting the number concentration (2-moment) for cloud ice. A gamma distribution is used for each hydrometeor type. In 2008 the parameterization was updated to improve upon numerous physical processes, especially for snow and ice, permitting this scheme to potentially produce accuracy similar to a double moment MP without the downside of increased computational time. One unique feature is the use of 'lookup tables'; tables of measured distributions with respect to diameter that can be drawn from for the calculations. This method is used to reduce overhead computation and attempt to capture the accuracy of a bin MP model (Straka 2009). The Thompson et al. scheme was tested initially on idealized flow over a hill, and development of a shallow cloud layer. Thompson et al. (2008) tested the scheme on deeper and colder cloud. However the initial motivation was to better represent the formation of supercooled liquid water for aircraft icing forecasts, and much of the validation of the MP has been performed with respect to shallow winter precipitating layers.

Morrison 2-Moment (Morrison et al. 2005, Morrison and Pinto 2006, Morrison et al. 2009): This MP is a 6-class 2-moment formulation, using gamma size distributions for all hydrometeor types. More detailed discussion of specifics is provided in the above references. The scheme was tested on idealized WRF simulations of a squall line. The 2-moment scheme improved upon its single-moment counterpart especially in the convective to stratiform transition and the development of a well-developed trailing statiform area. The rain intercept parameter was found to be critical, with a better representation of this parameter identified in the 2-moment form.

Millbrandt-Yau (2005, 2006 MIllbrandt et al. 2010): This parameterization is a 2-moment scheme with 7 hydrometeor classes (hail is treated as separate from graupel). Once again, the hydrometeor size distribution is a generalized gamma form. In this case however, special attention is paid to the shape parameter of the distribution, which typically is a fixed value in most schemes. In order to remain a 2-moment scheme, the shape parameter cannot vary independently, however, a diagnostic relationship may be developed between it, and another variable (e.g., diameter) based on physical insight. This MP therefore does not fix the shape parameter, instead diagnosing it from a monotonically increasing function of the mean-mass diameter. This formulation tends to control excessive size sorting, which can be important for ice-phase hydrometeors (snow, graupel, hail). It was mainly tested on convective precipitation.

5.3.2 Planetary Boundary Layer (PBL)

Accurate representation of the atmospheric PBL is important as the exchange of heat, moisture and momentum between the surface and overlying atmosphere typically

occur within this region (Lackmann 2011, p258). PBL schemes parameterize the complex processes that govern these exchanges (e.g., turbulent fluxes on model grid-scale), as well as relate them to surface properties, such as vegetation, radiative balance and cloud cover. Given that the chaotic, fine-scale and isotropic nature of turbulence are hard to characterize, fluctuations of the quantities of interest are often estimated over a several minute period. Different schemes make different assumptions regarding 'closure' – that is, fluxes must be represented by other dependant variables such that the number of unknown quantities equals known quantities (Lackmann 2011, p258). In a general sense, most schemes fall into either a 'local' or 'non-local' closure. In local closure, turbulent flux gradients are evaluated between adjacent model levels in the vertical, while a non-local technique evaluates fluxes from gradients over the depth of the PBL. Observational studies suggest that turbulence is contributed by eddies on a broad range of scales, and therefore a non-local scheme intuitively appears more reasonable.

WRF contains several PBL and surface layer options, two of which are particularly popular in the literature. While alternative schemes have some merit, for example, for ARW version 3.1, the QNSE (Sukorianski et al. 2006) PBL scheme was superior in simulating the shallow arctic front associated with the December 2007 freezing precipitation event in a 5-day un-nudged simulation (White et al. 2010, presentation), time considerations preclude a thorough analysis, and so only the most commonly used schemes are studied here:

Yonsei University (YSU, Hong et al. 2006): The YSU is a non-local PBL scheme developed from observations, and large eddy modeling (e.g., in the representation of

entrainment at PBL top, Noh et al. 2003). Much of the testing and validation of this scheme has been with respect to well-mixed convective boundary layers. As a result, YSU typically performs well in simulating low-levels winds, temperature, moisture and PBL depth during the daytime and with a well-mixed PBL. Calculations of entrainment at PBL top in YSU are meant to mimic the action of shallow clouds. Recent updates to the YSU scheme in the ARW 3.4 have corrected some errors in the representation of the nocturnal PBL, and improved measurements of low-levels winds, and the low-level jet (Hu et al. 2013).

Mellor-Yamada-Janjic (MYJ, Mellor and Yamada 1982): The MYJ is a popular local technique that determines eddy diffusion coefficients for the PBL from prognostically calculated turbulent kinetic energy (TKE) (Hu et al. 2010). This PBL form was primarily developed for stable PBL layers and therefore tends to produce large errors in near surface variables in highly unstable conditions. This scheme in particular tends to resolve the structure and wind fields of the nocturnal PBL with more accuracy. Furthermore, it typically outperforms non-local schemes for stable daytime PBL conditions (Shin and Hong 2011).

5.3.3 'Test' simulations

A set of simulations were performed, shown in table 5.1, using the December 9-11 2007 case study, where either the PBL *or* the MP scheme were varied with all other conditions fixed. In addition, since this portion of the study was conducted during the switch from WRF 3.1 to 3.4, two additional simulations with WRF 3.1 were evaluated against WRF 3.4. Each simulation used the nest configuration shown in Fig. 5.2, and

the setup described in section 5.2.2. The simulation was initialized at 00 UTC December 4 2007, and ran to 00 UTC 11 December 2007, with data output at 3, 2 and 0.5 hours for nests 1, 2 and 3 respectively. For domain 3, only data after 12 UTC 8 December 2007 was retained.

Figure 5.3 shows domain 3 simulated 48-hour accumulated precipitation, valid 00 UTC December 9-11 2007 for WRF 3.1 versus 3.4 for MYJ and YSU PBL. The larger panel on the right hand size shows the observed accumulation, based on Stage IV radar/gauge derived precipitation. Visual inspection indicates that in all cases WRF does not accurately reproduce the swath of greatest accumulation along an axis from southwest to northeast, although in all but WRF 3.4 YSU, evidence for such an axis exists. Typically in the WRF, the southern branch of precipitation (southeast domain) was amplified relative to the main axis, as were accumulations in the west. Furthermore, the simulation 'spreads out' precipitation and overestimated the spatial extent above 5 mm. WRF 3.4 YSU simulation produced the worst result, while arguably the 3.1 MYJ had slightly better precipitation accumulation within the central axis.

Figure 5.4 shows the results of changing the MP amongst the four options discussed above. The PBL scheme is fixed as MYJ. Visually, WSM6 and MY captured

Table 5.1: Description of each simulation testing the performance of the MP and PBL schemes described in section 5.3.

Simulation	ARW Core	PBL	MP
MYJ-3.1	3.1	MYJ	WSM6
YSU-3.1	3.1	YSU	WSM6
MYJ 3.4	3.4	MYJ	WSM6
YSU 3.4	3.4	YSU	WSM6
MP-8	3.4	MYJ	Thompson
MP-9	3.4	MYJ	Millbradt-Yau (2 moment)
MP-10	3.4	MYJ	Morrison (2-moment)

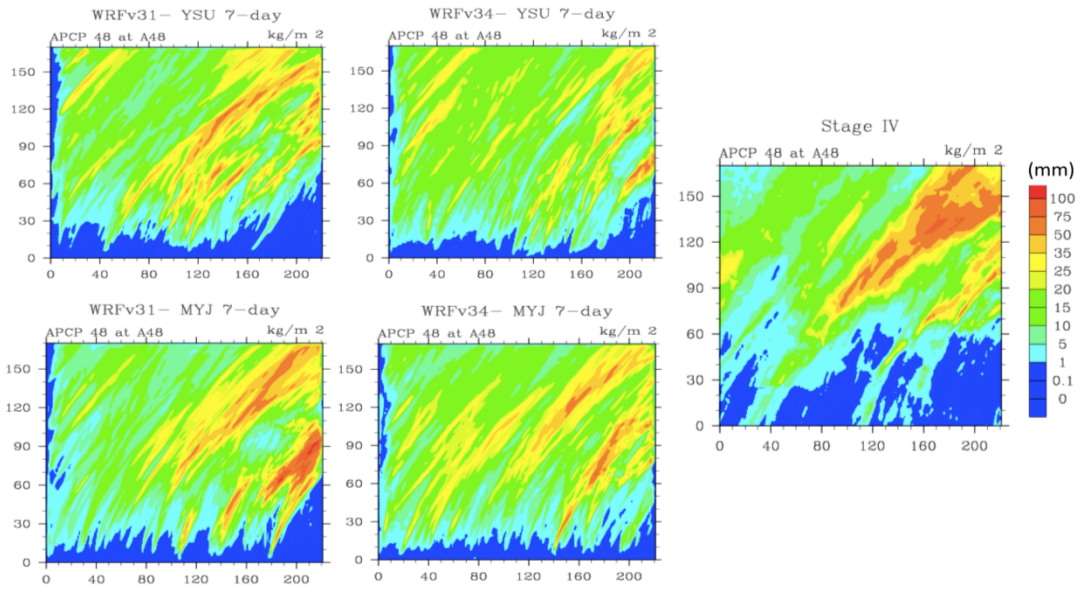

Figure 5.3: 48-hour accumulated precipitation (mm) from 00 UTC 9 – 00 UTC 11 December for domain 3 (x and y axis show grid point number). Top panels show YSU PBL 3.1 (left) and 3.4 (right) with WSM6 MP, while bottom panels show MYJ PBL 3.1 (left) and 3.4 (right). Stage IV observations (interpolated to WRF grid, see appendix section 5 for details) shown in the rightmost panel.

the observed morphology best, albeit WSM6 overestimated western domain precipitation, while the central axis was more diffuse in the Morrison scheme, and the western accumulation too great using Thompson MP. Figure 5.5 summarizes some key verification (skill scores) metrics for each simulation, calculated for three precipitation thresholds (0, 10, 25 mm) using a neighborhood method that evaluates a 5x5 gridpoint region (max radius 15 km). A neighborhood is often preferred for high-resolution simulations, where a single-station estimate could overly penalize the model, even if the variable in question was only slightly displaced. All scores were calculated using the Model Evaluation Toolkit (MET) version 3.1 (http://dtcenter.org/met/users). Multiple metrics were used, including standard contingency table, and skill scores such as critical success index (CSI), Gilbert score (GSS, 'equitable threat') and fractions (FSS) when

available. Brief descriptions of metrics used in this chapter are given in Appendix Sec. 5. Multiple scores were preferred as individually they do not necessary provide a complete picture of model performance, CSI for example shows decreased skill for rare events (e.g., higher precipitation thresholds). Used together we get a more holistic sense of skill across a range of parameters and thresholds. More emphasis was given to the model's ability to capture precipitation at the 10 and 25 mm thresholds. In general, WSM6 with WRF 3.1 gives a superior result, however, of the WRF 3.4 simulations, MY appeared to overall provide a slightly better simulation, with more discrimination of precipitation (higher hit rate, lower FAR, POFD, CSI at higher thresholds). These metrics, combined with the precipitation morphology, favored use of MY with WRF 3.4.

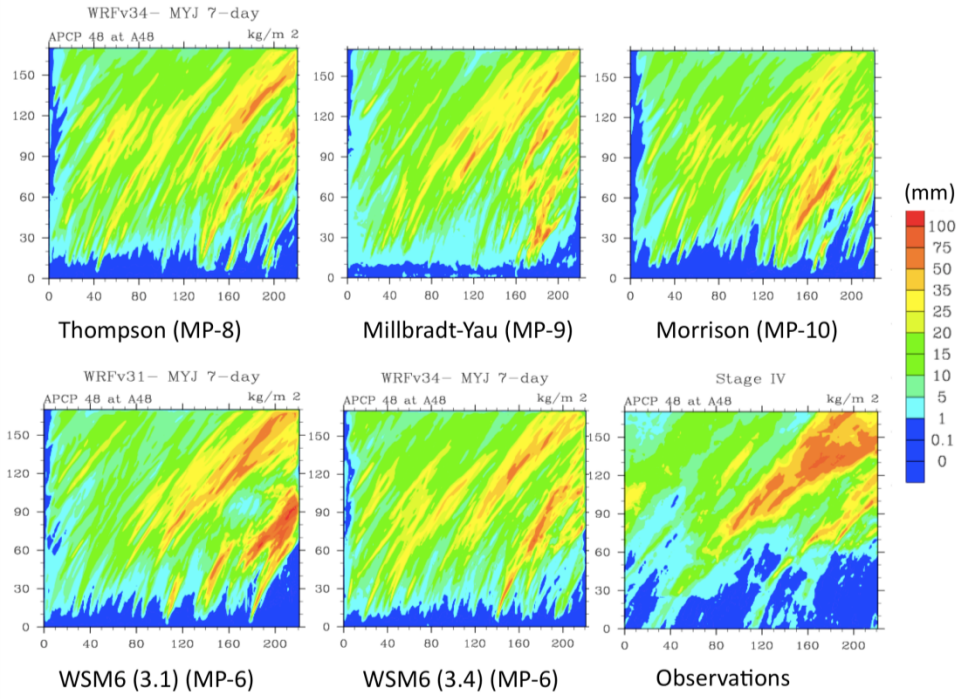

Figure 5.4: 48-hour accumulated precipitation (mm) as in Fig. 5.3 but for the four MP schemes evaluated, with PBL fixed as MYJ. Performance of WRF 3.1 and 3.4 using WSM6 are also shown, while observations from Stage IV (interpolated to WRF grid) are shown on the bottom right.

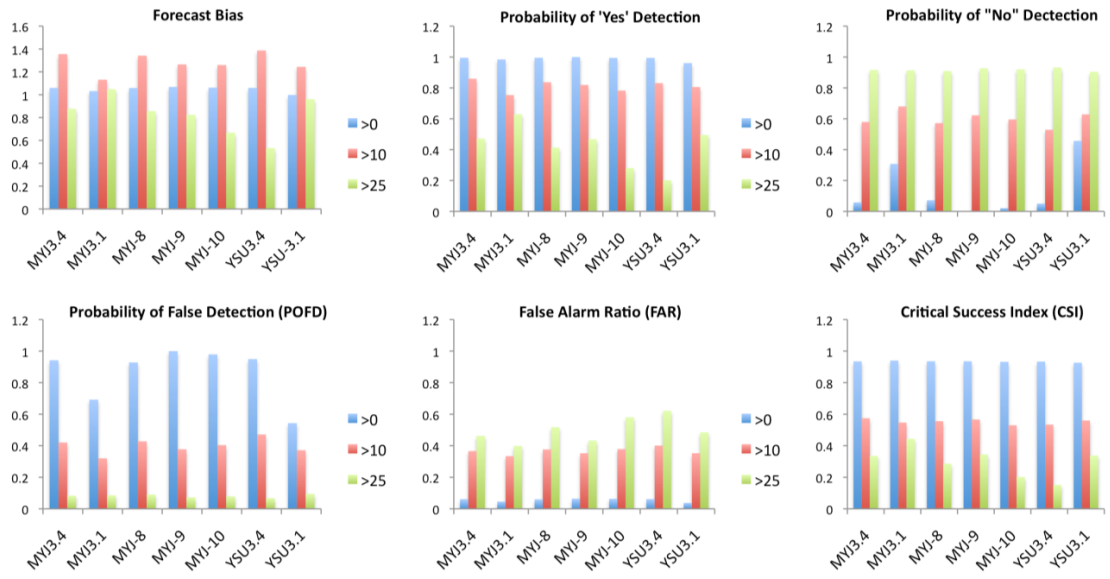

Figure 5.5: Selection of skill score metrics for each perturbed domain 3 simulation, using a neighborhood method of 25 gridpoints surrounding each gridpoint location. Scores are evaluated at three accumulation thresholds (based on 48-hour accum) of 0, 10 and 25 mm in blue, light green and red respectively. Microphysics scheme designations are provided in Fig. 5.4.

For temperature, root mean squared error (RMSE) was calculated at 35 locations over Oklahoma at 6-hour intervals, using Mesonet data interpolated to a 0.5x0.5^{o} grid (see appendix, section 5) as 'truth', shown in Figure 5.6 (note that data for 18 UTC is missing for the Mesonet). It is apparent that WRF 3.1 produced a much larger (positive) error in temperature throughout the event, especially with YSU PBL. The error maximized late afternoon (~00 UTC), suggesting a relationship to diurnal PBL structure, and possibly the shortwave radiation scheme (Dudhia), though this was not investigated. In WRF 3.4, the YSU PBL appeared to have a positive temperature bias on December 9, however by the evening this reduced and actually was slightly more accurate than the WRF 3.4 MYJ (coupled with WSM6 MP) for the remainder of the event. The three additional MP-perturbed simulations showed little difference from one another.

Figure 5.7 summarizes the average spatial RMSE over Oklahoma for the 48-hour duration. Of note were larger errors for the YSU scheme that orientate in the same fashion as the arctic airmass. This suggested failure of the scheme to simulate the correct southward movement of cold air. The non-local turbulent mixing, coupled with enhanced mixing at the PBL top may have erroneously weakened the shallow wedge of surface subfreezing air (which was only ~500 m deep), especially in conjunction with maximum daytime heating. Lackmann (2011) noted that use of the YSU PBL with the BMJ convective scheme (used for domain 1 and 2) tended to quickly eliminate cold air damming regimes, which he attributed to a duplication of processes representing shallow cloud layers at the PBL top, as both schemes represent this process in some fashion. The combined mixing in this layer ultimately becomes too strong.

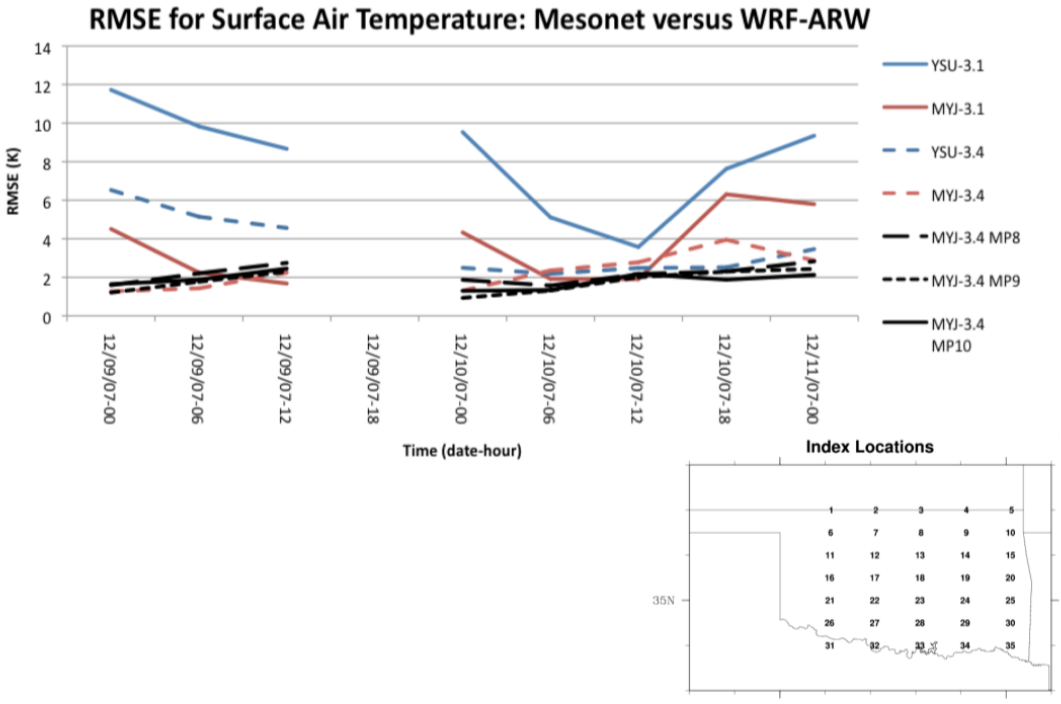

Figure 5.6: Root mean squared error (RMSE, K) for each perturbed simulation (domain 3) at 6-hour intervals over storm duration. The values are the average of 35 grid points (bottom right inset), and are calculated relative to interpolated Mesonet data at the same locations. Missing data at 18 UTC due to power outage.

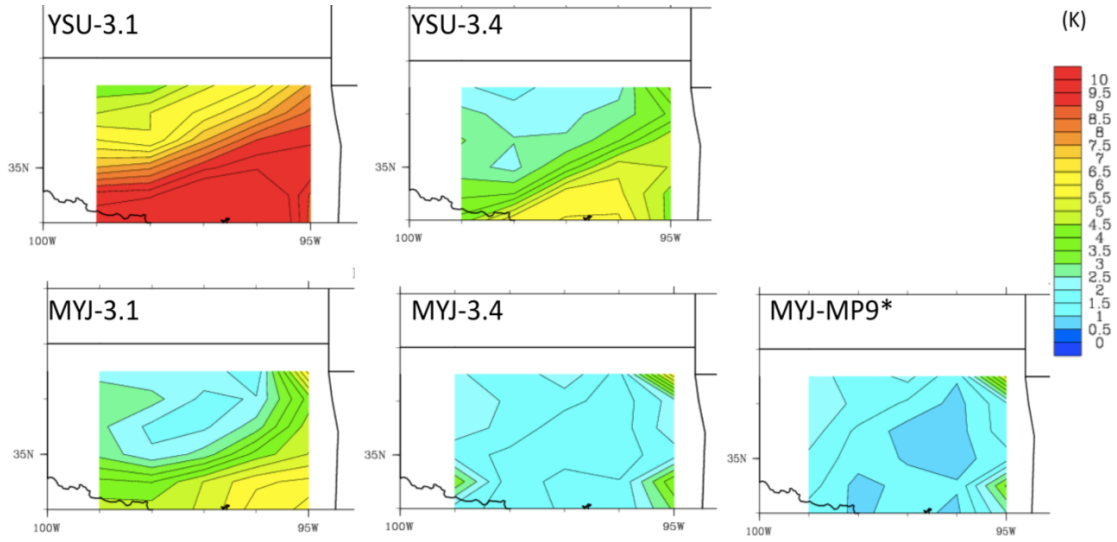

Figure 5.7: Spatial distribution of RMSE (K) relative to Mesonet data, interpolated to a 0.5x0.5 grid over Oklahoma ending at 99°W and 36.5°N. The spatial average is a storm total average (00 UTC 9 – 00 UTC 11 December). The four PBL simulations (two WRF-3.1, and two WRF3.4) are shown, with the retained configuration displayed by the bottom right panel (*).

Based on this subset of results, it was decided to continue with the use of WRF 3.4, and to use the MYJ PBL and Millbrandt-Yau 2-moment MP for the SST sensitivity study. The next section further verifies the results of the control simulations for our two case studies, and provides some thoughts on the precipitation accumulation errors identified for the December 2007 event.

5.4 Verification of Control Part I: December 2007

Numerous observations were employed to verify the simulation with emphasis on four key variables: precipitation, thermal profile, winds/synoptic evolution, and cloud properties. The aim was to identify key uncertainties and to determine whether the simulation was sufficiently skillful. The same verification procedure was applied for the January 2010 case study simulation in section 5.5.

5.4.1: Precipitation

Precipitation was assessed in three ways; (1) use of the MET toolkit to evaluate skill scores similar to section 5.3. In this case threshold accumulations were assessed using thresholds based on the observed precipitation accumulation distribution, including approximate median, 75th and 90th percentiles; (2) the use of the MODE tool to evaluate object based skill metrics, where the 'object' was spatial morphology of 48-hour accumulated precipitation ≥ ~75th percentile (see appendix section 5 for a brief summary of the tool); (3) the temporal evolution of precipitation and total domain accumulation. In each case, observed precipitation was derived from NCEP Stage IV. Verification was performed only for domain 3. Table 5.2 shows the results of the neighborhood verification, while Figure 5.8 and Table 5.3 show object based spatial domain (figure), and skill metrics (table). In general, neighborhood scores suggest a slight overestimate (bias > 1) of lower accumulations (e.g., 0 mm, 10 mm) consistent with the observed overproduction of precipitation ≤10 mm. Higher accumulations (20, 25 mm) were generally under-forecast or misplaced southeast. While 0, 10 mm show less discrimination (high precipitation hit rates, but areas of no precipitation poorly forecast), the 20, 25 mm thresholds indicated reasonable forecast with respect to location, albeit the false alarm ratio also increased. For the 90th percentile (40 mm), the model poorly reproduces the spatial coverage, with notable reduction in skill. Use of 3x3 verification neighborhood (9 gridpoints, ~20 km box, not shown) versus a 5x5 (25 gridpoints, ~33 km) did not yield large changes in the magnitude of the skill (~0.01-0.05), but it was common for the 5x5 method to produce slightly improved metrics (Table 5.2).

For the object-based method (20 mm, Fig. 5.8, Table 5.3), 48-hour accumulation spatial morphology indicates reasonable location and orientation of precipitation, albeit underestimated in width and southwestward extent (see appendix, sec 5). By 'matching' simulated and observed objects by overlaying them in space, object contingency and skill scores were evaluated. This approach yielded improvement in the majority of statistics, for example HSS, GSS (+0.06), FAR (-0.15), PODN (+0.08), POFD (-0.09). Nonetheless, the underestimate of precipitation accumulation along the central axis can clearly been seen (bias = 0.74). The temporal evolution of precipitation for the event was evaluated by obtaining precipitation timeseries at 6-hour intervals for 35 grid-point locations (see inset Fig. 5.6) over Oklahoma. Five sub-domains were then specified and the average precipitation accumulation (based on these sites) estimated for both Stage IV and WRF, shown in Fig. 5.9. A limitation of this method was the relatively coarse resolution of the sites chosen, nonetheless, general temporal consensus was indicated between the model and observations, especially over the central axis. WRF generally underestimated precipitation during the afternoon/evening of the 9th (18 UTC-06 UTC 10th), especially in the north, while precipitation was overestimated on the 9th in southeast Oklahoma.

Given that the event evolution (see chapter 4) indicated the prevalence of cellular elevated convection, the modeled mode of convection should also be assessed. Using the WRF post-processing software RIP4 (http://www.mmm.ucar.edu/mm5/documents/ripug_V4.html), simulated radar reflectivity was assessed at 1-hour intervals between 00 UTC December 9-11 and visually compared against National Weather Service level III composite radar

Table 5.2: Skill scores for 48-hour accumulated precipitation (domain 3) at thresholds of 0, 10 (~median), 20 (~75th percentile), 25 (~ 1 inch), and 40 mm (~90th percentile). Scores are calculated using a neighborhood of 5x5 grid points. This allows a precipitation 'hit' if precipitation falls within the grid box, which avoids unfairly penalizing a high-resolution model for a small displacement in location. Rightmost column shows perfect' value of each skill score. Data to 2 decimal places. Definitions for each skill metric in Appendix Sec, 5

Skill Metric	Score Threshold: > 0 mm	≥ 10 mm	≥ 20 mm	≥25 mm	≥ 40 mm	Perfect Value
Accuracy	0.94	0.72	0.82	0.86	0.89	1
Bias	1.07	1.29	1.10	0.82	0.18	1
Prob. Detection –Yes (PODY)	1.0	0.84	0.62	0.48	0.06	1
Prob. Detection – No (PODN)	0.0	0.62	0.88	0.93	0.99	1
Prob. False Detection (POFD)	1.0	0.38	0.13	0.07	0.01	0
False Alarm Ratio (FAR)	0.06	0.35	0.44	0.41	0.67	0
Critical Success Index (CSI)	0.94	0.58	0.42	0.36	0.05	1
Gilbert Skill Score (GSS)	0.0	0.29	0.31	0.29	0.04	1
Heidke Skill Score (HSS)	0.0	0.45	0.48	0.42	0.07	1
Fractions Skill Score (FSS)	0.97	0.79	0.67	0.61	0.15	1

Table 5.3: Precipitation object-based skill scores for 48-hour accumulations ≥ 20 mm (see also Fig. 5.8, appendix section 5).

Skill Metric	Score	Perfect Value
Accuracy	0.89	1
Bias	0.74	1
Prob. Detection –Yes	0.53	1
Prob. Detection – No	0.96	1
Prob. False Detection (POFD)	0.04	0
False Alarm Ratio (FAR)	0.29	0
Critical Success Index (CSI)	0.44	1
Gilbert Skill Score (GSS)	0.37	1
Heidke Skill Score (HSS)	0.54	1

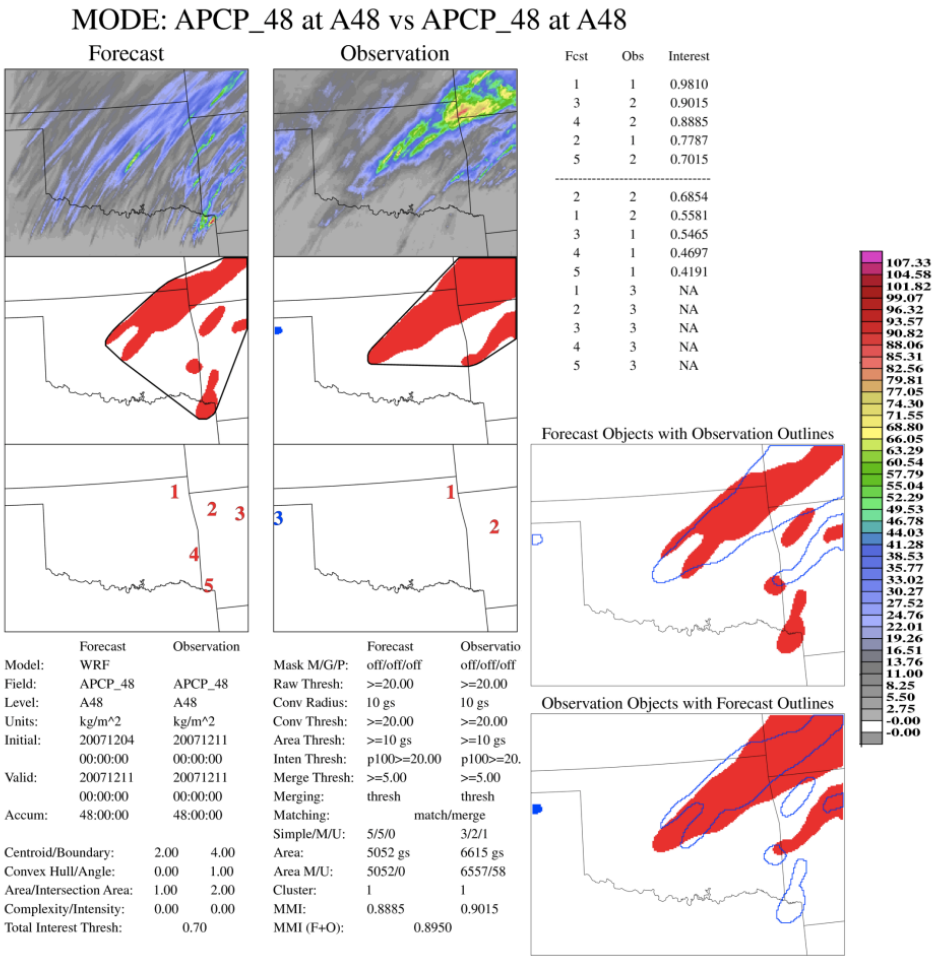

Figure 5.8: MODE tool in MET to evaluate precipitation by spatially matching accumulation thresholds > 20 mm. Top two panels show the original precipitation field (mm), while middle and bottom left hand panels show the method by which MET define precipitation objects. The technique is sensitive to smoothing radius (here we used 10 km, see appendix, sec 5) and threshold. The larger panels on the right show the spatially matched forecast (simulation) and observed (Stage IV) objects. Other parameters are defined in the users guide to METv3.1, and appendix, sec 5.

reflectivity (not shown). WRF produced convection in similar fashion to observed, but with generally lower peak reflectivities and reduced broad-scale mixed mode stratiform and convective elements. Apart from potential underestimates in intensity, lower accumulated precipitation and lateral spread may be due to differences in the placement of convective cells, with small displacements yielding much-reduced intensity along the

primary echo-training axis, and the reduction in stratiform transitions. Furthermore, fewer convective cells were simulated on the afternoon of December 9 (CST) compared with observations. A thorough analysis of the reasons for this discrepancy were outside of the scope of this work, however, the observed and simulated decrease in the magnitude of the low level jet may have reduced the strength of WAA and isentropic ascent into the domain. The model may have also more aggressively stabilized the lower atmosphere in response to the earlier convection. Additionally, the model's over-production of precipitation to the southeast may have had an impact on the axis of freezing precipitation. Further work would be needed to investigate these claims.

As a final salient point it should be noted that the nature and intensity of precipitation for domain 1 in particular, and domain 2 showed distinct differences from domain 3. In domain 1 (30 km) there was negligible freezing precipitation recorded over the SGP. Figure 5.10 illustrates this by comparing the 48-hour totals valid 00 UTC 11 December for the region in domains 1, 2 and 3. It appears that the horizontal resolution of domain 1 is not fine enough to resolve this type of elevated convection. Domain 2 initiates convection, but accumulations were lower and shifted to the north relative to domain 3. Persson and Warner (1993) suggested that models with coarser resolution were able to resolve convectively unstable (and/or convective symmetric instability) circulations, but with later onset and reduced intensity. They also suggested that in general the most unstable growth mode of convective instability can be resolved with maximum grid spacing 6-15 km horizontally, with 70-170 m vertically. The 30 km outer domain does not satisfy this (horizontal) criterion.

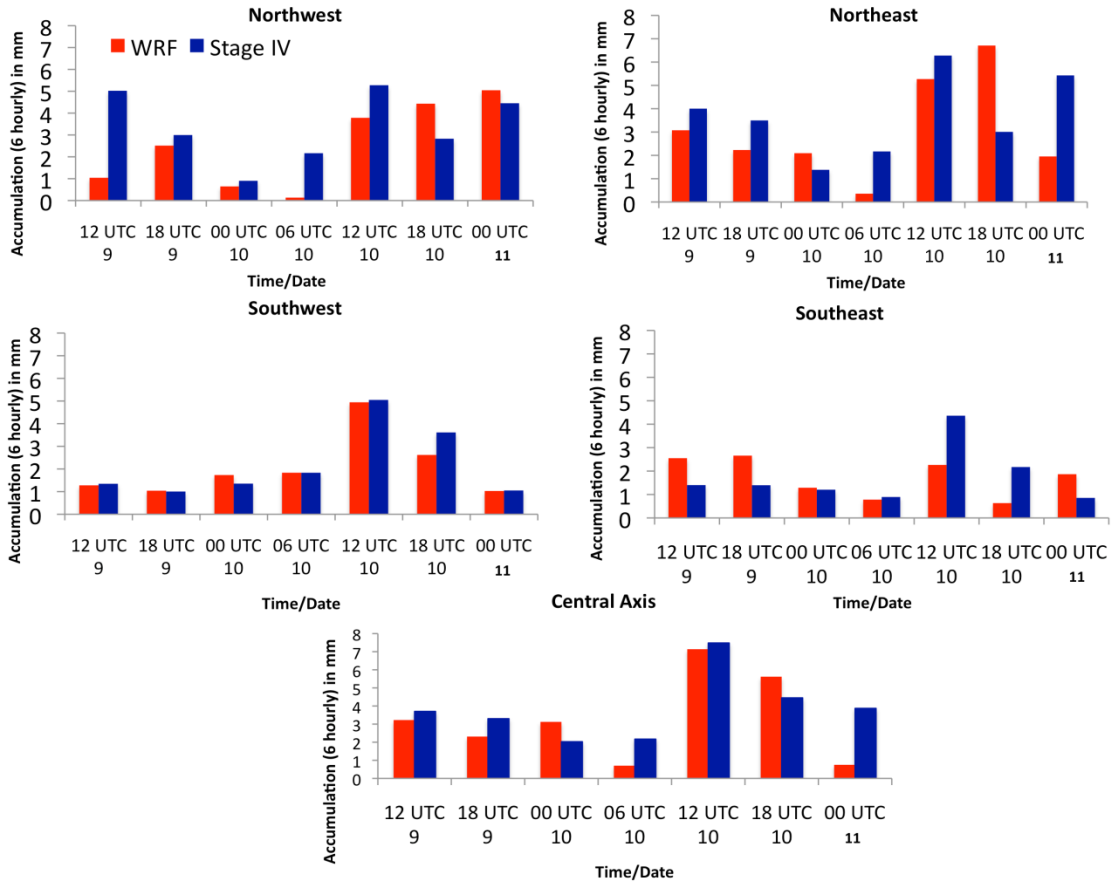

Figure 5.9: 6-hourly precipitation accumulation time series between 12 UTC 9 and 00 UTC 11 December for four quadrants over Oklahoma, and the central axis of freezing precipitation over Oklahoma, based on 35 grid point locations. WRF (Stage IV) shown in red (blue).

5.4.2 Thermal profile

The WRF-ARW temperature simulation was validated at the surface using Mesonet data, and aloft using ACRF-SGP best estimate data (CMBE version 2, Xie et al. 2010). CMBE vertical thermal profiles are primarily derived from atmospheric soundings. For 6-hour intervals, the surface temperature (domain 3) indicates good agreement with the (interpolated) Mesonet (see Figure 5.7, 5.9, MP9 simulation), based on the average of 35 gridpoints over Oklahoma. However, WRF tended to be slightly warmer than observations (not shown), especially later on December 10, and near 12

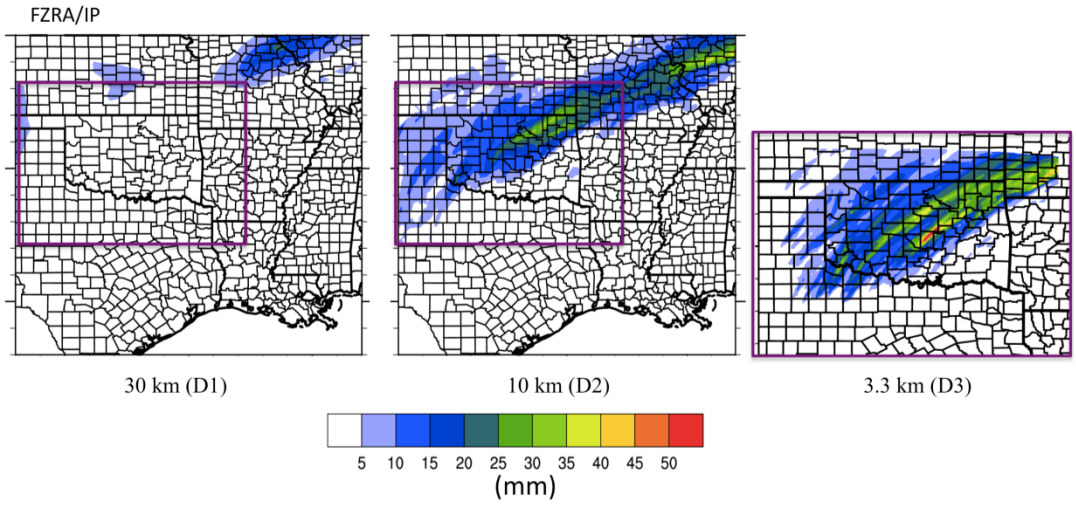

Figure 5.10: 48 hour precipitation accumulation in mm, valid 00 UTC December 11, for WRF-ARW domain 1 (left), 2 (center) and 3 (right) for mixed phase precipitation (freezing rain, ice pellets). Location corresponding to domain 3 shown by the purple box. County and State boundaries overlaid.

UTC December 9, when there was a slight northward bias in the location of the 0^{o}C isotherm. Such a result was not unusual as the majority of numerical models have problems resolving the speed of the shallow cold airmass. Fortunately, this simulation indicated only small departures (not shown).

The vertical profile of air temperature (Figure. 5.11) was evaluated at 6-hour intervals for domain 1, 2 and 3, using a gridpoint average surrounding the SGP coordinates (typically 0.5^{0}x0.5^{o}). The figure indicates that the vertical profile of temperature was well simulated, especially with regard to warm layer depth and magnitude, albeit observed peak temperatures tend to be underestimated in the model. Domain 2 and 3 had similar temperature evolutions, with larger differences for domain 1, probably due to the lack of simulated precipitation and its associated thermal effects on temperature. WRF remained warmer than observations through the majority of the event, particularly for domain 1.

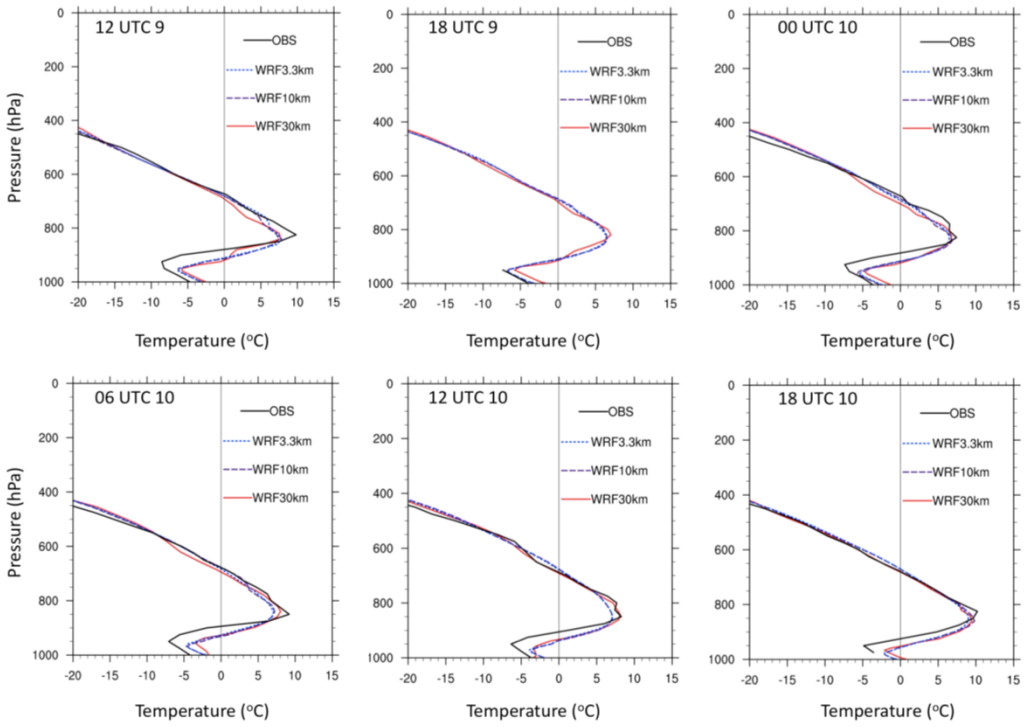

Figure 5.11: WRF vertical temperature profile for domains 1-3 (color-coded, see legend), and observations based on radiosonde information via ACRF-SGP (Lamont, OK), at 6-hour intervals during the ice storm. Thin grey line denotes the 0°C isotherm.

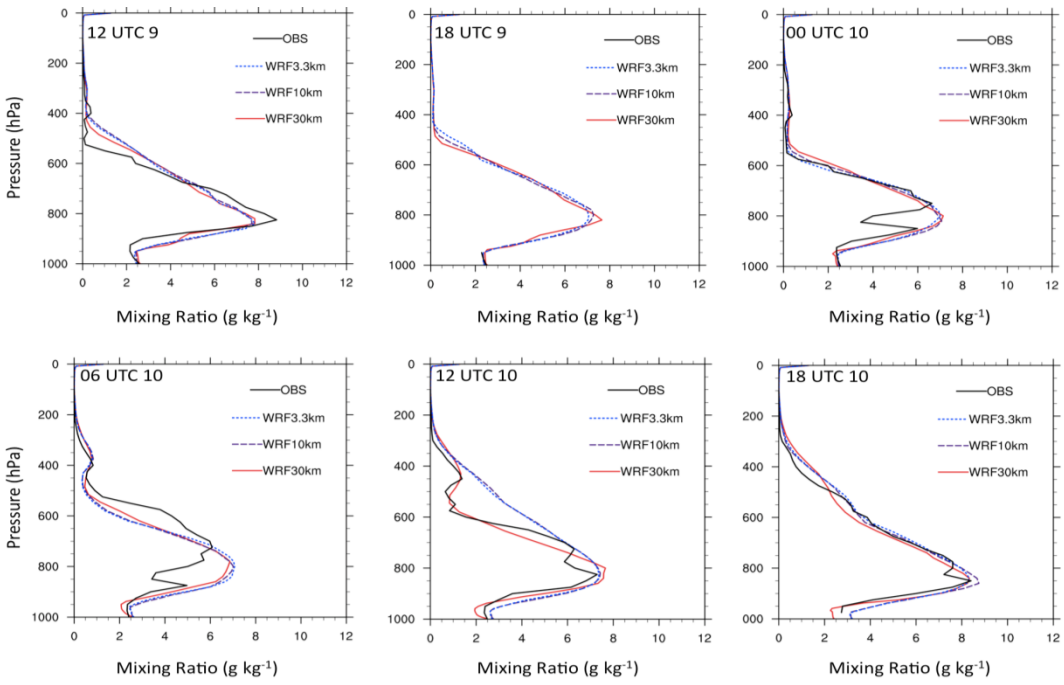

Figure 5.12: As Fig. 5.11 but for mixing ratio (g kg^{-1}).

The vertical profile of mixing ratio, calculated from the air temperature, pressure and dewpoint temperature is shown for the ACRF central facility in Fig. 5.12. In general, the moisture profile is well simulated, however, differences in the timing of precipitation at this location may be responsible for some discrepancies, especially on the 10th. The model reproduced the high moisture content of the warm layer.

5.4.3 Synoptic evolution

The evaluation of the synoptic flow was conducted with domain 1. The movement and change in amplitude of the western trough was well simulated, shown in Figure 5.13, as were its associated jet features (location, magnitude, not shown). Vertical profiles of zonal and meridional wind components also agreed well to ACRF observations, with no secular departures, but some localized low-level differences possibly related to convection (not shown). The SLP evolution in figure 5.14 relative to NARR data showed similar southeastward movement of higher pressure (based on 1026 hPa isobar), but a more rapid moderation and shrinking of this higher pressure in WRF. The lower SLP in the model corresponds well to the warm surface temperature bias, and the quicker northward retreat of the zero degree isotherm on the afternoon of December 10 (not shown). It may be that this airmass was more rapidly moderated by weaker cold air advection in the surface layer, and/or by more pronounced daytime heating. The latter is also possible due to the lack of convective activity for domain 1, which should have greatly altered the cloud characteristics for the outer domain.

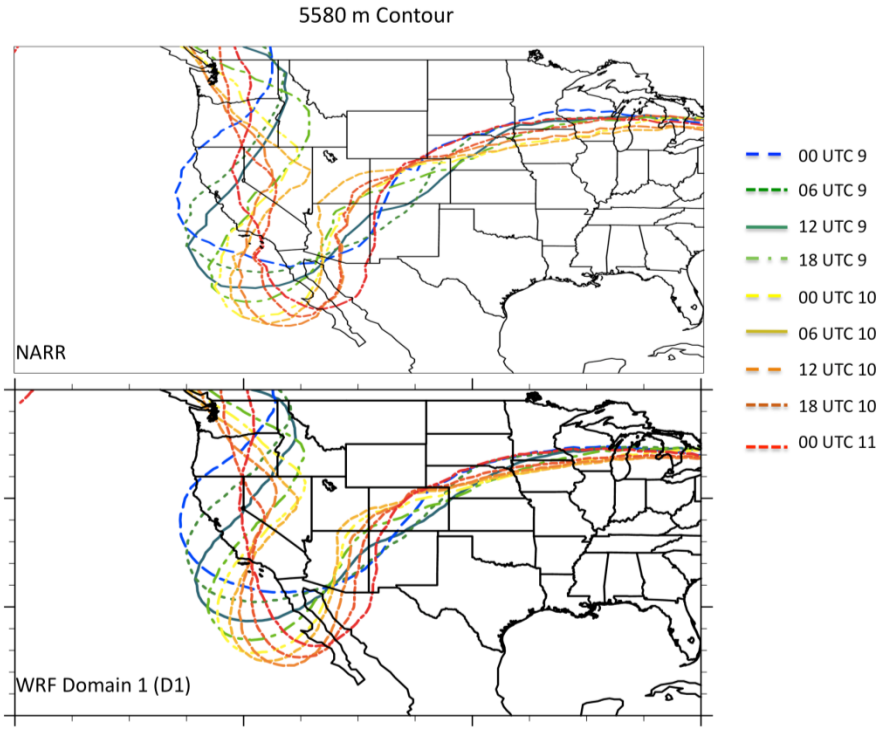

Figure 5.13: Evolution of the geopotential height field, as shown by a representative height contour of 5580 m, for NARR (top) and WRF domain 1 (bottom). Contours are plotted at 6-hour intervals between 00 UTC 9-11 December, with the color key legend on the right.

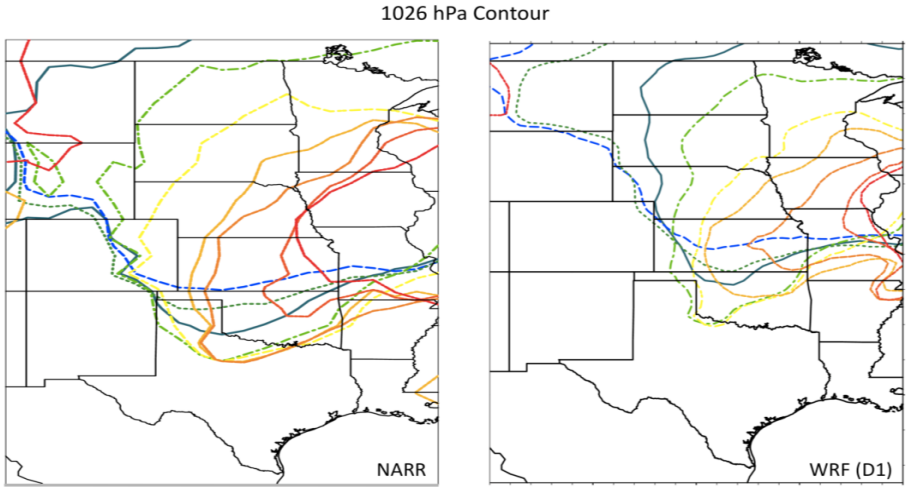

Figure 5.14: As Fig. 5.13 but for the 1026 hPa sea level pressure contour for NARR (left) and WRF domain 1 (right). Color code legend shown in Fig. 5.13.

5.4.4 Cloud properties/radiation

Due to the severity of this event, the ACRF instrumentation for cloud and radiation became iced over and unable to log data (e.g., Hartstock et al. 2008). A more complete assessment of cloud properties is provided in the validation of our second case study, which did have measurements available. Based on comparison of WRF solar radiation with that of available Oklahoma Mesonet for central Oklahoma (not shown), there were similarities in the (smoothed) magnitudes for December 8, and 9, with WRF actually indicating less solar radiation on the 9th. On December 10 WRF underestimated peak insolation, albeit on average generated a similar magnitude across the day. The peak in WRF was also shifted to the afternoon, while the Mesonet placed it in the morning. No longwave components were assessed in this brief comparison.

5.4.5 Summary

Table 5.4 provides a summary of the above information for the December 2007 case study. It was concluded that the simulation was sufficient to be used in the sensitivity analysis. The SST-sensitivity study configuration was provided in chapter 4, with results described in chapter 6.

5.5 Verification of Control Part II: January 2010

The January 2010 case study used the same setup as the December 2007 simulation, but with a larger domain 3 (Fig. 5.2) to better incorporate the mid-level and surface low, and associated precipitation structure. The simulation was initialized at 12 UTC January 23 and run 7 days through 12 UTC January 30, with the winter storm

Table 5.4: Summary table for the simulated December 2007 case study, and its verification against observations. Notable model biases are described for the variables considered.

Parameter	Bias Description – December 2007	Single Site Data?
Air Temperature (SFC)	RMSE ≤ 2.5 K, WRF slight warm bias	No
Air Temperature (upper)	Good agreement in warm layer, WRF warmer refreezing layer	Yes
Mixing Ratio (r)	Good agreement, no specific bias. WRF does not resolve warm layer decrease in r between 00 UTC -12 UTC 10th.	Yes
Winds (u,v)	Good agreement, zonal wind ~3-5 ms^{-1} weaker through troposphere in WRF, no notable meridional wind bias.	Yes
Synoptic GHT	Excellent agreement in timing, depth of GHT	No
Synoptic SLP	Good agreement, WRF lower SLP bias during latter part of event.	No
Cloud	---	Yes
Radiation	---	Yes
Precipitation (spatial)	Domain 1 of WRF not of sufficient resolution to capture elevated convection. D3 is an improvement, but underestimates precipitation accumulation, intensity in the central domain, and 'spreads out' precipitation over the domain- see skill scores.	No
Precipitation (temporal)	Timing of precipitation through D3 is generally well simulated, however some evidence of lack of precipitation in WRF during 00 UTC 10-06 UTC 10 compared to Stage IV radar observations.	No

commencing around 12 UTC January 28.

5.5.1 Precipitation

The same procedure described in Sec. 5.4.1 was used for validating precipitation for this event. Accumulations were 48-hour valid 00 UTC 28-00 UTC 30 January 2010.

At this time, precipitation was not phase-delineated. Neighborhood evaluation skill scores are shown in Table 5.5 for accumulation thresholds between 5 and 60 mm. The higher threshold of 60 mm represents approximately the 90th percentile of the observed precipitation distribution. Based on visual comparison of accumulated precipitation, good agreement was found between the model and Stage IV. At lower thresholds, especially 5 mm, there was virtually no discrimination as the entire domain 3 had non-zero accumulation (min ~ 1 mm), and 90% of the distribution exceed 10 mm. Above 25 mm, the model tended to overestimate precipitation, especially over western/northern Oklahoma and northwest Texas, leading to bias > 1 and lower accuracy (0.62). The 25 mm threshold exhibited a higher hit rate (0.7), but also a reasonable probability of false detection (0.49). Above 40 mm (~75th percentile) positive bias was still evident (1.13), while PODY decreased (0.48), PODN (probability of detection of regions below the threshold) increased (0.79), and POFD decreased (0.21). Above 60 mm the model struggled to place accumulations in the correct locations (lower PODY, higher FAR), but the rare-event nature of this threshold slightly increased GSS and HSS, showing that the model had some (albeit low) skill. Skill at the 90th percentile was better for this event compared with December 2007 (e.g., Table 5.2, 40 mm), due to the model being able to better capture the magnitude of precipitation.

As before, the object-based method was applied to accumulations above the 75th percentile (40 mm here), shown in Fig. 5.15, Table 5.6. It was apparent that the model overestimates the spatial extent of heavy precipitation. The object method improved accuracy (+0.11), whilst increasing PODN (+0.09), HSS (+0.05), GSS (+0.03). However, PODY, POFD, FAR, CSI showed little or no improvement, and the positive

bias worsened (+0.11). The differing shapes of the precipitation regions likely lead to this lack of change in the metrics. Overall the skill scores indicated reasonable simulation, but too much heavy precipitation in different locations with respect to the observed distribution.

Table 5.5: As Table 5.2 but for January 2010 using threshold values that correspond to near minimum (5 mm), median (25 mm), upper quartile (40 mm), and above 90th percentile (60 mm). Values to nearest 5 mm of distribution value.

Skill Metric	Score Threshold: > 5 mm	> 25 mm	> 40 mm	> 60 mm	Perfect Value
Accuracy	0.94	0.62	0.71	0.90	1
Bias	0.95	1.08	1.13	0.91	1
Prob. Detection –Yes (PODY)	0.95	0.70	0.48	0.35	1
Prob. Detection – No (PODN)	0.06	0.51	0.79	0.95	1
Prob. False Detection (POFD)	0.94	0.49	0.21	0.05	0
False Alarm Ratio (FAR)	0.004	0.35	0.57	0.62	0
Critical Success Index (CSI)	0.94	0.51	0.29	0.23	1
Gilbert Skill Score (GSS)	0	0.12	0.15	0.19	1
Heidke Skill Score (HSS)	0	0.21	0.27	0.31	1
Fractions Skill Score (FSS)	0.98	0.71	0.51	0.43	1

Table 5.6: As Table 5.3, but for the Jan 2010 event at an accumulation threshold of 40 mm (see Fig. 5.15 for precipitation objects).

Skill Metric	Score	Perfect Value
Accuracy	0.81	1
Bias	1.24	1
Prob. Detection –Yes	0.48	1
Prob. Detection – No	0.87	1
Prob. False Detection (POFD)	0.13	0
False Alarm Ratio (FAR)	0.61	0
Critical Success Index (CSI)	0.27	1
Gilbert Skill Score (GSS)	0.19	1
Heidke Skill Score (HSS)	0.32	1

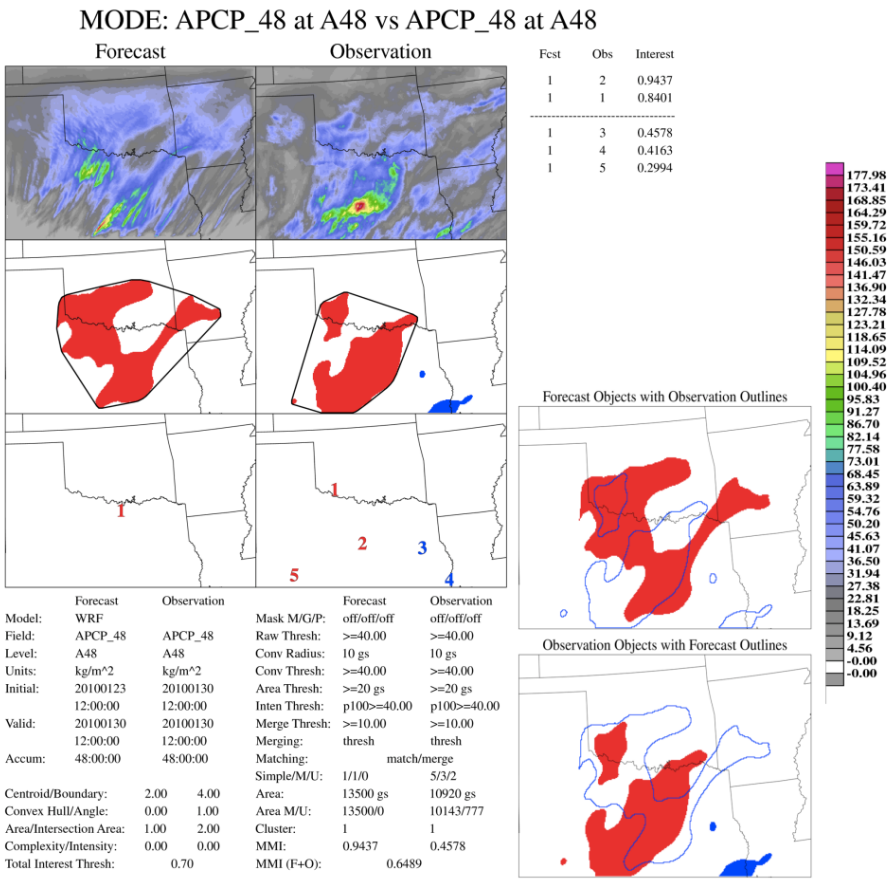

Figure 5.15: As Fig. 5.8 but for the January 2010 event, using 48-hour accumulations ending at 00 UTC January 30, and an accumulation threshold of 40 mm. Blue shaded area indicates a 'missed' object - observed but not simulated.

Temporal precipitation accumulation was examined for four domain 3 quadrants based on 30 gridpoint locations. Figure 5.16 shows the results of this calculation. For all domain 3, the total accumulated was actually slightly less (by ~2.6%) for WRF compared with observations. The northwest domain (33-36N, 100-98W) indicated an overestimate in precipitation on January 28, supported visually, while further south WRF under-predicted relative to Stage IV, especially 00-12 UTC 29. Accumulations in the southwest quadrant (31-33N, 96-92W) were generally in agreement, while the northeast indicated overestimated WRF accumulations later on January 29.

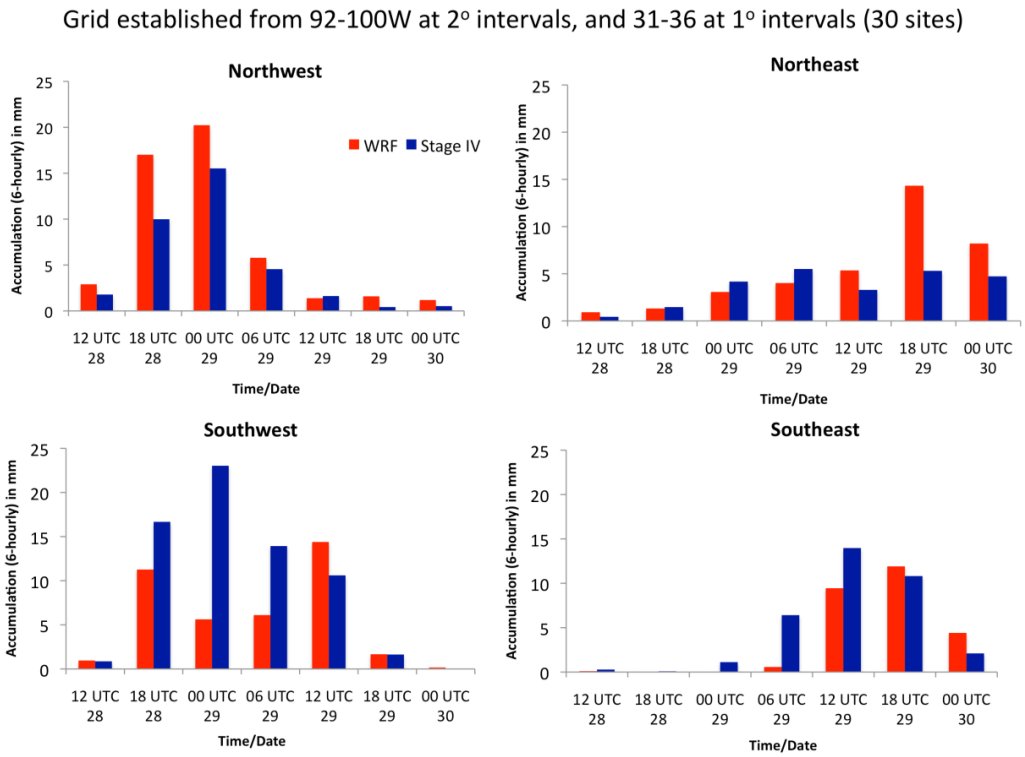

Figure 5.16: In the style of Fig. 5.9 but for four 'quadrants' in domain 3 of the Jan 2010 simulation at 6-hour intervals from 12 UTC 28-00 UTC 30. The extension and number of grid point locations used is described in the header of the plot.. Quadrants are: 'southwest' 31 to 33N, 98 to 100W; 'northwest' 34 to 36N, 98 to 100W; 'southeast' 31 to 33N, 92 to 96W; 'northeast' 34 to 36N, 92 to 96W.

Comparison of domain 1, 2 and 3 are shown in Figure 5.17 for freezing and rain phases of precipitation (for observations, see chapter 4, Fig. 4.17). Unlike December 2007, there was much less difference in total accumulation between the coarse and high-resolution domains. From chapter 4, the synoptic forcing associated with this event was a progressive trough and the development of a weak surface low. Based on quasi-geostrophic (QG) reasoning, ascent is promoted to the east of the trough axis, maximizing in the region of positive cyclonic vorticity advection and temperature advection, coupled with lift promoted by upper level diffluence and divergence. This stronger forcing over the domain promotes widespread precipitation. The mechanisms

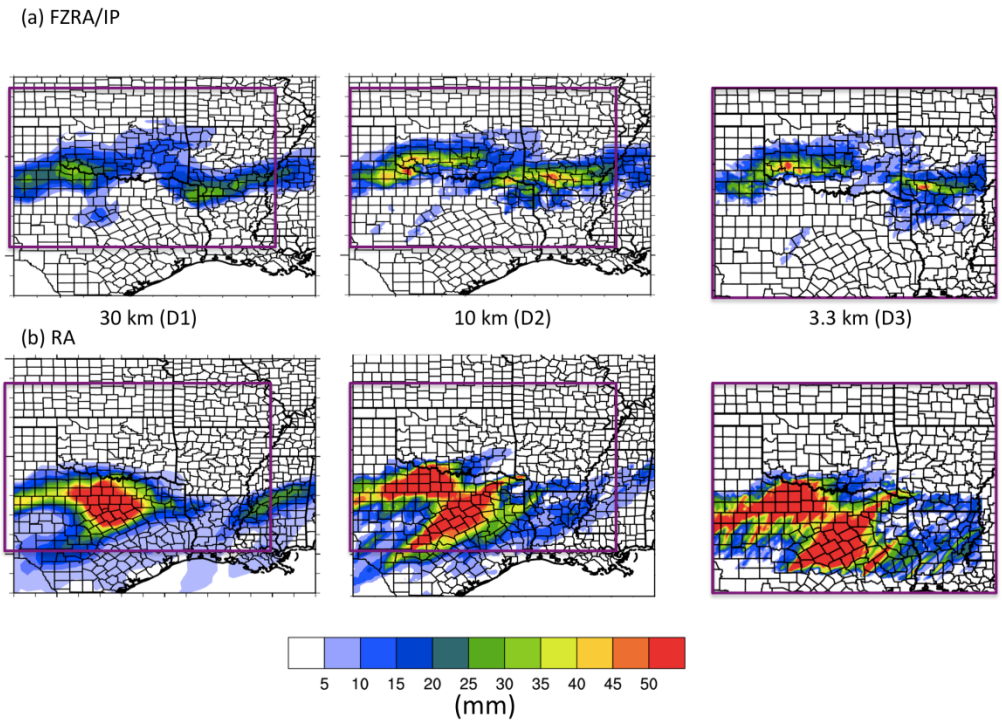

Figure 5.17: As Fig. 5.10 but for 48-hour WRF accumulated precipitation in mm, ending 00 UTC January 30 2010. Top (bottom) three panels display freezing precipitation (rainfall),

for its generation in this case were captured well by the coarser resolution model. Note that simulated freezing precipitation agrees reasonably well with Stage IV (Fig. 4.17), especially for southwestern Oklahoma. Domain 2 actually produced higher freezing precipitation over Arkansas than domain 3, but the latter was in better agreement to observations.

5.5.2 Thermal profile

Figure 5.18 shows surface temperature and RMSE at 6-hour intervals for Oklahoma, based on a WRF to Mesonet surface data comparison. In this case, simulated surface temperatures were typically lower than observed, especially between 00 UTC

and 12 UTC January 28. During the morning hours on the 28 (CST), the WRF temporally had a positive difference near 1^{o}C, but by 00 UTC 29, the model once again yielded a slightly lower temperature. In contrast to the December 2007 event, the initially larger RMSE indicates that the WRF may have overestimated cooling (at least over Oklahoma) from the southward moving arctic airmass, with potential further contributions from cloud cover/radiation (Sec. 5.5.4).

The vertical thermal profile, taken from the ACRF is shown in Figure 5.19. Due to missing data between 18 UTC 28 and 29, only four profiles were available. In general, modeled lower-tropospheric temperature (domain 1-3) agree well with observations, while the initial near surface cold bias in WRF was clearly shown at 00 UTC 28. It should be noted that the ACRF experienced mainly ice pellets and snow, with the deeper warm layer located southwest. By 12 UTC, the WRF now showed a warmer surface layer compared with observations, while aloft just domain 2 and 3 produced a shallow warm layer inversion. This trend was reversed by 18 UTC, with domain 2 and 3 being too cool aloft in the 800-900 hPa layer. By 18 UTC 29, model and observations show better agreement near the surface, while domain 2 and 3 were warmer (cooler) in the 800-900 (800-700) hPa layer than domain 1 and observations.

Mixing ratio profiles, shown in Fig. 5.20, were in good agreement in most cases, with differences typically resulting from the timing and intensity of precipitation at this location. The profile at 12 UTC 28 demonstrates that the model typically overestimated moisture aloft, while 18 UTC 28 shows moister lower levels than observed. None of the domains indicate significant improvement over each other, with their accuracy varying in time.

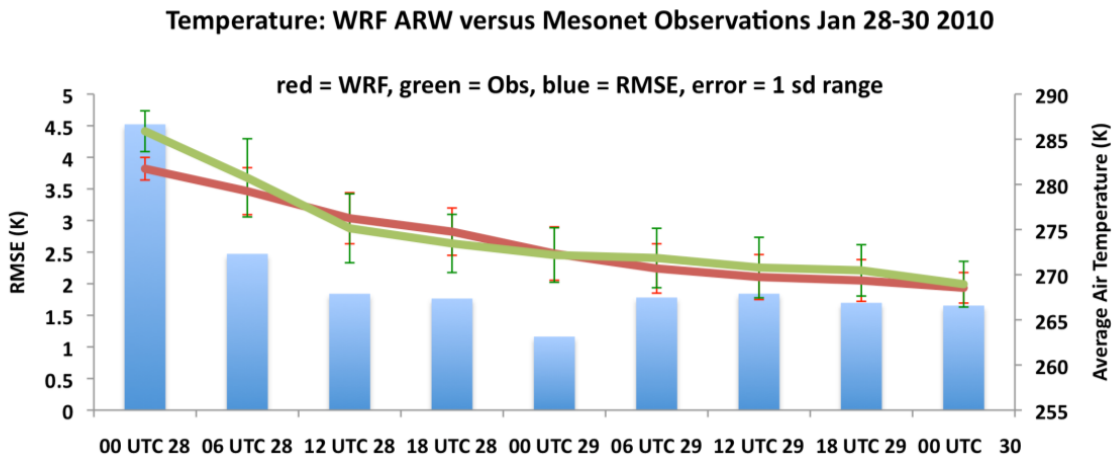

Figure 5.18: 6-hourly time series of surface air temperature (in Kelvin) for WRF (red) versus Mesonet (green), based on 30 grid point locations earlier described (Fig. 5.16), between January 28-30. Error bars denote one standard deviation about the mean temperature for the gridpoints. RMSE shown by the blue bars.

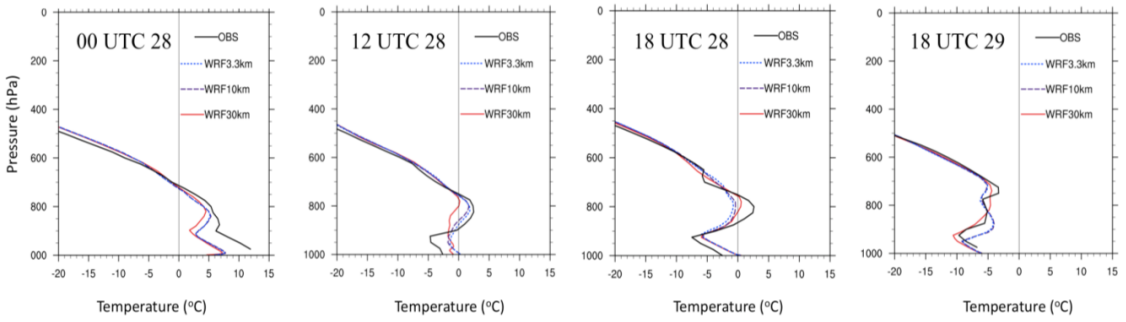

Figure 5.19: As Fig. 5.11 but for the January 2010 case study.

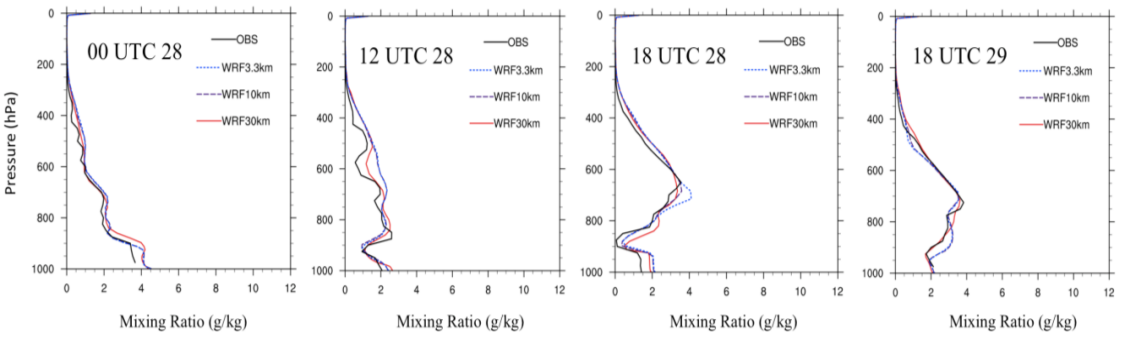

Figure 5.20: As Fig. 5.12 but for the January 2010 case study.

5.5.3 Synoptic evolution

Like the December 2007 case study, the evolution of the upper trough (amplitude, eastward movement) and associated jet circulation were well simulated. Figure 5.21 crudely illustrates this using geopotential height, compared with NARR. ACRF profiles of zonal and meridional wind (not shown) produce generally good agreement. The zonal wind maximum aloft (~60 ms^{-1}) was underestimated in the model, and displaced further aloft. Sea level pressure, based on the 1026 hPa isobar, was similar for NARR and WRF, except the latter does not capture the southwestward extension of higher SLP over the southern high plains (shown in Figure 5.22), and generally underestimated spatial area of higher pressure. In this case, this result was in apparent contrast to the low temperature bias in WRF (that might have indicated a deepening or extension of the shallow surface anticyclone), especially during January 29.

5.5.4 Cloud properties/radiation

Fortunately for this event, in-situ cloud observations were available and derived principally from ACRF CMBE data, as were estimates of shortwave and longwave radiation. Figure 5.23 shows the temporal cloud distribution (time-height profile) over the ACRF based on (a) ACRF cloud fraction observations; (b) cloud fraction from the WRF-ARW; and (c) WRF-ARW total hydrometeor mixing ratios for five species (rain, cloud water, ice, snow, graupel). The best agreement between observations and WRF appear to be when the microphysics representation of cloud presence was employed. The cloud fraction from the model radiation scheme suggests a deeper high cloud layer

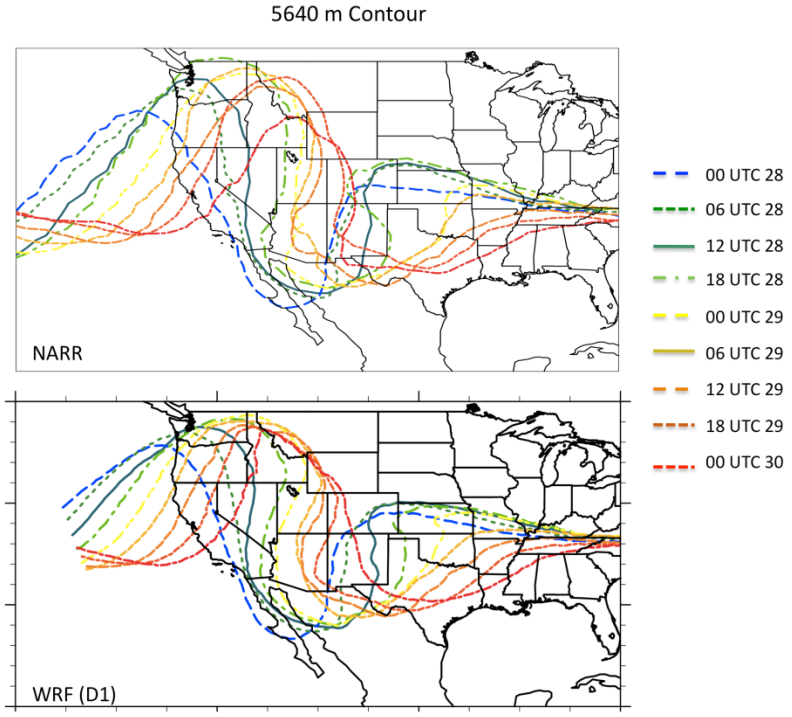

Figure 5.21: As Fig. 5.13 for the January 2010 case study, and displaying the 5640 m geopotential height contour.

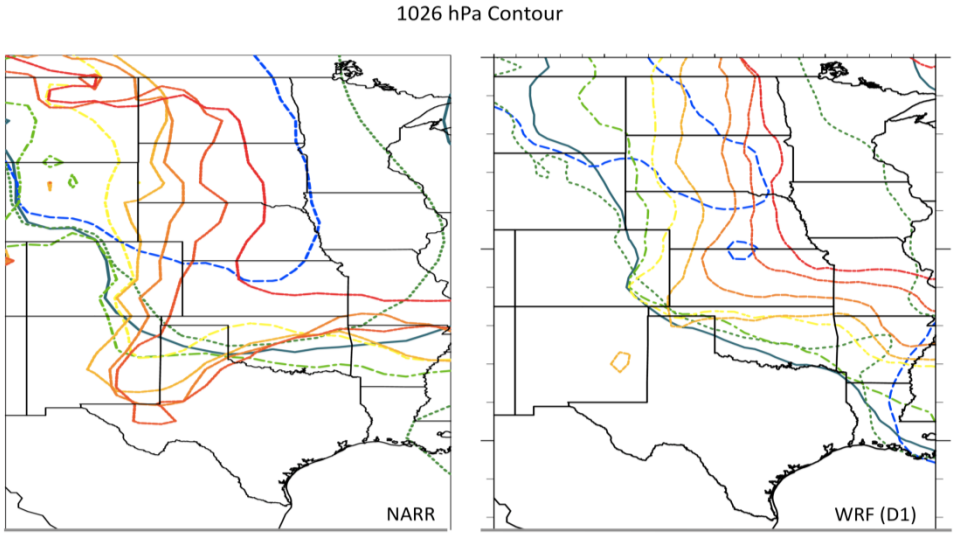

Figure 5.22: As Fig. 5.14 for the January 2010 event. The color legend is shown in Fig. 5.21.

throughout the event, but especially January 28 (0-24 on the x-axis). The vertical extent of the cloud layer at hour 20-25 (~21 UTC 28-03 UTC 29) also was not well represented by WRF cloud fraction, but evident using the model microphysics. The majority of the cloud phase at this time was ice (cloud ice, snow, not shown). It makes sense intuitively that the microphysics presentation of cloud should agree well with observations, as the cloud radar at the ACRF derives cloud fraction from the return of electromagnetic radiation from hydrometeors. The ACRF estimate of cloud would also likely incorporate precipitation due to the high frequency resolution, which leads to increased extinction of the radar beam.

Examination of longwave (LW) and shortwave (SW) radiation components at the ACRF (not shown) suggests that the model underestimates downward SW, indicative of potentially deeper modeled cloud cover. This corresponds to overestimates

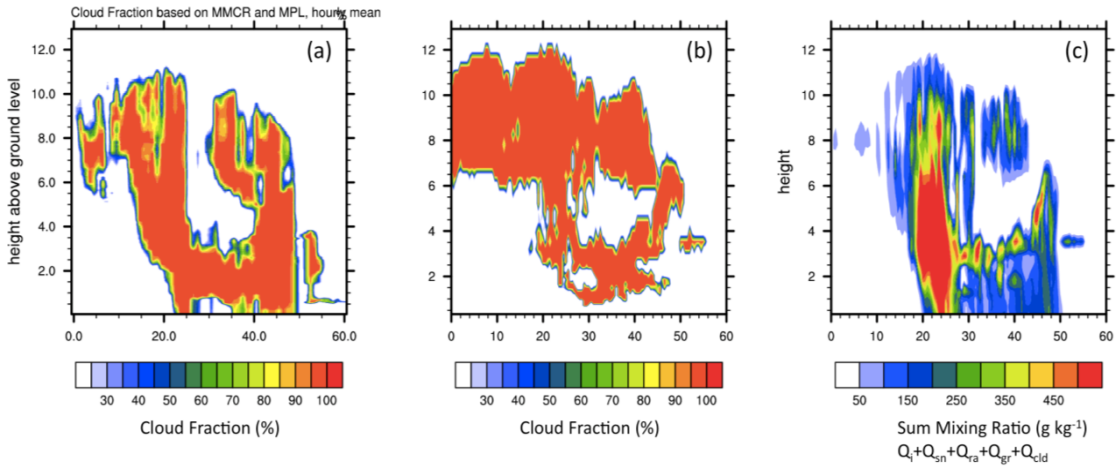

Figure 5.23: (a) Observed ACRF (Lamont, OK) cloud fraction, versus WRF simulated cloud (from the radiation scheme, panel b), and cloud presence as derived from an accumulated hydrometeor mixing ratio (water, ice, snow, graupel, rain) in panel (c). The x-axis for each shows time since 00 UTC January 28 (hours), while the y-axis shows height in km.

of high cloud depth and duration with WRF (radiation scheme) derived cloud fraction. The downward LW component suggested an increase in WRF versus observations, especially in the first 10-15 hours (00 UTC 28-15 UTC 28). This increase compensates somewhat (especially overnight) for the decrease in SW, but was a curious result when compared with the WRF cold bias during this same time, suggesting the cooler surface temperature was not primarily a result of the radiative forcing. The low-level meridional wind component showed higher velocity in WRF relative to ACRF, supporting the possibility of enhanced CAA during this time (not shown). The lower top of atmosphere (TOA) LW in WRF further supported overproduction of high cloud, with WRF and observations only coming into general agreement after hour 30 (06 UTC 29).

5.5.5 Summary

Table 5.7 summarizes the validation results shown here. The January 2010 was generally superior to the December 2007 with regard to the location and intensity of freezing precipitation. The validation suggests that the WRF sufficiently captured the case study evolution to warrant inclusion to the sensitivity analysis.

5.6 Final Note

This chapter has provided a validation of the WRF-ARW control simulations for both case studies against a suite of observations. Several key variables were assessed, and a summary of uncertainties gathered. It is worth noting that sensitivity studies by their nature consider the secular changes from a control, and as such the control's departure from the actual event is of secondary importance in subsequent chapters.

However, the reader may wish to refer back to this chapter, or at least bear in mind WRF biases relative to the observed events. As a summary to this chapter, Tables 5.8 show model specifications of the simulations examined in chapters 6 and 7.

Table 5.7: As Table 5.4, for the January 2010 case study.

Parameter	Bias Description – January 2010	Single point ob?
Air Temperature (SFC)	RMSE ≤ 2.5 K, WRF slight cool bias, especially between 00 UC-12 UTC 28, and after 00 UTC 29.	No
Air Temperature (upper)	Some missing data 00-18 UTC 29th. Location of sounding used in predominantly snowfall region. WRF cooler within the 900-800 hPa layer, especially at 18 UTC 28.	Yes
Mixing Ratio	Good agreement, WRF slightly moister on average.	Yes
Winds (u,v)	Generally good agreement, WRF underestimates peak zonal winds in mid-upper troposphere, no secular bias in meridional winds.	Yes
Synoptic GHT	Excellent agreement in timing, depth.	No
Synoptic SLP	Good agreement, WRF lower SLP bias during latter part of event.	No
Cloud	WRF CLDFRA overestimates high cloud and cloud layer depth. WRF hydrometeor assumption better resolves the temporal 'shape' of the cloud. Microbase IWC/LWC metrics do not agree well with WRF, with a large overestimate in IWC for the latter.	Yes
Radiation	Lower downwelling SW (possibly due to cloud cover bias), and lower upwelling LW at TOA through much of the event.	Yes
Precipitation (spatial)	Shape and intensity of precipitation (+ accumulation) generally well simulated (esp. D2 and D3). Northward shift in heaviest precipitation (rain) in WRF. Slight positive bias in above 40 mm. Freezing precipitation location and intensity well simulated, esp. Oklahoma, albeit underestimated total coverage, especially east. Snowfall locations well simulated, intensities spatially very relative to observations, e.g., decreased in east relative to obs.	No
Precipitation (temporal)	SW region shows underestimates 00-12 UTC 29th, also slight overestimate in precipitation during 29th in NE region of domain 3.	No

Table 5.8: Basic model setup for December 2007 (Case 1) and January 2010 (Case 2) sensitivity analysis

Simulation	Description
Start/Length	**Case 1**: 00 UTC December 4 2007/7 days **Case 2**: 12 UTC January 23 2010/7 days
Temporal Resolution	3 hr (D1), 2 hr (D2), 0.5 hr (D3)
Domain/Resolution	See Fig. 5.2 **Case 1**: 162x141 30 km (D1), 172x223 10 km (D2), 172x223 3.3 km (D3) **Case 2**: 162x141 30 km (D1), 172x223 10 km (D2), 322x223 3.3 km (D3)
Num. Vertical Levels	59 (D1-3)
Convection	BMJ (D1, D2) Explicit (D3)
Microphysics	MY (D1-3)
PBL	MYJ (D1-3)
Radiation	RRTM (Longwave, D1-3), Dudhia (Shortwave, D1-3)
Land Surface	NOAH (D1-3)
IP/BC	GFS Final Analysis 1^{o}, 6-hourly
Analysis Nudging?	Yes (D1), No (D2, D3)
SST	See Table 4.2 for descriptions. 0.5^{o}x0.5^{o}, daily updates, RTG (CLIM, P2, M2, REAL), OI V2 (LO, HI, GOM only). Part of IP/BC for D1.

Chapter 6: SST Sensitivity Study for the December 9-11 2007 Ice Storm

6.1 Introduction

In this chapter, the results from a suite of SST perturbations described in chapter 4 (sec. 4.4) and applied to a set of high-resolution WRF simulations, described in chapter 5, are summarized in detail for the first of our two case studies. The evolution of this event was previously described in chapter 4. With respect to the patterns obtained in chapter 3, this is an *Ice Pattern 3* case study, considered to be the 'archetypal' ice storm circulation for the central SGP due to notable moisture and temperature anomalies south of the subfreezing surface airmass, implicated in the formation of pronounced warm layers.

Unusually, the primary precipitation mode was convective, with training convection parallel to the upper level jet axis, just north of the 0^{o}C surface isotherm. The WRF simulation (domain 3, chapter 5) partially captured this orientation, but with greatly reduced intensity, while other locations had more precipitation than observations suggested (e.g., southeastern OK/AR, and much of west-central Oklahoma). This 'flattening' of the precipitation distribution was suspected to be due to misplacement of the convective cells along with some mode discrepancies (lack of convective-statiform transition and decreased spatial coverage/intensity). Nonetheless, the model captured the timing (especially nocturnally), cellular mode and phase of precipitation. There was strong dependence of precipitation accumulation and location on model horizontal grid spacing, likely due to a coarser resolution grid being unable to resolve the most unstable growth modes associated with upright elevated convective instability. Given that the

precipitation intensity was not particularly in agreement to the observed event, we express changes associated with SST relative to the REAL simulation. Readers may refer back to chapter 5 to interpret the results in light of known model bias and uncertainty for this event.

The variables analyzed in this chapter include: precipitation accumulation and intensity, thermal profile (warm and refreezing layers), synoptic and mesoscale features, such as fronts, forcing for ascent, locations and magnitude of low-level winds and moisture transport, and cloud and radiation. Finally we examine air parcel trajectories into the freezing precipitation region at two times during the ice storm. This lagrangian perspective on airflow is expected to aid interpretation of linkages between GOM SST and warm layer thermal/moisture profiles.

6.2 Precipitation Accumulation and Phase Partitioning

6.2.1 Total accumulation

Figure 6.1 and 6.2 display 48-hour accumulated precipitation for each SST simulation, valid 00 UTC 9 - 00 UTC 11 December, for freezing precipitation and rainfall respectively. Negligible snowfall accumulated over domain 3. In this evaluation, we used the Bourgouin (2000) area method to extract precipitation phase type for freezing precipitation. For rain and snow, a simple calculation was applied based on the average 900-700 hPa temperature, 850 hPa temperature, and surface phase type derived from hydrometeor mixing ratio. Rain was assumed with a non-zero rainwater mixing ratio, and surface temperature above 0^{o}C. Snow was assumed with 900-700hPa layer average and 850 hPa temperatures < 0^{o}C and snow mixing ratio >

0gkg^{-1} at the surface. The Bourgouin (2000) technique for identifying freezing precipitation is given in equation 6.1:

$$c_p|Area| = c_p\overline{T}\ln\left(\frac{\theta_{top}}{\theta_{bottom}}\right) \tag{6.1}$$

Where *Area* can refer to the refreezing or warm layer, $\overline{T}$ is the average temperature of the desired layer, c_p the specific heat capacity (fixed at 1004 Jkg^{-1}), and θ_{top}, θ_{bottom} the potential temperature at the top and bottom of the desired layer respectively. When *Area* is computed for the warm layer (refreezing layer), it is termed the positive area (negative area). The evaluation of the presence of ice pellets and freezing rain was determined by Bourgouin empirically, and expressed as:

$$\begin{aligned} &IP = if\,(NA > 0.66 + 0.66PA) \\ &FZRA = if\,(NA < 46 + 0.66PA) \\ &IP\ \&\ FZRA = if\,(46 + 0.66 \le NA \le 66 + 0.66PA) \end{aligned} \tag{6.2}$$

Where PA and NA refer to positive and negative areas respectively. Both equation 6.1 and 6.2 were calculated for all model gridpoints experiencing precipitation at 1-hour intervals. No distinction was made between ice pellets and freezing rain as determined from the algorithm in subsequent figures for this chapter. However, the algorithm determined the dominant precipitation type as freezing rain due to the substantial warm layer. For example, REAL produced 90% FZRA, 1.5% IP/FZRA and 8% IP. These proportions only changed by a fraction of a percent between P2 and M2 (not shown).

The results for freezing precipitation in Fig. 6.1 indicate that the band of precipitation along the central axis generally intensified with warmer SST, but with some variation in location, potentially from changes to location/movement and intensity of cellular convection. For M2 the reduction was visually pronounced, with a northward

shift in higher accumulations. Precipitation was also weakened in LO (REAL-1.69 K), especially over northeastern Oklahoma and southern Missouri. CLIM also lowered peak totals. For the warmer SST fields, HI (REAL+0.19 K), suggested a shift in the location of convection increasing accumulations in the northeast and southwest. P2 showed less spatial spread in higher precipitation (e.g., 20+ mm), while yielding greatest amounts in the southern branch of the central axis. There was no apparent shift in locations of freezing precipitation versus rainfall due to the depth of the warm layer (typically > 2 km), its intensity (> 8^{o}C), and its persistence.

For rainfall, shown in Fig. 6.2, there was a general indication of increased precipitation in Arkansas as basin average SST rose. Nonetheless, this was not a linear result. LO for example, produced a band of heavy precipitation over west central Arkansas of reduced spatial extent with respect to CLIM, REAL and HI, but similar intensity. The differences between the two extreme uniform perturbations, M2 and P2, yielded strongest evidence of a trend, which was expected as they were uniformly perturbed about REAL, whereas the other SST fields have alternate gradients and anomalies.

Additional quantitative information is summarized for domain 3 in Table 6.1, which, for each SST simulation, calculates the number of grid points experiencing a precipitation phase (48-hour accumulated), and the total summed accumulations above a given precipitation rate. Here, we used the 75th percentile of the precipitation distribution (by phase, and removing all zero values) as a base for assessing higher accumulations. These metrics provide a measure of spatial extent of phase types, and trends in their relative intensities. At the base of the table, results are expressed relative

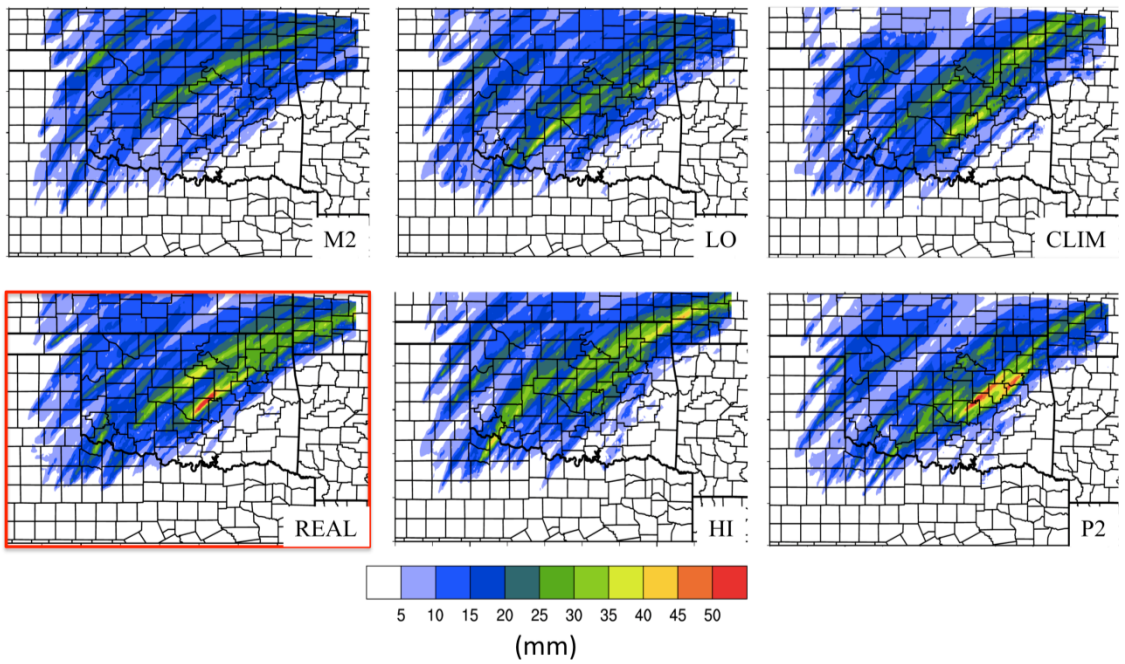

Figure 6.1: 48-hour accumulated freezing precipitation (FZRA, IP), valid 00 UTC December 11 2007 for WRF-ARW domain 3 for each SST simulation, denoted by the textbox. REAL is highlighted by the red box. State and county boundaries are overlaid.

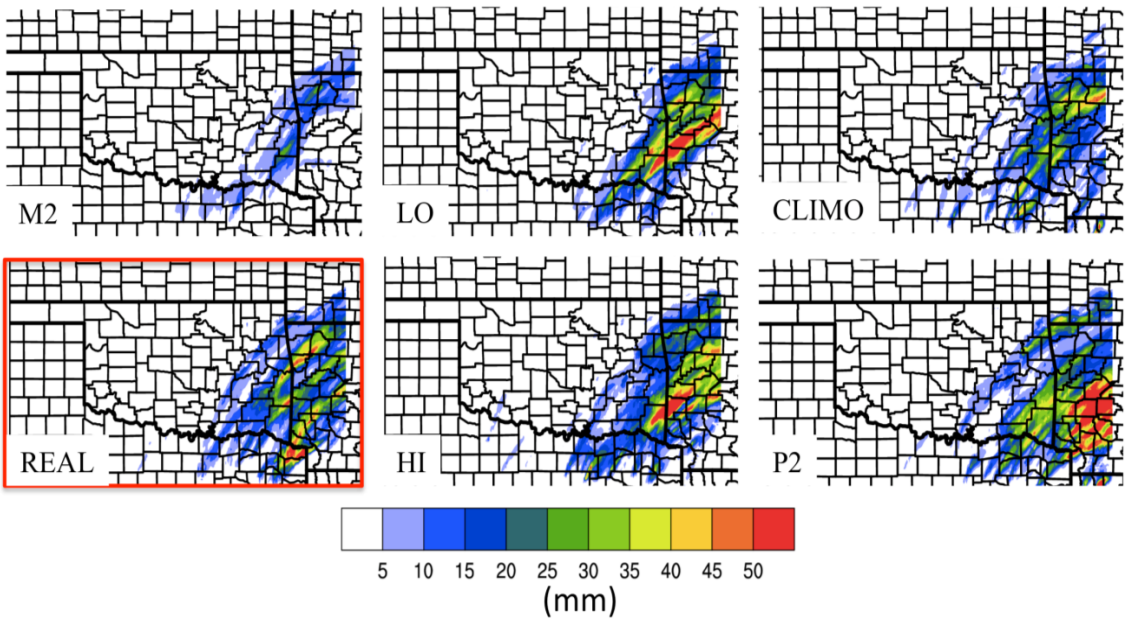

Figure 6.2: As Figure 6.1 for rainfall, with reduced southward edge of domain.

to REAL for all precipitation types ('Total') and FZRA/IP in parenthesis (Fig. 6.1).

The table quantitatively confirms earlier assertions. For example, the spatial extent (number of grid points) of non-zero precipitation changed little relative to REAL for each simulation (typically within 3%). However above the 75th percentile (~15 mm for ice, 20 mm for all phase) notable changes included increased spatial extent for all precipitation in HI and P2 (~+7-8%), while FZRA/IP above this threshold spatially contracted for all but HI (e.g., P2 -9.5%, CLIM -5%, LO -16% and M2 -30%). This contraction may relate to the more concentrated region of higher precipitation observed for P2, but conversely the weakening of precipitation in LO and M2. Due to fine-scale localized nature of the convective mode, percentage changes in total summer FZRA/IP accumulation were typically low, especially for warmer SST. For example, P2 actually decreased in accumulation by 7% and ~-3% at moderate or greater intensity (≥2.5 mmhr^{-1}, likely due to the aforementioned spatial contraction), HI indicated virtually no change at all thresholds, but a modest ~2.4% increase above 2.5 mm hr^{-1}. The larger percentage change for this phase occurred as SST was reduced. M2 (LO) produced an 8.5% (7.7%) decrease for all non-zero precipitation rates, and a 24% (15.3%) decrease above 2.5 mm hr^{-1}. For all-phase precipitation rates percentage changes were more notable, especially for M2, produced by the strong reduction in rainfall over Arkansas (~48% decrease above 2.5 mm hr^{-1}). Negative departures for CLIM and LO were more modest, with CLIM producing a larger decrease in moderate rainfall rates. P2 showed a ~31% increase, primarily in the rainfall region.

For all domain 3 (Fig. 6.3), radar reflectivity showed monotonic yet non-linear

Table 6.1: Precipitation characteristics and their change with SST, evaluated for freezing rain/ice pellets, snow and rain. For each, the total number of gridpoints with precipitation (and total number of total accumulation above the 75th percentile of non-zero values; ice=15 mm, all phase=20 mm), the total summed accumulation, and total summed accumulation for precipitation > 2.5 mmhr^{-1} are estimated. Furthermore, the ratio of these summed accumulations are shown to provide intensity proportion. At the base of the table, these results are expressed as a percentage difference from REAL for the total domain, and FZRA/IP in parenthesis.

Type	# Grid Points (# > 75th percentile Accum.)	Total Sum of hourly Accum. (1) x10^4 mm	Total sum Accum. > 2.5 mm hr^{-1} (2) x10^4	Ratio (2)/(1)
REAL	**Domain 3**			
FZRA/IP	28650 (7182)	32.6	12.1	0.37
RAIN	26510 (6343)	17.7	7.1	0.40
SNOW	21 (0)	0.0076	0	0
CLIM				
FZRA/IP	28110 (6806)	31.5	11.3	0.36
RAIN	26759 (5319)	15.7	4.5	0.28
SNOW	15 (0)	0.005	0	0
P2				
FZRA/IP	28860 (6499)	30.2	11.8	0.39
RAIN	26453 (7209)	24.0	13.5	0.56
SNOW	0 (0)	0	0	0
M2				
FZRA/IP	27884 (5036)	29.8	9.2	0.31
RAIN	27339 (1490)	7.4	0.75	0.10
SNOW	0 (0)	0	0	0
HI				
FZRA/IP	28532 (7336)	32.6	12.4	0.38
RAIN	26513 (7326)	20.2	8.8	0.44
SNOW	0 (0)	0	0	0
LO				
FZRA/IP	28336 (6204)	30.1	10.3	0.34
RAIN	26716 (5009)	17.1	6.8	0.40
SNOW	2 (0)	5.5x10^{-3}	0	0
Total (IP/FZRA)	**Departure from REAL (%)**			
CLIM	-0.54 (-1.89) *-19.23 (-5.24)*	-6.07 (-3.21)	-18.0 (-6.67)	
P2	+0.24 (+0.73) *+8.35 (-9.51)*	+8.00 (-7.13)	+31.75 (-2.61)	
M2	+0.08 (-2.67) *-58.34 (-29.88)*	-26.0 (-8.49)	-48.34 (-24.15)	
HI	-0.25 (-0.45) *+7.11 (+2.14)*	+5.1 (+0.06)	+10.27 (+2.35)	
LO	-0.23 (-1.10) *-16.93 (-15.76)*	-6.10 (-7.66)	-11.07 (-15.30)	

(in proportion to basin average SST, see chapter 4) increase in reflectivity with SST. Once again, a stronger response occurred for strongly negative SSTA, with a 33.9% decrease > 35 dbZ for M2, versus a 9.1% increase for P2. For the freezing precipitation region in Fig. 6.4, HI now produced the greatest positive change in reflectivity (+12%), albeit the precipitation accumulation response was more moderated (Table 6.1). M2 had the greatest decrease at -19.7%.

What is the physical basis for the apparent increased sensitivity to reduced SST (especially M2)? It is suspected that the atmospheric stability profile was particularly important. Figure 6.5 shows maximum layer convective available potential energy (CAPE) during initiation of the first round of precipitation, valid 06 UTC (00 CST) December 9. The 850 hPa CAPE is also overlaid (black contours) in order to demonstrate that instability was elevated to the approximate level of maximum warm layer temperature for the freezing precipitation zone. It is readily apparent that CAPE was strongly related to the SST scenario, likely due to the impact on lower tropospheric moisture content. For warmer cases, CAPE increased over the freezing precipitation zone, consistent with the increase in the intensity of the convective cells (e.g., Fig. 6.3, 6.4). Convection also initiated somewhat earlier, especially for P2 (not shown).

Figure 6.6 displays the thermal profile as a model derived sounding at Norman, OK 09 UTC December 9, when freezing precipitation was developing in M2, LO, and REAL. Whereas REAL shows a deep warm layer bounded by convective instability aloft, LO and M2 indicate cooling near 875 hPa, with a more pronounced secondary maximum further aloft in the vicinity of 700-750 hPa. It is suspected that the reduction in temperature in the 800-875 hPa layer was associated with decreased GOM SST and

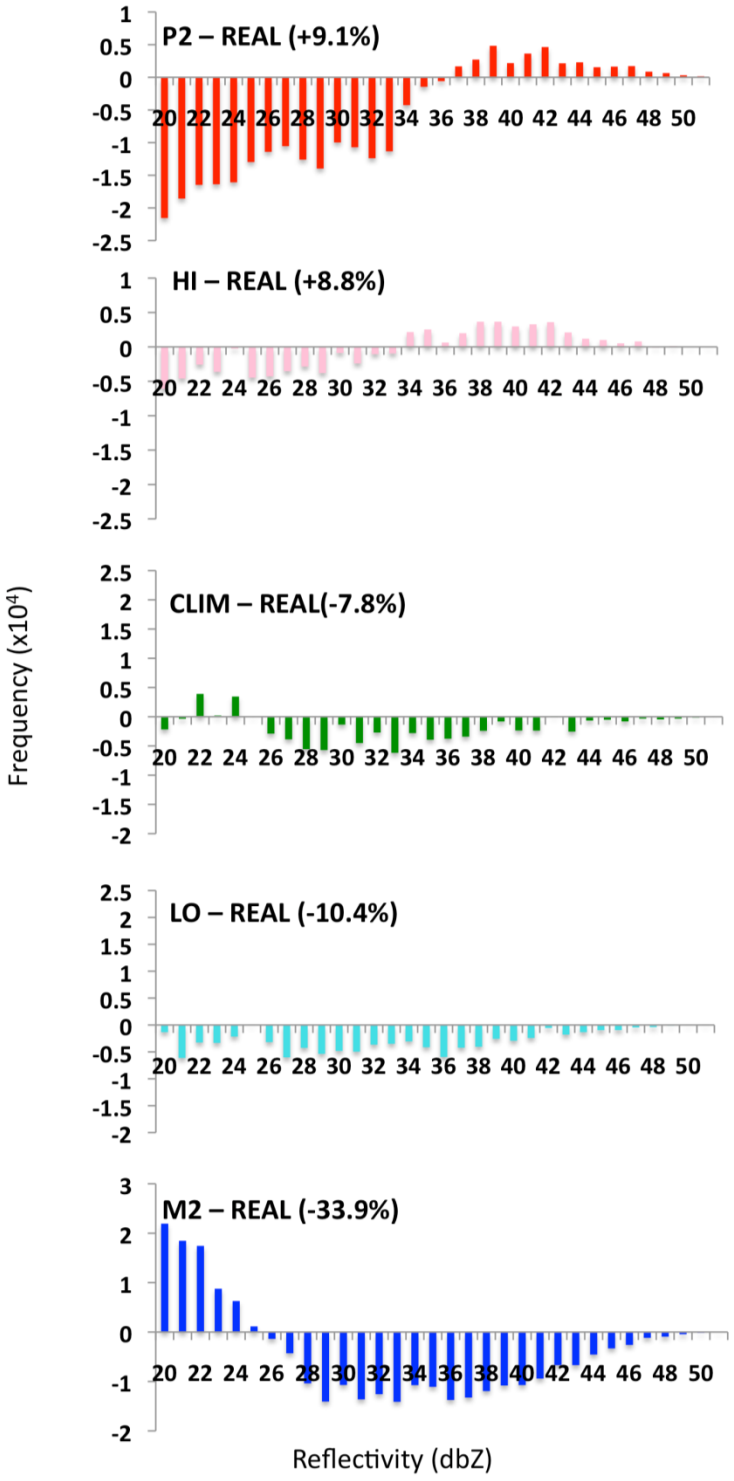

Figure 6.3: Simulated equivalent radar reflectivity histograms (> 20 dbZ) showing the change in frequency for each SST scenario with respect to REAL for all domain 3. The percentage value in parenthesis denotes the relative change in frequencies > 35 dbZ

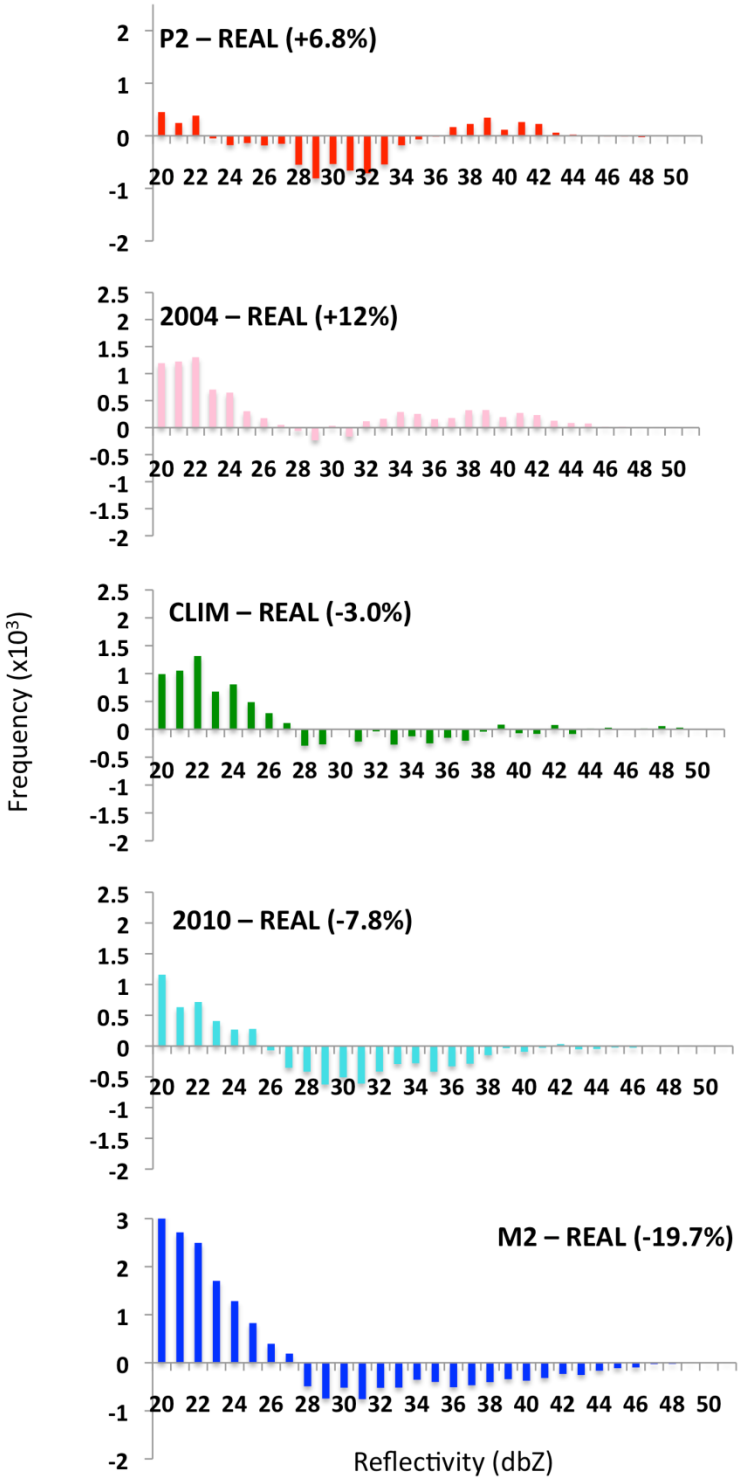

Figure 6.4: As Figure 6.3, but for central Oklahoma (approximately 34.5-35.5N, 96-98W).

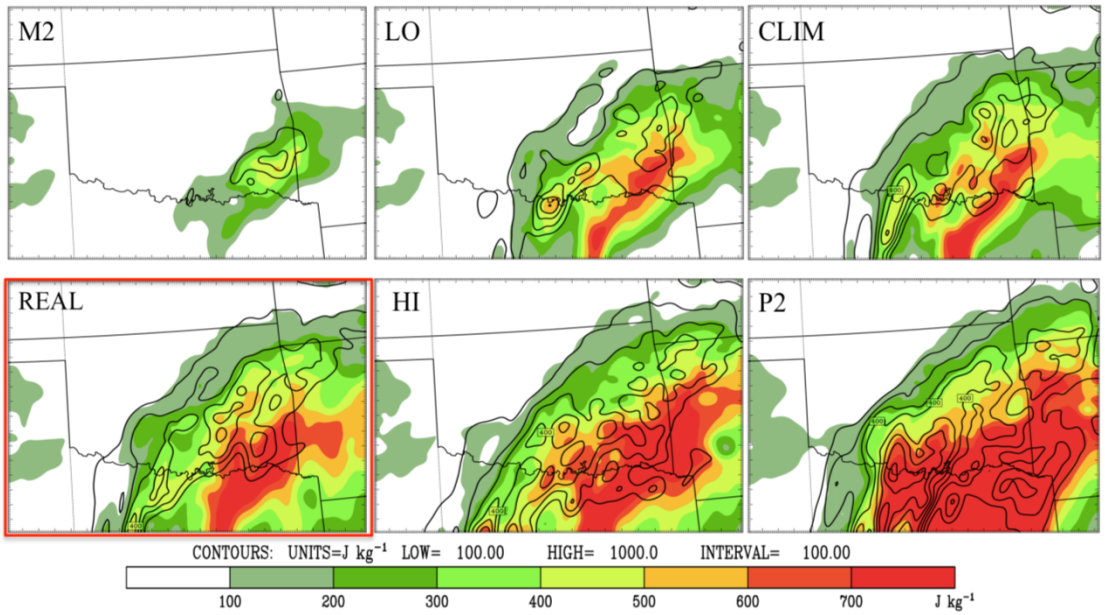

Figure 6.5: Maximum layer CAPE (shaded in increments of 100 Jkg^{-1}), and 850 hPa CAPE (contoured, every 100 Jkg^{-1}, from 100 Jkg^{-1}) for domain 3 of each SST simulation, valid at 06 UTC December 09 as convection was beginning to initiate. REAL is highlighted by the red box.

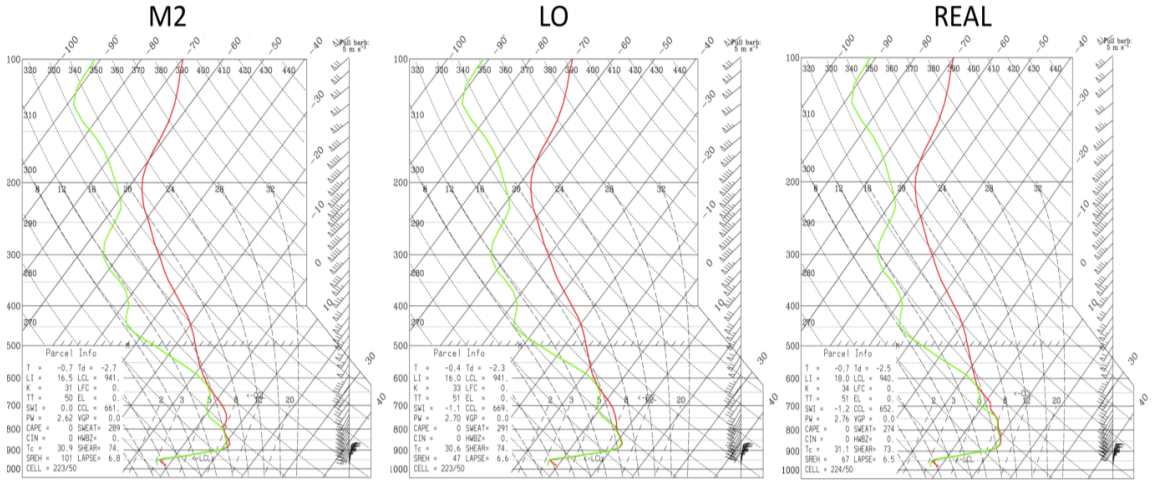

Figure 6.6: Thermodynamic (skew-T) profile valid at 09 UTC December 9 near Norman, Oklahoma for M2, LO and REAL.

the advection of this cooler airmass into the freezing precipitation zone. The origins of the airmass ~700 hpa is investigated in section 6.5. Assuming that an air parcel was lifted to 850 hPa in M2 and LO, the isothermal layer further aloft would have increased stability by acting against the vertical motion of the buoyant air parcel. Figure 6.7 displays simulated radar reflectivity over the domain at 09 UTC December 9, indicating that for this example M2 produced only weak updrafts and light precipitation, while LO indicated isolated regions of stronger convection but a general decrease in spatial extent relative to the remaining simulations.

6.3 Thermal Profile

The evolution of the lower tropospheric thermal profile is particularly important for freezing precipitation, as warm layer characteristics influence phase partitioning (chapter 2). In this case study, the low-levels were particularly deep and warm, forming well prior to the ice storm (chapter 4). The simulated evolution of the melting and refreezing layers across simulations was investigated by calculating the Environmental Melting and Refreezing potentials, EMP and EFP respectively (see chapter 2, equation 2.1,2.2) over central Oklahoma 00 UTC 9-00 UTC 11 December, shown in Figure 6.8. The 850 hPa (surface) air temperature is provided in Fig. 6.9.

Both figures confirm warm layer intensity, and indicate that the SST perturbations exert a relatively minor influence on its thermal properties. Warm layer formation was insensitive to the SST field, at least over the preceding several days, appearing to be more a consequence of anomalously warm surface temperatures over southern Texas/northern Mexico, and prolonged southerly-component flow over the

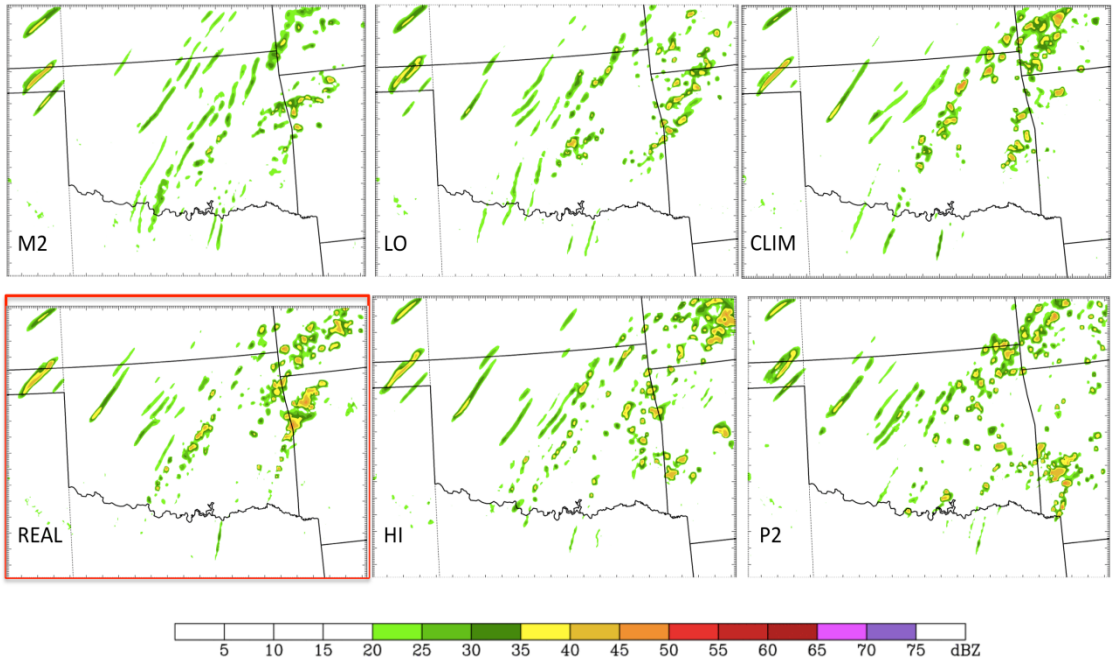

Figure 6.7: Simulated radar reflectivity (dbZ) valid 09 UTC 9 December for each SST simulation. REAL highlighted by the red box.

southern and eastern U.S. Nonetheless, varying SST still promoted some alteration of peak warm layer intensity. Compared to REAL, the initial cooling of the M2 850 hPa layer before precipitation onset maximized at 1.5-2°C near t20, and near 1°C or less for LO and CLIM (Fig. 6.9). HI and P2 produced a warmer inversion on the order of 0.5-1°C at the same time. The resultant changes in EMP (Fig. 6.8) reflect these temperature variations and show on average 1000-2000 °Cm reduction for M2, little distinction between CLIM and REAL, and increased temporal persistence of higher EMP near 18,000 °Cm for HI and especially P2 during t12-t24. During convection (~t24 onwards), cooling due to melting and downdraft evaporation results in small decreases in EMP/temperature, but the warm layer intensity precluded phase change. The broader lowering of EMP t20 to t40 may be a combination of precipitation and dynamic changes

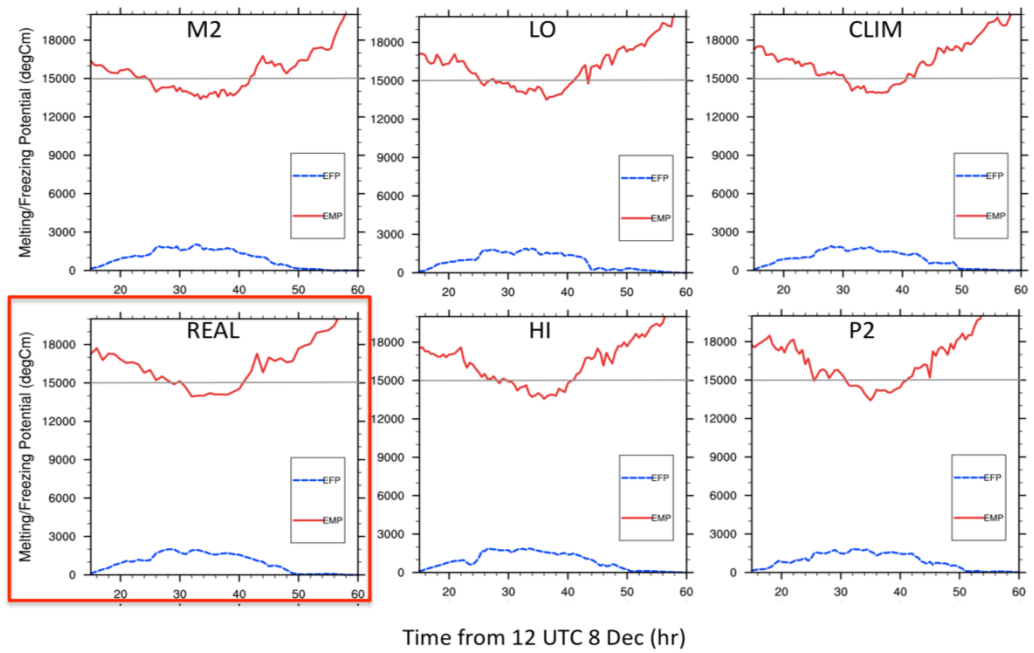

Figure 6.8: Timeseries of environmental melting potential (EMP, red), and freezing potential (EFP, blue) in ^{o}Cm valid for 34.9-35.3 ^{o}N, and 97-98^{o}W between 00 UTC December 9 (t12) and 00 UTC December 11 (t60). Horizontal gray line at 15,000 ^{o}Cm to aid interpretation.

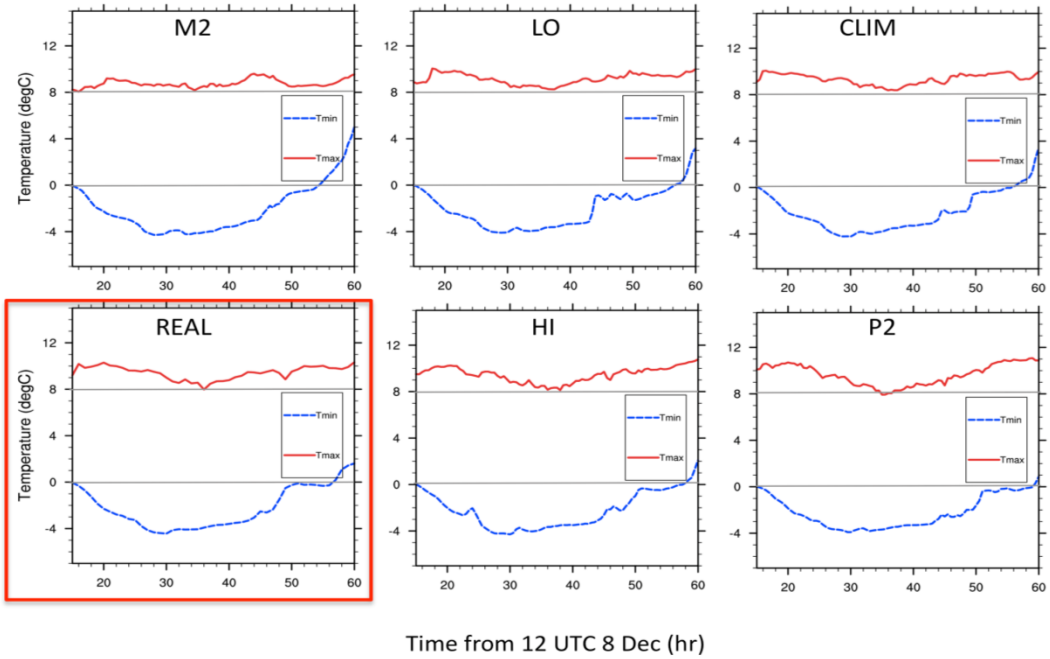

Figure 6.9: As Fig. 6.8 for maximum warm layer air temperature (red) and minimum refreezing layer temperature (blue). Horizontal gray lines at 0 and 8^{o}C shown to aid interpretation. .

(e.g., reduction in warm air advection, possible sensible and radiative heat transfers. More investigation required). The refreezing layer surface temperature showed negligible change between simulations, however, the refreezing layer actually eroded more rapidly (by about 3 hours) for M2, LO relative to REAL, being retained for a slightly longer period of time for HI and P2 (~2-4 hours).

A transition to above freezing temperatures in central Oklahoma occurred late on December 10 as the upper trough approached the domain, eroding the surface refreezing layer by associated pressure falls, decrease in cold air advection and southerly component near-surface flow. Nonetheless, there was an apparent additional contribution from radiative forcing and cloud cover that explained the timing changes in each case. Figure 6.10 and 6.11 show downward shortwave component, and longwave radiation components respectively. For central Oklahoma (left), downward SW radiation was increased on December 10 for LO and M2, while outgoing LW was increased hours 40 and 50, particularly for M2. These results imply lower cloud cover shortly before the time surface temperatures rose above 0^{o}C. While the domain average shortwave on December 10 was virtually indistinguishable for each scenario, the longwave components implied that lower SST simulations had reduced or thinner cloud cover.

Figure 6.12 shows cloud cover in central Oklahoma, derived from a summation of all hydrometeor mixing ratios. It is apparent that convective activity in this region was reduced in M2 and LO, especially on December 9 (t12-36). Furthermore, during the same time, the summed mixing ratios indicate a more persistent low cloud layer. This is supported to some extent by a decrease in downward shortwave radiation for M2 and

LO (on average). Convection was apparent in the other scenarios, with a deep cloud layer near t40-45 (it appears that for HI, this convection was displaced westwards, not shown). This very deep precipitating cloud layer is likely responsible for reduced solar insolation and the maintenance of a shallow refreezing layer that was not observed for M2, as heavier precipitation for M2 had lifted north to an axis through north-central Oklahoma (Fig. 6.1).

6.4 Moisture and Dynamics

In this section, the identified changes in precipitation response to SST are examined in light of the synoptic and mesoscale evolution of the event in each of these perturbed simulations. Given that the evolution of this ice storm (chapter 4) was associated with two primary episodes of precipitation (Fig. 4.11), this discussion considers both in turn.

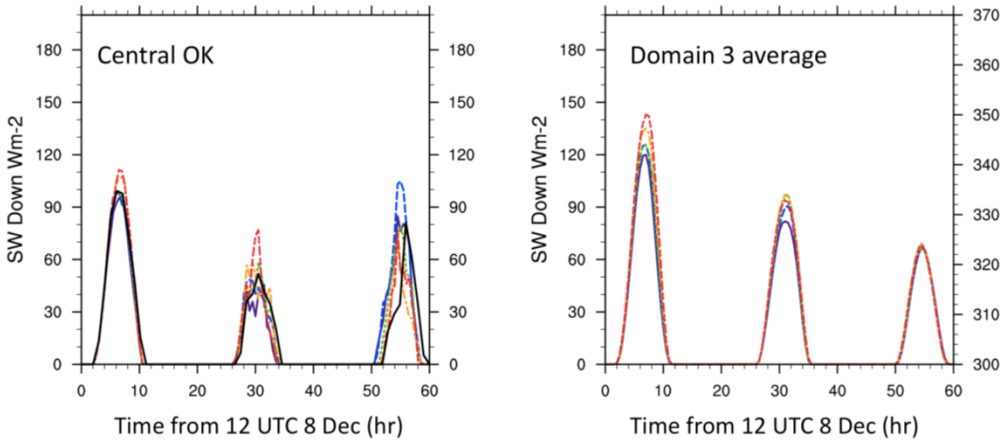

Figure 6.10: Timeseries of WRF downward shortwave (solar) radiation flux calculated over central Oklahoma (left), and all domain 3 (right) in Wm^{-2}. Line color designations are: red = P2, orange = HI, black = REAL, green = CLIM, blue = LO, purple = M2.

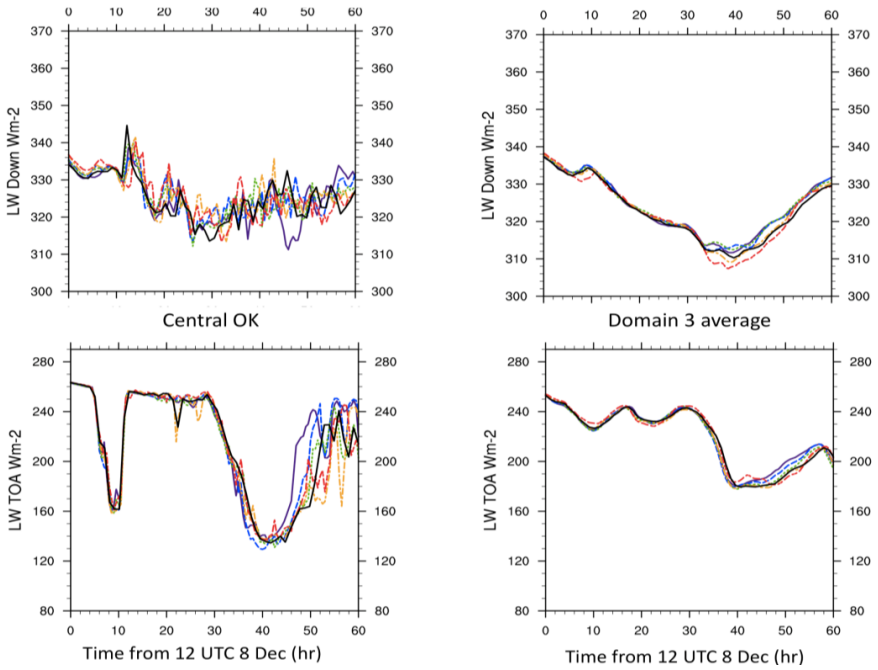

Figure 6.11: Timeseries of WRF longwave radiation components for each SST simulation. Top is downward flux for (left) central Oklahoma and (right) domain, while bottom is the top of atmosphere outgoing longwave flux. See Fig. 6.10 caption for line color key.

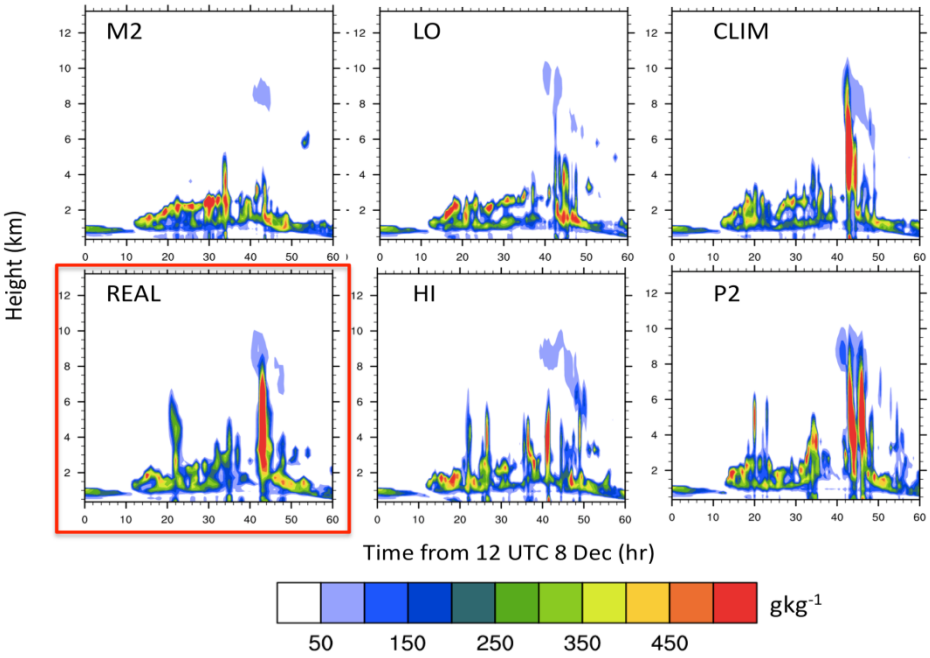

Figure 6.12: Sum of rain, snow, graupel, ice and cloud mixing ratios as a proxy for cloud cover valid over the ACRF Lamont site for all SST scenarios (REAL highlighted by a red box). The x-axis of each panel shows time (hour) from 12 UTC December 8, while the vertical axis shows height in km above ground.

6.4.1. First convective period: December 9

Precipitation initiated between 05 UTC and 09 UTC on December 9. Convective precipitation continued to form along the central domain axis throughout the day, albeit the model tended toward less afternoon (CST) convection than observed (chapter 5, sec. 5.4/5.5). Figure 6.5 demonstrated that elevated CAPE was present above the refreezing layer, and that the magnitude and northward extent of this instability was increased with warmer SST (HI, P2).

Figure 6.13 shows 875 hPa frontogenesis 09 UTC December 9 as convection was developing. The displayed parameters are based on the equation of Miller (1948, here equation 6.3), considering the shearing and deformation (stretching) terms only (terms 1 and 2 on the right hand side) calculated using RIP4 ('Read Interpolate Plot' v 4) software for WRF post-processing.

$$F = [\frac{\partial \theta}{\partial x}(\frac{\partial u}{\partial y})] + [\frac{\partial \theta}{\partial y}(\frac{\partial v}{\partial y})] + [\frac{\partial \theta}{\partial p}(\frac{\partial \omega}{\partial y})] - [\frac{\partial}{\partial y}(\frac{d\theta}{dt})] \qquad (6.3)$$

Equation 6.3 is the form given by Lackmann (2011, p136). The shearing term (term 1) describes the change in front strength due to differential potential temperature advection by the front parallel wind, while the deformation term (term 2) examines the change in potential temperature in the front normal direction (i.e., across the front). The tilting and diabatic contributions (terms 3 and 4) are typically weaker, especially the tilting term, as vertical motion near the surface is much smaller in magnitude than the horizontal wind components. The diabatic contribution, accounting for processes such as differential surface heating, heat flux and solar insolation (Lackmann 2011, p138) was

evaluated briefly, and did not contribute much in the freezing precipitation zone, albeit localized diabatic frontogenesis was observed in the warm airmass to the south (not shown).

Figure 6.13 indicates that frontogenetic forcing for ascent was present in the vicinity of convection, as was isentropic lift (not shown). This was indicative of these mechanisms being important in the lifting of air parcels to their level of free convection. Notably, frontogenesis over the central axis was weak or not present at this time for M2. Weak shearing frontogenesis appeared after 10 UTC for M2, corresponding with the formation of weak cellular convection. LO also indicated generally reduced low-level shearing term relative to REAL. CLIM, REAL and HI all produce frontogenesis over central Oklahoma, and convection developing shortly afterward. P2 showed a broader and earlier forming frontogenetic zone over the central axis, where convection initiated in this location 2-3 hours ahead of REAL (not shown). Based on the horizontal profile of potential temperature, it was observed that warmer air moves into the domain for higher SST, and this aids in strengthening frontogenetic shearing in particular through increased air temperatures on the warm side of the frontal boundary.

Of particular importance to development of precipitation was the availability of deep moisture. Figure 6.14 shows the magnitude of the column integrated moisture transport for domain 2, based on the equation given by Ressler et al. (2012, eqn. 6), shown below:

$$\vec{Q}_w = \frac{1}{g}\int_{400hPa}^{900hPa} q\vec{v}\,dp \qquad (6.4)$$

Where g is gravity (9.81 ms^{-1}), q is mixing ratio (gkg^{-1}), and v is the horizontal **u** and **v**

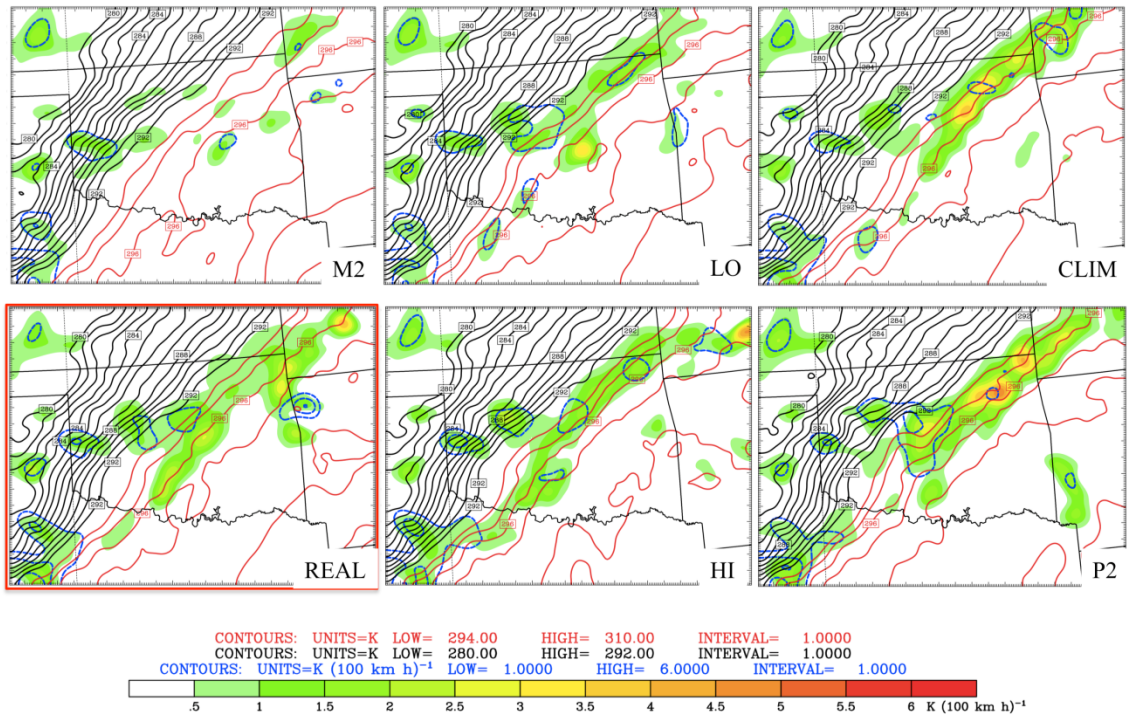

Figure 6.13: Domain 3 shearing (shaded) and deformation (blue contoured) frontogenesis in K (100 kmh^{-1}) valid at 09 UTC December 9 for each SST scenario. REAL is highlighted by the red box. Potential temperature (θ) contours are overlaid at 1 K intervals, with θ ≤ 294 K in black, and θ ≥ 294 K in red.

winds. The equation is expressed as a vector, composed of a **u** and **v** component. From these a scalar magnitude (x10^2 kgm^{-1}s^{-1}) is created and displayed as an average between 00 UTC – 18 UTC December 9. The moisture transport is primarily influenced by the magnitude of the mixing ratio, and the horizontal tropospheric wind. The moisture dependence on SST was immediately apparent, with a reduction in 850 hPa mixing ratio, especially over the far southern U.S and northern GOM with reduced SST. Note the similarity in moisture content between HI and REAL. Total basin average SST was only ~0.2 K warmer for HI, with much of this increased warmth in the western GOM. This difference produced only localized increases for HI. In all simulations 300 kgm^{-1}s^{-1}

moisture transport was present over the central SGP axis, while the axis of > 400 $kgm^{-1}s^{-1}$ expanded as SST increased. This result was promoted by enhanced mixing ratios, coupled with changes to the wind fields.

To examine the low-level wind field more closely, Figure 6.15 displays the average magnitude of the 850 hPa winds and geopotential height contours valid 00-18 UTC December 9 for domain 2. The 850 hPa level showed an axis of 30 + kt flow extending from the northern GOM into the SGP. This flow was associated with the strong temperature gradient across the frontal zone, the geopotential height gradient across the GOM basin, and the topographic deflection of low-level flow against the mountains of eastern Mexico. The analyzed period encompassed the nocturnal strengthening of this low-level jet circulation. Although comparison between M2 and P2 yielded generally greater 850 hPa wind velocities for the latter, the remaining scenarios showed little secular trend. On average, the wind maximum was located over northeast Oklahoma, extending northeast. For HI and P2, another area of 35+ kt flow was observed further south over southwestern-central Oklahoma. Differences in magnitude were not particularly large (< 5 kt).

Figure 6.16 concludes this discussion by displaying the total 24 hour accumulated precipitation from 00 UTC December 9. It is apparent that the increased thermal stability with decreasing SST, coupled with the reduction in moisture, and weakened forcing for ascent resulted in a strong decrease in precipitation in this first convective period for M2 (-31%). This was especially evident for accumulations exceeding 10 mm, where there was a 69% reduction (all phase types). LO (CLIM) also showed a decrease of 26% (23%) above this threshold. Conversely, HI, and P2 evidence

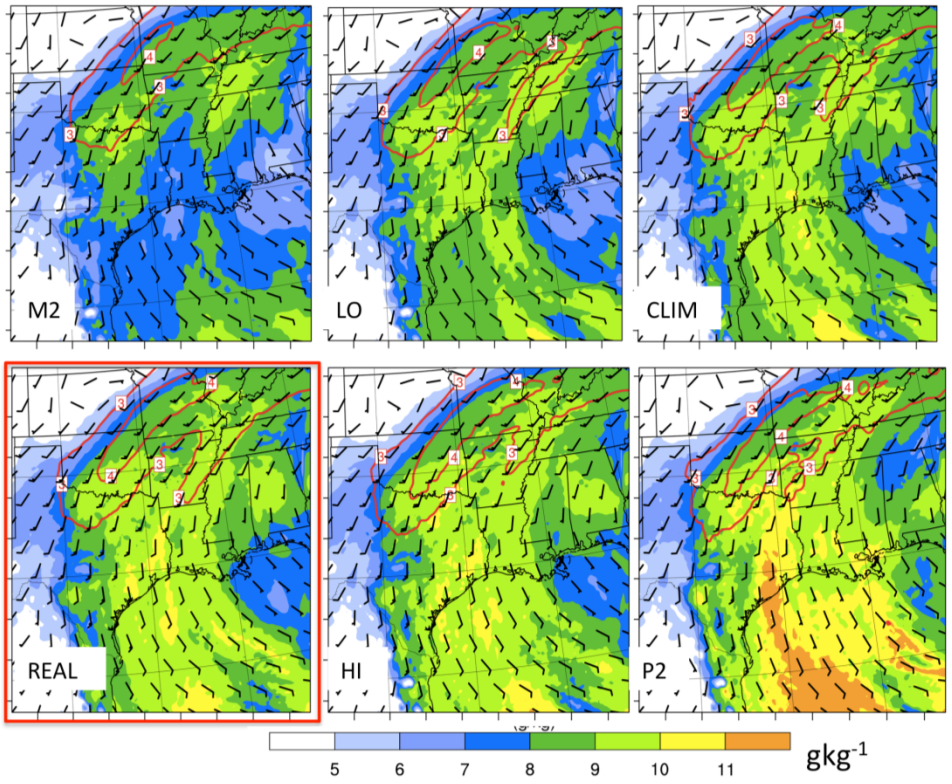

Figure 6.14: WRF domain 2 850 hPa mixing ratio (g kg^{-1}), wind fields (barbs, ms^{-1}) and 900-400 hPa integrated horizontal moisture transport ($kgm^{-1}s^{-1}$) contoured in red at intervals of 0.5 above 3 x 10^2 $kgm^{-1}s^{-1}$ for 00 UTC 18 UTC December 9. REAL highlighted by the red box.

moderately greater accumulations(~28-33% increase > 10mm) over this interval for opposite reasons.

6.4.3 Second convective period: December 10

After a temporary decrease in precipitation on the evening of December 9, further convection began to develop by 06 UTC December 10 in southwestern Oklahoma/western north Texas. This precipitation continued over much of the central axis until 18 UTC December 10 before lifting northward. The upper level trough at 06 UTC December 10 had moved southeast, and was beginning to assume a near-neutral

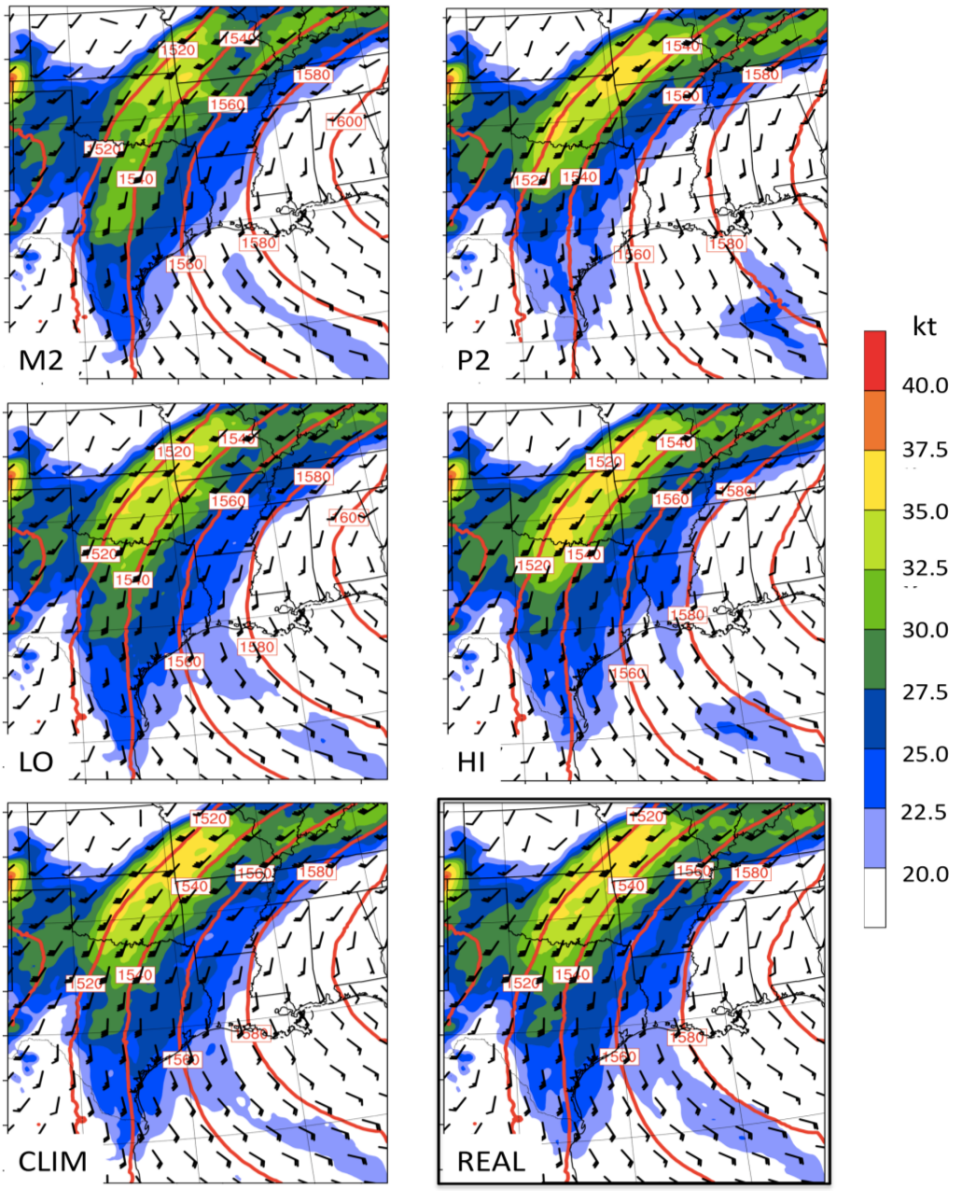

Figure 6.15: WRF 850 hPa vector winds (barbs, knots), magnitudes (shaded, knots), and 850 hPa geopotential height (m) for domain 2, averaged 00-18 UTC December 9. REAL highlighted by a black box.

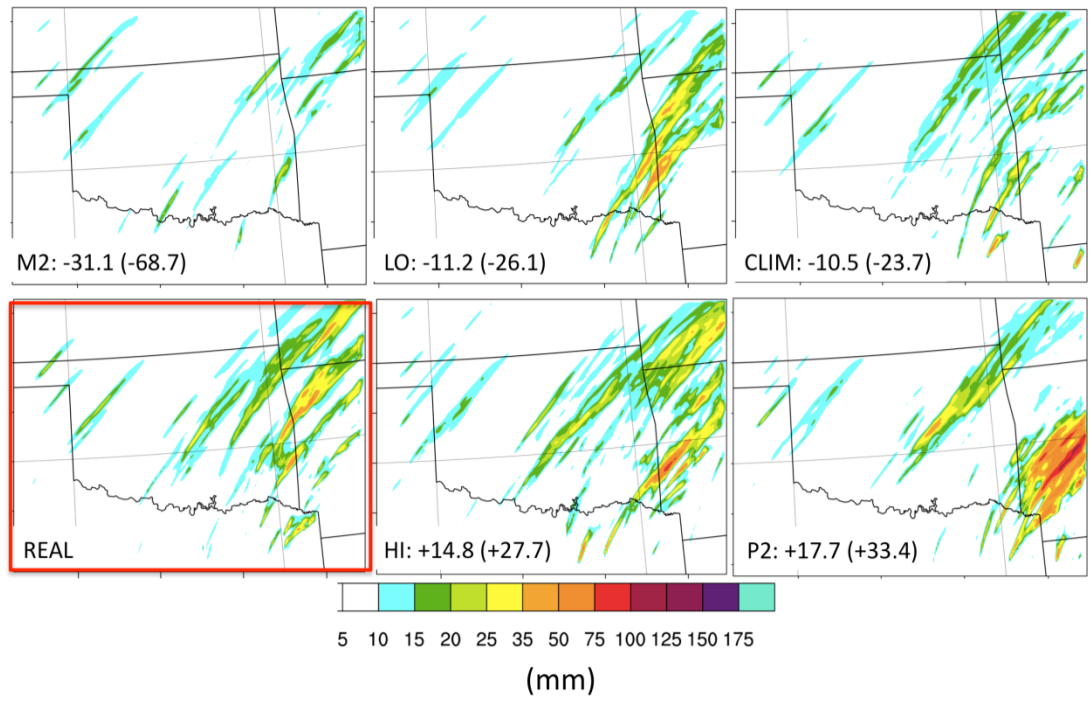

Figure 6.16: WRF 24-hour accumulated precipitation (all phase types) for December 9 2007 in mm. Only values above 10 mm are shaded. REAL highlighted by the red box. Values for each SST simulation panel (values in parenthesis) are the percentage departure from REAL for total accumulated precipitation (accumulations > 10 mm).

tilt (not shown). A deep plume of moist air was present over the SGP in association with continued subtropical moisture advection from the GOM (and Pacific; 700-500 hPa layer). Examination of model-derived soundings near Norman, Oklahoma (09 UTC, not shown) confirmed this assertion, indicating deep cloud and saturated ascent along the moist adiabat. CAPE at 6 UTC December 10 (not shown) indicated lower values during this second convective period, especially over the central freezing precipitation axis (< 100 Jkg^{-1}). This reduction was possibly associated with the mid-level moistening and stabilizing associated with moisture advection and earlier precipitation.

Forcing for ascent during this convective period appears to have involved continued potential instability, low-level frontogenetic forcing, and isentropic ascent. A weak shortwave ejecting ahead of the long-wave trough (not shown) may have been responsible for enhanced lift and increased precipitation relative to December 9. Figure 7.17 shows shearing and deformation frontogenesis at 875 hPa valid at 06 UTC December 10. In general, HI, and in particular P2 evidence southward displacement in maximum frontogenesis at this time relative to REAL. In contrast, LO and M2 showed a northward extension of frontogenetic forcing. Furthermore the magnitude of the deformation and shearing components increased, particularly in northwestern Texas. Over the subsequent several hours, this pattern continued, and was borne out in a more rapid northward movement of convection in LO and especially M2 (not shown). Additionally, 850 hPa wind velocity was observed to have increased over western north Texas into central Oklahoma in M2. Figure 7.18 shows the average 850hPa wind velocity and geopotential height field for 00-18 UTC December 10. While the average changes were not particularly great, the intensified flow over Oklahoma into Missouri in M2, relative to REAL, was well collocated to the northward increase in frontogenesis, and northward maximum precipitation (Fig. 6.20). P2, in contrast, suggested a weakened jet over Oklahoma, and stronger flow and horizontal convergence over north Texas, corresponding to the southerly displacement in maximum ascent and convection. The remaining simulations fell between these extremes.

One of the possible reasons for the change in flow strength was the apparent weakening of the longitudinal gradient in geopotential height with increased SST.

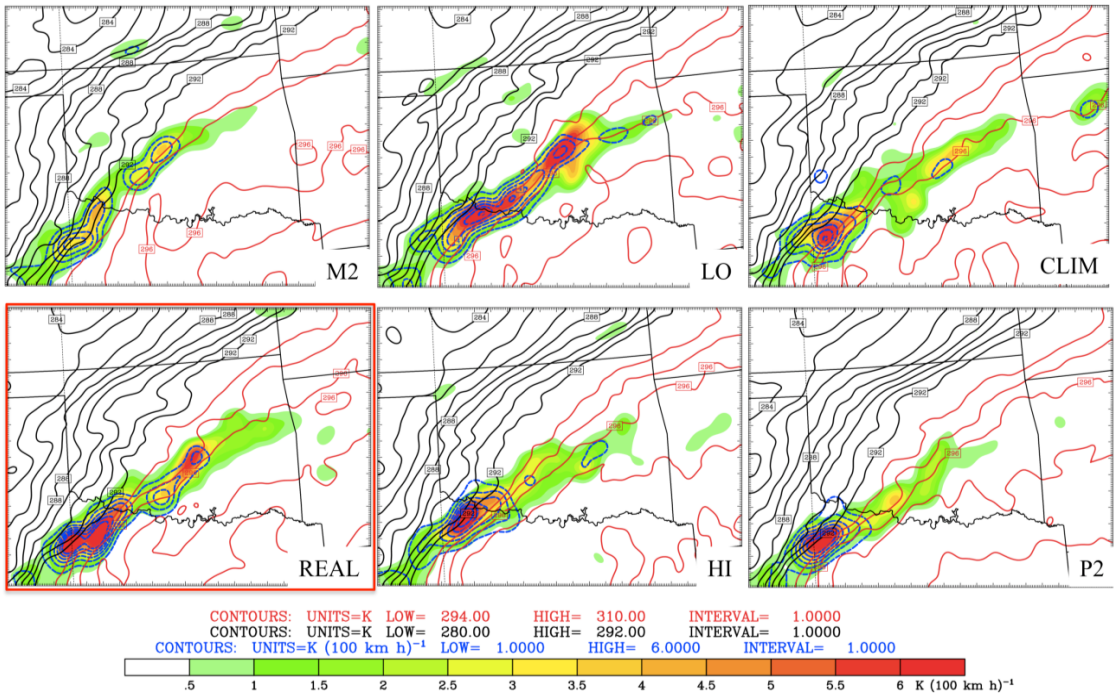

Figure 6.17: As Fig. 6.13 but for 06 UTC December 10.

While differences between REAL, CLIM, LO and HI were not so discernable, M2 versus P2 show an eastward shift in the 850hPa geopotential ridge over the GOM and southeastern U.S for the latter. It is possible that the increased temperatures in P2 yielded a reduction in height akin to the formation of a 'thermal' low in regions of anomalous warmth, acting to decrease (increase) height at low (upper)-levels. Yongning (1996) suggested development of an anomalous low-level cyclonic circulation over the GOM associated with a uniform 5 K SST perturbation in a climate model sensitivity study.

The effect of the low-level jet circulation and moisture changes are shown in the integrated moisture transport shown in Figure 6.19. Higher mixing ratios continue to be supplied to the domain as SST was increased. The role of the low-level wind field perturbations shown in Fig. 6.18 was to generally increase the max magnitude and areal

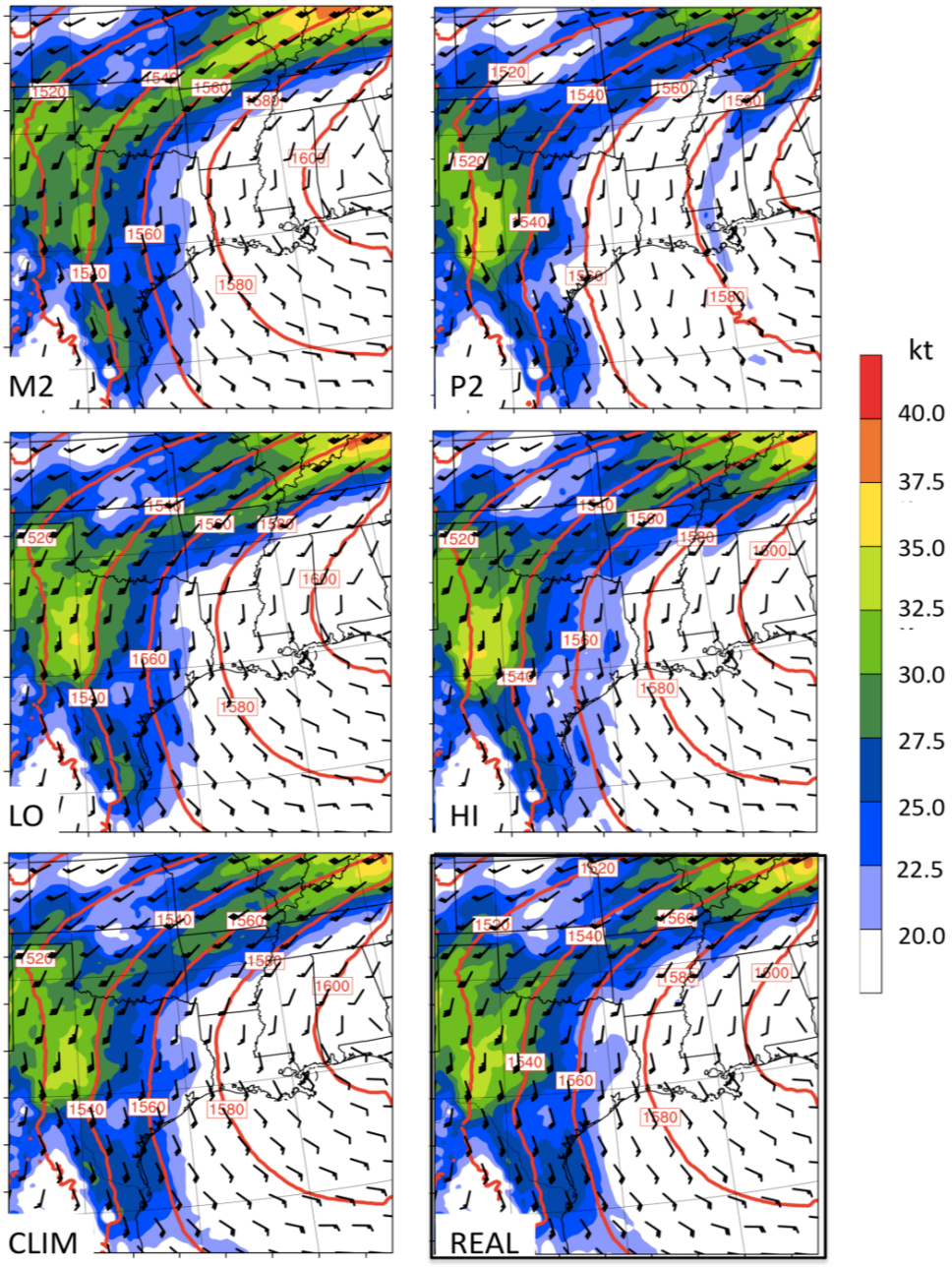

Figure 6.18: As Fig. 6.15 but for 00 UTC -18 UTC December 10.

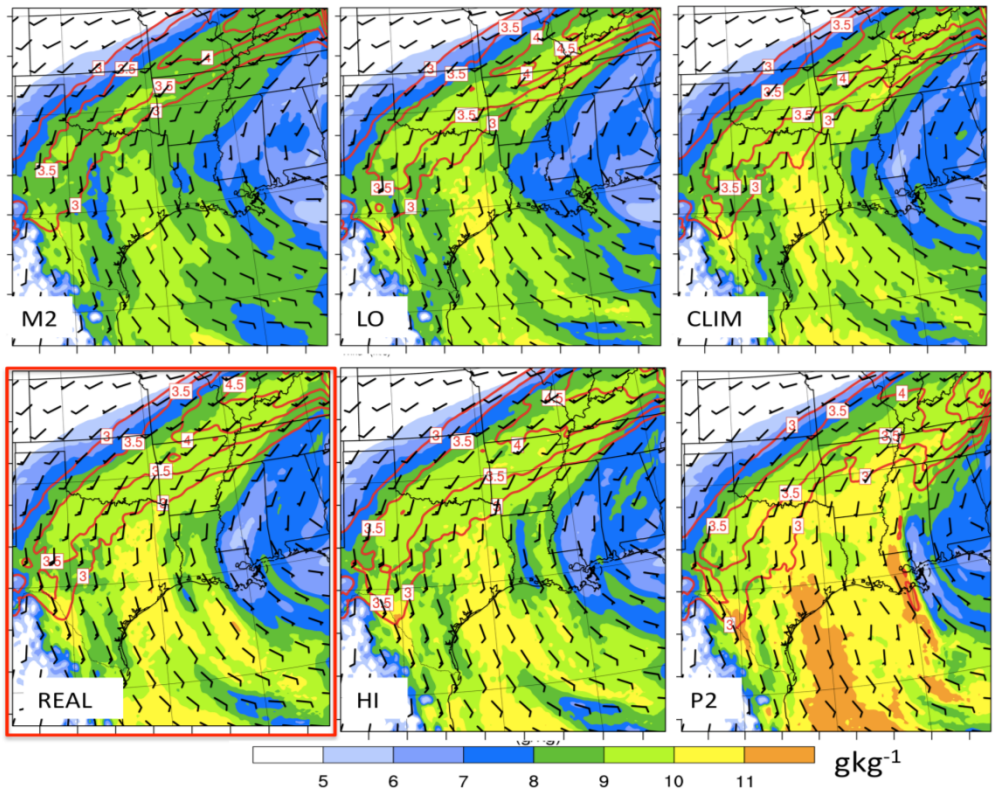

Figure 6.19: As Fig. 6.14 for 00 -18 UTC December 10.

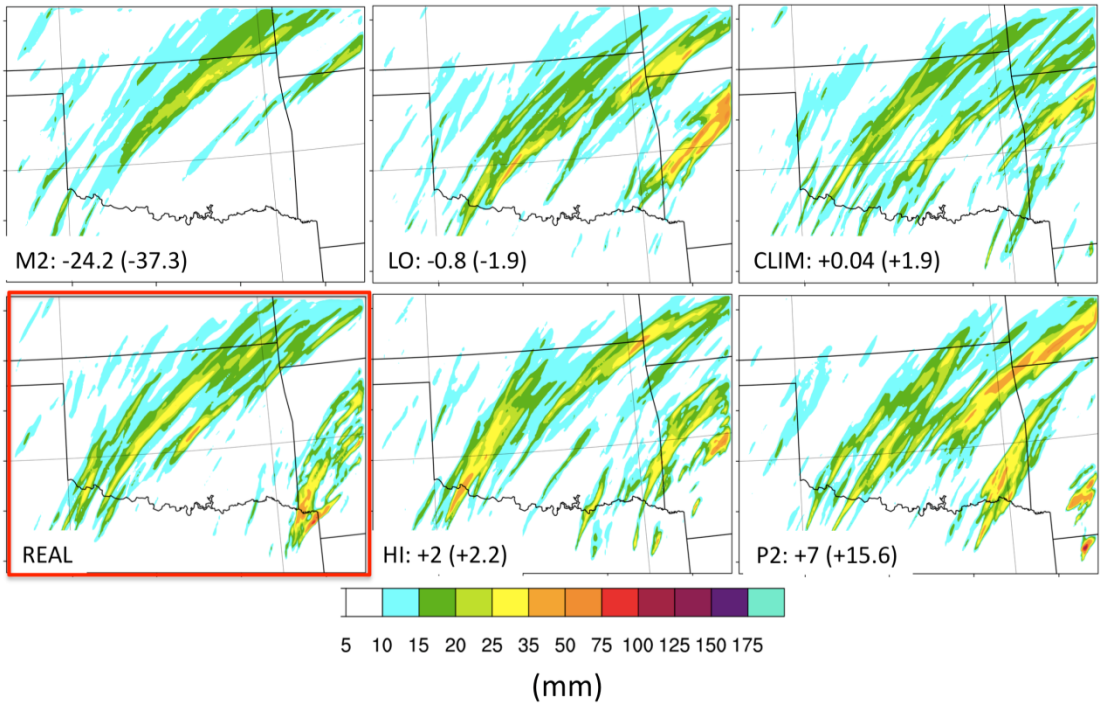

Figure 6.20: As Fig. 6.16 for December 10 2007.

extent of moisture transport as SST was reduced, while the higher mixing ratios for warmer SST act to increase moisture availability. These completing effects produced generally similar magnitudes of moisture transport with scenario for the SGP. Figure 6.20 shows the domain 3 24-hour accumulation of precipitation on December 10. This second convective episode produced widespread precipitation, with evidence of moisture-strengthened updrafts with higher SST (especially P2, e.g., Lackmann 2013). In general, the difference in accumulations was reduced relative to the first convective period, with M2 producing the strongest departure of -37% (above 10 mm). LO, CLIM, REAL and HI had very similar accumulation (albeit the spatial distribution was altered), while P2 showed the largest positive departure.

6.5 Air Mass Trajectories and Meteorological Characteristics

An advantageous way of examining air mass characteristics within the thermal profile during freezing precipitation is a lagrangian method that can resolve the approximate path of incident air parcels, and the meteorological characteristics along this path. Such a technique was introduced in chapter 4, and based on the work of Gyakum and Roebber (2001), and Fuhrmann and Konrad (2013). In the context of this investigation, trajectory analysis may aid to identify the extent of, and processes by which air parcels are modified by their environment, including impacts of varying SST structures on warm layer properties. The discussion in much of this chapter has been from the perspective of evaluating SST impacts based on their basin average anomaly. However, regional SST anomalies may be as important in modifying the warm layer. Trajectory analysis allows further preliminary investigation of this question.

Here 4-day (96-hour) back trajectories were evaluated for central Oklahoma during freezing rain, at 12 UTC December 9 (first convective episode), and 12 UTC December 10 (second convective episode). The definition of a back trajectory was provided in chapter 4 (sec 4.2). Trajectories were calculated using RIP4 WRF post-processing software. RIP4 computes trajectories using model u, v and w wind components based on user specified starting location, start and end times. Domain 1 was used for the calculation, with model data available at 3-hr intervals. The program interpolates between these intervals and generates trajectory locations every 30 minutes, while meteorological information, including mixing ratio, humidity, potential temperature, air temperature, solar insolation were calculated every 3-hours. RIP4 did not include latent heat flux as a variable and thus WRF simulated latent heat flux was calculated for the GOM basin, using a 48-hour average prior to the trajectory end time, t0 (the time that the trajectory enters the freezing precipitation zone).

Ideally, a set of ensemble trajectories in both altitude and location should be generated to account for local variability and/or model uncertainty in the wind field. The technique would potentially provide more accurate assessment of flow fields into the warm layer (e.g., Fuhrmann 2011). Given time constraints, this methodology was not used, but remains a potential avenue for future research. The reader may refer to the appendix to this chapter (and chapter 7) to compare the path of the calculated 'instantaneous' trajectories to an example RIP4-generated ensemble. Trajectories were calculated at 975 hPa (near surface), 850 hPa (warm layer), 725 hPa (~top of warm layer) and 500 hPa.

6.5.1 Central Oklahoma: 12 UTC December 9

Near-surface trajectories (975 hPa, not shown) indicated negligible influence of SST perturbations on path and altitude. All simulations produced southeastward advection of air parcels from South Dakota through Missouri between t-96 (96-hours before trajectory endpoint) and t-24, subsequently curving southwestwards before entering the precipitation region from the north-northeast. Trajectory altitudes suggested gradual descent over this time from near 1.2 km to 0.4 km (above sea level, AMSL). This movement aided gradual warming of the air parcel from near -10^{o}C at t-96, to -2^{o}C at t0. Furthermore, the air parcel generally remained within a humid environment.

Air parcels terminating at 850 hPa level, shown in Fig. 6.21, generally indicated direct northward flow from the western GOM, with the exception of CLIM at this specific time. A brief examination of the CLIM trajectory in the subsequent 6 hours (not shown, but see appendix for ensemble spread) revealed that a direct GOM trajectory did eventually evolve. The continent-based CLIM trajectory circulated over a region of relatively warm and moist air, whilst remaining within the PBL throughout its duration before ascending into the precipitation domain (the magnitude of this change in height with time indicates strength of vertical motion). GOM air parcels remained generally near the surface over the open ocean, with the exception of HI, which moved aloft over the Yucatan Peninsula between t-96 and t-72 (it should be noted that the uncertainty in trajectory location increases with time from t0). The air parcels moved onshore between t-24 and t-30, with HI advecting slightly more rapidly (onshore at t-21).

Meteorological characteristics of the 850 hPa layer were examined by evaluating temperature, humidity and precipitation following the air parcels in Figure 6.22. The air

temperature and θ_e timeseries (Fig. 6.22, top) show that GOM trajectories were associated with very warm temperatures and high moisture content (mixing ratios > 12 gkg^{-1}, not shown), with maximum θ_e (air temperature) values near or in excess of 340 K (20^oC) over open water. Latent heat flux into the air parcel was generally weak (Fig. 6.21), but did increase over the western basin with increased SST, maximizing near 100 Wm^{-2}. Strong latent heat flux (e.g., > 200-300 Wm^{-2}) might occur in circumstances where a cold or dry airmass advects over the warm water, however neither is true for GOM trajectories shown here. Thus, the dominant mechanism by which these air parcels maintained heat and moisture appeared to be adiabatic (e.g., turbulent mixing), with localized diabatic modulations (e.g., solar heating, precipitation, and latent heat flux).

Between t-48 and t0, the altitudes and location of all perturbed SST GOM trajectories were similar, isolating the role of the SST distribution. Fig. 6.22 (top) showed higher temperature/θ_e during this time for HI and P2, which both have > +1.5 K SST anomalies in the western GOM (Fig. 6.21). The higher θ_e near t-36 for HI was due to its more southerly location. LO and M2 exhibited similar temperatures at this stage (potentially due to the ~100 m higher altitude of LO, and its slightly northerly location with respect to M2), which decreased with time, rather than remaining quasi-steady as for HI and P2. The lower SSTs in these latter cases yielded a maximum difference of ~20 K (~8^oC) for θ_e (air temperature) relative to HI and P2 (Fig. 6.22, top). In the final 12 hours, θ_e and mixing ratio (not shown) decreased at a greater rate for HI and P2, manifested as increased precipitation at this location (Fig. 6.1, 6.22, bottom). The warm/moist conditions over the southern U.S precluded a sharp decrease in moisture

content as the air parcel moved over land. For CLIM, its continent based path produced much lower initial temperature/θ_e, but as the air parcel moved southward, it gradually moderated to the regional environment. In the final 24-hours moisture and temperature rapidly increased as the trajectory looped anticyclonically over north central Texas. The sharp rise in θ_e implied a diabatic heating contribution, possibly enhanced sensible heat flux during peak solar insolation.

The 725 hPa endpoint, shown in Figure 6.23, followed air parcels incident to the upper portion of the warm layer. While t-96 to t-48 trajectory locations showed variability between scenarios, the final 48-hours were generally consistent. The air parcels moved northeastward aloft from the subtropical eastern Pacific, descended to ~2.5-3.5 km over the Mexican Plateau, and into southwestern Texas at altitudes near 1.5 km, finally ascending northwards to the precipitation zone. The trajectories attained their maximum temperature in the warm air over southwestern Texas, while minimal changes in θ_e occurred over the 96-hours (not shown). In general, θ_e was ~3 K greater for P2 and HI, with this difference largely explained by altitude.

The effect of GOM SST was only discernable as a modest increase in mixing ratio at this level (e.g., Fig. 6.23). By referring back to the thermal profile shown in Fig. 6.6 (sec 6.2.2), it was apparent that the temperature profile of the upper warm layer was primarily associated with trajectory evolution shown here, that is, the northeastern advection of a warm, comparatively dry airmass from the Mexican Plateau. Since this airmass was not strongly affected by temperature, moisture or circulation changes promoted by SST, it was likely responsible for the layer of stability that developed in M2 and LO as the 800-850 hPa layer temperature was reduced.

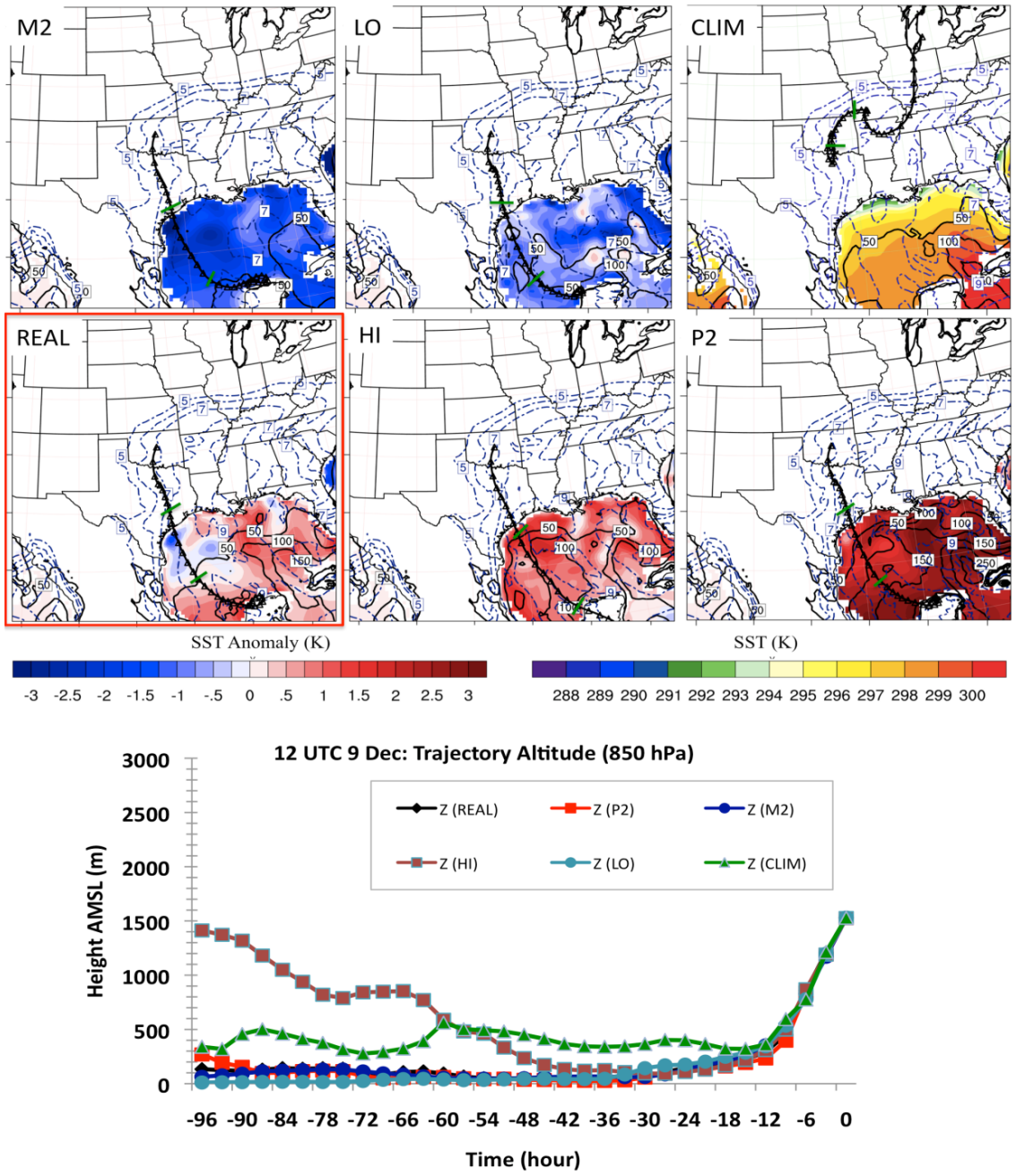

Figure 6.21: Top: 850 hPa back trajectories, valid 12 UTC December 9 during the first convective episode. Each trajectory displays triangular markers at 3-hour intervals, with intersecting green line at T-24 and T-48. Overlaid on each panel is the SST anomaly field relative to climatology (CLIM displays full SST), with 48-hour average latent heat flux (Wm^{-2}) ending at 12 UTC (black contoured lines), and 850 hPa mixing ratio (blue dashed lines) at intervals of 1 gkg^{-1} (>5 gkg^{-1}). Bottom: Time series of trajectory altitudes for each SST simulation.

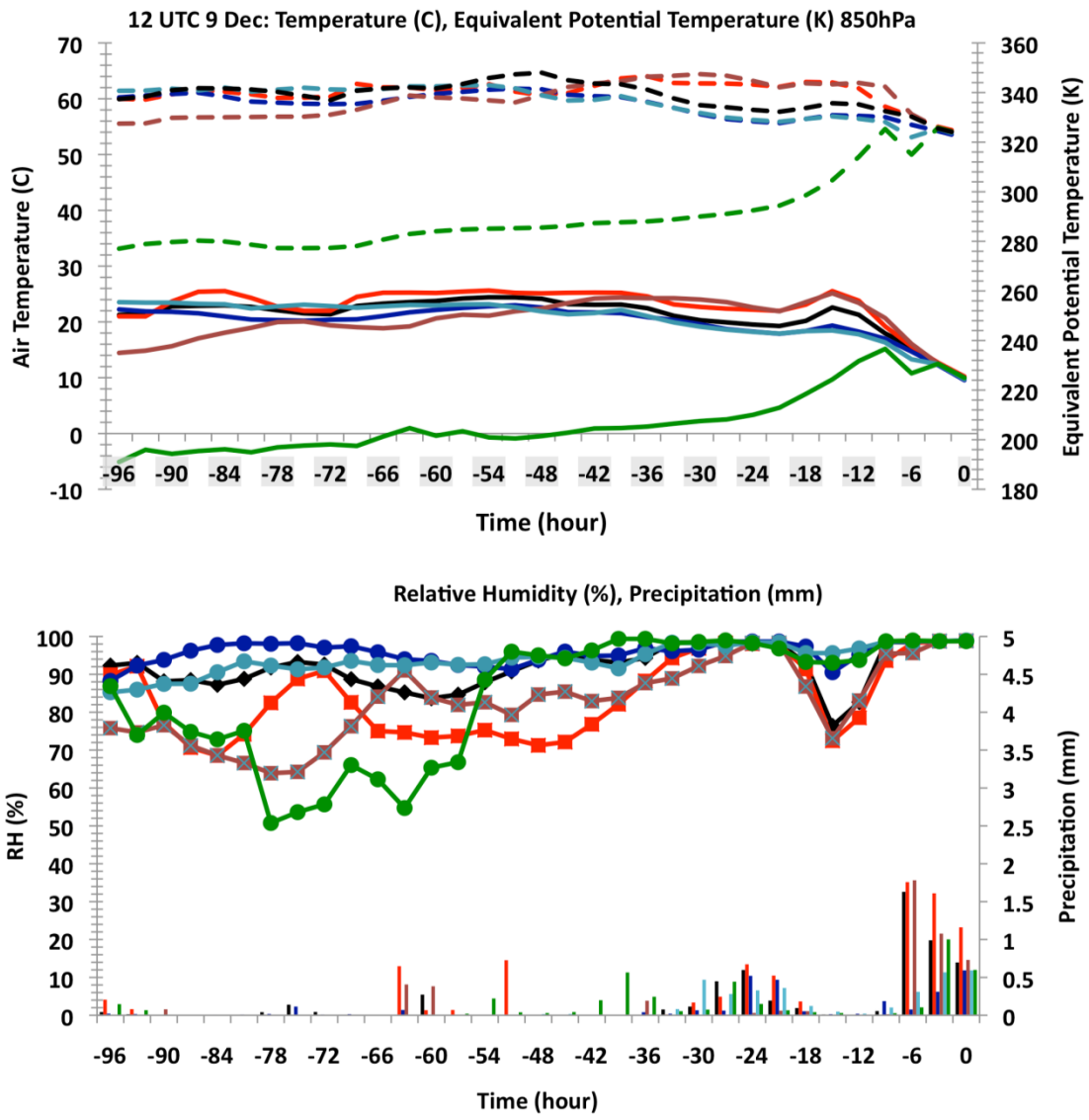

Figure 6.22: Top: timeseries of air temperature (solid lines, ^{o}C), and θ_e following the trajectory for each SST simulation ending at 850 hPa in the warm layer. Bottom: relative humidity (solid lines, %), and precipitation (bars, mmhr^{-1}). The color key is the same as that of Fig. 6.21 (bottom), that is: red = P2, maroon = HI, black = REAL, green = CLIM, light blue = LO, dark blue = M2.

At the 500 hPa level (not shown), trajectory paths for each simulation were visually identical. The strength of the mid-level jet stream as evident, with the trajectory curving southeastward at t-48 over the eastern Pacific, southeast to Baja California at t-

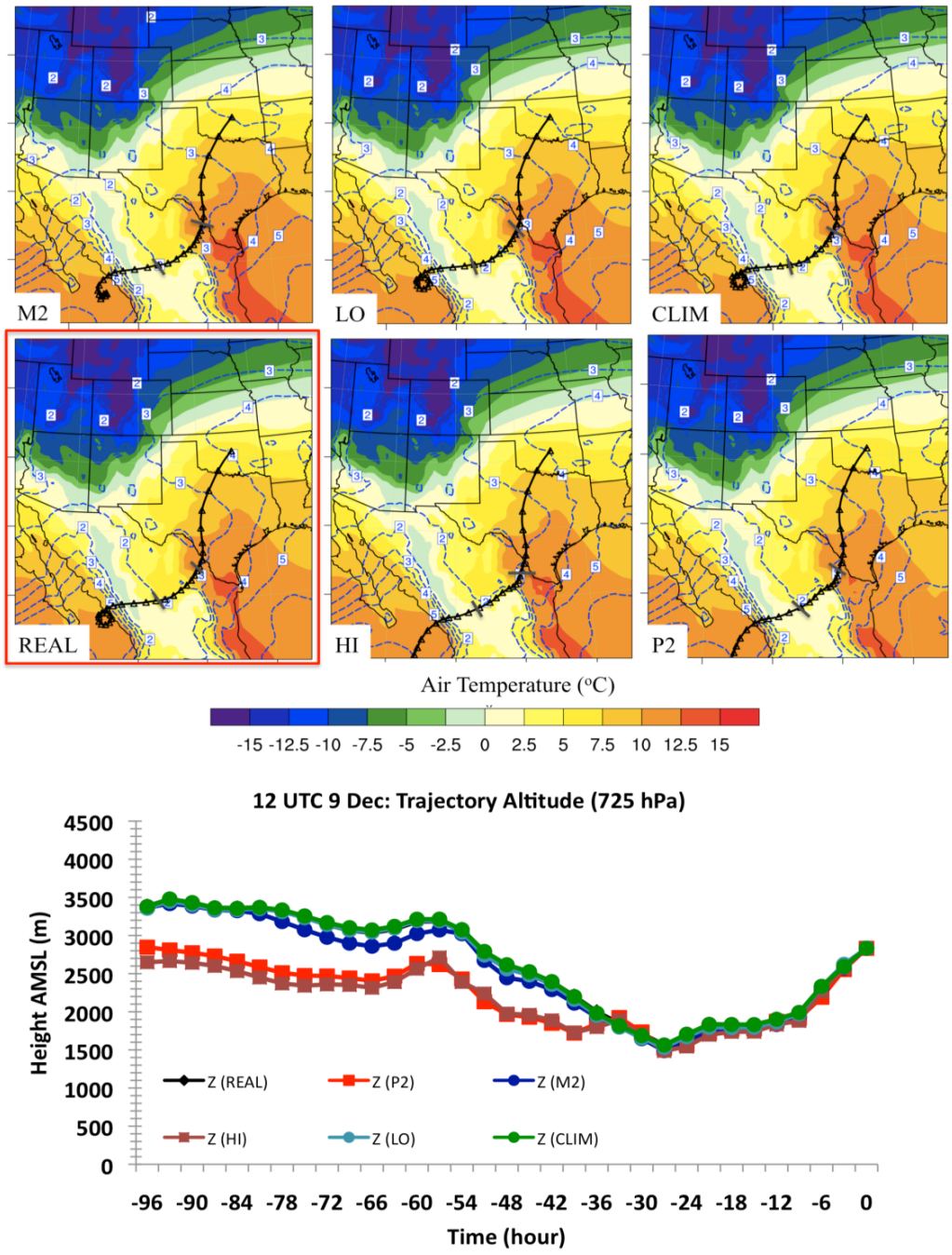

Figure 6.23: Top: 725 hPa trajectory paths for each SST scenario. Trajectories displayed as in Fig. 6.22. Air temperatures (filled contours) averaged over 48-hours ending at 12 UTC 9 for the 650-850 hPa layer, while mixing ratio (blue dashed lines) estimated over the same time and layer. Bottom: timeseries of trajectory altitudes for each SST simulation.

24, and northeastward into the domain. The altitude of the air parcels remained within 5-6 km AMSL. At this time, mid-level moisture was low along the direct path (RH < 30%), which may have contributed to intensify instability through increased lapse rates.

6.5.2 Central Oklahoma: 12 UTC December 10

At this time, convective freezing precipitation had redeveloped over central Oklahoma. The 975 hPa trajectories (not shown) continued to remain consistent between SST simulations, and indicated stronger advection of cold air, based on the air parcel origination location of Canada at t-96. The altitude change was once again characterized by descent from initially ~1.5 km AMSL, while air temperature was gradually modified through adiabatic compression and modification, ultimately remaining similar in magnitude to that of the previous morning (Sec. 6.5.2).

The 850 hPa layer trajectories, shown in Figure 6.24 now suggest little change between simulations with respect to path. Air parcels moved northwestwards from the Caribbean into the central GOM, subsequently northwards over central Texas to the freezing rain region. Trajectory altitudes identified that air parcels continued to spend extensive time within the marine PBL. Consequently, high maximum air temperature and θ_e persisted, and even slightly increased relative to December 9 (Fig. 6.25). The higher trajectory altitude of M2 and cooler SST field produced the lowest total moisture/temperature. By t0, these distinctions were reduced, possibly increased moisture content with higher SST being converted to higher vertical velocity/precipitation and warm layer cooling due to enhanced melting rates. Interestingly, HI did not show increased air parcel temperature over REAL etc,

especially in the final 36-hours, instead maximizing near t-48 associated with its movement over anomalously warm SST in the northwestern GOM. The slower northward movement of the air parcel lead to HI (and P2) spending more than 36 hours over the southern U.S, whereas accelerated flow for M2, LO, CLIM and to a lesser extent REAL moved air parcels onshore near t-27 to t-24, and thus more time over the open ocean, mitigating the differences due to SST distribution at this time. Once trajectories for LO, M2 and CLIM moved onshore they more rapidly decreased in θ_e and temperature. The humidity profile (Fig. 6.25, bottom) displayed high values throughout the trajectory path, along with frequent precipitation after t-24.

At the 725 hPa layer, shown in Figure 6.26, trajectories shifted eastward with respect to the first convective period, likely in response to movement of the upper trough. Air parcels were located over the far western GOM, with t-96 to t-48 marked by track-dependant altitude changes, while by t-48 (southwestern GOM), air parcels move northward near 1.5 km AGL, gradually ascending onshore and aloft of the frontal zone. This track increased layer θ_e relative to the first convective period, resulting from moistening and air parcel temperatures reaching 20^{o}C over the basin (~t-36). This trajectory thus demonstrated the origins of increased layer tropospheric moisture observed for the second convective episode. Furthermore, increased mixing ratio was also indicated at the 500 hPa level (not shown), where the southeastward digging of the broad trough allowed for a deep plume of moist air (700-500 hPa average > 4 gkg^{-1}) to extend at mid-levels from the subtropical Pacific. Trajectories were now orientated along this axis, air parcels moving from ~2 km above the subtropical Pacific over

Mexico into the domain, albeit ascent and precipitation over the windward side of the Mexican plateau slightly reduced available moisture to the SGP.

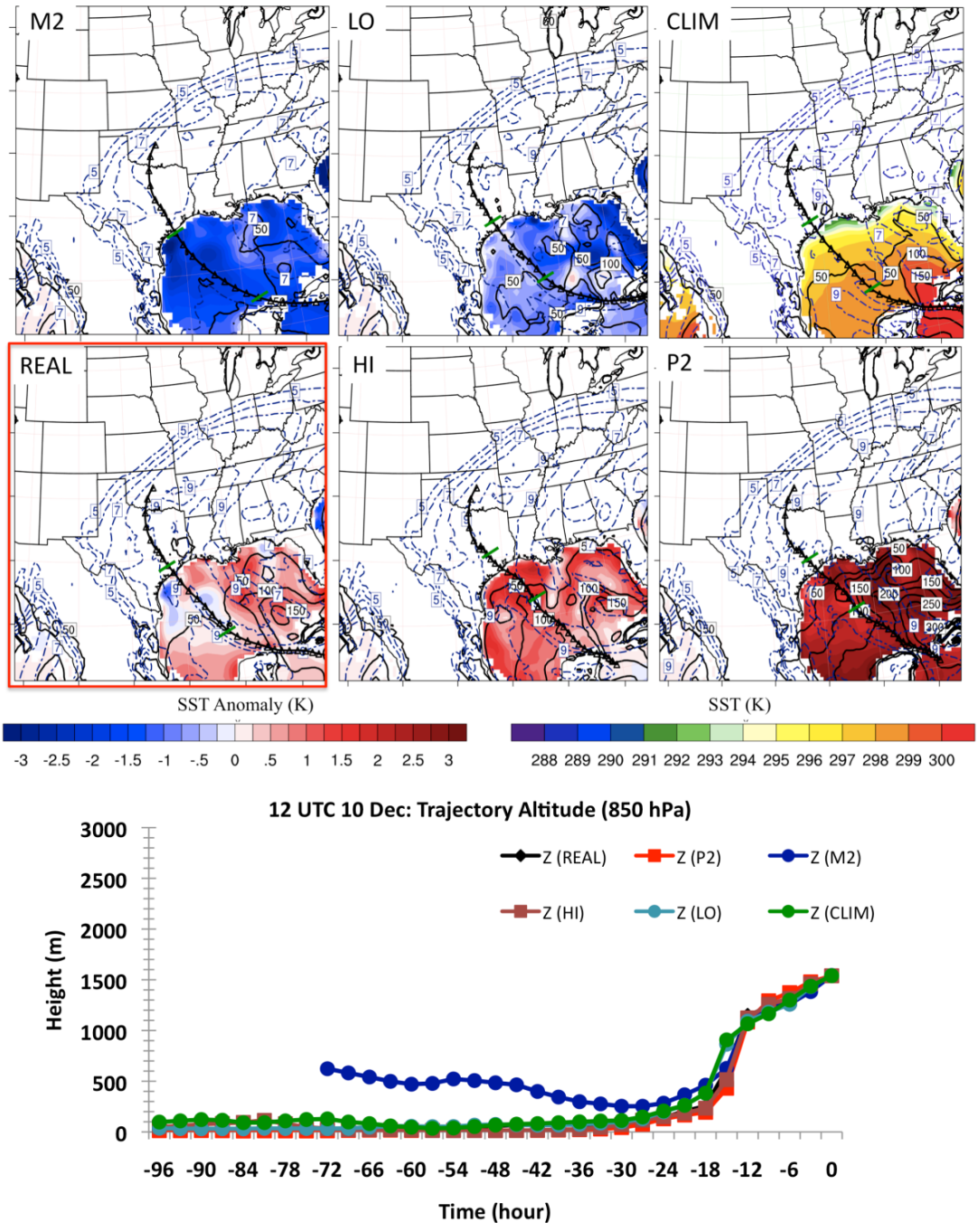

Figure 6.24: As Fig. 6.21, for 12 UTC December 10.

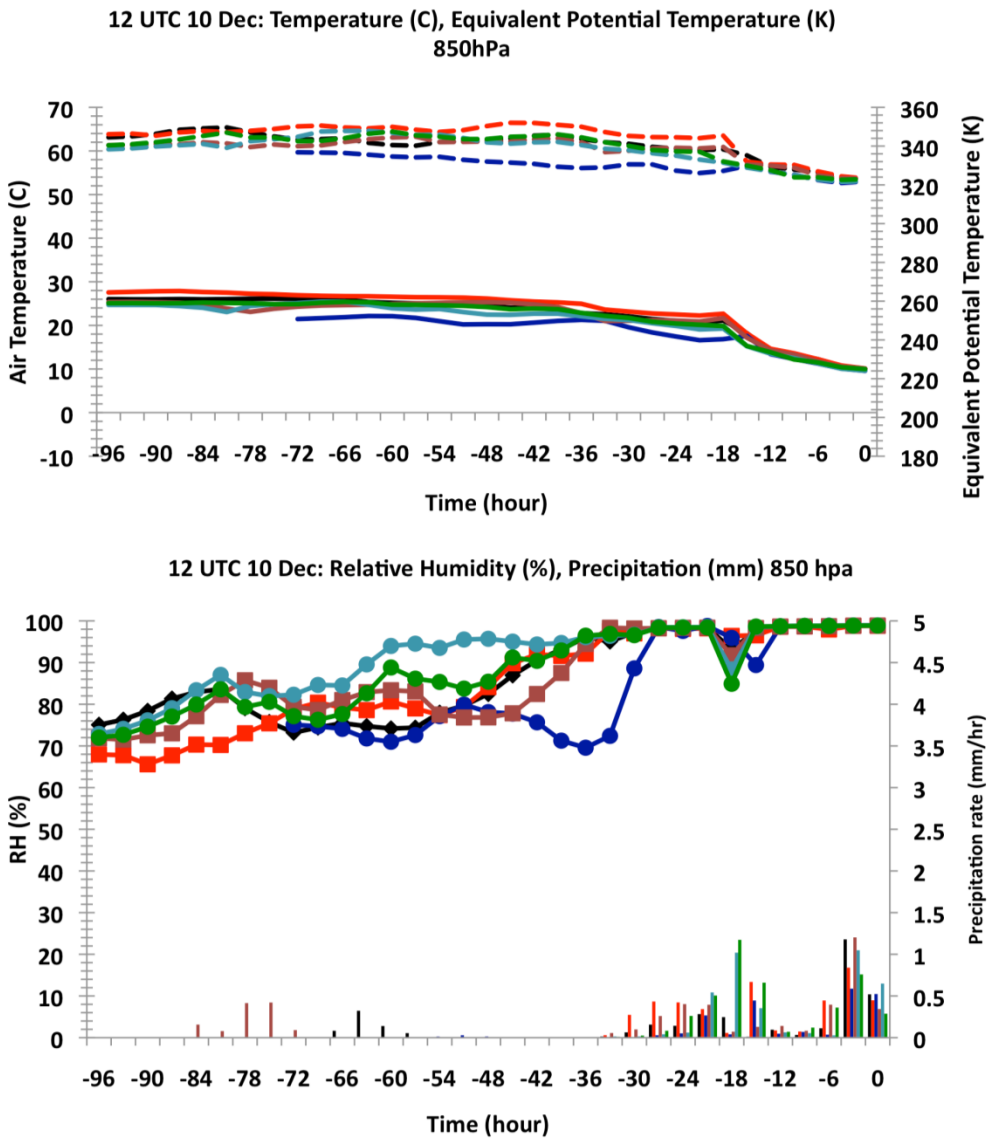

Figure 6.25: As Fig. 6.22, for 12 UTC December 10.

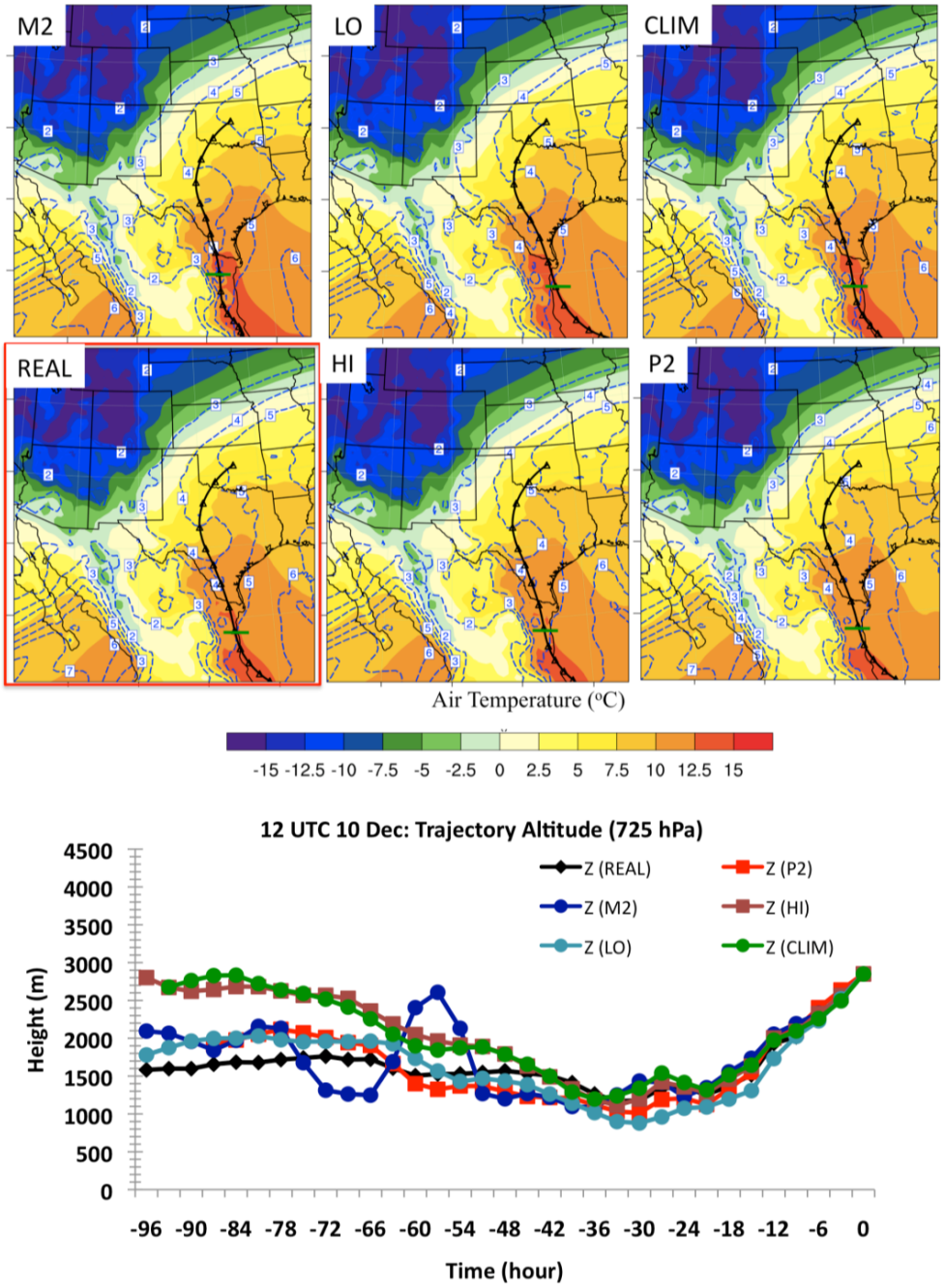

Figure 6.26: As Fig. 6.23 for 12 UTC December 10.

6.6 SST Impacts to Ice Storm Severity

Based on these results, there was discernable influence of GOM SST perturbations on the evolution of the December 2007 ice storm. This chapter provided detailed physical interpretation of the processes that were key to translating the SST

anomalies into changes in precipitation and warm layer evolution. Given that simulated ice accumulations did not well represent the actual event (e.g., chapter 5, sec 5.3, 5.4), we refrain from a more detailed assessment of potential impacts. In the next chapter, the better spatial agreement for freezing precipitation allowed for firmer conclusions. Nonetheless, with reference to the 'REAL':

- Lower SST gradually reduced convective activity, particularly on December 9. While LO weakened convection, M2 produced a substantial decrease. In fact, according to M2, the first round of freezing precipitation was very light (< 10 mm over 24 hours), particularly against the moderate intensification of ice along the central axis for HI and P2. These differences in the timing of icing might have limited infrastructural and socioeconomic disruption on December 9 with strongly negative SSTA. Weak negative SSTA relative to control produced a more minor but still discernable decrease in central axis ice accumulations (e.g., CLIM).
- December 10 produced a more northern zone of icing for very low SST, leading to a comparatively weak ice storm for central Oklahoma. LO, CLIM, REAL and HI generally had similar total accumulations, with changes in location. HI for example, had a more westward maxima in freezing precipitation during this time. P2 showed an intensified southern branch of the central axis, but in general the increase in total precipitation (ice) was small. We might suggest that only slight exacerbation of disruption would have been anticipated on this day for strongly positive basin-wide SSTA, especially within the physically constrained magnitudes of this present climate.

Chapter 7: SST Sensitivity Study for the January 28-30 2010 Winter Storm

7.1 Introduction

Chapter 6 presented the impact of SST modulation on the December 9-11 2007 ice storm. The suite of simulations revealed that by increasing the average temperature of GOM SST, moisture potential and precipitation regionally increased, particularly for the first episode of convection on December 9. The SST perturbations also produced low-level circulation changes, including weakening with time of the low-level south-southwesterly flow resulting from a reduced geopotential height gradient over the SGP for high basin-wide positive SSTA. Freezing rain was generally most sensitive to moisture content changes, and negative SSTA (e.g., M2), which stabilized the lower-troposphere and produced a sharp decrease in convective updraft strength and spatial coverage.

In this chapter, we present the results of the SST perturbation analysis for the January 28-30 2010 winter storm, an *Ice Pattern 1* event. The synoptic-dynamic evolution of this event was notably different to the former case study. The goals and organization of this chapter are similar to chapter 6.

7.2 Precipitation Accumulation and Phase Partitioning

7.2.1 Total accumulation

Figure 7.1, 7.2, and 7.3 display 48-hour accumulated precipitation, valid 00 UTC 28 to 00 UTC 30 January for freezing precipitation, rainfall, and snowfall

respectively. The simple technique (Bourgouin 2000) used to obtain these phase delineations was discussed in chapter 6. In this case, because the event cycled through multiple precipitation type, we estimated an 'upper limit' for the freezing rain (FZRA) component. This was derived by assuming that when IP was detected by the algorithm, and the surface temperature was above -5^{o}C, half of it fell as FZRA, while when a mix or FZRA was detected, all was in the form of FZRA. Simulated precipitation (REAL), including freezing precipitation accumulation, was found to be in reasonable agreement to observations, particularly for Oklahoma, using the above assumptions (e.g., chapter 5, sec 5.5, chapter 4, Fig. 4.16). In addition to the figures, Table 7.1 (in the form of Table 6.1, chapter 6) quantitatively examined WRF simulation responses to varying SST.

For freezing precipitation (FZRA/ IP, Fig. 7.1, Table 7.1 parenthesis), results suggested both magnitude and location changes between simulations. Cooler basin SST, particularly M2, reduced accumulations over southwestern Oklahoma and displaced a maxima southwest to Lubbock, TX. Icing over Arkansas especially was notably weaker than REAL and shifted 1-2 counties southward. Using the 75th percentile of the control FZRA/IP distribution as a threshold (~13 mm), the spatial retraction of affected grid points was near 12% (rapidly decreasing to -67% above 20 mm, not shown). Furthermore, decreases in freezing precipitation intensity were marked at 58% above 2.5 mmhr^{-1}. LO (REAL-0.61 K) and REAL were visually similar (within 4% for all accumulations above 5 mm, base of Table 7.1), but with reduction in peak accumulations (e.g., > 40 mm) for the former. Both cases produced the maximum in precipitation over southwestern Oklahoma on January 28, but with LO further

southwest. REAL indicated a narrow swath of higher freezing precipitation totals in southwestern Arkansas on the 29th, while LO weakened and shifted this zone westward. Interestingly the 75th percentile icing broadened spatially (+5.6%, Table 7.1), with weak (< 5%) positive response against REAL for total precipitation accumulation and moderate precipitation rates.

For CLIM (REAL+0.85 K), precipitation over southwestern and west central Oklahoma appeared to intensify, evidenced by the broader area of above 50 mm totals. Meanwhile over Arkansas the south-central portion of the state showed peak accumulation, with eastward extension and northward shift. Compared to REAL there was an 11% increase in grid point extent above 75th percentile and an 18% increase > 2.5 $mmhr^{-1}$. HI (REAL+1.69 K) and P2 showed a change in peak accumulation morphology with a longitudinal extension from southwest through central Oklahoma. The latitudinal breadth of this region also contracted relative to REAL, CLIM and LO. In the eastern domain, HI showed a similar location but greater total accumulation to REAL, while P2 displayed increased icing to east-central Arkansas. Quantitatively both P2 and HI increased spatial extent (75th percentile) by 16%, 11.5% respectively. Above 20 mm P2 dropped to 5.5% while HI increased to 12.5% evidencing P2 grid point reduction in peak accumulation (supported visually, Fig. 7.1). Both also revealed increased precipitation intensity (~18 and 24% respectively).

Storm total rainfall (Fig. 7.2, Table 7.1) showed that warmer scenarios, in particular HI and P2, increased the spatial extent of 50+ mm accumulation. Table 7.1 provides further support. The number of grid points of accumulation above the 75th percentile for rainfall (~30 mm) and summed hourly totals were both increased,

especially for P2. Conversely, LO and M2 reduced spatial extent and total accumulations. The southwesterly contracted rainfall shield was visually apparent for M2. For snowfall (Fig. 7.3, Table 7.1) M2 produced greater amounts over much of central, southern and eastern Oklahoma, and through all but southeastern Arkansas. The northward shift of snowfall was apparent with the warmest SST simulations (HI, P2) yielding light snow or snow-free conditions central OK through central AR. Locations of relative maxima also changed. In a general sense, and over Arkansas in particular, an eastward shift in the heaviest snowfall was indicated for HI and P2. The values in Table 7.1 implied weakened intensity but broader spatial coverage when SST was reduced (e.g., M2), while both overall intensity and extent decreased as SST increased (especially P2).

Finally, Table 7.1 (bottom) also included percentage changes from control for all phase types ('total'). While the spatial coverage of total precipitation was not markedly different between simulations, differences at the 75th percentile (~45 mm) were more distinct, especially for P2 (+32%) and M2 (-37%). Accumulations for all phases increased between 3-9%, and 7-15% (> 2.5 mm hr^{-1}) for CLIM, HI and P2, while LO and M2 indicated a -6 and -20% difference, and -13%, -38.6% for rates above 2.5 mm hr^{-1} respectively. When referencing HI and LO to the climatology (HI=CLIM+0.84, LO=CLIM-1.46), negative changes in extent and accumulations for LO (-25, -10, -20% three left hand columns respectively) were greater than positive changes for HI (+17, +0.7, +0.8%), even after accounting for the proportional differences in SST (for all but grid point extent and assuming linear changes). Like the results of chapter 6, precipitation response to SST was seemingly greater as SST

Table 7.1: As Table 6.1 in chapter 6, but for the January 2010 case study, using the designation of FZRA/IP as discussed in the text (sec. 7.2). *The number of FZRA/IP gridpoints is accumulation > 5 mm, which was chosen since no portion of the domain had zero accumulation. Upper quartile of each phase type and all phase distributions used as measure of upper distribution change without compromising too much of the sample size: ice = 13 mm, rain = 30 mm, snow = 20 mm, and all phase (total) = 45 mm.

Type	# Grid Points* (# > 75th percentile Accum.)	Total Sum of hourly Accum. (1) x10^4 mm	Total sum Accum. > 2.5 mm hr^{-1} (2) x10^4	Ratio (2)/(1)
REAL	**Domain 3**			
FZRA/IP	25863 (12903)	31.4	14.1	0.45
RAIN	33770 (13670)	49.9	37.4	0.75
SNOW	22579 (8169)	17.6	6.1	0.35
CLIM				
FZRA/IP	27150 (14336)	34.8	16.7	0.48
RAIN	33948 (13634)	51.4	38.8	0.76
SNOW	21304 (6592)	16.4	6.4	0.39
P2				
FZRA/IP	24901 (15002)	32.7	16.6	0.51
RAIN	35851 (17361)	60.7	45.3	0.75
SNOW	21893 (4000)	14.0	4.6	0.33
M2				
FZRA/IP	23947 (11373)	23.8	5.9	0.25
RAIN	28696 (10896)	37.7	26.5	0.70
SNOW	25928 (5307)	16.7	3.0	0.18
HI				
FZRA/IP	26208 (14391)	34.4	17.5	0.51
RAIN	34495 (14353)	52.8	38.8	0.73
SNOW	21267 (6266)	16.1	6.0	0.38
LO				
FZRA/IP	24982 (13627)	32.4	14.3	0.44
RAIN	30850 (12161)	44.0	31.7	0.72
SNOW	22577 (6481)	16.7	4.3	0.26
Total (IP/FZRA)	**Departure from REAL (%)**			
CLIM	+0.23 (+5.00) *+7.00 (+11.34)*	+3.75 (+10.81)	+7.32 (+18.42)	
P2	+0.53 (-3.72) *+32.18 (+16.27)*	+8.66 (+4.31)	+15.27 (+17.87)	
M2	-4.43 (-7.41) *-36.59 (-11.86)*	-20.90 (-24.25)	-38.55 (-58.00)	
HI	-0.29 (+1.34) *+23.66 (+11.53)*	+4.41 (+9.51)	+8.08 (+24.31)	
LO	-4.63 (-3.41) *-18.18 (+5.61)*	-5.85 (+3.18)	-12.88 (+1.45)	

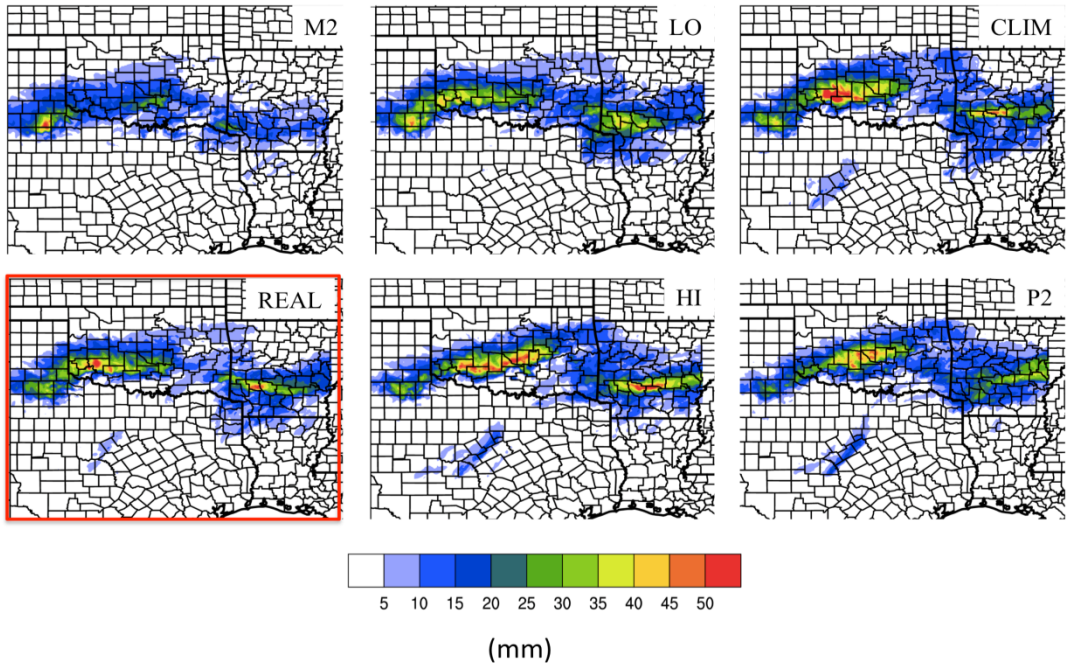

Figure 7.1: 48-hour accumulated freezing precipitation (FZRA, IP) for 00 UTC 28 – 00 UTC 30 January 2010 for WRF-ARW domain 3 for each SST simulation, denoted by the textbox. REAL is highlighted by the red box. State and county boundaries are overlaid.

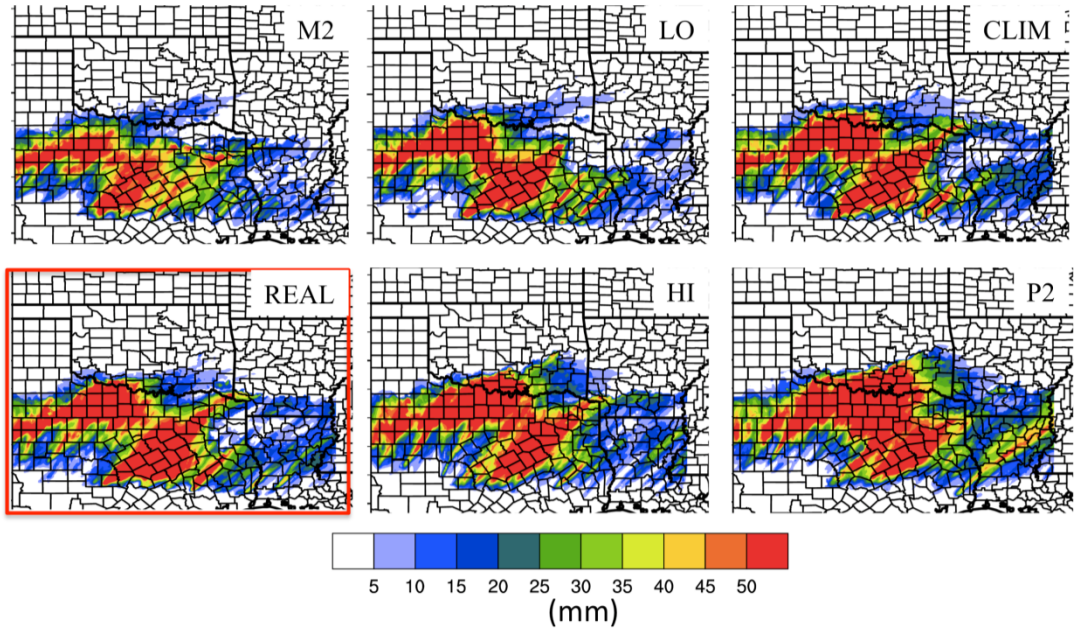

Figure 7.2: As Fig. 7.1 for 48-hour accumulated rainfall (mm).

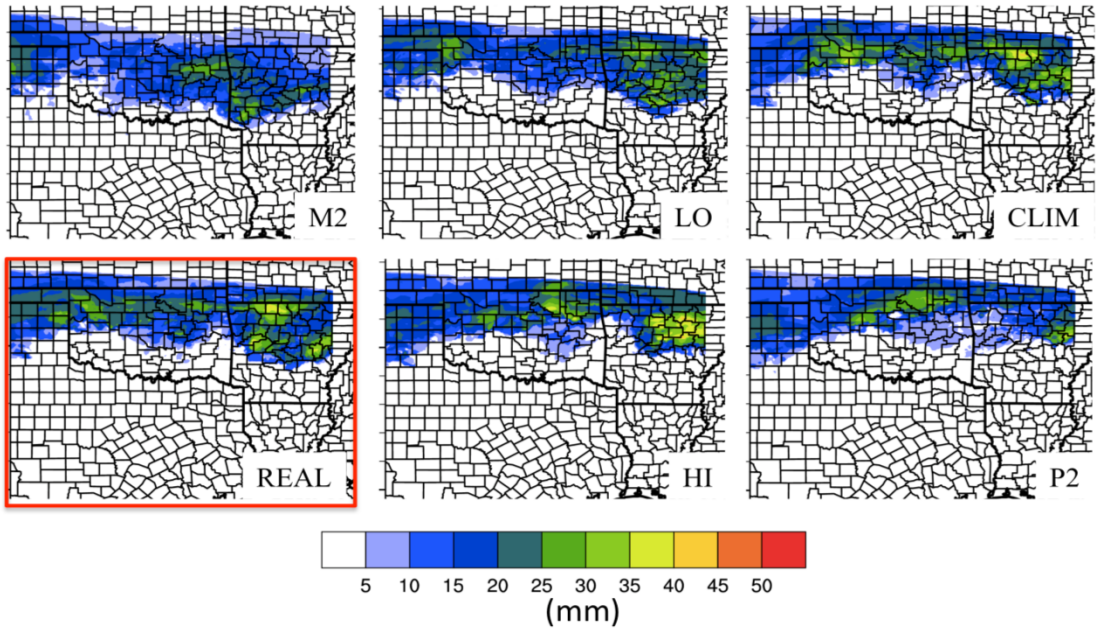

Figure 7.3: As Fig. 7.1 for accumulated snowfall (mm)

reduced from a control.

7.2.2 Radar reflectivity, and changes in precipitation intensity.

The methodology and rationale for the reflectivity distribution analysis was described in chapter 6 (Sec. 6.2.2). Here, the whole domain 3, and a zone over west/southwest Oklahoma were evaluated in Figures 7.4 and 7.5 respectively. The most interesting results are in the tails of the distribution. Radar reflectivities above 20 dbZ increased with increasing SST for the whole domain (Fig. 7.4), with very little difference between HI and P2, and a greater response to M2. For southwestern OK (Fig. 7.5), the M2 case yielded a large negative change (-70%) in reflectivity, attributed to the southward displacement of the heaviest precipitation. CLIM, HI, P2 all produced increased frequency at or above 35 dbZ reflectivity by 25-29%, with the greatest increase for CLIM. From Fig. 7.1, it is evident that the bulk of the highest (mixed

phase) accumulation remains in the southwestern quarter of Oklahoma (approximate location of domain used) for CLIM, but extended northeastward with HI and P2. As an example of the simulated reflectivity values from the WRF-ARW, Figure 7.6 shows the location of precipitation at 18 UTC 28 (12 noon CST). The figure clearly displays the larger and more intense precipitation shield for CLIM, HI and P2.

7.3 Thermal Profile

The evolution of the warm layer for this case study was introduced in chapter 4. Observations showed warm layer inversion development in the 12-hours prior to the initiation of precipitation (00-12 UTC January 28), as subfreezing air filtering into the region at the surface. The effect of SST on the thermal profile was investigated in the same fashion as chapter 6, sec 6.3 for two locations: southwest Oklahoma (Figure 7.7 7.8), and west-central Arkansas (Figure 7.9, 7.10).

7.3.1 Southwestern Oklahoma

Fig. 7.7 displays EMP and EFP for 12 UTC 28-12 UTC 30 January at 1-hour intervals. The non-zero EFP at 12 UTC (t12) indicated conditions suitable for mixed phase precipitation. According to results in chapter 2, and prior literature, greater EMP relative to EFP indicates an environment favorable for freezing rain over ice pellets. Such conditions were ongoing from t12-t20 for all SST scenarios, with the area between the EMP and EFP contours over this time typically greater for P2, HI and CLIM. Between t20 and t30 (20 UTC 28-06 UTC 29), REAL revealed a brief (< 2 hour) absence of a warm layer. This abrupt change in the thermal environment was well

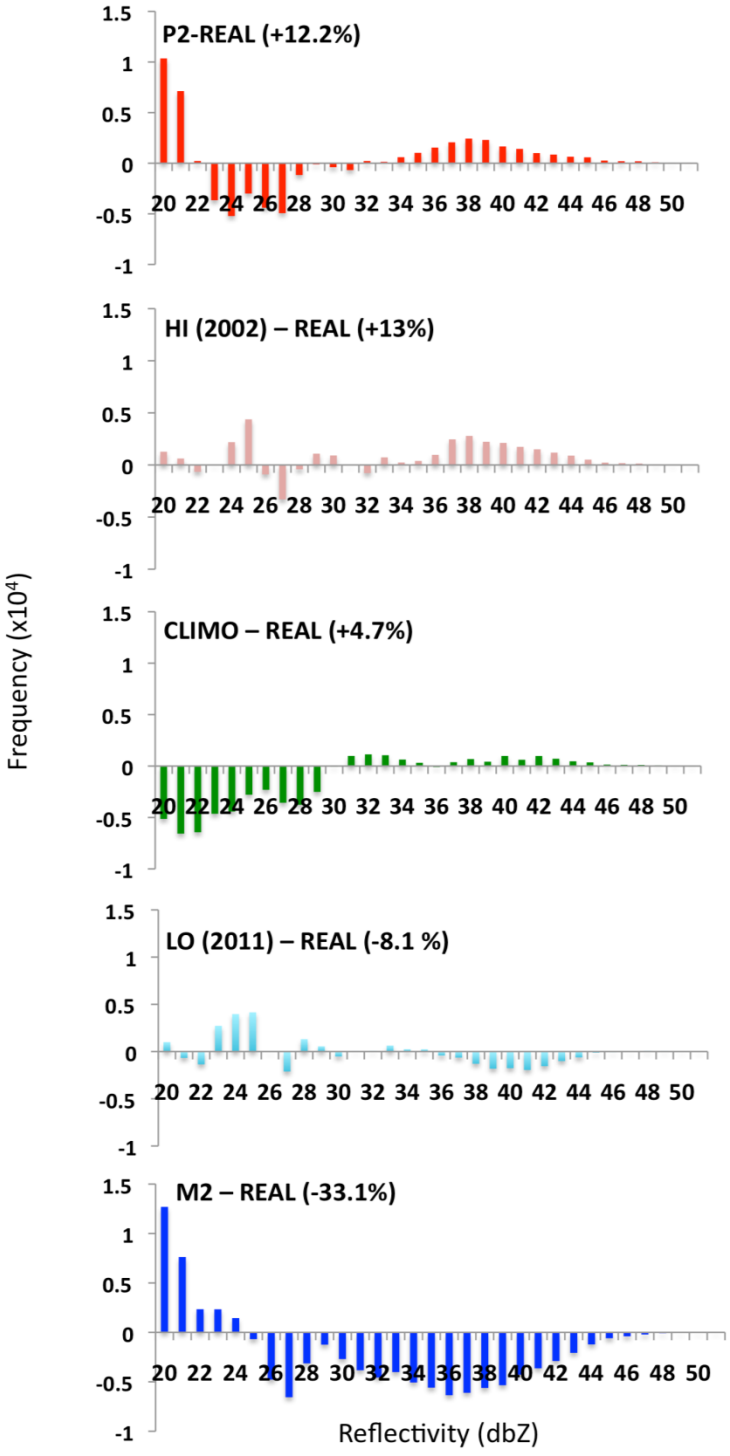

Figure 7.4: Simulated equivalent radar reflectivity histograms (> 20 dbZ) showing the change in frequency for each SST scenario with respect to REAL for all domain 3. The percentage value in parenthesis denotes the relative change in frequencies > 35 dbZ.

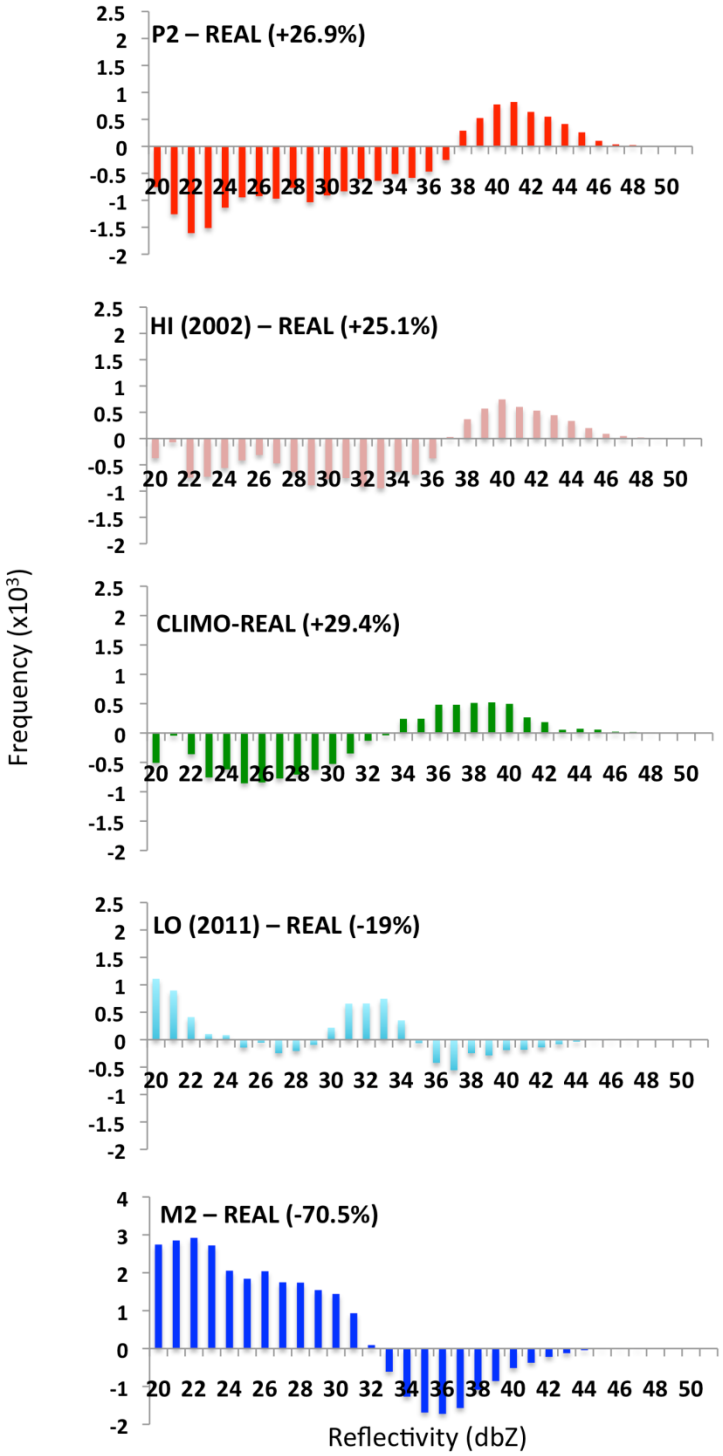

Figure 7.5: As Fig. 7.4 but for central-western Oklahoma bounded by 34.2-35.7°N, -97 to -99.5°W.

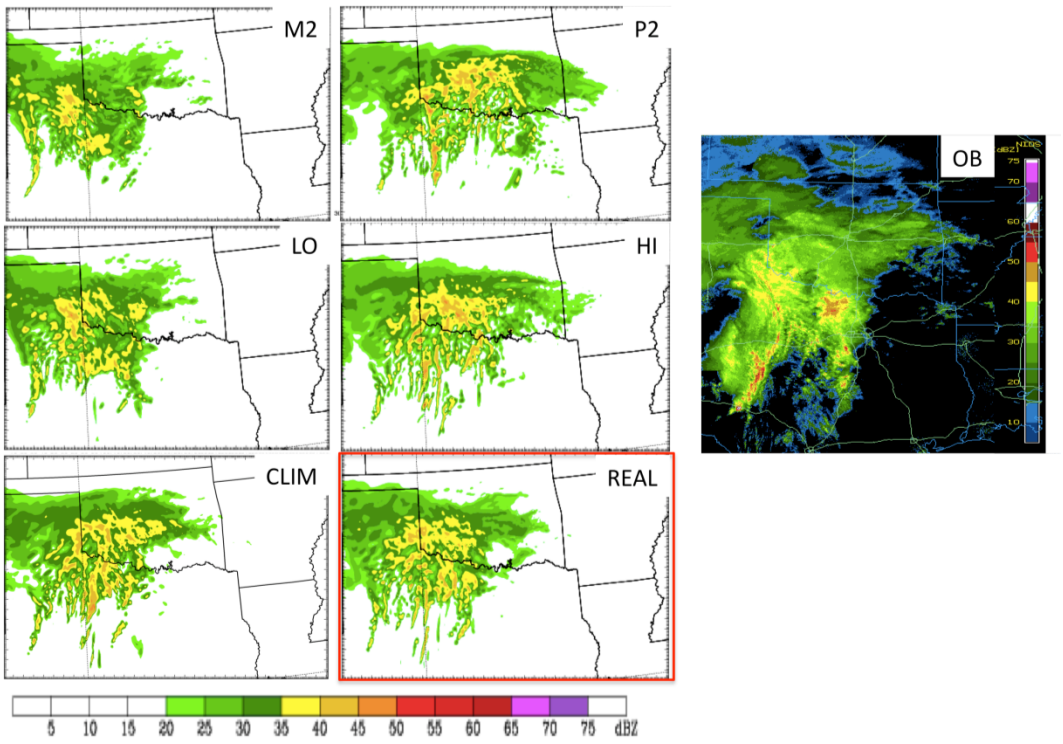

Figure 7.6: WRF-simulated equivalent radar reflectivity (dbZ) for each SST scenario valid at 18 UTC January 28. REAL highlighted by the red box. The observed composite reflectivity is shown on the right hand panel for the same domain. Note the difference in color-scheme for the observed case.

timed to increased precipitation rates (> 4 $mmhr^{-1}$), potentially cooling the inversion (not shown). The precipitation increase was on the northern edge of a developing linear convective line propagating east-southeast over Texas. The resulting mesoscale circulation (e.g., surface cold pool, low-level rear inflow jet) temporarily disrupted warm southerly flow into the freezing precipitation region.

During t24 and t30 the warm layer reestablished but not to its initial magnitude, and was co-located with a gradual increase in EFP due to a deepening refreezing layer. After t30, REAL EMP declined with complete erosion by t40. This pattern was more of less replicated by LO and M2. In the latter case, the warm layer was absent between

t24 and t28. Between t24-t30, EFP overtook or equaled EMP in magnitude, indicative of an environment potentially more conducive to ice pellets (e.g., REAL, LO, M2). CLIM and HI displayed the longest duration thermal profile for freezing rain between t12 and t30. The initially pronounced inversion for P2 (between t12 and t20) declined rapidly by t22, concurrent with heavy precipitation (not shown). An enhancement in EFP t20-t30 suggested a briefer window for purely freezing rain at this location.

Figure 7.8 is analogous to Fig. 7.7, except maximum (minimum) air temperatures at the 850 hPa (surface) layer are displayed. Between t12-t20 warm layer temperature was generally consistent between scenarios. The negative SSTA LO and M2 showed only weak recovery of above 0^{o}C temperatures after t30, while REAL showed greater temporal persistence. The warm layer of CLIM and HI was not interrupted during heavy precipitation, therefore yielding the greatest temporal duration, especially CLIM (28 hours, versus 18 REAL, 15 M2, 24 HI). HI also showed the most consistent warmth. P2 produced a warm layer as temporally persistent as HI but with reduced temperature t20-t36. The surface temperature evolution also showed faster decline after t20 for HI and P2 in particular (decreases below -5^{o}C at t30, t26 respectively), while M2, LO cooled more gradually (t50, t44 respectively). Apart from precipitation and mesoscale dynamics, these thermal responses are possibly tied to the progression of the 850 hPa low circulation and surface pressure field, explored in sec 7.4.

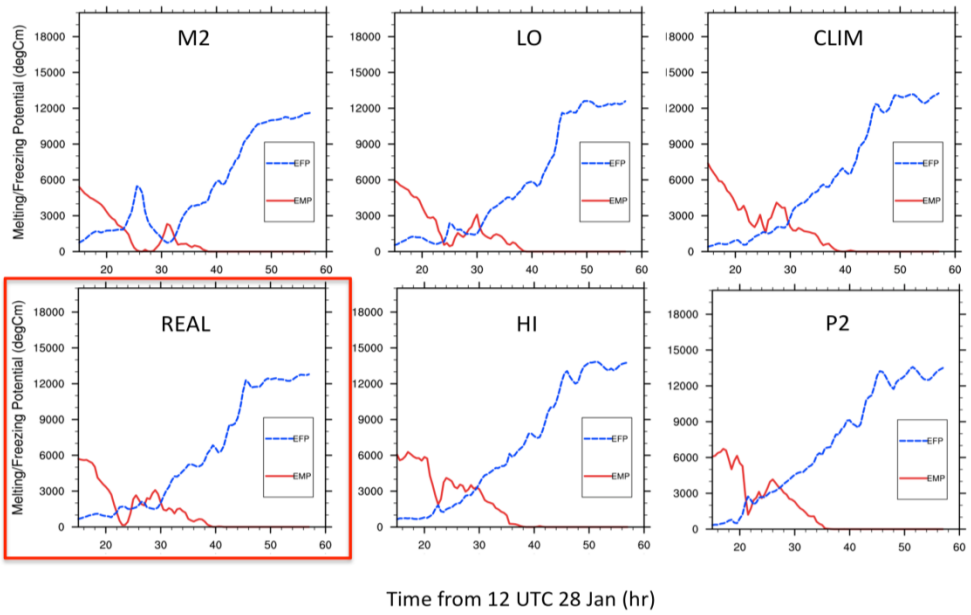

Figure 7.7: Timeseries of environmental melting potential (EMP, red), and freezing potential (EFP, blue) in ^{o}Cm valid for 34.9-35.3 ^{o}N, and 97.4-98^{o}W between 12 UTC January 28 (T12) and 12 UTC January 30 (T60).

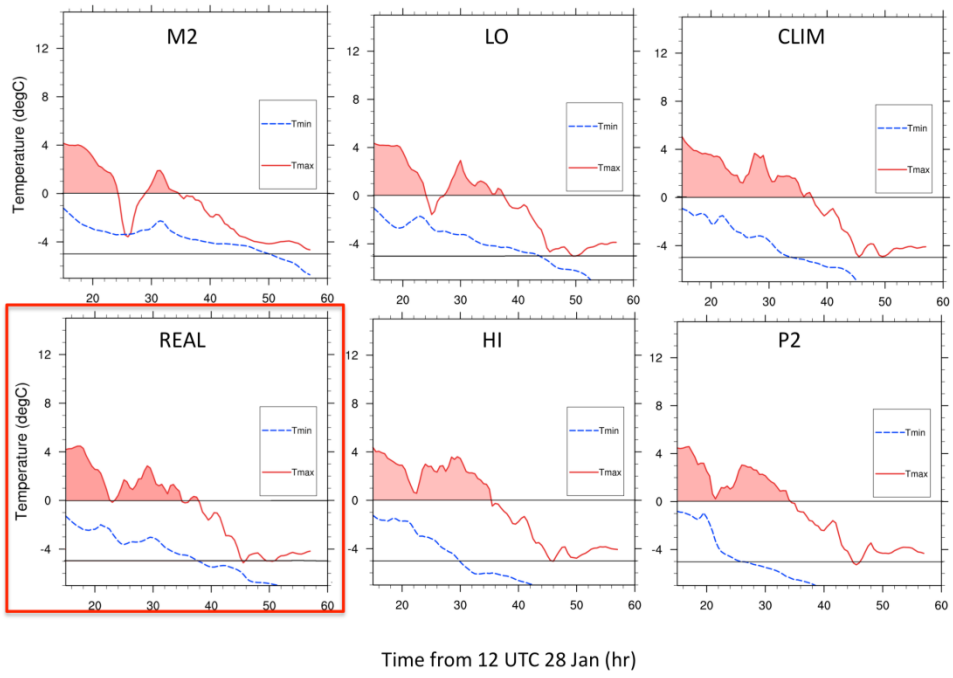

Figure 7.8: As Fig. 7.7 for maximum 850 hPa warm layer air temperature (red) and minimum surface temperature (blue). Area > 0^{o}C shaded to aid interpretation.

7.3.2 *Western Arkansas*

Figures 7.9 and 7.10 display EMP/EFP and air temperature characteristics of the warm and refreezing layers respectively for west-central Arkansas. In this region, freezing precipitation primarily occurred on January 29 (t24-t48). From t12 to t20, EFP = 0, and therefore no refreezing layer was present. For REAL, EMP exceeded EFP between t30 and t42, with the timing of warm layer development differing for the simulations in a more pronounced manner than observed for Oklahoma (e.g., Fig. 7.1). For M2, a very weak inversion (EMP < 500 ^{o}Cm) developed between t24 and t38, while the EFP ranged from 9000-3000 ^{o}Cm over the same period. This would likely favor IP and snow over freezing rain. The evolution for LO and REAL was generally similar, showing the most prominent inversion t30-t40. CLIM, HI and P2 revealed a deeper and earlier forming warm layer at t20. The period wherein EMP exceeded EFP ranges from t28-t42 (CLIM), to t20-t44 (HI, P2).

Figure 7.10 further reinforced assertions made above, and demonstrated pronounced change in warm layer (850 hPa) temperature and temporal duration with SST, confirming the sensitivity of freezing rain potential to SST for this location. The specific warm layer qualities are not necessarily in linear relationship with basin average SST. For example, LO evidenced slightly higher warm layer temperature, while HI showed greater duration with temperature > 3^{o}C compared with P2. These variations may be in part due to precipitation intensities in addition to dynamical differences, and possibly a greater contribution from regional SSTA within the fetch of this location (sec 7.5).

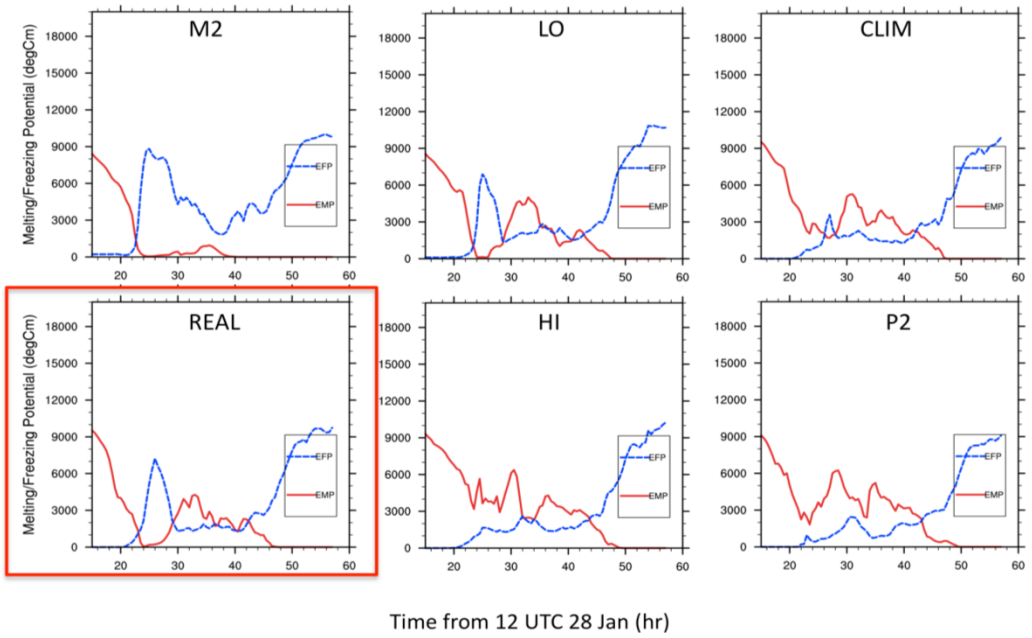

Figure 7.9: Timeseries of environmental melting potential (EMP, red), and freezing potential (EFP, blue) in ^{o}Cm valid for 34.7-35.0 ^{o}N, and 93.2-93.7^{o}W between 12 UTC January 28 (t12) and 12 UTC January 30 (t60).

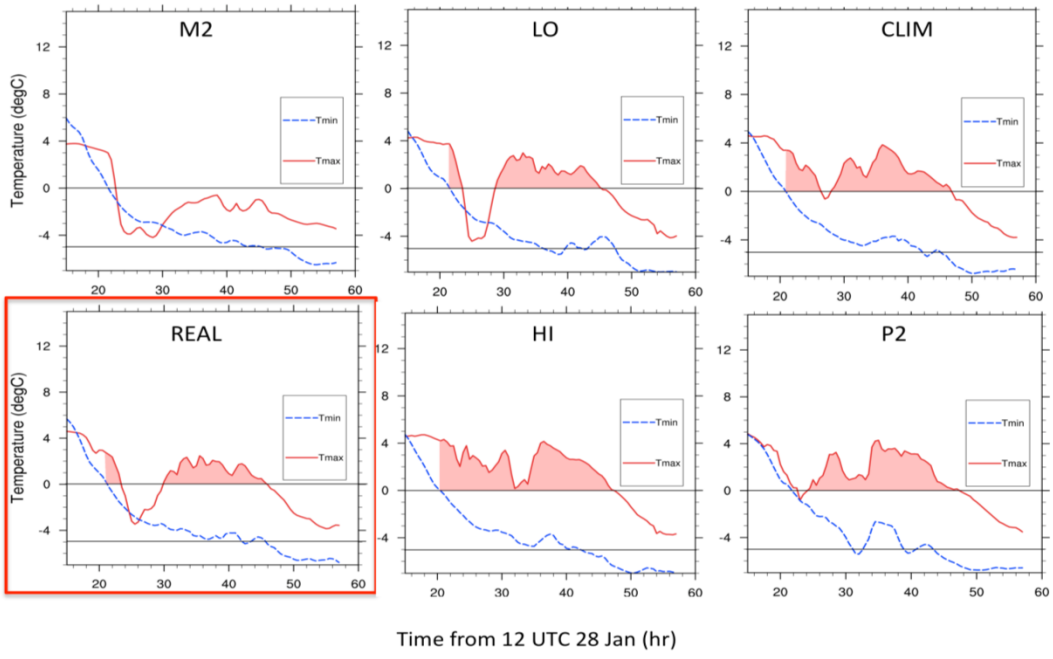

Figure 7.10: As Fig. 7.9 for maximum 850 hPa warm layer air temperature (red) and surface temperature (blue). Area > 0^{o}C shaded to aid interpretation.

7.3.3 Cloud and radiation

Figure 7.11 shows the change in cloud cover with SST, valid for the ACRF-SGP (Lamont, OK) in order to be directly comparable to the observed cloud profile shown in chapter 5. The magnitude of total mixing ratio (proxy for cloud), and its vertical penetration increased with increasing SST during hours 15-30. Furthermore, after hour 30, a more notable decrease in cloud cover was implied for HI and P2, especially for mid-high cloud. In contrast, M2, LO and REAL suggested precipitating cloud through hour 50. This provides further evidence of a dynamical change with SST resulting in more rapid eastward movement of precipitation. Consistent with Figure 7.11, longwave and shortwave radiation components (not shown) for the same location support increased (decreased) shortwave (downward longwave) radiation for lower SST (especially M2), while a domain 3 average evidenced reduced solar radiation for positive SSTA on January 28, and increased radiation on January 29.

7.4 Moisture and Dynamics

So far in this chapter we have demonstrated a robust response of precipitation and warm layer characteristics to the six SST simulations described in chapter 4. For this case study, results show more similarity to Ramos De Silva et al. (2006) in the warmer and earlier-forming warm layer response to increased SST. However our work also revealed differences in location and intensity of precipitation that the aforementioned study did not specify. Here, dynamical evolution indicated precipitation primarily in response to strong warm air and moisture advection aloft and north of a near stationary surface cold front and in the northeastern quadrant of an 850 hPa low.

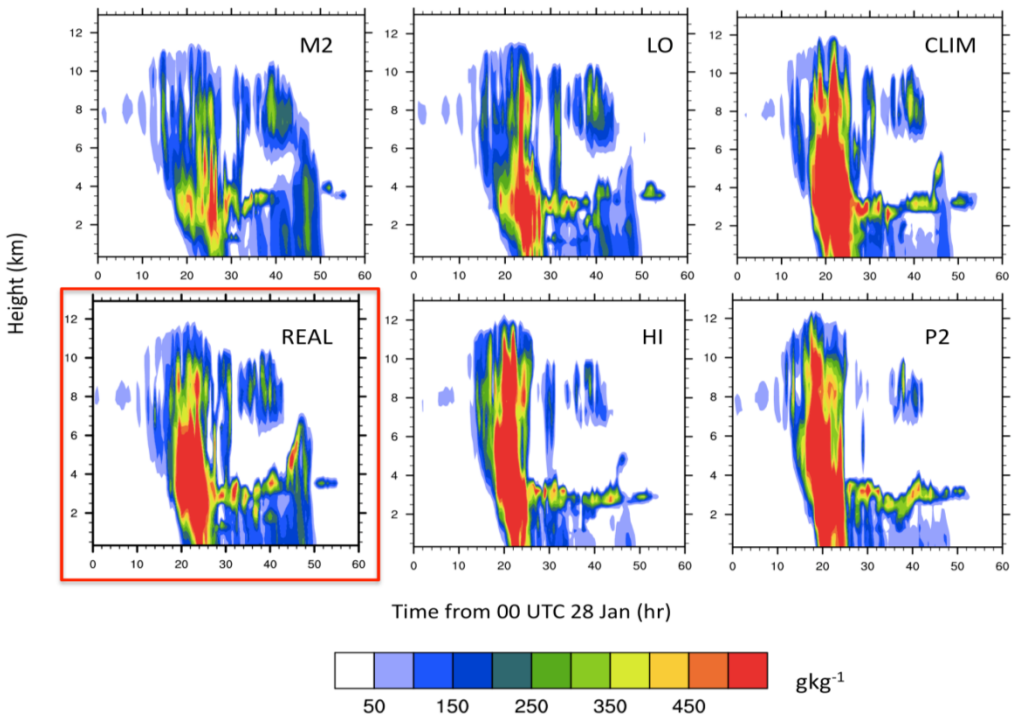

Figure 7.11: Sum of rain, snow, graupel, ice and cloud mixing ratios as a proxy for cloud cover valid over ACRF Lamont for all SST scenarios (REAL highlighted by a red box). The x-axis of each panel shows time (hour) from 00 UTC January 28, while the vertical axis shows height in km above ground.

This circulation and attendant precipitation translated eastward and centered over northwestern Texas early on January 29. The approaching trough axis overtook the surface quasi-stationary front near the Gulf coast and intensified a weak low perturbation into a surface low-pressure system, however by this time the potential for mixed-phase precipitation had departed the SGP. The role of SST in producing dynamical changes to the movement and strength of this system is now considered.

Figure 7.12 displays a hovmuller diagram of sea level pressure difference from REAL, calculated over 30-38^{o}N in latitude. The diagram tracks the longitudinal movement and intensification of a weak open wave surface low with time (12 UTC Jan 28-12 UTC Jan 30). When comparing the 'extremes', M2 and P2, it is apparent that P2

(M2) lowered (raised) mean sea level pressure by up to 4-6 hPa relative to REAL, with the other simulations generally falling monotonically within these evolutions. Although the location center of the developing low-pressure did not change, the central pressure changes were confirmed by plotting SLP every 2 hours over the domain for the duration of the event (not shown).

Examination of model 500-850 hPa thickness and pressure falls shown in Fig. 7.13 further confirmed the intensification of the low, especially in P2 and HI. The equation below for QG thickness tendency (Lackmann 2011, eqn. 5.6) can be used to provide insight into these findings:

$$\frac{\partial[T]}{\partial t} = -\vec{V}_{g1000}\nabla[T] + \omega(\Gamma_{ad} - \Gamma_{env}) + [\frac{Q}{C_p}] \qquad (7.1)$$

Where thickness tendency (left hand side) is related to the advection of thickness by the geostrophic wind (first term on the right hand side), a term composed of the difference between observed and adiabatic lapse rates, multiplied by the vertical velocity (second RHS), and the net diabatic heating/cooling in the air column (third RHS).

For each simulation, the mid-level trough did not vary discernibly in its location and amplitude (not shown). Therefore, the dominant changes resulting from the imposed SST fields were likely in response to lower tropospheric thermodynamic changes. The warmer surface environment over the far southern U.S and GOM promoted by a warmer GOM was linked to an increase in latent heat flux (see next section), and low-level warm air advection (Fig. 7.13). It is anticipated that this warmer

and moister near surface layer decreased low-level static stability. This assertion was investigated by plotting cross sections of static stability at 2-hour intervals from the northern GOM to the Oklahoma Panhandle using domain 2 (not shown). It was apparent that layer static stability was reduced above 850 hPa as SST increased (see also Fig. 7.16). This promoted decreased resistance to pressure falls, primarily through weakening of RHS term 2 in Eqn. 7.1. Term 2 typically acts as a brake to development, as increased vertical velocity (ω) acts against thermal advection. For moister, warmer conditions, term 2 is reduced, as a saturated airmass yields use of the saturated adiabatic lapse rate, which is smaller than the comparable unsaturated magnitude.

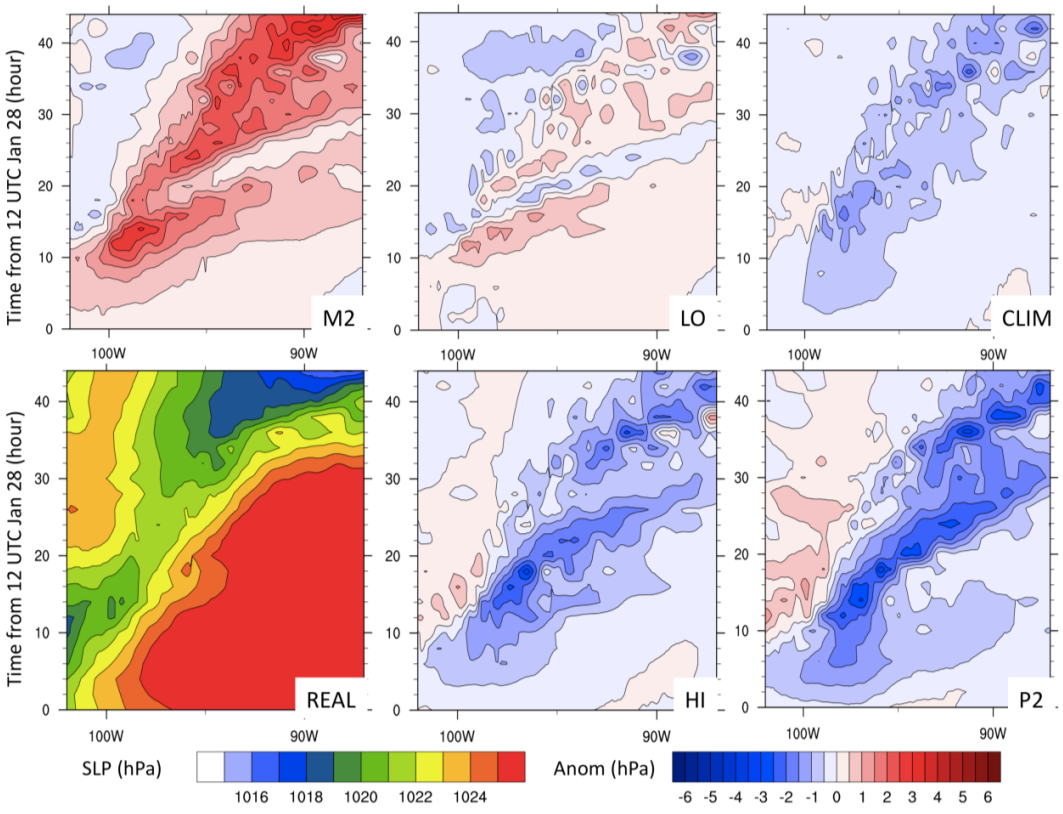

Figure 7.12: Longitude-time hovmuller diagram of sea level pressure (SLP) averaged over latitude band 31-38°N. Each scenario other than REAL is expressed as a difference from REAL in hPa, while full SLP for REAL is displayed. The y-axis shows the time from 12 UTC January 28, ending at hour 48 (12 UTC January 30).

Figure 7.13 highlights the increase (decrease) in low-level thickness and pressure falls ahead of the surface and 850 hPa low when SST was increased (decreased). The signal for the 850 hPa circulation may be more evident from this figure, which indicated a northeastward displacement in the warmer SST cases, toward the location of greatest positive thickness advection. Positive 500-850 hPa thickness implies a reduction in surface-850 hPa geopotential height, with a greater magnitude of this parameter suggestive of a deeper attendant circulation. This result is consistent with baroclinic energetics. We calculated a measure of baroclinic instability using the Eady parameter (growth rate, day^{-1}, not shown) given by Graff and LaCasce (2014). Zonal and time averaged magnitudes plotted as a function of height, latitude evidenced northward (southward) displacement in the maximum for P2 (M2), and an intensification for the former, particularly ~850 hPa (+0.6-0.8 day^{-1} versus REAL, near $3N^{o}N$, compared with +0.4-0.6 day^{-1} at ~750 hPa near $32^{o}N$ for M2). The thermal gradient and associated baroclinic instability was indistinct between LO and REAl, while HI produced a northward displacement to $34^{o}N$, but of weaker magnitude, and lower vertical penetration. CLIM was similar to HI but further reduced on both counts. P2 evidenced a more substantial northward tilt in baroclinicity with altitude. This poleward orientation is likely reflective of strengthened positive temperature flux, which is necessary for growing disturbances but enhanced in this case. The added (reduced) warmth supplied with strongly positive (negative) SSTA implies increased (decreased) low-level thermal anomalies (Fig. 7.13), and by conservation of potential vorticity increases (decreases) low-level vorticity, and the strength of the circulation.

Graff and LaCasce (2014) among others note that stronger systems tend to self-advect more rapidly, consistent with our observation.

Figure 7.14 and 7.15 show the magnitude of the column integrated moisture transport, based on equation 6.1, given by Ressler et al. (2012) averaged 12 UTC 28 – 00 UTC 29 (Fig. 7.14), and 12 UTC 29 – 00 UTC 30 (Fig. 7.15). Also displayed are 850 hPa winds (ms^{-1}), and mixing ratio (gkg^{-1}). The results suggest that the column integrated vertical moisture transport increased, generally monotonically, with increasing basin SST. For example, in Fig. 7.14, M2 showed a narrow plume of 5+ gkg^{-1} mixing ratio at low-levels with a moisture transport of $3.5x10^2$ kgm^1s^{-1} in the warm sector, while REAL was associated with higher mixing ratio and moisture transport of 4.5-5 $x10^2$ $kgm^{-1}s^{-1}$. P2 produced the broadest region of higher mixing ratio, and 5.5-6 $x10^2$ $kgm^{-1}s^{-1}$ transport. This represents roughly a 40-50% increase between M2 and P2. Additionally, the spatial extent of $3x10^2$+ $kgm^{-1}s^{-1}$ approximately doubled, and the location of the maxima shifted east-northeastward, resulting from the previously discussed greater height/pressure falls and baroclinicity promoted by the warmer lower boundary. Furthermore, average wind speed between approximately 900-200 hPa supported increased southwesterly steering flow (not shown). The increased moisture transport was at least partially in response to the intensification of a low-level jet east of the low, which exhibited a 5-7.5 kt increase (decrease) relative to REAL for P2 (M2), based on a 24-hour average of 850 hPa wind speed between 12 UTC 28-29 (not shown). The increase was attributed to the drop in SLP and increase in low-level geopotential height gradient over the Southern Plains.

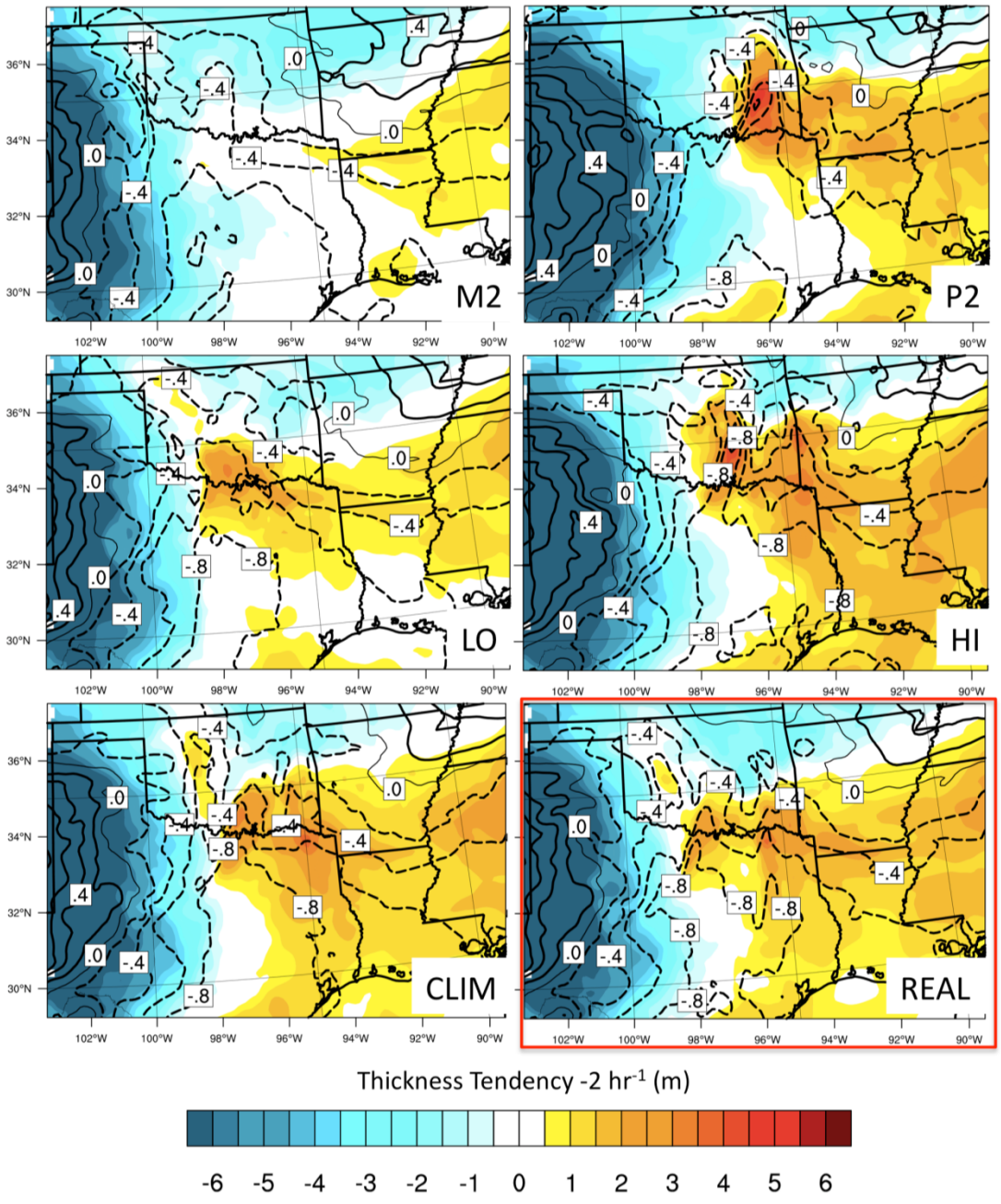

Figure 7.13: Average 850-500 hPa thickness tendency per 2-hours between 12 UTC 28-12 UTC 30 January (shaded, in m). 850 – 500 hPa used in place of 1000-500 hPa layer due to higher terrain in the west. Sea level pressure average tendencies are contoured (black lines), with dashed > 0, intervals of 0.2 hPa per 2 hours.

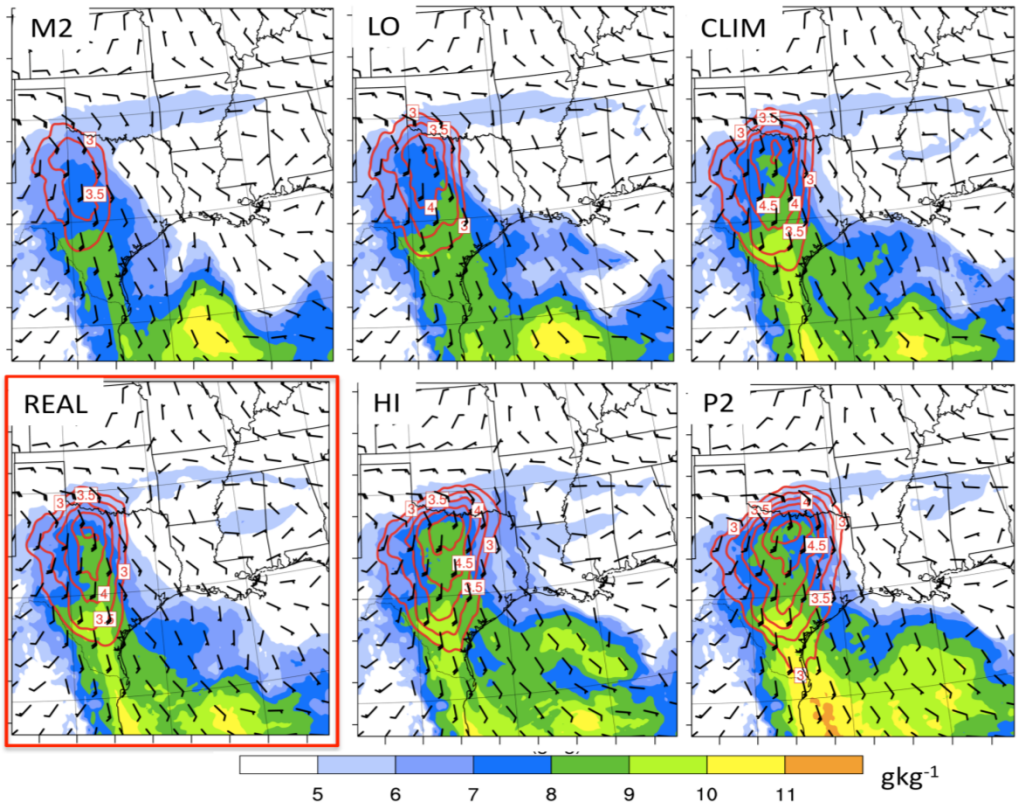

Figure 7.14: WRF domain 2 850 hPa mixing ratio (g kg^{-1}), wind field (barbs, ms^{-1}) and 900-400 hPa integrated horizontal moisture transport (x10^{2} kgm^{-1}s^{-1}) contoured in red at intervals of 0.5 above 3x10^{2} for 12 UTC 28 – 00 UTC 29 January. REAL highlighted by the red box.

In order to further examine the diabatic contribution to dynamical changes in the system we can use 'PV thinking' (e.g., Brennan et al. 2008). Potential vorticity (PV) is given by equation 7.2 below:

$$PV = -g(\zeta_\theta + f)\left(\frac{\partial \theta}{\partial p}\right) \qquad (7.2)$$

PV is conserved for frictionless, adiabatic flow, and is a function of absolute vorticity and static stability. Lackmann (2011, p. 86-88) suggests that diabatic processes can be determined through the appearance of localized, non-conserved cyclonic maxima in the

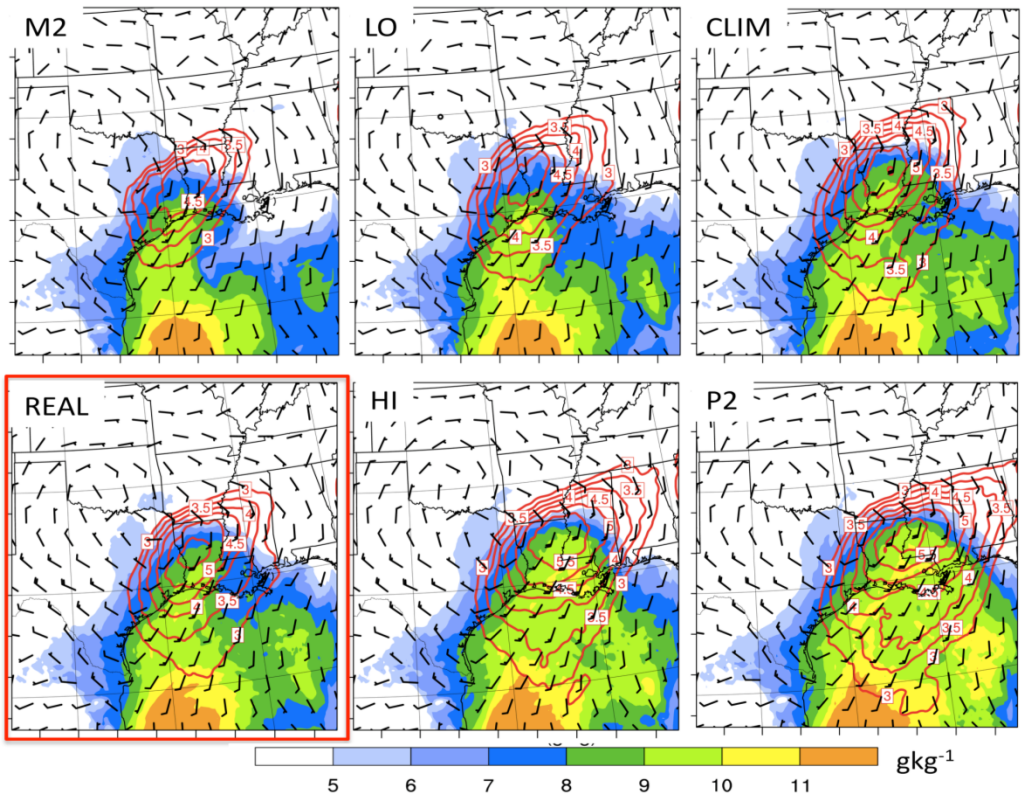

Figure 7.15: As Fig. 7.14 for 12 UTC 29 – 00 UTC 30 January.

PV field (positive PV anomalies). Lower tropospheric maxima in particular indicate diabatic processes associated with layer heating (also indicated by the increased vertical separation of potential temperature, θ in the lower troposphere, and an increased low-level static stability below the level of maximum heating). Commonly this is in response to condensational heating and latent heat release during heavy precipitation (e.g., Hoskins 1990, Lackmann, 2002, Ludwig et al. 2013). Piecewise inversions of the PV field have been calculated by numerous studies to recover wind and height fields associated with a given PV anomaly (e.g., Davis and Emanuel, 1991, Stoelinga 1996, Lackmann, 2002, Brennan and Lackmann, 2005). Among others, this work

demonstrated that low-level PV anomalies can profoundly impact the wind field in their vicinity, with implications for moisture transport.

To determine whether such processes were operating here, we examined the spatial distribution of 850 hPa positive PV against radar reflectivity and the low-level wind field, shown in Fig. 7.16 for M2, REAL and P2. Furthermore, we evaluate a cross section of these variables along an axis roughly perpendicular to the temperature gradient over the SGP, valid at 20 UTC January 28 as heavy precipitation moved into west-central portions of the state. REAL (center) indicates a region of high low level PV (> 2.5 PVU) extending over northwestern Texas, in the vicinity of the center of the 850 hPa cyclonic circulation and in the wake of heavy precipitation. Furthermore, low-level cyclonic PV tended to show northward development in the vicinity of strong low-level condensational heating promoted by precipitation (not shown), suggestive of production via latent heat release. Compared to REAL, M2 indicated a smaller spatial region of positive PV, potentially resulting from the weaker precipitation intensity north and east of the center of circulation. P2 in contrast showed a northerly and easterly expansion of high PV into south central Oklahoma. The effect of this anomaly was to perturb the low-level wind field, inducing an enhanced cyclonic circulation (Fig. 7.16, center, e.g., Ahmadi-Givi et al. 2004). The stronger 850 hPa flow for P2 may therefore have been promoted by the expansion of positive PV during heavy precipitation. This appears to enable a positive feedback mechanism where increased low-level WAA promoted by warmer SST contributed to lowering static stability (e.g., Fig. 7.16, bottom) and encouraging ascent, coupled with increased moisture potential enhancing precipitation. Increased precipitation promoted diabatic PV generation, which supported

the persistence of a low-level cyclonic circulation anomaly, the enhancement of low-level wind speed, and subsequently moisture transport (e.g., Fig. 7.16 center, Lackmann 2011, p113). These responses likely further promoted pressure/height falls east of the PV anomaly and low-level circulation, aiding in its intensity and eastward movement.

Though not shown here, further examination of the evolution of the system through January 29 supported observations of the event in showing drier air advecting into the region late on the 28th, disrupting the precipitation shield. Concurrently to the south a convective line developed and moved southeastward. The early development of this line can be seen for P2, and to some extent REAL in Fig. 7.16 as positive PV is intensified in a north-south orientation. This PV anomaly separates from the region to the west associated with the low-level circulation and mid-level trough, and follows the convective line, aiding in the enhancement of northward temperature and moisture advection to its east and into the mixed-phase region over Arkansas, especially for P2 (not shown).

Notably, the reservoir of high stratospheric PV was largely separated from the cyclonic low-level PV during the mixed-phase portion of the SGP winter storm (not shown). During the passage of the system over the 48-hour period strong cyclogenesis was not evident. The aforementioned Eady parameter did not extend through the depth of the troposphere, implying no phase lock and strong growth potential with the approaching upper trough. Nonetheless, low-level baroclinic instability, height falls increased latent heat flux, and moisture transport promoted modest strengthening of the 850 hPa low, and dynamically induced intensification of precipitation with greater SST that appeared to exceed what might have been anticipated from moisture effects alone.

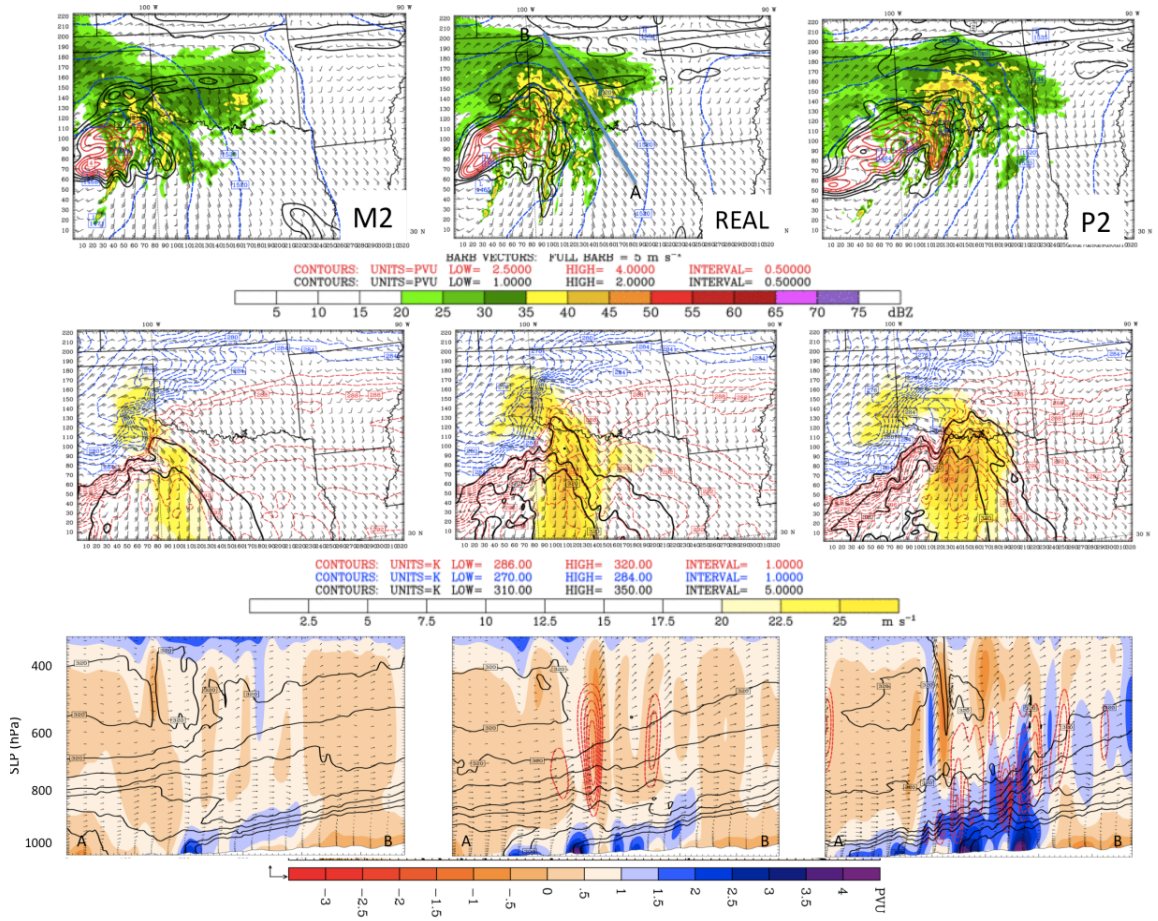

Figure 7.16: Multi-panel plot depicting the spatial distribution of potential vorticity and associated circulation during heavy precipitation at 2000 UTC January 28 for M2 (left), REAL (center), and P2 (right). Top panels show PV in PVU (1 PVU = 10^{-6} K $kg^{-1}m^{-2}s^{-1}$), with black (red) contours below (above) 2.5 PVU at 0.5 PVU intervals. Simulated radar reflectivity (dbZ) is shaded, and 850 hPa geopotential height (blue contours) and wind vectors overlaid. Center panels show 850 hPa winds and wind speed, with values > 20 ms^{-1} shaded. Equivalent potential temperature (θ_e) overlaid in black contours (intervals of 5 K above 310 K), and potential temperature above (below) 284 K in red (blue) at 850 hPa. The 284 K isotherm when reduced to 100 hPa is approximately 273 K. The bottom panels show a cross section SE-NW through A-B (top center) north of the center of circulation and roughly perpendicular to the low-level temperature gradient. PV is shaded in PVU, with condensational heating above 2 K hr^{-1} (red contours), and θ_e in K (black contours).

The converse was observed for M2, where the large negative departure in SST promoted a weaker circulation displaced to the south, and reduced northward extent of warm-moist air, subsequently weakening precipitation rates for Oklahoma/Arkansas, while still generally retaining high (yet spatially contracted) precipitation totals over Texas where moisture transport maximized.

7.5 Air Mass Trajectories and Meteorological Characteristics

Similar to chapter 6, 4-day (96 hour) back trajectories are evaluated for two times, and in this case, two locations during mixed phase precipitation, that is, west-central Oklahoma at 2100 UTC 28 January, and southwestern Arkansas at 12 UTC 29 January. Trajectories were calculated for the near surface (975 hPa), warm layer (near 850 hPa), 725 hPa, and 500 hPa.

7.5.1 West-central Oklahoma

During heavy freezing precipitation at 21 UTC (15 CST), the 975 hPa near surface trajectory (not shown) supported southward advection of cold air from western Canada, with a southeastward movement until t-24 hours, when the trajectory decelerated and curved into the freezing precipitation zone from the northeast. Path changes with SST were negligible. Temperatures near the surface over the northern and central Plains were < -10^{o}C and did not change with simulation, while warmer SSTA produced a very slight increase in near surface temperatures over the far southern states (< 1^{o}C, not shown). The air parcel southward movement was also marked by gradual descent from ~1.5 km AGL (to ~400 AGL), and associated adiabatic warming.

At the 850 hPa (warm) layer, shown in Fig. 7.17, each scenario revealed a similar trajectory path and altitude change, depicting the gradual descent of southeastward moving cold air into the marine planetary boundary layer (PBL) over the north central GOM. Subsequent anticyclonic recurvature into the warm sector of the developing low, and rapid ascent into the freezing precipitation zone was observed (indicative of strong upward vertical motion). This movement is perhaps representative of a warm conveyor belt structure (WCB), linked to strong ascent, and poleward energy and moisture transport (Fuhrmann 2011, Eckhardt et al. 2004). On average, the air parcel spent nearly 28 hours in the GOM PBL, being subject to heat and moisture fluxes from the ocean surface. Each panel displays the 48-hour average (t-48-t0) SSTA field for the simulation used, 850 hPa mixing ratio, and latent heat flux in Wm^{-2}. Mixing ratio in Fig. 7.17 indicates the earlier northward advection from the western GOM, while at this time the trajectory was offset to the east of the maxima, associated with the progression of the trough. The increase in mixing ratio reflects increased basin SST.

Meteorological characteristics into the warm layer, including equivalent potential temperature (θ_e) and air temperature, humidity and precipitation, diabatic heating/cooling and mixing ratio are plotted in Figs. 7.18, 7.19 and 7.20 respectively. The method for estimating diabatic temperature change was provided in Fuhrmann and Konrad (2013), calculated as the difference between the adiabatic and observed temperature at 6-hour intervals. In Fig. 7.18, increases in θ_e correspond well to initial movement over the GOM from the continent (~t-42). It is expected that the influx of moisture associated with latent heating over the ocean produced the observed increase, being most notable for warmer SST (CLIM, HI, P2) (see also Fig. 7.19, 7.20). In these

cases, the air parcel temperature also markedly increased as the trajectory descended over the GOM, while moisture was most rapidly accumulated between t-42 and t-24 as it reached its southernmost extent over the northern GOM. The greatest positive SST for this region of the Gulf were actually in HI, where the trajectory passed over a region of +1-2 K SSTA and 150-200 Wm^{-2} latent heating. Contrast to P2, where SSTA in the same region was closer to +0.5-1 K, producing only a small difference from CLIM, due to the generally weak positive anomalies over which the air parcel passed more directly (Fig. 7.17).

For lower SST (REAL, LO and M2) moisture was accumulated at a later stage (See Fig. 7.17, 7.18), typically between t-36 and t-30. For M2, the greatest influx of moisture occurred at the air parcel's southernmost point, and also possibly during a maximum in solar insolation (18 UTC, 12 CST), with (average) latent heating near 100 Wm^{-2}. REAL and LO were associated with similar latent heat and temperature profiles for the northern GOM, and the increase in moisture appeared to correspond with trajectory path over a region of maximum latent heat flux for the region (~150 Wm^{-2}).

Diabatic changes for the final 60 hours of the trajectory, shown in Fig. 7.20, indicate that the initial advection over the GOM was associated with strong diabatic heating into the air parcel for P2 and CLIM, weaker positive heating for HI, while REAL LO and M2 were only weakly positive or even weakly negative at the stage where mixing ratio was increased for these scenarios. This diabatic cooling under a regime of rapid moisture accumulation may be related to other effects, such as radiative cooling. In the final 6-12 hours, adiabatic and diabatic cooling occurred through ascent, switching to diabatic heating likely associated with precipitation condensation, for all

but M2. The rapid decrease in mixing ratio was associated with moisture removal via precipitation (Fuhrmann and Konrad 2013). End point (t0) mixing ratios remained slightly higher for HI, and lowest for M2.

Trajectory locations and altitudes terminating at 725 hPa (approximate top of warm layer) are shown in Fig. 7.21, while 7.22 and 7.23 display select meteorology. In each simulation the majority of the back trajectory was over the GOM. Typically this was a direct northward movement from the southwestern Gulf, however P2 indicated a slow recurvature over the western and central basin. The trajectory altitudes were variable, with initially higher altitudes accompanying paths skirting mountainous eastern Mexico. Gradual descent occurred for most trajectories between t-24 and t-6 over the southern U.S, prior to rapid ascent into the precipitation region. These differing paths, particularly between t-96 and t-48, also produced more distinct differences in the meteorological character of each trajectory (Fig. 7.22, 7.23). Between t-48 and t0, the lower altitude of P2 (after t-60), coupled with warm SST basin-wide, produced a notable increase in temperature/θ_e. After t-30, when all trajectories descend below 2 km over the ocean, the magnitudes of temperature fell in line with the basin average, that is, monotonic increase between M2 and P2, with ~4 K (8 K) difference between these two extremes at t0. Due to the extended residence time over the basin, most trajectories had relative humidities in excess of 70% through the final 48-hours, decreasing slightly over the southern Plains, before increasing as the air parcel ascends to saturation by t0. M2 was notable for its low relative humidity t-96 to t-12, indicative of a drier air mass aloft over the GOM.

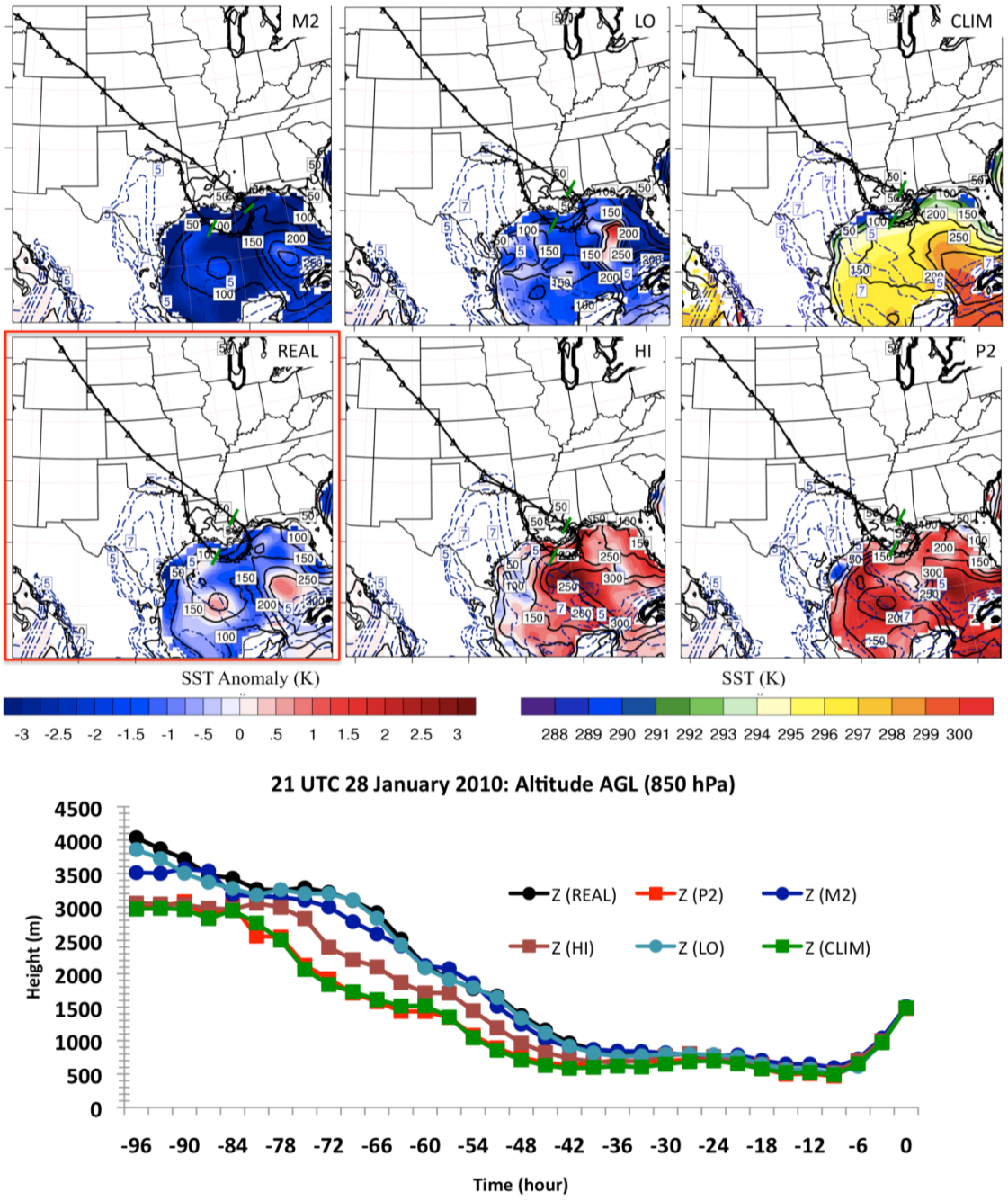

Figure 7.17: Top: 850 hPa back trajectories into west-central Oklahoma (~35°N, 98°W), valid at 21 UTC January 28. Each trajectory displays triangular markers at 3-hour intervals, with intersecting green line at t-24 and t-48. Overlaid is the SST anomaly field relative to climatology (CLIM displays full SST), with 48-hour average latent heat flux (Wm^{-2}) ending at 21 UTC (black contoured lines), and 850 hPa mixing ratio (blue dashed lines) at intervals of 1 gkg^{-1} > 5 gkg^{-1}. Bottom: timeseries of trajectory altitudes for each SST simulation**.**

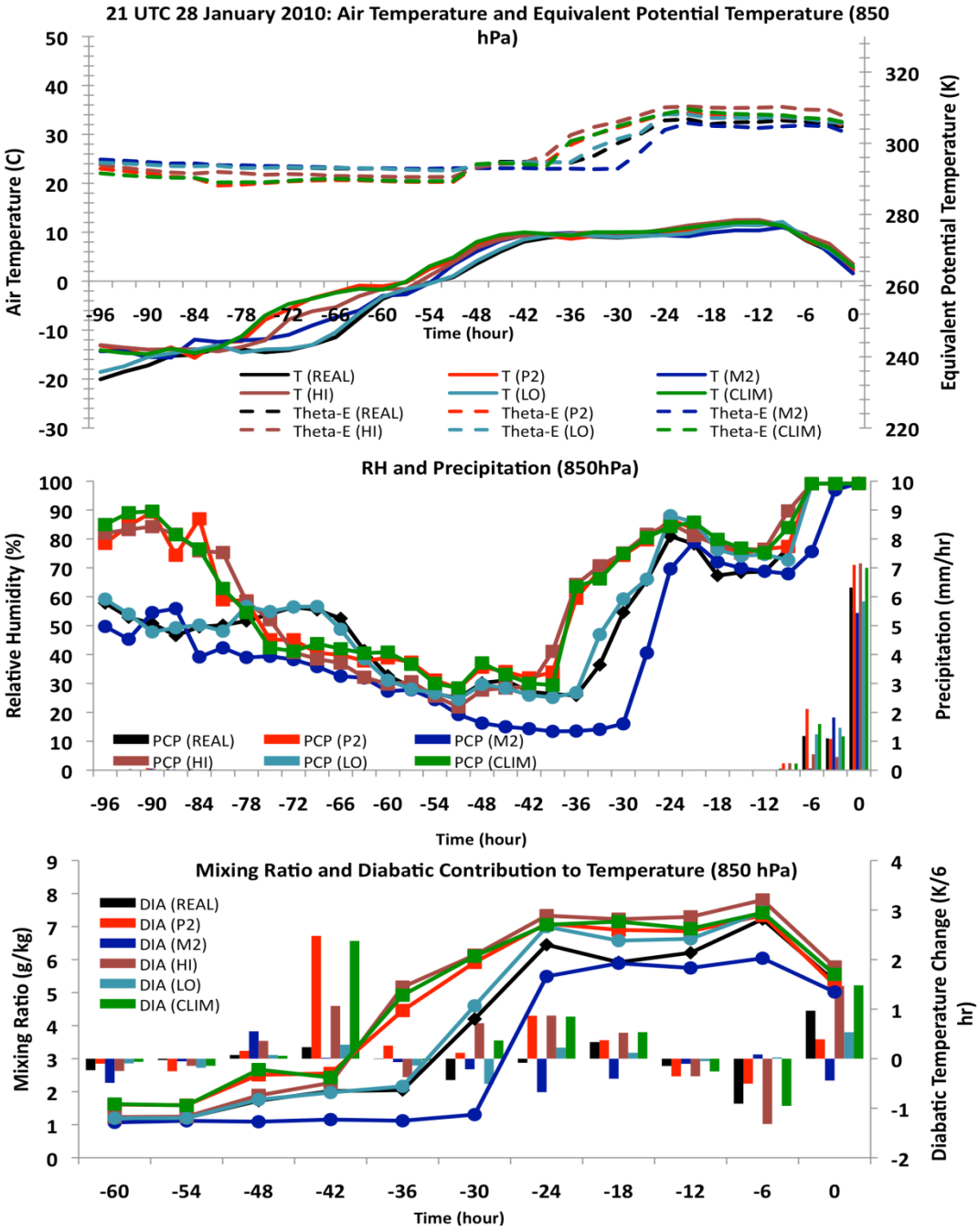

Figure 7.18: (TOP): Timeseries of air temperature (solid lines, ^{o}C), and θ_e (dashed lines, K) following the trajectory for each SST simulation ending at 850 hPa (21 UTC Jan 28). **Figure 7.19** (MID): Relative humidity (solid lines, %), and precipitation (mmhr^{-1}) along trajectory (color code as in Fig. 7.17, 7.18). **Figure 7.20** (BOT): Mixing ratio (gkg^{-1} lines), and diabatic contribution to temperature (bars, 6-hour accumulated temperature change) for the final 60-trajectory hours into the 850 hPa layer. Diabatic component calculated as in Fuhrmann and Konrad (2013).

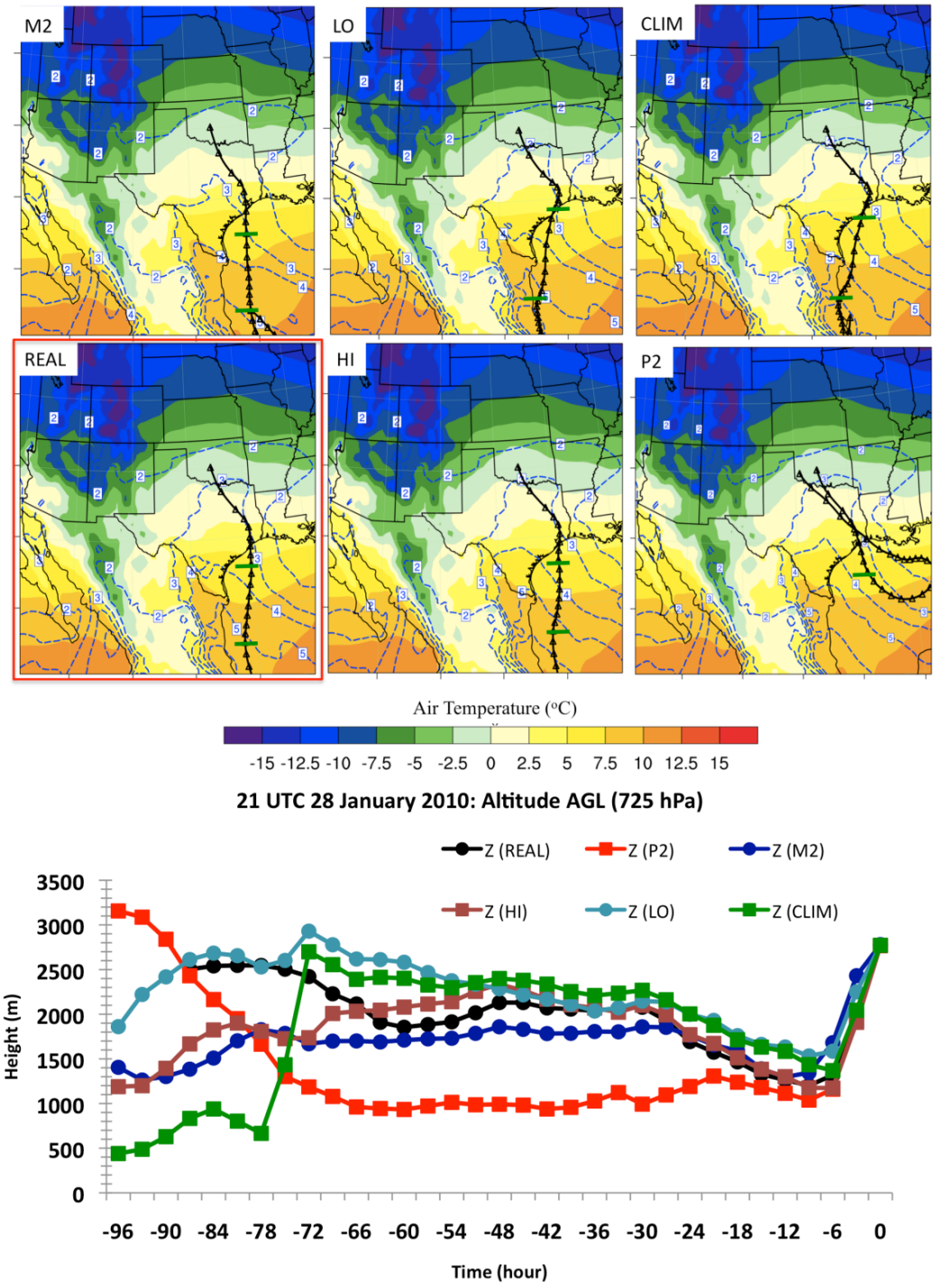

Figure 7.21: Top: 725 hPa trajectory paths. Trajectories displayed as in Fig. 7.18. Air temperatures (filled contours) averaged over 48-hours ending at 21 UTC 28 for the 650-850 hPa layer, while mixing ratio (blue dashed lines) was estimated over the same time and layer. Bottom: Timeseries of trajectory altitudes for each simulation.

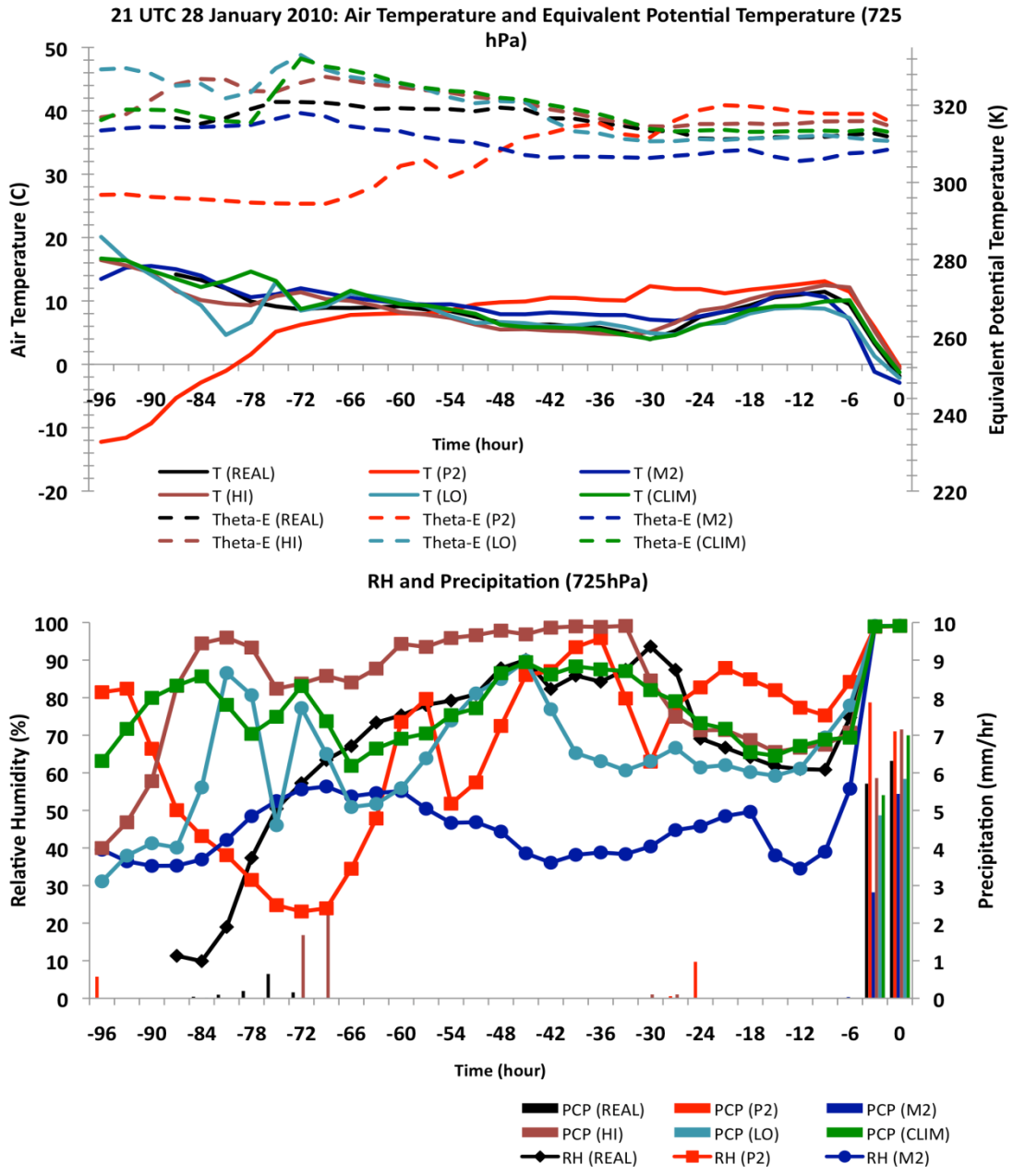

Figure 7.22: (TOP) As Fig. 7.19 for the 725 hPa trajectories in Fig. 7.22. **Figure 7.23 (BOT):** As Fig. 7.20 but for the 725 hPa trajectories.

Trajectory and altitude profiles for the 500 hPa layer and its meteorological parameters were analyzed, but for the sake of space were not displayed. All trajectories were over or adjacent to the GOM basin, with the majority of scenarios indicating

anticyclonic flow. M2 was associated with flow northward from the Yucatan largely over coastal eastern Mexico. This trajectory also remained at high altitude, possibly associated with the regional terrain. These circulation differences may have been related to the progression of the low. Moisture and temperature characteristics at this level were strongly tied to the path and altitude of each trajectory, with M2 notably cooler and drier. The long path over the GOM allowed for the accumulation of moisture, which was again enhanced with warmer SST. The bulk of the moisture for HI and P2 was obtained t-66 - t-18, where θ_e increased from ~295 K to 330 K (not shown). The times where moisture was most rapidly increased by the air parcel also agreed well to the trajectory location over a relative maximum in SSTA and latent heat flux.

7.5.2 West-central Arkansas

Prior sections of this chapter indicated that Arkansas experienced freezing precipitation during 29 January, which was sensitive to SST. M2 produced little/no accumulation, while HI and P2 showed greater freezing precipitation intensity (Fig. 7.1, 7.9). At 975 hPa (not shown) the northerly component near-surface flow increased in speed. Between t-48 and t-24, air parcels moved from the Canadian border to southern IL, thereafter decelerating and curving in a similar fashion as previously observed to approach the region from the northeast. The gradual descent of the air parcel was consistent with earlier observations, as was the increase in its temperature, albeit less modification of the airmass was indicated due to the stronger cold air advection. There was once again little change in evolution between simulations, confirming that airflow at this level was primarily influenced by the arctic continental airmass.

By 12 UTC 29, the maximum temperature within the warm layer was observed in REAL to have shifted aloft near 800 hPa, and it is therefore this layer that was evaluated instead of 850 hPa shown in Fig. 7.24. At this time and location, the duration of curvature of the air parcel trajectory over the GOM PBL had expanded to near 60 hours. Once again, the movement of the initially cool airmass over the warm ocean basin generated abundant latent heating of the air parcel. Trajectory paths were predominantly over the northeast and north central basin.

The lagrangian meteorological characteristics, shown in Figure 7.25, 7.26 and 7.27 are displayed in the same fashion as Figs. 7.18-7.20 respectively. As before, the resulting moisture and temperature profile of the trajectory incident to the warm layer was sensitive to altitude, SSTA, and latent heat fluxes along its path. For example, in REAL, moisture increased most rapidly t-45 to t-30, shown by relative humidity increases of 60% (Fig. 7.26), and mixing ratio from 1 gkg^{-1} to $7gkg^{-1}$ (Fig. 7.27). At this time the air parcel was moving over a local SSTA maximum (Fig. 7.23). Latent heat flux in this region was 200-250 Wm^{-2}. The air parcel subsequently moved northward into a region of lower SST, and the near constant θ_e (Fig. 7.25) implied little further diabatic heat flux. In the precipitation zone, it was again apparent that the greatest moisture was associated with greater SST along the trajectory path, this moisture generally being realized in higher precipitation rates. The HI trajectory gained the majority of its moisture between t-33 and t-18, where θ_e increased by 25 K, humidity by 50%, and mixing ratio by 8 gkg^{-1}. Concurrently, the trajectory passed from a localized zone of neutral/weakly negative SSTA to a positive SSTA zone near +2 K, with 200-250 Wm^{-2} average latent heat flux. This enhanced the heat and moisture content of the

air parcel, which continued to gradually increase as the air parcel remained over anomalously warm SSTA until t-12. For P2, the temporal evolution was similar, but the maximum SSTA over which the air parcel passed in its final 12-15 hours were lower than HI. This result further emphasizes that location of the SSTA maxima (or minima) may be important to the eventual warm layer temperature and moisture magnitude of a given region. In this case, the pronounced positive SSTA in HI over the northern basin. Diabatic contributions to temperature, shown in Fig. 7.27, supported the earlier heating maximum for M2, linked to trajectory passage over the warmest (often southernmost) portion of the basin. In contrast, CLIM, P2 and HI maximized diabatic contributions in the final 30 hours.

At 725 hPa, shown in Fig. 7.28, the trajectory path and altitude evolution was similar to the 800 hPa layer, with the exception of a longer fetch over the GOM As such, the meteorological parameters also resemble those discussed, and are therefore not displayed. At this level the amount of moisture in the precipitation zone increased with higher SST, but with HI once again yielding the highest moisture into this region.

At 500 hPa (not shown) all but M2 continued to derive thermal and moisture characteristics from the GOM. The air parcel trajectory for M2 was sourced from the Pacific Ocean (t-96). Large differences in altitude resulted from M2 passing over the intermountain west. LO, REAL and CLIM skirted higher terrain in eastern Mexico, while HI and P2 remaining purely oceanic. In the final 6-hours, the weaker ascent rate for M2 demonstrated reduced vertical motion, corroborated by low precipitation rates at this time (e.g., Fig. 7.26). The meteorological characteristics at this layer are not shown, however, the trajectory path was a strong factor in the temperature and moisture

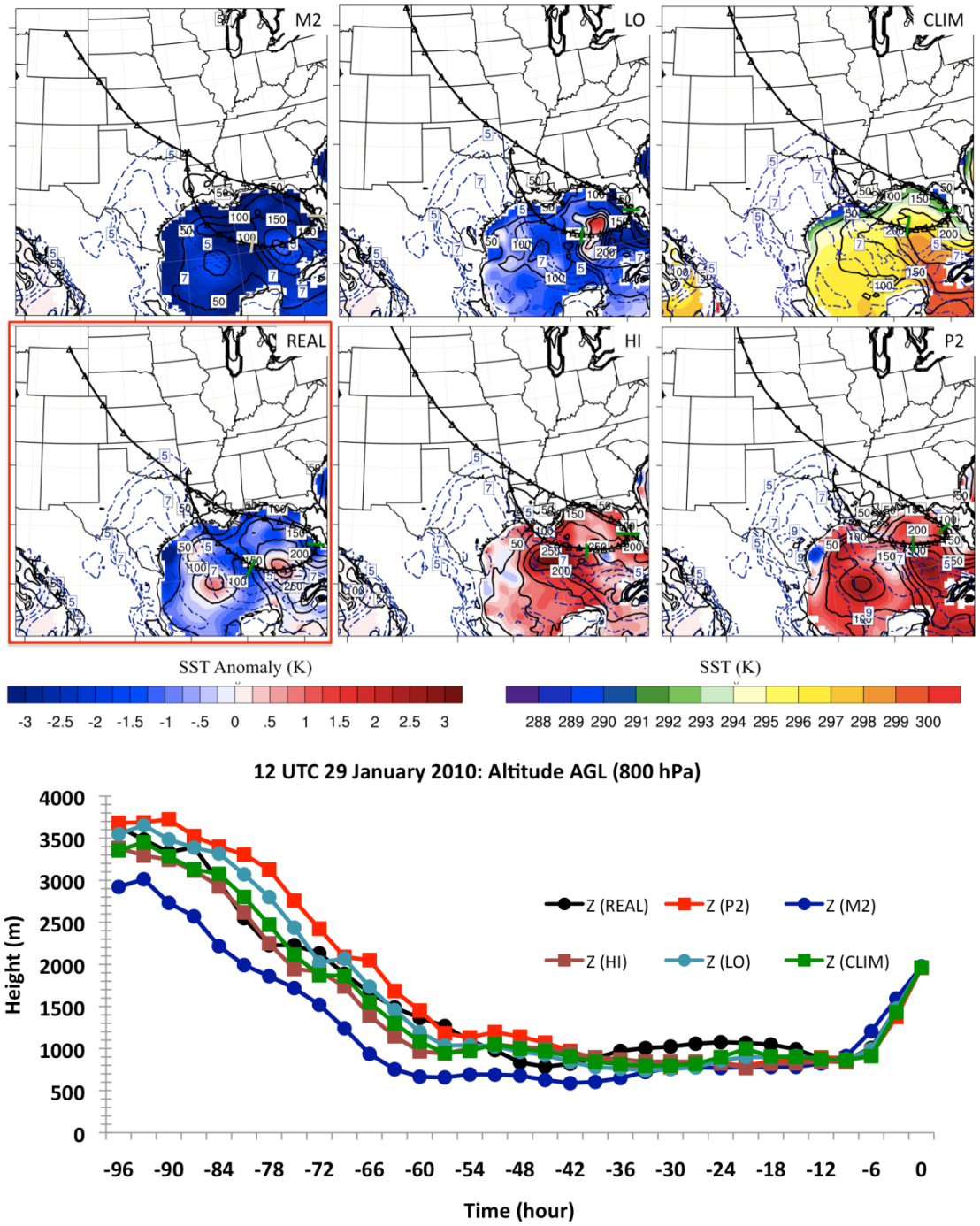

Figure 7.24: As Fig. 7.17 but for trajectories incident to west central Arkansas during heavy freezing precipitation on 12 UTC January 29. The 800 hPa is used as the warm layer maximum temperature was observed to be closer to this altitude at this time (not shown).

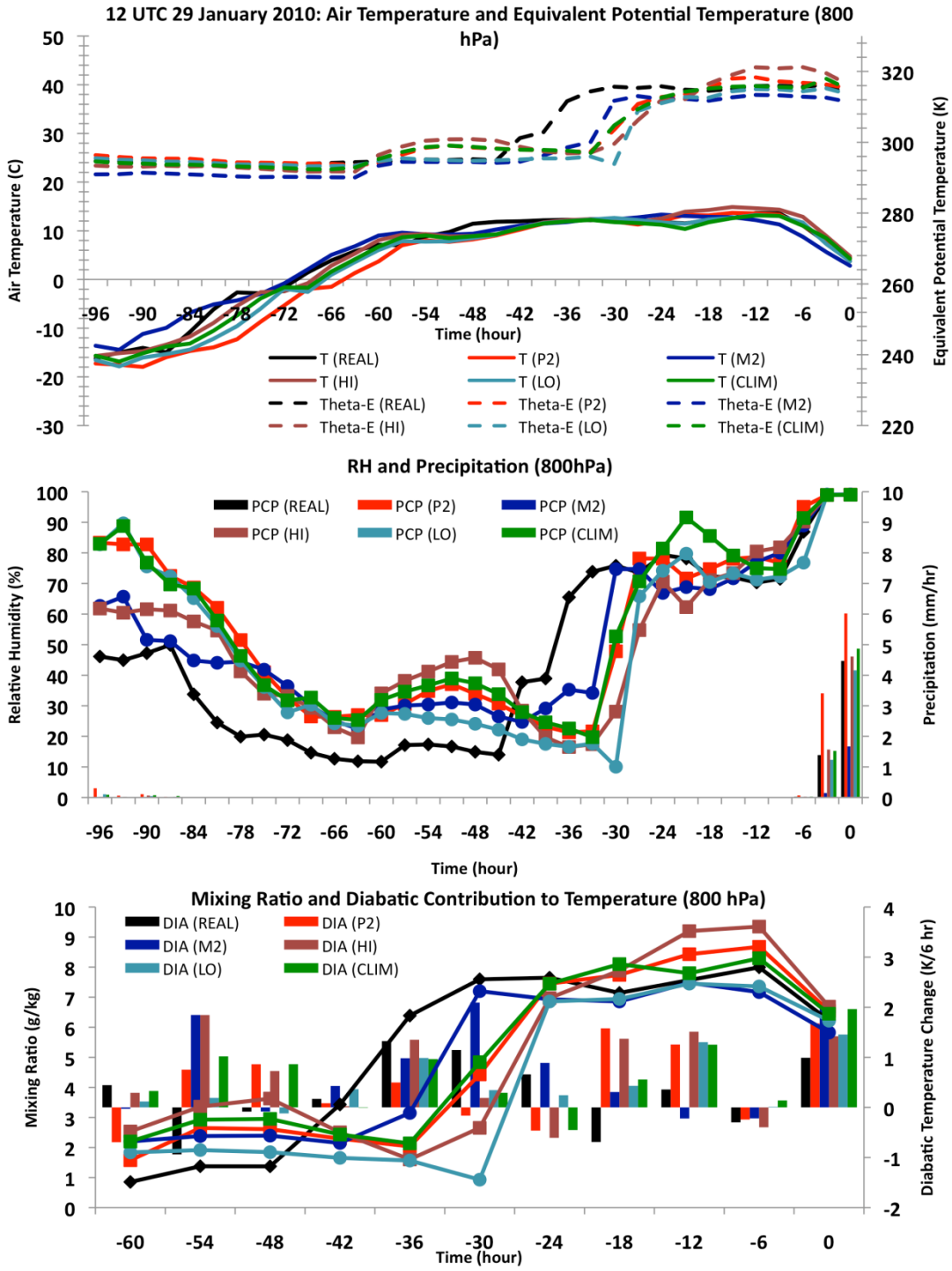

Figure 7.25: (TOP), Figure 7.26 (MID) and 7.27 (BOT): As Figs 7.18-7.20 but for the 800 hPa layer, 12 UTC January 29 west-central Arkansas

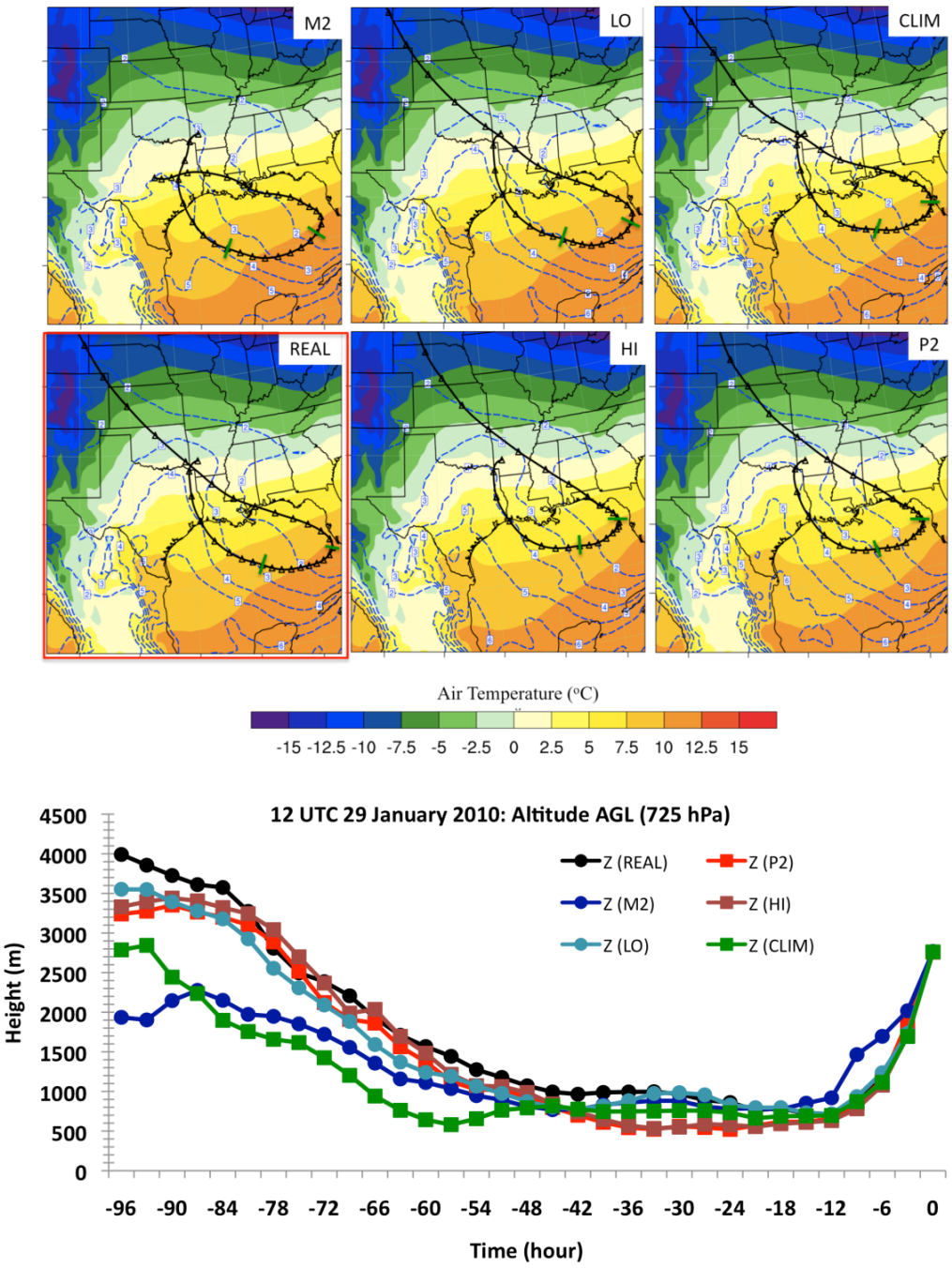

Figure 7.28: As Fig. 7.21 for 12 UTC January 29 west-central Arkansas

content. Nonetheless, the dramatic ascent and adiabatic cooling in the final 6-12 hours lead to only small temperature differences between SST simulations with additional moisture in HI and P2 likely transferred to heavier precipitation.

7.6 Ice Storm Impacts by SST Scenario

This chapter has revealed another notable link between SST and the subsequent evolution of winter precipitation to the SGP domain, but for a different synoptic context compared to that of chapter 6. Based on the model verification from chapter 5, the spatial location and accumulation of freezing precipitation was reasonably simulated. This latter case study is therefore investigated briefly from a socioeconomic perspective. Recently a system to rank ice storm severity in terms of a dimensionless 0-5 scale 'SPIA©' (Sperry-Piltz Ice Accumulation) index was developed by Sydney Sperry (Director of Public Relations, Communications and Research, Oklahoma Association of Electric Cooperatives), and Steven Piltz (Meteorologist in Charge, NWS Tulsa). This index uses a set of key parameters, such as surface temperature, wind speed and precipitation accumulation, deriving an estimate of the potential damage of an approaching event. The technique was developed principally with electrical infrastructure in mind. The SPIA© index rankings are available on the website http://www.spia-index.com/. Similar to the Fujita measure for tornados, ice storm severity increases with index, with ranks of 0-1 indicative of weak icing and 3+ major icing. Ice accumulations can be lower under conditions of high-wind to obtain a higher index, since strong winds increase the risk of damage to utilities.

Using the set of criteria for wind and ice accumulation defined by SPIA©, 48-hour precipitation accumulations (00 UTC 28-00 UTC 30 January) were expressed in index form. This required an assessment of the freezing rain component of total precipitation, which meant using a scheme to assess the relative proportion of precipitation falling as ice pellets (IP) versus freezing rain (FZRA). We use our upper

limit assumption described in sec. 7.2, with an additional estimate for ice accretion. Freezing rain accretion on a given surface is highly complex and dependent on numerous variables including precipitation rate, wind speed and direction, temperature, orientation of surface object, evaporative cooling and latent heat of freezing. In order to simplify these processes and maximize utility, ice accretion models use assumptions including uniform radial thickness, and typically concentrate on parameters such as wind speed, and precipitation rate (e.g., Pytlak et al. 2010). A full discussion on the processes used to estimate accretion is tangential to this work. Nonetheless, it is necessary to mention that total accumulated precipitation in the form of freezing rain is not at a 1-1 ratio with the total liquid equivalent precipitation on a given surface. An equation for radial ice accumulation from Pytlak et al. (2010) is given as:

$$R_{eq} = \sum_i \frac{1}{\rho_i \pi} [(P_i \rho_w)^2 + (3.6 V_i w_i)^2]^{1/2} \qquad (7.3)$$

Where R_{eq} is the radial thickness, ρ_I and ρ_w the density of ice (~900 kgm^{-3}) and water (~1000 kgm^{-3}) respectively, P the precipitation rate at time i, V the vector wind perpendicular to the object of interest (ms^{-1}), and w the liquid water content of the air during precipitation, calculated via:

$$w_i = 0.067 P_i^{0.846} \qquad (7.4)$$

These equations were used to approximate the 48-hour total ice accretion for each simulation from hourly freezing precipitation accumulations. It was assumed that the

wind is everywhere perpendicular to the object (worst case scenario). An approximate SPIA©-like index was subsequently derived from this estimate.

Figure 7.29 displays the spatial severity index for each SST scenario. Wind velocities did not change remarkably and were generally at or below 15 kt, thus the primary change was in ice accumulation. For REAL, the maximum index value was 3-4 over southwestern Oklahoma, which qualitatively agreed with impacts experienced by that region. CLIM intensified potential ice storm impact in southwestern Oklahoma, with isolated 4-5 values, and a broader zone of 3-4 extending northeastward to central Oklahoma. The result was a ~54% increase in the spatial extent ≥ 3. For HI, the region of 3-4 was extended further northeast now impacting metropolitan central Oklahoma, with a ~62% increase in spatial extent over REAL. P2 actually showed a reduction in spatial extent, but a problematic location of the highest index with respect to major population centers. LO and M2 decreased in the higher index values, especially M2, where the highest index was now 2-3, and Arkansas experiences only minor icing potential relative to warmer SST. Based on this result, we may conclude that the increased SST generally produced a higher-impact icing event, with Arkansas having the greatest secular change in icing potential. CLIM produced a worse ice storm for southwestern and west-central Oklahoma, while the greatest impacts from HI and P2 were across central Oklahoma. Possibly resulting from the faster eastward progression of precipitation in P2, total ice accumulations were reduced over southwestern Oklahoma, and central Arkansas.

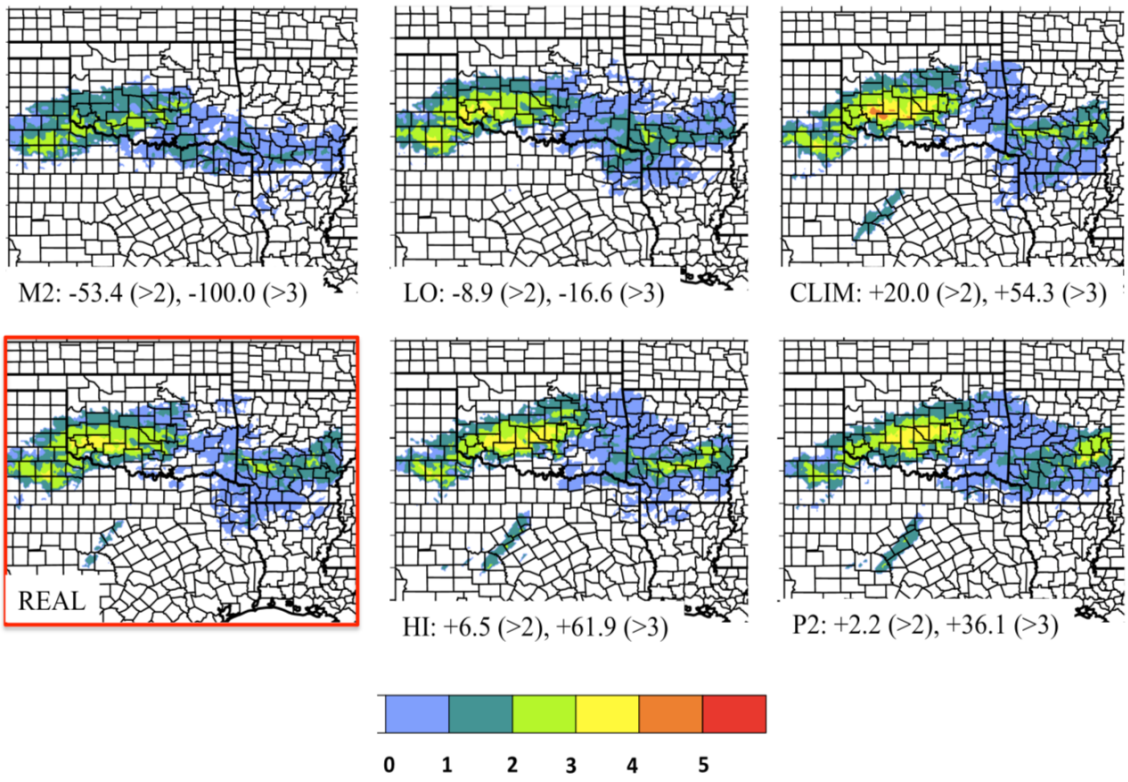

Figure 7.29: Derived SPIA© index, based on upper limit FZRA assumption from Sec. 7.2, and calculated accretion of the 48-hour precipitation accumulation (assessed based on conditions over 1-hour intervals). The text indicates the spatial extent (number of grid points) with an index greater than 2 and 3 relative to REAL.

Chapter 8: Conclusions and Future Work

8.1 Overview

This dissertation is a comprehensive assessment of freezing precipitation for the Southern Great Plains (SGP). Although the regional frequency of ice storms is low in comparison to northeast and Appalachian states, notable events have occurred, and will likely continue to occur. The lower frequency has potentially been a deterrent for climatological studies, given the low sample size. Here, we have attempted to extend the current state of knowledge through a multi-parameter study including deriving spatial statistics, thermodynamic and synoptic environments conductive to freezing rain, ice pellets and snow. In particular, this work identified regional environmental ingredients and precursors promoting mixed phase precipitation, including inter-comparison of a subset of prominent synoptic evolutions and their distinguishing characteristics.

Accompanying the derived climatology, a regional high-resolution WRF-ARW modeling study was configured and performed for two recent winter storms corresponding to common pattern types. Based on the preliminary climatology and past literature (e.g., Ramos De Silva et al. 2006, Fuhrmann 2011), this dissertation hypothesized that warmer SST in the Gulf of Mexico may influence the characteristics of the warm layer during freezing rain, including moderating the temperature and moisture - thereby impacting the timing and severity of icing. Furthermore, given the diversity of synoptic evolutions, we also wished to determine whether SST variability discernibly impacted warm layer development across systems, thus providing inter-event context. The motivation for the SST study was primarily to determine the

magnitude of effects on both moisture and dynamics with an eye to possible impacts of warming SSTs, either as a result of natural variability (e.g., AMO) or anthropogenic climate change, and assuming no systematic changes in cold air outbreaks. Additionally, understanding the magnitude and interdependencies of system modulation to SST may be useful in medium-term forecasting, or in gaining appreciation of how these anomalies are physically linked to system evolution as a tool for forecast guidance. Climatologists may find interest in the detailed retrospective case study evaluations, and inter-pattern differences in sensitivity. This work also is unusual in that it considers the role of SST on an inland event on a meteorological timescale, as oppose to the broader climate studies that have delivered assessments over inter-annual-decadal periods, and remains one of the few to tackle mixed-phase winter precipitation. WRF was used with 6 perturbed SST inputs reflecting the climatological mean (1981-2010), a uniform increase and decrease in SST, and a physically based upper and lower limit and distribution from ~30 years of SST data.

This chapter summarizes some of the pivotal findings of this work pertaining to both aspects of the research in turn (section 8.2, 8.3). Section 8.4 provides the reader with a set of potential future topics based on these outcomes.

8.2 Climatology: Principal Results

8.2.1 Thermodynamic Profile

A database was created to examine spatial and thermodynamic properties of mixed-phase precipitation for the SGP (Fig. 2.1). Derivation of the spatial distribution required estimation of the observed frequency for freezing precipitation or snow within

a given climate division. This information was garnered primarily through the *Storm Event/Storm Data* archive, corroborated through sources such as local climate summaries (LCDs, NCDC, 3 hour interval for observations), synoptic analyses (NCDC), and NARR daily categorical precipitation. Due to the lack of a quantitative data source, precipitation of any duration was denoted as 1-day (24 hour UTC), thus expressing frequency as the number of days per year, normalized by the relative areas of each climate division (Appendix, Sec. 2). Data was also allocated into four sub-region zones and expressed as a temporal average (1993-2011) November - March. This information indicated that freezing precipitation ('ice') was generally most frequent over the central domain, while snow maximized west and northwest. The ratio of freezing rain to snow and thus likelihood of mixed phase precipitation increased southeastwards (Fig. 2.3). The temporal plot suggested that ice was most common during December – February, with few events in November or March, whereas snowfall had broader seasonal range (Fig. 2.4). These results corroborated earlier findings including Grout et al. (2012), Kovacik et al. (2010), Changnon and Karl (2003).

Vertical profile information pertaining to temperature, moisture, winds and cloud cover were derived from 97 radiosonde profiles of freezing precipitation from eight station sites (Fig. 2.1), sub-divided into hydrometeor categories: freezing rain (FZRA, all) = 57, ice storm (HZR) = 25, ice pellets (IP) = 19, freezing drizzle (FZDR) = 21, non-ice storm freezing rain (LZR) = 32. These profiles were contrasted with a small sample for snowfall (SN) (24). This regional study produced results broadly consistent with prior literature (e.g., Zerr 1997, Rauber et al. 2000, 2001, Robbins and Cortinas 2002). FZRA, FZDR and IP were predominantly associated with a warm layer in this

sample (though it was not determined whether freezing rain in no-warm layer cases was necessarily uncommon). LZR, FZDR exhibited shallow cloud layers, a cooler inversion, and evidence of weaker warm air advection. Dry air aloft and/or multiple cloud layers were present in 40% of cases. IP, SN and HZR showed deep cloud layers with active ice microphysics. Warm layers for HZR were typically pronounced, often well above 5^{o}C (median 8.4^{o}C), with abundant moisture. The small SN sample profiles were subfreezing, generally with cold air advection in the lower troposphere. IP had two profiles, one resembling the classic cool warm layer overlaying a deep cold refreezing layer, while the second evidenced a deep warm layer overlaying a deep refreezing layer. IP also tended to occur during a subsaturated lower troposphere, encouraging further cooling via evaporation (Table 2.1-2.3, Fig. 2.8,2.9).

When compared with other national and regional studies, SGP thermal profiles were evidence of the possibility of substantial warm layer inversions, with a range similar to the southeastern U.S (e.g., North Carolina). The proportion of freezing rain relative to freezing drizzle was also generally greater than regions further north and distant from large water bodies (Table 2.5).

8.2.2 Synoptic circulation

Another goal of the climatology was to ascertain common regional synoptic patterns associated with freezing precipitation and snowfall. Based on prior work, e.g., Rauber et al. (2001), general synoptic evolutions with respect to freezing precipitation are known, but less attention has been paid to the structure of the mid-tropospheric geopotential height (notable exceptions include Castellano 2012 and Ressler et al. 2012)

A mixture of principal component (PC) and composite analysis was employed to derive 10 patterns, 5 each for snow and ice, using the geopotential height field as the initial and grouping variable at the approximate onset time for precipitation (T_0). PC techniques were used to identify these groups from a sample of 33 ice (winter storms with a prominent mixed-phase transition region) and 42 snow (weak or absent transition region) events. This limited sample size yielded only preliminary conclusions. Composites for each pattern type for variables including temperature, winds, sea level pressure, and precipitable water were derived using NARR 1^{o}x1^{o} data and displayed before, during and after the evolution of winter precipitation in the domain.

The resolved patterns produced some differing characteristics. All were associated with a trough of varying amplitude, proximity and progression. While the aim was to derive specific synoptic features, the patterns resolved generally fell within two main groups – western trough of varying amplitude (similar to Ressler et al. 2012), and a proximal amplified shortwave. A distinct pattern for ice events evidenced a longwave trough with a center over Baja California accompanied by strong southwesterly mid-level flow (e.g., *Ice Pattern 2, 3*). This orientation allowed transport of mid-tropospheric moisture from the sub-tropical Pacific, while slow eastward progression facilitated persistence of thermodynamic conditions favorable for freezing rain. Lower tropospheric features included a southeastern anticyclone with strong GOM moisture transport via 25-30 kt flow, pronounced positive temperature anomalies throughout the U.S south/southeast, bounded to the north by a strong baroclinic gradient and quasi-stationary frontal zone, and significant positive moisture departures (> 2 standard deviations). Similar circulation patterns were identified from a composite

analysis of major south central ice storms from Sanders et al. (2013), and the St Valentine's day mid-western storm (Rauber et al. 1994). The distance of the major trough lead to differing evolutions amongst constituent events, some favoring prolonged weak precipitation, while mobile shortwave troughs and/or convective instability accompanied by strong warm air advection promoted heavy precipitation in other cases.

For freezing precipitation with more progressive troughs (e.g., *Ice Pattern 1, 4*), synoptic vertical velocity was greater leading to generally higher precipitation rates, but a frequent reduction in temporal duration, supporting Ressler et al. (2012). Each pattern showed differing low-level thermal structure due to the southward extent of the subfreezing air, the trough location, and incumbent airmass. The greatest temperatures available to the warm layer were indicated where air south of the Arctic front was anomalously warm, often in conjunction with anticyclonic flow and ridging over the southeastern U.S. These conditions also showed a strong subtropical southwesterly jet aloft. The location of freezing precipitation for each constituent event showed variability, even amongst those within the same pattern type, due to differing near surface environments, orientation of the mid-level trough, and locations of greatest moisture availability. For each ice pattern, high pressure over the north central Plains was a ubiquitous feature at T_{-24} hours, and strong down-gradient flow and inverted troughing east of the Rockies suggested a highly stable airmass (Fig. 3.7-3.12). A conceptual model of these common evolutions is provided in Fig. 8.1.

For snowfall, two common pattern subsets encompassing the derived types were identified. Firstly, a high-amplitude progressive trough and associated surface cyclone development (e.g., *Snow Pattern 2, 4*). This cyclone typically initiated off the lee of the

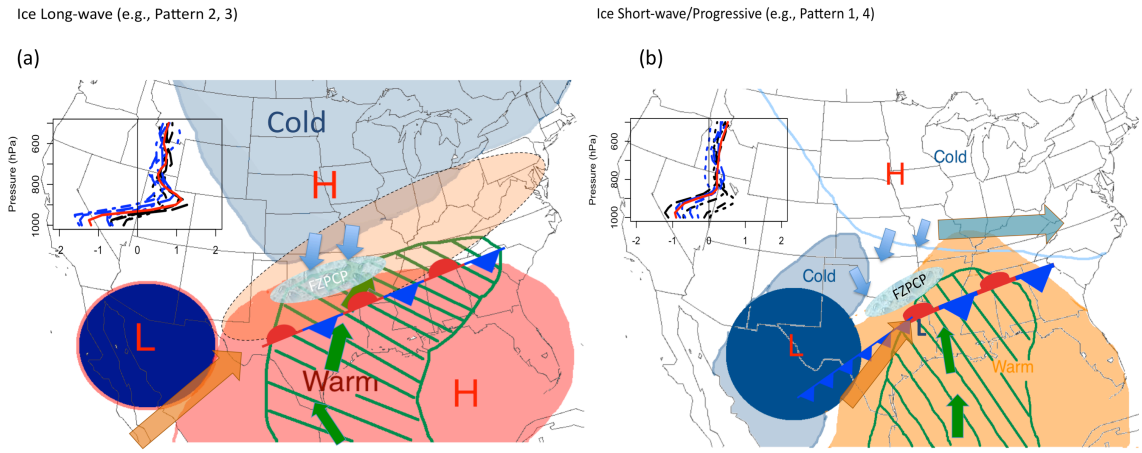

Figure 8.1. Conceptual diagrams for ice patterns at T_0 corresponding to the derived subgroups for the SGP. (a) Shows freezing rain in association with a slow moving broad amplified 500 hPa trough ('L') with anomalous warm (cold) air over the southern (northern states-shaded, color approximating strength of anomaly), moisture advection via strong low-level flow (green, arrows, length proportional to 850 hPa wind speed approximated from ch 3 patterns), and a broad upper southwesterly tropospheric jet (orange shaded, arrow); (b) Freezing rain during the passage of a amplified shortwave ('L') in the presence of an arctic high to the north ('H') and cold air advecting in behind the trough and weak surface low. Region bounded approximately in the left exit and right entrance region of two jet streaks (orange, blue arrows). In each case, the inset figure displays temperature advection in the freezing rain zone at 6-hour intervals T_{-24}, T_{+24} for representative composites (a, ice pattern 3, b ice pattern 1) with units of K hr^{-1} (100 km^{-1}).

southern Rockies and tracked east- northeast, with snowfall to its north-northwest. Surface cold air was typically absent prior to the cyclone, and accompanied it into the region. It is suspected that enhanced dynamic lift and faster transition to cold air advection tends to limit any warm layer that forms, precluding substantial freezing rain component for the SGP. For snowfall not associated with a surface cyclone (e.g., *Snow Patterns 1, 3*), the trough axis was generally located further west, with the region typically under an intense arctic airmass, and cold air extending into the far southern States. In such cases, the arctic high may be too deep and/or the warm air advection over a surface frontal zone sufficiently weak to limit the intensity of a warm layer. It

was apparent from our results that temperature anomalies south of the front were not as pronounced as those accompanying ice, suggesting that the antecedent environmental conditions were important to event evolution. Lift for precipitation may be similar to long duration ice cases, including the passage of multiple shortwaves or broad low-amplitude trough. The locations of snowfall for most patterns were generally concentrated in the northern half of the domain (Fig. 3.13-3.17). Conceptual evolutions for these snow subgroups are shown in Fig. 8.2.

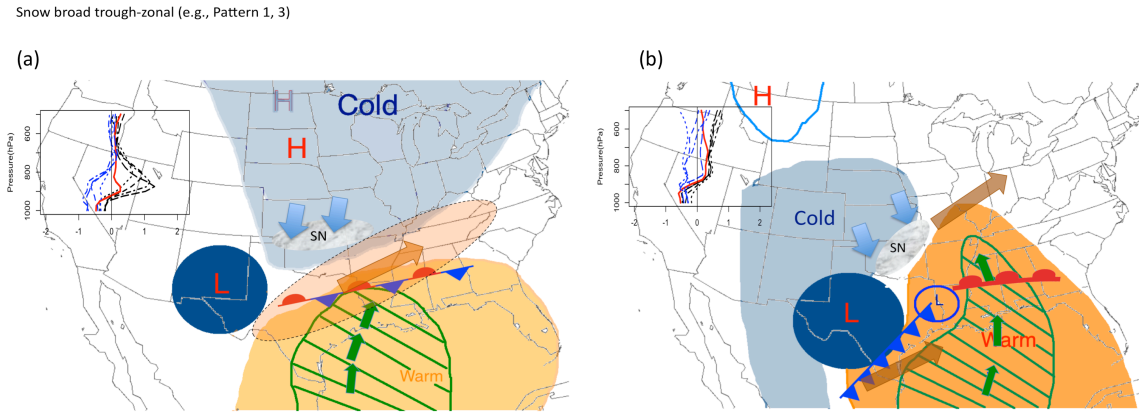

Figure 8.2. As Fig. 8.1 but for derived snow subgroups. (a) Shows snow produced from broad zonal trough and/or weak amplitude shortwave ('L'-diameter approximates amplitude) with a pronounced arctic airmass ('H') cold air advection (blue arrows) and cooler air over the subtropics (shaded); (b) depicts a well-developed surface cyclone with attendant high-amplitude mid-level trough ('L'), with arctic air absent over the northern Plains, and cold surface air advecting into the region behind the low (shaded). Air east of the cyclone center is warm and moist, while favorable upper jet streak locations (brown arrows) promote ascent. Advection profiles as before but for (a) snow pattern 3, and (b) snow pattern 2.

8.3 Modeling: Principal Results

8.3.1 Role of Microphysics and PBL

The modeling component of this work required assessment of the WRF ability to reliably reproduce the major properties of both analyzed case studies. Without this component, it would not have been possible to determine whether the experiment was reliable to the evolution of the physical event(s). Complete inter-comparison of multiple model parameterizations was beyond this study. Instead, analysis of two PBL and four MP schemes (all standard, well-used options in the literature) performance for the December 9-11 case study temperature and precipitation was conducted. These experiments allowed identification of a 'best fit' configuration for the remainder of the experimental work. Results showed:

- The older WRF version 3.1 had poorer near-surface temperature simulation for both MYJ and YSU. Reasons for this were not entirely clear but were related to the diurnal cycle, implying possible connection to the radiation scheme, and exacerbated for the non-local YSU where simulated surface temperature showed strong warm bias (Fig. 5.3-5.6). The particularly shallow depth of surface subfreezing air may have allowed mixing of higher inversion layer temperatures to the surface. Since WRF 3.1 various PBL improvements have been implemented, including fixes to the Prandtl number in YSU, MYJ fix to PBL height computation and upgrade to operational version (http://mmm.ucar.edu). In WRF 3.4, the MYJ produced a much-improved simulated surface temperature (e.g., RMSE ≤ 4 K). YSU errors were also reduced, but this scheme still overestimated temperatures, and also produced a less accurate precipitation

simulation. Lackmann (2011) suggested that the BMJ convective scheme used with YSU may not be advisable given the duplication of processes related to cumulus entrainment at PBL top. Of the two schemes, MYJ was more suitable for this application.

- Domain 3 precipitation showed notable variation across the four different microphysics parameterizations. WSM6 produced highest accumulations, but with a shift to the southeast relative to observations. Thompson et al. MP overproduced precipitation over the west, and generally had the weakest representation of a central axis (other than YSU-WSM6). Morrison produced lower total precipitation for the central axis, but better simulated the western domain. Millbrant Yau showed a wider more diffuse central axis but generally yielded the best representation for WRF 3.4. Visually the WRF 3.1 MYJ WSM6 configuration produced the most intense central precipitation axis, but with the aforementioned larger surface temperature errors. All schemes overproduced (under-produced) light (heavy) precipitation (Fig. 5.3-5.5).

8.3.2 Verification of Case Study Simulations

For the verification of the control (REAL) simulations for December 9-11 2007, and January 28-30 2010, key findings included:

- Strong dependence for precipitation on horizontal resolution, prominently for the December 2007 event, which produced convection of small horizontal scale under a weaker dynamical forcing regime. Domain 1 (30 km) did not capture this precipitation at all, while domain 2 (10 km) produced precipitation, but of

lower accumulation and shifted northward with respect to domain 3. Domain 3 convective mode was reasonably simulated, but suspected small displacements in location, weaker updrafts, and some mode discrepancies (e.g., reduced convective to straiform transition in WRF, underrepresentation of coverage) yielded broader, lower total precipitation along the central axis compared with observations (Fig. 5.10). Object-based skill score metrics identified that the model did capture a central precipitation axis with reduced intensity of up to 50% (Fig. 5.8-5.9, Table 5.2-5.3). Total precipitation content was within 5% of observed, indicating good representation of observed precipitable water.

- In contrast to December 2007, domain differences in precipitation *accumulation* for January 28-30 2010 were less pronounced. This event had a proximal trough axis and greater upper level dynamical support implying improved WRF intensity simulation with moderate-strongly forced systems in the absence of advanced methods to constrain errors, such as data assimilation. Precipitation errors in this event were generally to overestimate accumulations at moderate-high thresholds, especially over western and central Oklahoma (Fig. 5.15, Table 5.5-5.6). The spatial pattern of freezing precipitation (algorithm derived) was reasonably reproduced. Underestimated peak accumulations were possibly due to heavier precipitation eroding the warm inversion to below the range specified for FZPCP.
- Temperatures at the surface were well simulated, with a slight warm (cool) bias for December 2007 (January 2010, e.g., Fig. 5.6-5.7, 5.18). Synoptic evolution was in good agreement for both events (Fig.5.13, 5.21). Cloud cover for the

January 10 event suggested overproduction of WRF high cloud, with subsequent impacts to longwave and shortwave radiation components and the surface temperature (Fig. 5.23).

8.3.3 SST Impacts for Case Study 1

The December 9-11 2007 ice storm was regarded as one of the worst in recent memory for Oklahoma. WRF captured the synoptic aspects of this event, and also the precipitation mode, timing and thermodynamic profile. Nonetheless, precipitation intensity and location had pronounced departures from observed. The six derived SST fields were input to the model and run in a seven-day simulation to allow the model thermal and moisture profile to come into balance with the perturbed SST. We examined responses in key variables including temperature, precipitation, moisture, and synoptic-dynamic evolution. This sensitivity experiment produced the following outcomes:

- *Increased (freezing) precipitation with higher SST, especially December 9*. Total precipitation for domain 3 increased with basin average SST, primarily for the rainfall phase (Fig. 6.1, 6.2, Table 6.1). Percentage increases based on higher SST such as HI and P2 were generally weaker than the decreases in the LO and especially M2 cases. Phase partitioning and spatial extent of precipitation types was not found to discernibly change due to the pronounced warm layer inversion. On December 9, precipitation was forced primarily by convective instability aloft and north of a quasi-stationary front with low-level frontogenetic forcing and strong warm air advection. For HI and P2, convection was generally

more intense yielding greater freezing precipitation along the central axis (Fig. 6.4, 6.16), while convection weakened for negative SSTA. Even a climatological field discernibly reduced accumulations for this convective period implying that the observed warm SSTs were a contributor to the magnitude of icing. On December 10 all scenarios produced more widespread convection, but shifted to the north (south) for M2 (P2) (Fig. 6.20). Precipitation percentage changes were smaller for this period. For the whole event, reflectivities above 35 dbZ showed a slight increase for HI, P2, and decrease for CLIM and LO. M2 produced the greatest decrease in intensity (Fig. 6.3, 6.4). The non-linear responses of precipitation may relate to the differing SST fields (e.g., different SSTA distribution, REAL, CLIM, HI, LO), and the *convective instability profile.* Thermal profile and trajectory data revealed that the lower warm layer (~850 hPa) was influenced by SST, while the upper warm layer (~725 hPa) derived temperature characteristics from southwest Texas and northern Mexico (Fig. 6.21, 6.23). Cooler SST stabilized the atmosphere above 850 hPa and reduced convection, primarily on December 9 (Fig. 6.5, 6.6). The degree of stabilization of LO, M2 implied that unrealistically large basin-wide anomalies would be required to fully cut off convection. Positive SSTA changes were not as large and indicated primarily a moisture-induced intensification of convection, and slight expansion of coverage (Fig. 6.7).

- *Weak Warm layer thermal changes*. Based on observations, the warm layer was established well in advance of the event, primarily associated with an anomalously warm sub-tropical airmass over the southern U.S (Fig. 4.6). As

such, the influence of SST for the 7-day simulation was generally weak, with typically a near +1^{o}C (-2^{o}C) temperature change over central Oklahoma for P2 (M2) relative to REAL (Fig. 6.8, 6.9). The greatest influence of the thermal profile was in the modulation of low-level stability as discussed. Location and depth of cloud influenced the surface temperatures on December 10, with the northward displacement for M2 leading to greater solar insolation over the central domain, and faster erosion of the refreezing layer (Fig. 6.9, 6.11,6.12)

- *Time-varying dynamical response.* On December 9, precipitation was slightly enhanced for HI and P2 due to aforementioned stability changes, the increase in moisture availability (mixing ratio, Fig. 6.14), and enhanced warm air advection. Shearing frontogenesis along the central axis was observed as spatially broader for these higher SST scenarios, and weakened considerably for M2 (Fig. 6.13). The 850 hPa winds slightly increased for HI, P2 overnight and during the morning of the 9th (Fig. 6.15). In contrast, on December 10, 850 hPa flow to the region weakened, especially for P2, linked to a reduction in geopotential height gradient over the southern U.S and Gulf of Mexico (Fig. 6.18). Nonetheless, mixing ratios were still enhanced for warmer SST, these two processes partially canceling one another to show similar moisture transports on December 10 across simulations (Fig. 6.19). Ultimately this produced similar precipitation accumulations for REAL, CLIM, LO, HI and P2 on December 10 (Fig. 6.20), while M2 showed faster northward movement of convection, possibly due to stronger 850 hPa steering flow, and more northwesterly low-level shearing and deformation frontogenesis (Fig. 6.17).

Figure 8.3 shows schematically the observed response of this event to SST, while Fig. 8.4 provides a diagrammatic descriptive summary.

8.3.4 SST Impacts for Case Study 2

The January 28-30 2010 sensitivity study was performed in the same manner as the previous. The dynamical evolution of this event was distinctly different. Key findings included:

- *Increased total precipitation with higher SST, and modulations in the location of phase types.* Increases in basin-averaged SST produced higher precipitation accumulation for much of domain 3 (Fig. 7.1, 7.2, 7.3, Table 7.1). Relative to REAL, heavy rainfall (e.g., > 40 mm) was expanded eastward and northward for CLIM, HI, P2. Furthermore the southward extent of snowfall declined with warmer SST. Mixed phase (freezing) precipitation was increased over southwestern Oklahoma for CLIM (in this case study climatological SST was warmer than control), and markedly reduced for M2. HI and P2 showed a more longitudinally (latitudinally) expanded (contracted) freezing precipitation zone for Oklahoma, and increased icing for central Arkansas. As precipitation was ongoing, greater reflectivity returns for higher SST (Fig. 7.4, 7.5,7.6) suggest that precipitation rates were intensified. In similar fashion to case 1, domain average changes indicated greater percentage change for strongly negative SSTA. However for this event the positive percentage changes were also notable (Table 7.1), especially for the freezing precipitation zone in HI and CLIM.

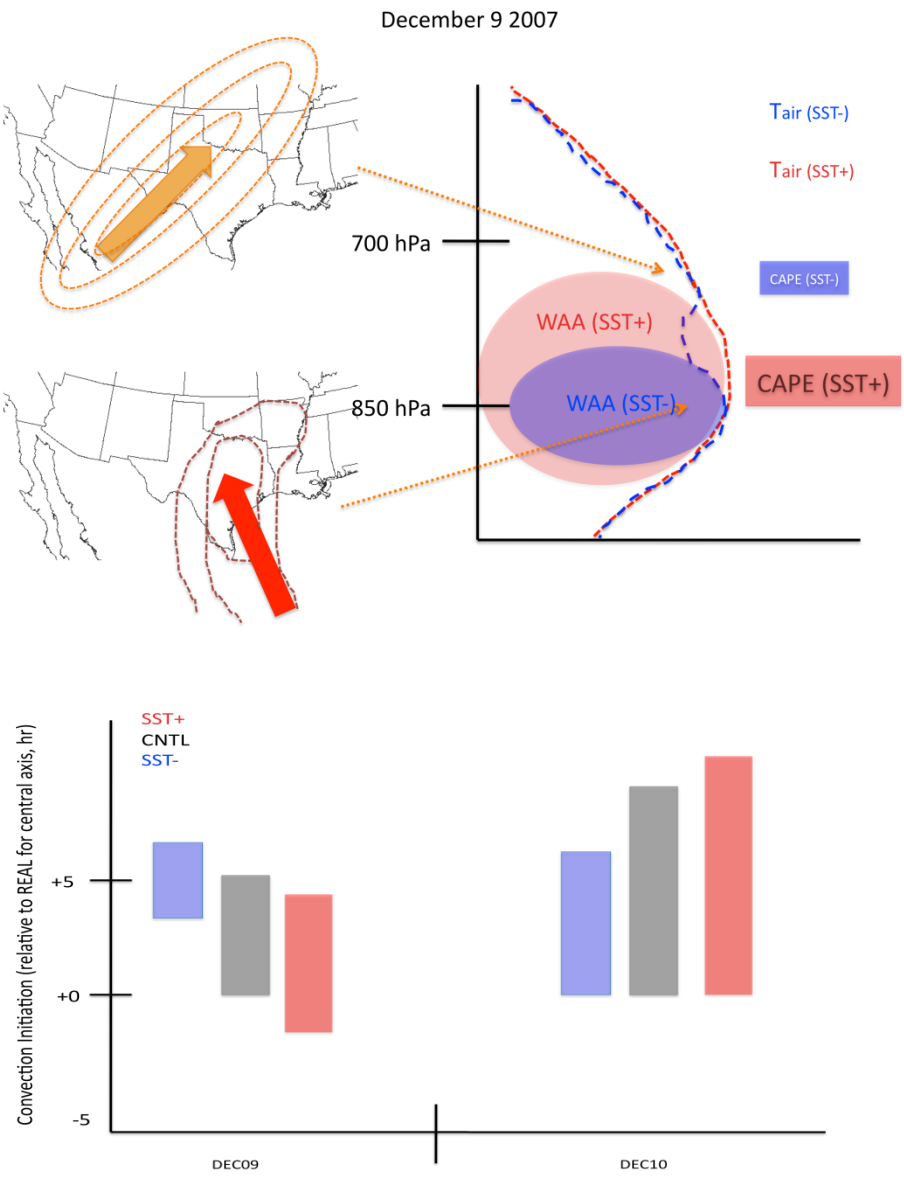

Figure 8.3: Top: Schematic diagram depicting the airflow characteristics incident to the lower and upper warm layer (e.g., windspeed and direction, 'jet' shown by concentric rings). The impact of these trajectories is shown on the right hand side, displaying an idealized warm layer profile for positive and negative SSTA (crudely analogous to the differences between LO/HI, M2/P2). WAA denotes warm air advection. Bottom: Timing of precipitation and relative accumulations for REAL (CNTL), positive and negative SSTA for December 9 and 10. Y-axis shows start time relative to REAL (hour), while the length of the bar is proportional to precipitation accumulation.

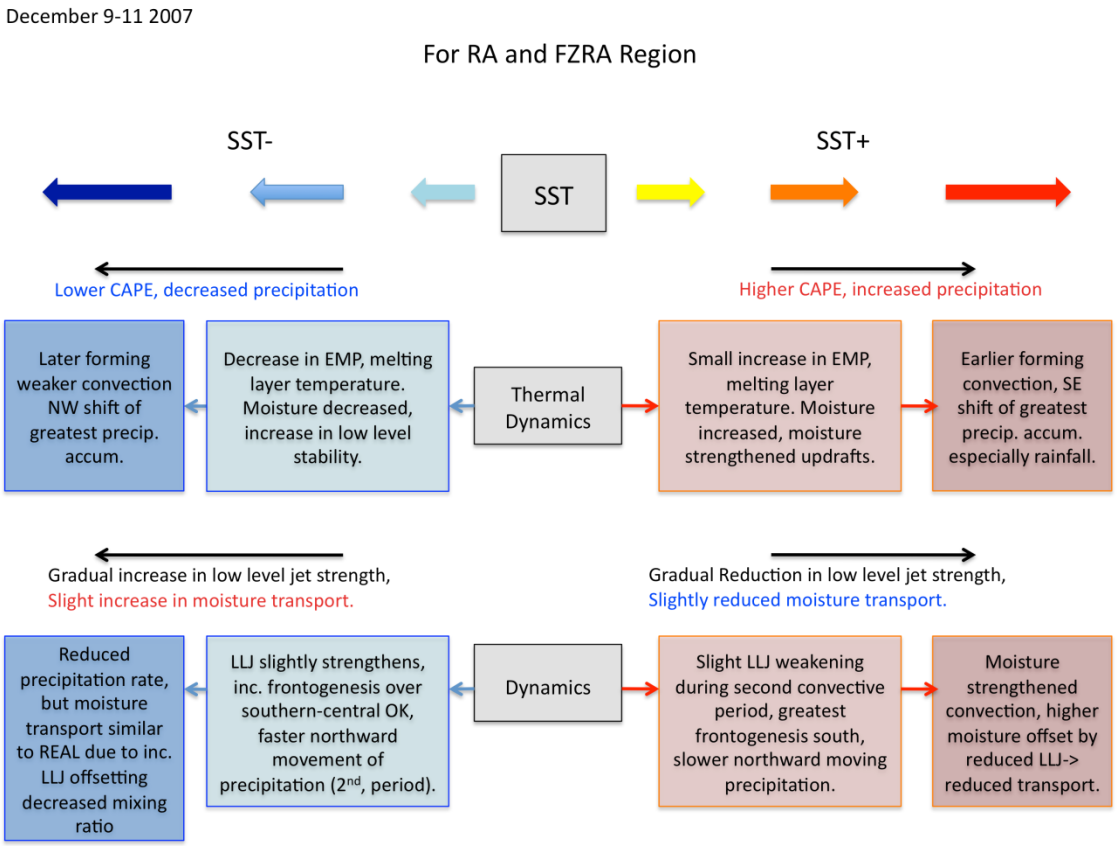

Figure 8.4: Flowchart describing some observed changes from control for positive and negative SSTA. Top row shows changes to the stability and thermal profile, while the bottom describes changes to low-level jet (especially December 10), and moisture transport. Here melting layer = warm layer.

- *Increase in northward extent, warm layer intensity with SST.* In advance of this winter storm, a cooler airmass impacted much of the low-levels, depleting them of a warm layer (Fig. 4.13). Consequently, low-level warm air advection in advance of precipitation was more pivotal in eventual warm layer intensity and northward penetration. Based on trajectory analysis (Fig. 7.18, 7.25) low-level air parcels originated over the continental U.S, moved southward and curved anticyclonically over the GOM basin before entering the icing zone. This evolution was in contrast to case 1 where the air parcels moved directly northward from the tropical Caribbean (Fig. 6.24). As a result, diabatic

aggregation of heat and moisture was more critical for this case study. Cooler SSTs favored lower air parcel temperatures, which resulted in a weaker and/or southward shift in the warm layer, especially for Arkansas (Fig. 7.7-7.10). For southwestern Oklahoma the warmest and longest-duration inversion was observed for CLIM and HI. Warm layer temperature were generally also increased for P2, but freezing rain was possibly mitigated by low-level cooling from increased precipitation rates, and a decrease in refreezing layer temperatures resulting from faster eastward progression of the 850 hPa circulation.

- *Intensification of a geopotential low and dynamical strengthening of precipitation via moisture transport.* For this event, strengthening of the 850 hPa geopotential low circulation over north Texas was clearly observed from the model as SST increased. Warmer SST produced stronger positive thickness advection east of the low, enhancing baroclinity and its northward extent, with accelerated eastward progression of precipitation (Fig. 7.6, 7.13). The 850 hPa geopotential height (and surface pressure) decreased, which increased the height gradient and 850 hPa southerly low-level jet. This, coupled with increased mixing ratio in the higher SST cases, yielded a notable increase in moisture transport on both January 28 and 29 (Fig. 7.14, 7.15). The spatial area of transport above 300 kg $m^{-1}s^{-1}$ was observed to approximately double between P2 and M2. This dynamical contribution likely increased precipitation changes with SST above what might have been anticipated from mixing ratio alone.

- *Sub-basin SST variability may in some cases be similarly as important as the basin-average in modulating precipitation.* For case study 1, the western GOM was generally most important for the freezing precipitation zone, based on the analyzed low-level trajectory. Warmer SST in this region might be expected to have a greater effect on the region as this is the direct area experienced by the incident air parcels. For case study 2 the north central GOM was important. We observed for HI that a region of particularly warm SST was present for the central and northern basin (e.g., Fig. 7.18), which was diabatically and adiabatically transferred to increasing air parcel temperature and moisture content. It was found that the peak temperature sustained by the air parcel in HI was greater than P2 in some cases (Fig. 7.19), as was the mixing ratio (Fig. 7.21). This result seemingly confirms the importance of sub-domain SSTA in warm layer and precipitation intensity, although further analysis is desired to fully separate this signal from the dynamical response. We noted that the freezing precipitation in HI was greater than that for P2 for central Oklahoma and west-central Arkansas, possibly aided by this favorably located strongly positive SSTA zone.

Figures 8.5 and 8.6 schematically summarize the results of this section.

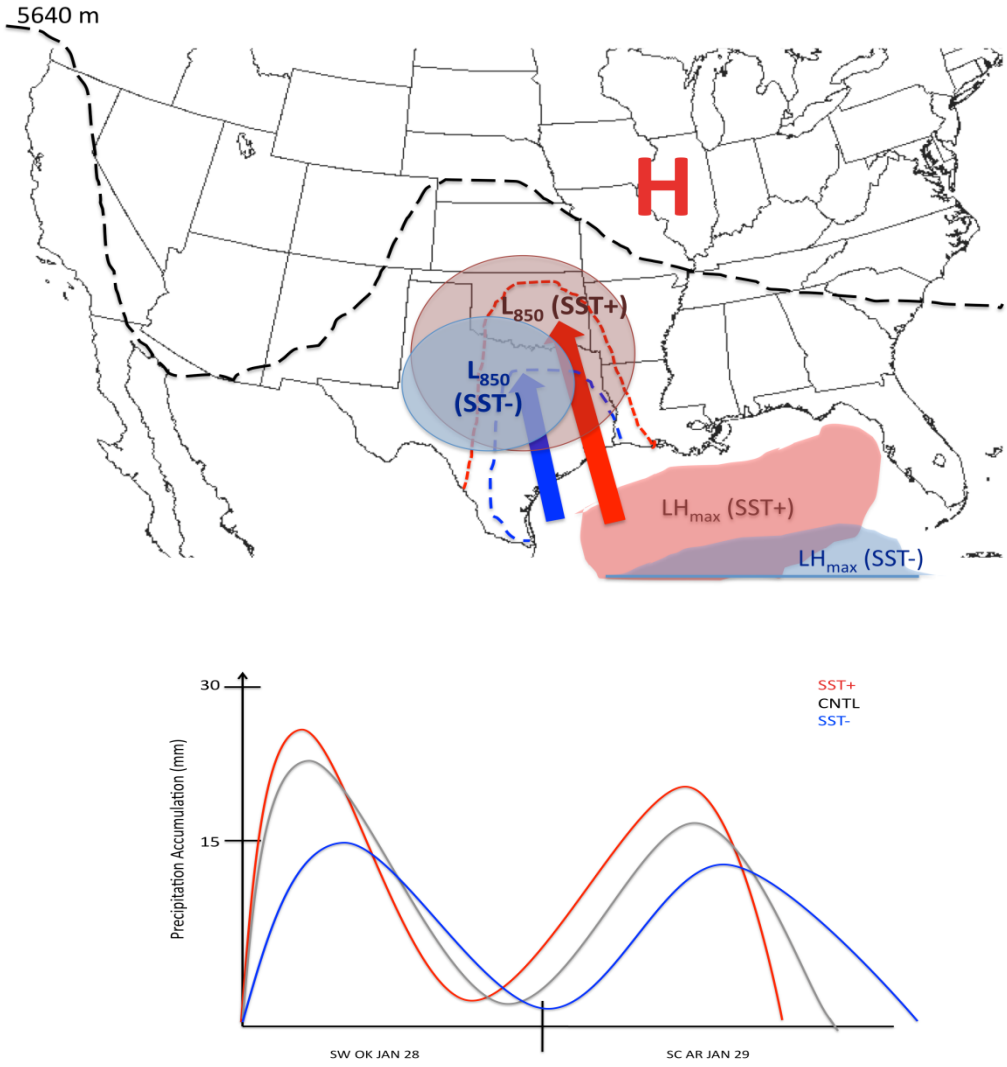

Figure 8.5: Top: Thermal and dynamical changes with positive and negative SSTA. Larger L_{850} denotes deeper circulation, while dashed curved lines denote northward extent of warmer air through advection. Arrows display wind direction, with size approximating relative speed. LH_{max} describes the latent heat flux contribution from the GOM. Bottom: Timing and approximate precipitation intensity with SST changes, and REAL (CNTL) for southwest Oklahoma (left), and south central Arkansas (right), indicating the higher (lower) precipitation and faster (slower) progression with warmer (cooler) SST.

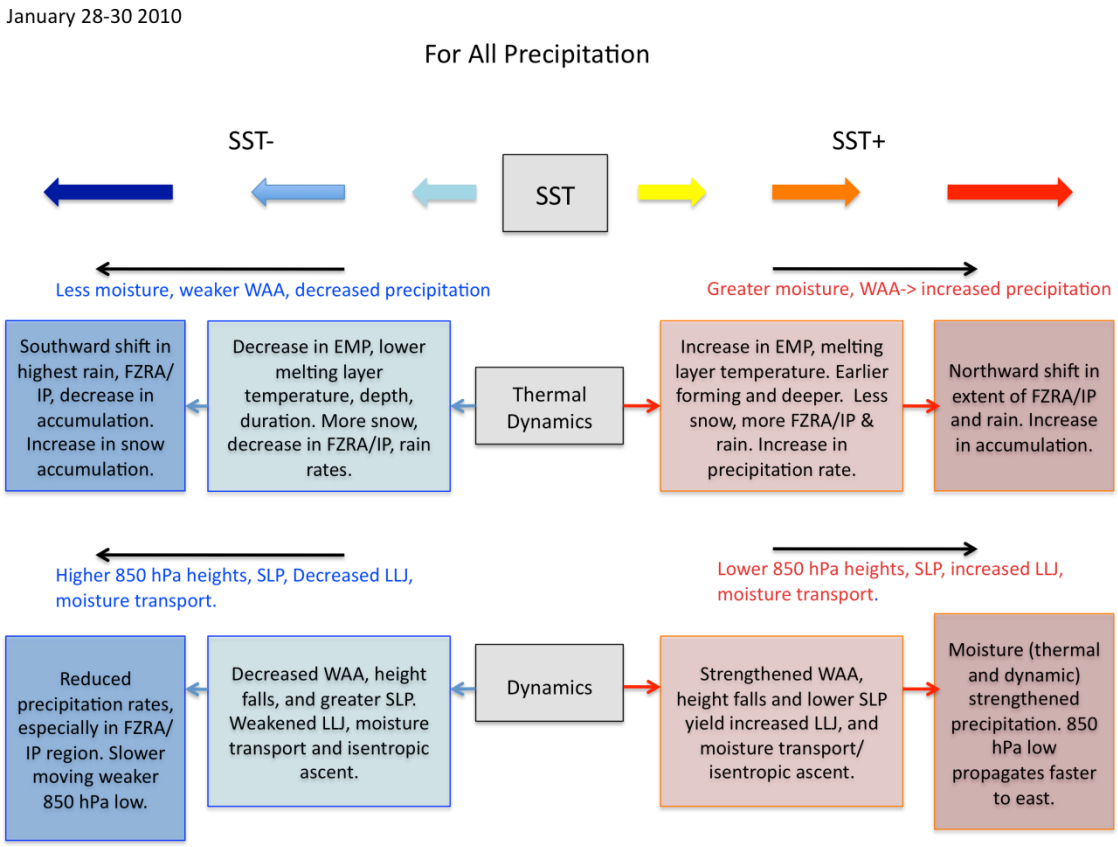

Figure 8.6: Flowchart description of thermal (top) and dynamical (bottom) changes to winter storm evolution with SST. Here melting layer = warm layer.

8.3.5 Discussion

With respect to the above results, and with regard to the inter-comparison between case studies, it was concluded that:

- *Warm layer characteristics are fundamentally determined by synoptic evolution.* For case 1, the deep and intense warm layer was largely insensitive to SST, whereas in case 2 there was a more notable response that resulted in discernible changes to phase partitioning. Clearly the characteristics of atmospheric circulation in the days prior determine the available warm layer. For case 1 a particularly warm sub-tropical maritime airmass was firmly entrenched in the

southeastern U.S. For case 2, an active regime was evident with troughing in the eastern U.S and a generally cool airmass prevailing. Case 2 also evidenced a return flow-type event where low-level temperature and moisture derived from the northern GOM basin 24-48 hours before the storm. Based on this observation, one may conclude that the positive trend observed for melting potential (EMP) against SST (Fig 4.4) does not correspond well to the results of the modeling work where magnitude changes in warm layer were weaker (e.g., only ~0.25-0.5 K rise for every 1 K increase in basin average SST). It would however be difficult to argue against the evidence that our hypothesis was upheld. Results also revealed that changes in FZPCP were strongly sensitive to moisture perturbations.

- *Synoptic fields lead to dynamical differences in how SST anomalies are translated to influence circulation.* For case 1, the long wave trough was not impacted by the modulation of GOM SST. Warm air advection increased with SST in the lower warm layer (~850 hPa), but the southwestern sourced air for the upper warm layer was largely unaltered. The two key dynamical responses to SST occurred with the stability response in the thermal profile (especially December 9), and the geopotential height gradient/wind field perturbation, particularly M2 and P2, on December 10. For case 2, the developing surface and 850 hPa low was deepened by the enhanced availability of warm-moist air, which set into motion a response that intensified the low-level jet, moisture transport and precipitation. Coupled with the weaker and more transient warm layer, case 2 suggested more robust change in freezing precipitation.

- *The extent to which SST influences ice storms is non linear.* The diverse response for case 1 and case 2 show that increased SST within the fetch of a developing ice storm do not necessarily exert strong influence on resulting ice potential as the magnitude of SSTA, baroclinic, dynamic and moisture response can enhance or mitigate precipitation. *In general* higher SST promotes advection of warmer air into the region, and higher moisture content, which can increase precipitation rates. Strongly negative SSTA shows a larger weakening of mixed-phase precipitation, but the reasons for this differ between case 1 and 2. Ice storm conditions may be affected more strongly in circumstances where the warm layer is weaker, later forming and associated with diabatic airmass modification over the GOM. Access to high-quality SST data for input to operational models, and incorporating observations of SST anomalies and their distribution, coupled with air parcel trajectories, may be a useful addition to a regional forecasters 'toolbox' for gaining situation awareness and facilitating critical decision-making in medium-term prediction. Nonetheless additional work is necessary to better understand the interactions and relative roles of the multiple processes and their feedbacks forced from SSTA.

8.4 Future Work

8.4.1 Database Extension and Alternate Climatology

Expansion of the 1993-2011 database to at least 30 years is a vital task. Existing resources described in chapter 2 could be further utilized, especially *Storm Data* and NARR categorical precipitation type. Extension of the database back to 1979 would encompass the complete NARR dataset, and would allow some of the work from

chapter 2 and 3 to be repeated with a larger sample size. Additionally, given the limitations of extracting pattern types discussed in Chapter 3, particularly with maintaining good quality and accurate input data (e.g., constraining T_0), another technique that could be applied is a station by station assessment of composite synoptic evolutions corresponding to ice and snow events partitioned into different groups and severity. The advantage of this method is that T_0 is fully constrained, and more accurate assessment of the quantity of event liquid water equivalent/accumulation may be assessed from site meteorological data. A potential disadvantage is the potential to average over highly different synoptic patterns, which Chapter 3 of this work was attempting to avoid. Early work in this regard for Oklahoma City, 1979-2013, has shown that severe icing (> 0.75 in LWE, > 6 hours length) is largely associated with a synoptic flow type similar to *Ice Pattern 3*, while long duration weak icing (< 0.25 in LWE) tends to a western low-amplitude trough. The trough *amplitude* is important to promoting northward advection of deep moisture and warmer temperatures while trough *location* at T_0 informs duration. Detailed Station-by-station climatologies: synoptic, thermal, and time-series, should be constructed and could be highly beneficial as a pattern recognition tool for forecasters. In addition to temporal expansion, it is advisable to spatially extend the dataset to include all of Arkansas, Kansas, Missouri, Texas, and possibly east into Tennessee and the southeast.

8.4.2 Model Development

Modeling studies have not comprehensively been performed for ice storms. High resolution WRF provides many opportunities for mesoscale and microphysical

studies. In our validation and configuration work for example, we could test additional microphysics, PBL and other parameterizations over multiple case studies to further examine whether a 'best' configuration exists. Unfortunately, in the case of microphysics development there are limitations on data quality during ice storms for much of the high-resolution in-situ facilities such as the SGP-ACRF and Oklahoma Mesonet. One possible avenue for future work might be to use dual-polarimetric radar facilities during freezing precipitation to gather information on hydrometeor types above the warm layer. It is often assumed that snowfall and aggregates are most common, but what about potential for graupel? How might this affect standard hydrometeor algorithms? For poorly simulated precipitation structure, and complex evolutions such as the December 2007 case study, it may be interesting to examine further avenues for precipitation improvement, including data assimilation.

8.4.3 Synoptic and Climate Dynamics

This work has identified that that models generally reproduce well the large-scale evolution of winter storm events. Temperature and moisture content (e.g., precipitable water, mixing ratio) was also reasonably resolved here. It may be possible to further categorize synoptic structures by their common airflow trajectories, creating a trajectory climatology, as it were, for various synoptic types during freezing precipitation and snow, much like the work of Fuhrmann and Konrad (2008). This identification may help forecasters identify common regions of the GOM for example, and monitor SST conditions in that region, or for further identification of trajectories common to severe and weak icing to develop the climatological record. A useful extension to this dissertation work might be to evaluate warm layer trajectories at

multiple locations/times or an ensemble approach to provide stronger support for the trajectories analyzed (chapter 6, 7) and their relationship to temperature and precipitation.

On a longer time scale, it may be possible to determine seasonal and inter-annual predictability of ice storm frequency based on large-scale teleconnections and/or SST variability. This work assumed that the SST field is independent of the overlying atmosphere. However, during this research it was observed that severe ice storms, typically of pattern 2 or 3 (chapter 3), tended to basin-average positive SSTA, whereas events associated with a surface low had neutral or negative SSTA. These conditions were generally present over the preceding month (not shown). Figure 8.7 shows the difference in geopotential height between 5 high and low SST events. Is there a link between seasonally warm SST and the evolution of certain synoptic circulations? Examination of the relationship between winter weather and atmospheric teleconnections or other large-scale circulation anomalies may provide vital planetary scale context. Figure 8.8 illustrates a composite of the highest and lowest three years in our database with respect to the number of SGP ice events, showing that circulation over the northern hemisphere tends toward a strong high over the north Pacific, coupled with anomalously warm SST in that region, and over the eastern Atlantic. The sea level pressure trend shows a weak increase over the Northern Plains. This circulation pattern may suggest more frequent blocking patterns over the Pacific Northwest, which have been linked to increased dislodging of arctic high pressure into the mid-latitude U.S. To the south, the Atlantic anticyclone and warm GOM provides extra moisture potential, and the two may possibly be interlinked (e.g., easterly or southerly flow over the GOM

driving warm water north from the Caribbean? solar warming of the ocean surface layer?).

At this time, it is not certain how global climate change may impact the incidence of cold air outbreaks (CAO) to the south central U.S. Research into future trends of CAO frequency have shown mixed results (e.g., Vavrus et al. 2006, Cohen et al. 2012). However global sea surface temperatures have been increasing. Trends in 0-700 m Atlantic basin temperature are prominent (IPCC AR5, WGI), and approximately +0.1-0.3^{o}C per decade (1971-2010) over the central North Atlantic extending northeastward from Florida to Western Europe. The Gulf of Mexico shows a weaker positive trend. Over the 21st Century the super-position of climate variability and climate change will continue to promote high intra-seasonal variability of winter weather. The results of this study provide physical mechanisms by which freezing precipitation events may be thermodynamically enhanced by regional SST, and can be part of the conversation of winter weather events in a warming world.

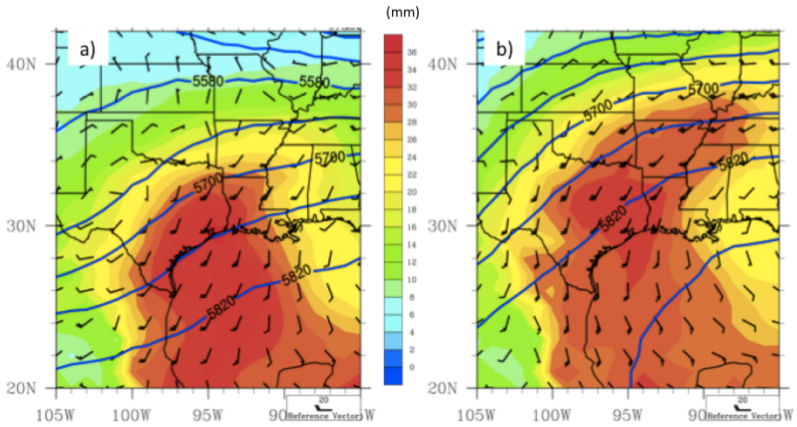

Figure 8.7: Composites of 5 bottom (a) and top (b) ice storm events by basin average SST anomaly (from 22 cases). Geopotential height (gpm, blue contours), 850 hPa wind vectors (barbs, intervals 5 kt), and precipitable water vapor (mm, shaded). Note the more meridional long-wave pattern for higher-SST cases, including an eastern ridge and GOM basin anticyclonic flow.

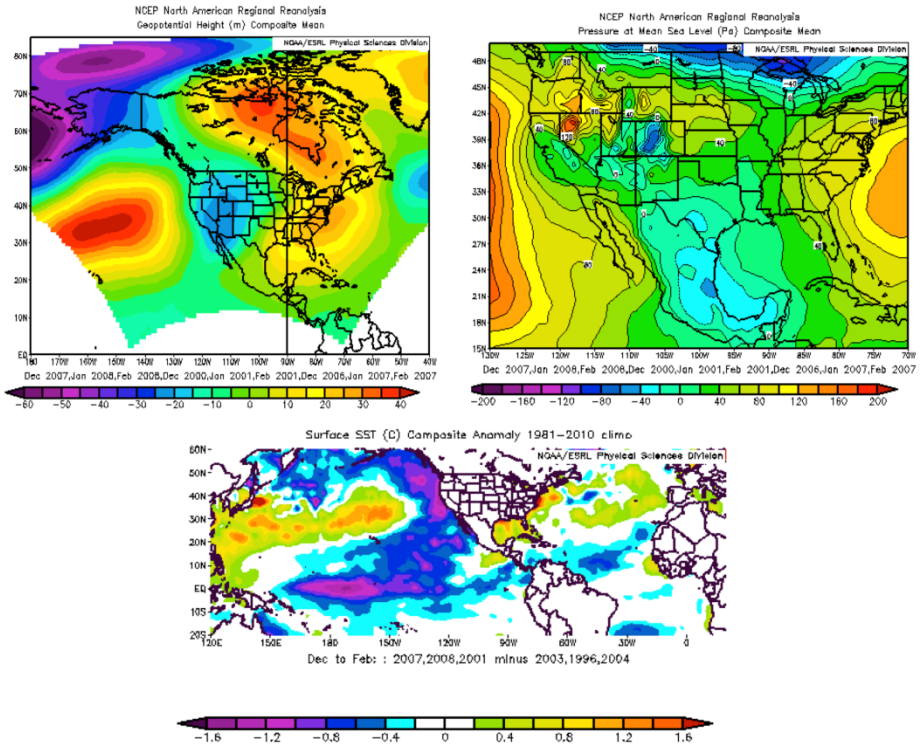

Figure 8.8: Composite Circulation anomalies (winter DJF) for three years of high ice frequency minus three years of low ice frequency (based on 1993-2011 database). Top left is geopotential height at 500 hPa (gpm anomaly), top right, sea level pressure (pa, anomaly) and bottom center is SST over much of the global tropics and mid-latitudes (K, anomaly).

References

Ackerman, T.P., G. M. Stokes, 2003: The Atmospheric Radiation Measurement Program. *Physics Today*., **56**, 38-44.

Ahmadi-Givi, F., G. C. Graig, and R. S. Plant, 2004: The dynamics of a midlatitude cyclone with very strong latent heat release. *Quart. J. Roy. Meteor. Soc.,***130**, 295-323.

Anderson, C., and C. Clark. 2011: Dependence of Midwest U.S spring precipitation extremes on Gulf of Mexico SST, *WCRP Climate Conference 2011,* Session C39, Poster TH110A.

Arabey, E. N., 1975: radiosonde data as means for revealing cloud layers. *Meteor. Gidrol.,* **6,** 32-37.

Baldwin, J., 1973: The climates of the United States. NOAA, 113 pp. [NTIS COM-74-11708/6.].

Baldwin, M.R, and S. Contorno, 1993: Development of a weather-type prediction system for NMC's mesoscale ETA model. Pre-prints, *13th Conf. on Weather Analysis and Forecasting,* Vienna, VA, Amer. Meteor. Soc., 86-87.

Baldwin, M., R. Treadon, and S. Contorno, 1994: Precipitation type prediction using a decision tree approach with NMCs mesoscale eta model. Preprints, *10th Conf. On Numerical Weather Prediction*, Portland, OR, AMS 30–31.

Bao, Q., J. Yang, Y. Liu, G. Wu, and B. Wang, 2010: Roles of anomalous Tibetian Plateau warming on the severe 2008 winter storm in central-southern China. *Mon. Wea. Rev*., **138**, 2375-2384.

Bell, G. D., and L. F. Bosart, 1988: Appalachian Cold-Air Damming. *Mon. Wea. Rev.*, **116**, 137–161.

Bennett, I., 1959: Glaze: Its meteorology and climatology, geographical distribution, and economic effects. Environmental Protection Research Division Tech. Rep. EP-105, Headquarters, U.S. Army Quartermaster, Research and Engineering Command, Natick, MA, 217 pp. [NTIS AD-216668.]

Bernadet, L., J. Wolff, L. Nance, A. Loughe, B. Weatherford, E. Gilleland, and B. Brown, 2009: Comparison between ARW and NMM objective verification scores. *23rd Conference on weather analysis and forecasting/19th conference on numerical weather prediction.* American Met. Soc., Omaha, NE,1-6.

Bernstein, B.C, 2000: Regional and Local Influences on Freezing Drizzle, Freezing Rain, and Ice Pellets. *Wea. Forecasting*, **15**, 485-508.

---, M. K. Politovich, and F. McDonough, 1998: Surface weather features associated with freezing precipitation and severe in-flight aircraft icing. *Atmos. Res.,* **46**, 57-73.

---, and B. Brown, 1997: A climatology of supercooled large drop conditions based upon surface observations and pilot reports of icing. Preprints, *Seventh Conf. on Aviation, Range, and Aerospace Meteorology,* Long Beach, CA, Amer. Meteor. Soc., 82– 87.

Blackmon, M.L., 1976: A Climatological Spectral Study of the 500 mb Geopotential height of the Northern Hemisphere, *J. Atmos. Sci.,* **33**, 1607-1623.

Bluestein, H.B., 1993: *Synoptic Dynamic Meteorology in Mid-Latitudes Vol II*. Oxford University Press. 608pp.

Blunden, J., and D. S. Arndt, 2011: Analysis of freezing rain patterns in the south central United States: 1979-2009. *Extended Abstract, Amer. Meteor. Soc 93rd Annual Meeting, Seattle, WA*.

Bond, N.A., M. F. Cronin, and M. Garvert, 2010: Atmospheric sensitivity to SST near the Kuroshio extension during the extratropical transition of Typhoon Tokage, *Mon. Wea. Rev.,* **138**, 2644-2663.

Booth, J. F., L. Thompson, J. Patoux, and K. Kelly, 2012: Sensitivity of mid-latitude storm intensification to perturbations in the sea surface temperature near the Gulf Stream, *Mon. Wea. Rev.,* **140**, 1241-1256.

Bosart, L.F., and F. Sanders, 1991: An early-season coastal storm: conceptual success and model failure. *Mon. Wea. Rev.,* **119**, 2831-2851.

Bourgouin, P., 2000: A method to determine precipitation types. *Wea. Forecasting.* **15**, 583-592.

Bragg, D. C., M. G. Shelton, and B. Zeide, 2003. Impacts and management implications of ice storms on forests in the Southern United States. *Forest Ecology and Management*, **186**, 99-123.

Branick, M. 2001: Monthly and Geographic Distribution of Heavy Snow events in Oklahoma, 1951-2001. Available at: [*http://www.srh.noaa.gov/oun/?n=climate-heavysnow-study.*]

---, 1997: A climatology of significant winter-type weather events in the contiguous United States, 1982-1984. *Wea. Forecasting*, **12**, 193-207.

Brayshaw, D. J., 2006: Large-scale forcing of the north Atlantic storm track, *PhD*

Thesis, University of Reading, Reading, UK.

Brennan, M. J., and G. M. Lackmann, 2005: The influence of incipient latent heat release on the precipitation distribution of the 24-25 January 2010 east coast cyclone. *Mon. Wea. Rev.,* **133**, 137-1937.

Brimelow, J.C., and G.W. Reuter, 2005: Transport of atmospheric moisture during three extreme rainfall events over the Mackenzie River Basin. *Journal of Hydrometeorology*, **6**, 423-440.

Brock, F. V., K. C. Crawford., R. L. Elliott., G. W. Cuperus., S. J. Stadler., H. L. Johnson., M. D. Eilts, 1995: The Oklahoma Mesonet: A Technical Overview. *J. Atmos. Oceanic. Technol.,* **12**, 5-19.

Call, D.A., 2009: As assessment of National Weather Service warning procedures for ice storms. *Wea. Forecasting*, **24**, 104-120.

----, 2010: Changes in ice storm impacts over time: 1886-2000, *Wea. Climate Soc.*, **2**, 23-25.

Castellano, C. M, 2012: Synoptic and mesoscale aspects of ice storms in the northeastern U. S. *M.S. Thesis, Dept. Atmospheric and Environmental Sciences,* University of Suny-Albany.

Casola, J. H., J. M. Wallace, 2007: Identifying Weather Regimes in the Wintertime 500-hPa Geopotential Height Field for the Pacific–North American Sector Using a Limited-Contour Clustering Technique. *J. Appl. Meteor. Climatol.*, **46**, 1619–1630.

Chang, Y.-L., and L.-Y. Oey, 2010: Eddy and wind-forced heat transports in the Gulf of Mexico, *J. Phys. Oceanogr.,* **40**, 2728-2742.

Changnon, S. A., D. Changnon, T. R. Karl, 2006: Temporal and Spatial Characteristics of Snowstorms in the Contiguous United States. *J. Appl. Meteor. Climatol.*, **45**, 1141–1155.

Changnon, S. A., 2003: Characteristics of ice storms in the United Sates. *J. Appl. Meteor.*, **42,** 630–639.

----, and T. R. Karl, 2003: Temporal and spatial variations of freezing rain in the contiguous United States, *Journal of Applied Meteorology*, **42(9),** 1302-1316.

Chernykh, I. V., and R.E Eskridge, 1996: Determination of cloud amount and level from radiosonde soundings. *J. Appl. Meteor*., **35**, 1362-1369.

Cochrane, J. D., 1972: Separation of an anticyclone and subsequent developments

in the loop current (1969), *Contributions on the Physical Oceanography of the Gulf of Mexico*, Vol II, L. R. A. Capurro, and J. L. Reid, Eds. Gulf Publishing Co., 3-51.

Cohen, J., J. C Furtado, M. A Barlow, V. A Alexeev, J. E Cherry, 2012: Arctic warming, increasing snow cover and widespread boreal winter cooling. *Environ. Res. Lett.,* **7**, 014007

Colle, B. A., and C. F. Mass, 1995: The Structure and Evolution of Cold Surges East of the Rocky Mountains. *Mon. Wea. Rev.*, **123**, 2577–2610.

Cortinas Jr., John V., Ben C. Bernstein, Christopher C. Robbins, J. Walter Strapp, 2004: An Analysis of Freezing Rain, Freezing Drizzle, and Ice Pellets across the United States and Canada: 1976–90. *Wea. Forecasting*, **19**, 377–390.

Cortinas Jr., J. V., 2000: A climatology of freezing rain over the Great Lakes region of North America. *Mon. Wea. Rev.*, **128,** 3574–3588.

Czys, R.R, R.W Scott, K.C Tang, R.W Przybylinski, M.E Sabones, 1996: A Physically based, non Dimensional Parameter for Discriminating between Locations of Freezing Rain and Sleet (*Wea. Forecasting*, **11**, 591-598).

Davis, C. A., and K. A. Emanuel, 1991: Potential vorticity diagnostics of cyclogenesis. *Mon. Wea. Rev.,* **119**, 1929-1953.

DeGaetano, A.T, 2000: Climatic perspectives and impacts of the 1998 northern New York and New England ice storm. *Bull. Amer. Meteor. Soc.,* **81**, 237-254.

Draxler, R.R., and G. D. Rolph, 2011. HYSPLIT (HYbrid Single-Particle Lagrangian Integrated Trajectory) Model access via NOAA ARL READY Website (http://ready.arl.noaa.gov/HYSPLIT.php). NOAA Air Resources Laboratory, Silver Spring, MD.

Draxler, R.R., 2003: Evaluation of an ensemble dispersion calculation. *Journal of Applied Meteorology*, **42**, 308-317.

Eckhardt, S. A. Stohl, H. Wernli, P. James, C. Forester, and N. Spichtinger, 2004: A 15-year climatology of warm conveyor belts. *J. Climate*, **17**, 218-237.

Elliott, B. A., 1979: Anticyclonic rings and the energetics of the circulation of the Gulf of Mexico. PhD Thesis, Dept. of Oceanography, Texas A&M University, 188pp.

Elsner, J.B., S.W Lewers, J.C Malmstadt, and T.H Jagger, 2011: Estimating contemporary and future wind-damage losses for hurricanes affecting Elgin air force base, Florida. *J. Appl. Meteor. Clim.,* **50**, 1514-1526.

Forbes, G. S., R. A. Anthes, and D. W. Thompson, 1987: Synoptic and mesoscale aspects of an Appalachian ice storm associated with cold-air damming. *Mon. Wea. Rev*, **115,** 564–591.

Frankenfield, H. C., 1915: Sleet and ice storms in the United States. *Mon. Wea. Rev*, **43,** 608.

Fuhrmann, C. M., and C. E. Konrad II, 2013: A trajectory approach to analyzing the ingredients associated with heavy winter storms in central North Carolina, *Wea. Forecasting.,* **28**, 647-667.

Fuhrmann, C.M., 2011: A trajectory approach to analyzing the ingredients associated with heavy winter storms in Central North Carolina. *PhD Dissertation, Department of Geography, University of North Carolina*. 220pp.

---, and C. E. Konrad II, 2008: Synoptic-scale airflow and moisture transport associated with freezing rain events in central North Carolina, *65th Eastern Snow Conference, Vermont, USA*. Available at [http://www.unc.edu/~fuhrman1/FuhrmannKonradFZTrajectories.pdf].

Gao, Y., T. Wu., B. Chen., J. Wang., and Y. Liu, 2013: A numerical simulation of microphysical structure of cloud associated with the 2008 winter freezing rain over southern China, *Journal of the Meteor. Soc. Japan,* **91(2)**, 101-117.

Gay, D. A., and R. E. Davis, 1993: Freezing rain and sleet climatology of the southeastern USA. *Climate Res*, **3,** 209–220.

Graff, L. S., and J. H. LaCasce, 2014: Changes in cyclone characteristics in reponse to modified SSTs, *J. Climate*, **27**, 4273-4296.

Grout. T, H. Yang, J. Basara, B. Balasundaram, Z. Kong, and T. S. Bukkapatnam, 2012: Significant Winter Weather Events and associated Socioeconomic Impacts (Federal Aid Expenditures) across Oklahoma: 2000–10. *Wea. Climate Soc.*, **4**, 48–58.

Gustafsson, M., D. Rayner, and C. Deliang, 2010: Extreme rainfall events in southern Sweden: where does the moisture come from? *Tellus*, **62**, 605-616.

Gyakum, J. R., and P. J. Roebber, 2001: The 1998 ice storm—Analysis of a planetary-scale event. *Mon. Wea. Rev., **129***, 2983–2997.

Harman, H.H. 1976: *Modern Factor Analysis*. University of Chicago Press, Chicago, IL.

Hartstock, D., D. J. Rusk, B. W. Orr and P. J. Lamb, 2008: The ice storm of December

2007 at the SGP. *2008 ARM Science Team Meeting,* Online at: http://www.arm.gov/publications/proceedings/conf18/poster/P00095.pdf

Hauer, R.J., M.C Hruska, and J.O Dawson, 1994: Trees and ice storms: The development of ice storm-resistant urban tree populations. Department of Forestry, Univ. Illinois at Champaign, Urbana, III. Spec. Publ. 94-1.

Higgins, R.W., Y. Yao, and X. L. Wang, 1997: Influence of the North American monsoon system on the U.S summer precipitation regime. *J. Climate*, **10**, 2600-2622.

Hondula, D.M., L. Sitka, R.E. Davis, D.B. Knight, S.D. Gawtry, M.L. Deaton, T.R. Lee, C.P. Normile, and P.J. Stenger, 2009: A back-trajectory and air mass climatology for the Northern Shenandoah Valley, USA. *International Journal of Climatology*, **30**, 569-581.

Hong. S. Y., J. Ock, and J. Lim, 2006: The WRF single moment 6-class microphysics scheme (WSM6), *Journal of the Korean Met. Soc.,* **42(2)**, 129-151.

---, Y. Noh., and J. Dudhia., 2006: A new vertical diffusion package with an explicit treatment of entrainment processes, *Mon. Wea. Rev.,* **134**, 2318-2341.

Horel, J. D., 1981: A Rotated Principal Component Analysis of the Interannual Variability of the Northern Hemisphere 500 mb Height Field. *Mon. Wea. Rev.,* **109,** 2080-2092.

Hosek, J., P. Musilek, E. Lozowski., and P. Pytlak, 2011: Forecasting severe ice storms using numerical weather prediction: the March 2010 Newfoundland event., *Nat. Hazards. Earth. Syst. Sci.,* **11**, 587-595.

Hoskins, B. J., 1990: *Theory of extratropical cyclones*. Extratropical Cyclones: The Eric Palmen Memorial Volume, C.W. Newton and E.O. Holopainen, Eds., American Meteorological Society 129-153.

Houston, T. G., and S. A. Changnon, 2007: Freezing rain events: a major weather hazard in the conterminous U.S, *Nat. Hazards*, **40**, 485-494.

Houze, R.A., 1993: *Cloud dynamics*. Academic Press, San Diego, 573 pp.

Hu, X. M., P. M. Klein., and M. Xue, 2013: Evaluation of the updated YSU planetary boundary layer scheme within WRF for wind resource management and air quality assessments, *J. Geophys. Res. Atmos.,* **118(18)**, 10,490-10,505.

---, J. W. Nielson-Gammon., and F. Zhang, 2010: Evaluation of three planetary boundary layer schemes in the WRF model, *J. Appl. Meteor. Climatology,* **49**, 1831-1844.

Huffman, G. J., and G. A. Norman Jr., 1988: The supercooled warm rain process and the specification of freezing precipitation. *Mon. Wea. Rev.*, **116,** 2172–2182.

Huh, O. K., W. J. Wiseman Jr., and L. J. Rouse Jr., 1978: Winter cycle of sea surface thermal patterns, northeastern Gulf of Mexico, *J. Geophys. Res. Oceans,* **83**, 4523-4529.

Hurlburt, H. E., and J. D. Thompson, 1980: A numerical study of loop current intrusions and eddy shedding, *J. Phys. Oceanogr.,* **10,** 1611-1651.

Ikeda, K., M. Steiner, J. Pinto, and C. Alexander, 2013: Evaluation of cold-season precipitation forecasts generated by the hourly updating high-resolution Rapid Refresh Model. *Wea. Forecasting,* **28**, 921-939.

IPCC, Working Group I, 2013: The physical science basis, Fifth assessment report. Stocker, T. F and 9 co Eds. *Cambridge Univ. Press, Cambridge UK*. 1522pp.

Jones, K. F., A. C. Ramsey, and J. Neil Lott, 2004: Icing severity in the December 2002 freezing-rain storm from ASOS data. *Mon. Wea. Rev.,* **132**, 1630-1644.

Kain, J.S., 2004: The Kain-Fritsch convective parameterization: An update. *J. Appl. Meteor.,* **43**, 1701-81.

Kain, J.S., S.M. Goss, and M.E. Baldwin, 2000: The melting effect as a factor in precipitation-type forecasting. *Weather and Forecasting*, **15**, 700-714.

Kalnay E., and 21 Coauthors 1996: The NCEP/NCAR 40-year Reanalysis. *Bull Am Meteor Soc.,* **77**, 437-471.

Kennedy, A. D., X. Dong, B. Xi., S. Xie, Y. Zhang, and Y. Chen, 2011: A comparison of MERRA and NARR Reanalysis with the DOE ARM SGP data. *J. Climate*., **24**, 4541-4557.

Kidon, J., G. Fox, D. McKenney, and K. Rollins, 2001: Economic impacts of the 1998 ice storm on the eastern Ontario maple syrup industry. *Forestry Chronicle,* **77**, 667-675.

Kovacik, C, J. Hocker, M. Shafer, 2010: An analysis of southern U.S ice storm frequency from 2000-2009. Available at: [http://www.caps.ou.edu/reu/reu10/papers/Kovacik.pdf].

Kunkel, K. E., and 24 coauthors, 2013: Monitoring and understanding trends in extreme storms: State of knowledge. *Bull. Amer. Meteor. Soc.,* **94**, 499-514.

Lackmann, G., 2013: The south-central U.S flood of May 2010: present and future. *J.*

Climate, **26**, 4688-4709.

---, 2011: *Midlatitude Synoptic Meteorology: Dynamics, Analysis and Forecasting.* Amer. Meteor. Soc. 345pp.

---, 2011: Improving understanding and prediction of warm season precipitation systems in the southeastern and Mid-Atlantic regions, *Final Report to NOAA-CSTAR.* Available at: [http://www.erh.noaa.gov/rah/science/NSCU_CSTAR_III_Final_Report.pdf].

---, 2002: Cold-frontal potential vorticity maxima, the low-level jet, and moisture transport in extratropical cyclones. *Mon. Wea. Rev.,* **130**, 59-74.

---, K. Keeter, L. G. Lee, and M. B. Elk, 2002: Model representation of freezing and melting precipitation: implications for winter weather forecasting. *Wea. Forecasting,* **17**, 1016-1033.

Laflamme, J. N., and G. Périard, 1998: The climate of freezing rain over the province of Québec in Canada: A preliminary analysis. *Atmos. Res.*, **46,** 99–111.

Lamb, P.J., D. H Portis, A. Zangvil, 2012: Investigation of large-scale atmospheric moisture budget and land surface interactions over U.S Southern Great Plains including for CLASIC (June 2007). *J. Hydromet.,* **13**, 1719-1738.

Leatham, W. E., P. C. Burke, and A. A. Taylor, 2010: Verifying model forecasts of arctic fronts in advance of winter storms in the Southern Plains. *REU for Undergraduates Research.* Available at: [http://www.caps.ou.edu/reu/reu10/papers/Leatham.pdf]

Lin, Y. L., R. D. Farley, and H. D Orville, 1983: Bulk parameterization of the snow field in a cloud model. *J. Climate Appl. Meteor.,* **22**, 1065-1092.

Ludwig, P., J. G. Pinto, M, Reyers, and S. L. Gray, 2013: The role of anomalous SST and surface fluxes over the southeastern North Atlantic in the explosive development of windstorm Xynthia, *Quart. Journ. Roy. Met. Soc.,* DOI: 10.1002/qj.2253.

Maddox, R. A., 1983: Large-scale meteorological conditions associated with mid-latitude, mesoscale convective complexes. *Mon. Wea. Rev*., **111**, 1475-1493.

Martner, B. E., J. B. Snider, R. J. Zamora, G. P. Byrd, T. A. Niziol, and P. I. Joe, 1993: A remote-sensing view of a freezing-rain storm. *Mon. Wea. Rev*, **121,** 2562–2577.

Mass, C.F., and D.M. Schultz, 1993: The structure and evolution of a simulated midlatitude cyclone over land. *Monthly Weather Review*, **121**, 889-917.

Matsuo, T., and Y. Sayo, 1981: Melting of snowflakes below freezing level in the atmosphere. *Journal of the Meteorological Society of Japan*, **59**, 10-25.

McGrath, R., T. Semmler, C. Sweeney, and S. Wang, 2006: Impact of balloon drift errors in radiosonde data on climate statistics, *J. Climate*, **19**, 3430-3442.

McKay, G. A., and H. A. Thompson, 1969: Estimating the hazard of ice accretion in Canada from climatological data. *J. Appl. Meteor.*, **8,** 927–935.

McPherson, R. A., and 19 Coauthors 2007: Statewide Monitoring of the Mesoscale Environment: A Technical Update on the Oklahoma Mesonet. *J. Atmos. Oceanic. Technol.,* **24**, 301-321.

Mellor, G. L., and T. Yamada, 1982: Development of a turbulence closure model for geophysical fluid problems. *Rev. Geophys. Space. Phys.,* **20**, 851-875.

Meisinger, C. L., 1920: The precipitation of sleet and the formation of glaze in the eastern United States, January 20 to 25, 1920, with remarks on forecasting. *Mon. Wea. Rev.,* **48,** 73–80.

Mesinger, F., and coauthors, 2006: North American Regional Reanalysis. *Bull. Amer. Meteor. Soc.*, **87**, 343–360.

Miller, J.E., 1948: On the concept of frontogenesis. *J. Meteoro*., **5**, 169-171.

Millbrandt, J. A., M. K. Yau, J. Mailhot, S. Belair, R. McTaggart-Cowan, 2010: Simulation of an orographic precipitation event during IMPROVE-2. Part II: Sensitivity to the number of moments in the bulk microphysics scheme, *Mon. Wea. Rev.,* **138**, 625-642.

---, and M. K. Yau, 2006: A multimoment bulk physics parameterization. Part III: Control simulation of a hailstorm, *J. Atmos. Sci.,* **63**, 3114-3136.

---, and M. K. Yau, 2006: A multimoment bulk physics parameterization. Part IV: sensitivity experiments, *J. Atmos. Sci.,* **63**, 3137-3159.

---, and M. K. Yau, 2005: A multimoment bulk microphysics parameterization. Part I: Analysis of the role of the spectral shape parameter, *J. Atmos. Sci.,* **65,** 1528-1548.

Mitra, S.K., O. Vohl, M. Ahr, and H. R. Pruppacher, 1990: A wind tunnel and theoretical study of the melting behavior of atmospheric ice particles IV: experiment and theory for snowflakes. *J Atmos. Sci*., **47**, 584-591.

Molinari, R. L., 1978: An overview of the circulation in the Gulf of Mexico, *Summary*

Report: Working conference on the circulation of the Gulf of Mexico. Wilson Sturges and S. L. Shang, Eds., Dept. of Oceanography, Florida State University, 29-30.

Morrison, H., G. Thompson, and V. Tatarskii, 2009: Impact of cloud microphysics on the development of trailing stratiform precipitation in a simulated squall line: Comparison of 1-moment and 2-moment schemes, *Mon. Wea. Rev.,* **137**, 997-1007.

---, and J. O. Pinto, 2006: Intercomparison of bulk cloud microphysics schemes in mesoscale simulations of springtime arctic mixed-phase stratiform clouds. *Mon. Wea. Rev.,* **134**, 1880-1900.

---, J. A. Curry, and V. I. Khvorostyanov, 2005: A new double-moment microphysics parameterization for application in cloud and climate models. Part I: Description, *J. Atmos. Sci.,* **62**, 1665-1677.

Mullens, E.D., L. M. Leslie, and P.J. Lamb: A regional climatology and synoptic pattern analysis of winter storms in the Southern Great Plains 1993-2011. *In preparation.*

Namias, J**.,** 1962: Surface-air Interaction as a Fundamental cause of Drought and other Climatic Fluctuations, Proceedings of Symposium on Arid Zone Research, Changes in Climate, 345–359, *UNESCO, World Meteorol. Organ., Geneva*.

Noh, Y., W. G. Cheon, S.-Y. Hong, and S. Raasch, 2003: Improvement of the K-profile model for the planetary boundary layer based on large eddy simulation data. *Bound. Layer. Meteor.,* **107**, 401-427.

Nowlin, W. D., 1972: Winter circulation patterns and property distributions. *Contributions on the Physical Oceanography of the Gulf of Mexico*, Vol II, L. R. A. Capurro, and J. L. Reid, Eds. Gulf Publishing Co., 3-51.

Olthof, I., D. J. King, and R. A. Lautenschlager, 2004: Mapping deciduous forest ice storm damage using Landsat and environmental data. *Remote Sensing of Environment*. **84**, 484-496.

Otkin, J. A., and T. J. Greenwald, 2008: Comparison of WRF-model simulated and MODIS-derived cloud data, *Mon. Wea. Rev.,* **136**, 1957-1970.

Persson, P. O., and T. T. Warner, 1993: Nonlinear hydrostatic conditional symmetric instability: Implications for numerical weather prediction. *Mon. Wea. Rev.,* **121**, 1821-1833.

Pielke, R. A., and Coauthors, 1992: A comprehensive meteorological modeling system-RAMS. *Meteor. Atmos. Phys.,* **49**, 69-91.

Pruppacher H.R., and Klett, J.D, 1981: *Microphysics of clouds and precipitation.* Dordrecht: D. Reidel Publishing.

---,1997: *Microphysics of clouds and precipitation.* 2nd Ed. Dordrecht: D. Reidel Publishing

Pytlak, P., P. Musilek, E. Lozowski, and D. Arnold, 2010: Evolutionary Optimization of an Ice Accretion Forecasting System (IAFS), *Mon. Weather Rev*., **138**, 2913–2929.

Ramer, J., 1993: An empirical technique for diagnosing precipitation type from model output. Preprints, *5th International Conf. On Aviation Weather Systems,* Vienna, VA, AMS, 227–230.

Ramos Da Silva, R., G. Bohrer, D. Werth, M.J. Otte, and R. Avissar, 2006: Sensitivity of ice storms in the southeastern United States to Atlantic SST – Insights from a case study of the December 2002 storm. *Monthly Weather Review*, **134**, 1454-1464.

Rauber, R. M., L. Olthoff, M. Ramamurthy, D. Miller, and K. Kunkel, 2001: A synoptic weather pattern and sounding based climatology of freezing precipitation in the United States east of the Rocky Mountains. *J. Appl. Meteor.,* **40**, 1724-1747.

---, L. Olthoff, M. Ramamurthy, and K. Kunkel, 2000: The relative importance of warm rain and melting processes in freezing precipitation events. *J. Appl. Meteor.*, **39,** 1185–1195.

---, M. K. Ramamurthy, and A. Tokay, 1994: Synoptic and mesoscale structure of a severe freezing rain event: The St. Valentine's Day ice storm. *Wea. Forecasting*, **9,** 183–208.

Ressler, G M., S.M. Milrad, E.H. Atallah, and J.R. Gyakum, 2012: Synoptic-Scale Analysis of Freezing Rain Events in Montreal, Quebec, Canada. *Wea. Forecasting.*, **27**, 362–378.

Reynolds, R. W., T. M. Smith, C. Liu, D. B. Chelton, K. S. Casey, and M. G. Schlax, 2007: Daily high-resolution blended analyses for sea surface temperature, *J. Climate*, **20**, 5473-5496.

---, and T. M. Smith, 1993: Improved global sea surface temperature analyses using optimal interpolation, *J. Climate.,* **7**, 929-948.

Richman, M.B., 1986: Rotation of Principal Components. *J. Climatology.,* **6,** 293-335.

Riehl, H., and and Coauthors, 1952: *Forecasting in Middle Latitudes*. *Meteor. Monogr,* No. 5, Amer. Meteor. Soc., 80 pp.

Robbins, C., and J. V. Cortinas Jr., 2002: Local and synoptic environments associated with freezing rain in the contiguous United States. *Wea. Forecasting*, **17,** 47–65.

Robbins, C. C., 1998: An investigation of the local and synoptic environments associated with freezing rain in the contiguous U.S. M.S Thesis, Dept. of Atmospheric Science, University of Oklahoma, Norman, OK, 112pp.

Roberts, E., and R. E. Stewart, 2008: On the occurrence of freezing rain and ice pellets over the eastern Canadian Arctic, *Atmospheric Research*, **89**, 93-109.

Roebber, P.J., and L.F. Bosart, 1998: The sensitivity of precipitation to circulation details, Part I: An analysis of regional analogs. *Monthly Weather Review*, **126**, 437-455.

---, and Gyakum, 2003: Orographic influences on the mesoscale structure of the 1998 ice storm. *Mon. Wea. Rev.,* **131**, 27-50

Rutledge, S. A., and P. V. Hobbs, 1983: The mesoscale and microscale structure and organization of clouds and precipitation in mid-latitude cyclones. VIII: A model for the "seeder feeder" process in warm frontal rainbands. *J. Atmos. Sci.,* **40,** 1185-1206.

Sanders, K. J., C. M. Gravelle, J. P. Gagen, and C. E. Graves, 2013: Characteristics of major ice storms in the central United States. *J. Operational Meteor.,* **1**, 100-113.

Schultz, D.M., 2001: Reexamining the cold conveyor belt. *Monthly Weather Review*, **129**, 2205-2225.

---, J.V. Cortinas, and C.A. Doswell, 2001: Comments on "An operational ingredients-based methodology for forecasting midlatitude winter season precipitation". *Weather and Forecasting*, **17**, 160-167.

Shi, J. J., and Coauthors, 2010: WRF simulations of the 20-22 January 2007 snow events over eastern Canada: Comparison with in-situ and satellite observations. *J. Appl. Meteorology and Climatology,* **49**, 2246-2266.

Shin, H. H., and S.-Y. Hong, 2011: Intercomparison of planetary boundary layer parameterizations in the WRF model for a single day from CASES-99, *Bound. Layer. Meteor.*, **139**, 261-281.

Skamarock, W. C., and Coauthors, 2008: A description of the advanced research WRF version 3. NCAR Tech. Note NCAR/TN-475+STR, 88pp.

Stensrud, D. J., 1996: Importance of low-level jets to climate: A review, *J. Climate*, **9**, 1698-1711.

Stewart, R.E., D. T. Yiu, K. K. Chung, D. R. Hudak, E. P. Lozowski, M. Oleskiw, B. E. Shepard, and K. K. Szeto, 1995: Weather conditions associated with the passage of precipitation type transition regions over eastern Newfoundland. *Atmos.-Ocean,* **33**, 25-53.

Stewart, R. E., and P. King, 1987: Freezing precipitation in winter storms. *Mon. Wea. Rev*, **115,** 1270–1279.

Stewart, R.E., 1985: Precipitation types in winter storms. *Pure and Applied Geophysics*, **123**, 597-609.

Stoelinga, M. T., 1996: A potential-vorticity based study of the role of diabatic heating and friction in a numerically simulated baroclinic cyclone. *Mon. Wea. Rev.,* **124**, 849-874.

Stohl, A., 1998: Computation, accuracy and applications of trajectories – a review and bibliography. *Atmospheric Environment*, **32**, 947-966

---, and P. Seibert, 1998: Accuracy of trajectories as determined from the conservation of meteorological tracers. *Quarterly Journal of the Royal Meteorological Society*, **125**, 1465-1484.

Stokes, G. M., Schwartz, S. E, 1994: The Atmospheric Radiation Measurement (ARM) Program: Programmatic Background and Design of the Cloud and Radiation Test bed., *Bull. Amer. Meteor. Soc.,* **75**, 1201-1221.

Straka J., 2009: *Cloud and Precipitation Microphysics*, Cambridge University Press, Cambridge, UK, ISBN: 978-0-521-88338-2. 392pp.

Strapp, J., R. Stewart, and G. Isaac, 1996: A Canadian climatology of freezing precipitation and a detailed study using data from St. John's, Newfoundland. *Proc. FAA Int. Conf. on Aircraft Inflight Icing,* Vol. 2, Springfield, VA, FAA, DOT/FAA/AR-96/81, 45– 56.

Strong, M., Z. D. Sharp, and D. S. Gutzler, 2007: Diagnosing moisture transport using D/H ratios of water vapor, *Geophys. Res. Lett.,* **34(3)**, DOI: 10.1029/2006GL028307

Stuart, R., and G. Isaac, 1999: Freezing precipitation in Canada. *Atmos.–Ocean*, **37,** 87–102.

Sturges, W., and J.C. Evans, 1983: On the variability of the Loop Current in the Gulf of Mexico, *Journal of Marine Research*, **41**, 639-653

Sukorianski, S., B. Galperin, and V. Perov, 2006: A quasi-normal scale elimination

model of turbulence and its application to stably stratified flows, *Nonlinear Processes in Geophysics,* **13**, 9-22.

Sun, J., and S. Zhao, 2010: The impacts of multiscale weather systems on freezing rain and snowstorms over southern China. *Wea. Forecasting*, **25**, 388-407.

Thompson, G., P. R. Field., R. M. Rasmussen, and W. D. Hall, 2008: Explicit forecasts of winter precipitation using an improved bulk microphysics scheme. Part II: Implementation of a new snow parameterization. *Mon. Wea. Rev.,* **136**, 5095-5115.

---, M. Rasmussen, and K. Manning, 2004: Explicit forecasts of winter precipitation using an improved bulk microphysics scheme. Part I: Description and sensitivity analysis. *Mon. Wea. Rev.,* **132**, 519-542.

Uccellini, L.W., D. Keyser, K.F. Brill, and C.H. Wash, 1985: The Presidents' Day cyclone of 18-19 February 1979: Influence of upstream trough amplification and associated tropopause folding on rapid cyclogenesis. *Monthly Weather Review*, **115**, 2227-2261.

Vavrus, S., J. E Walsh, W. L Chapman, D. Portis, 2006: The behavior of extreme cold air outbreaks under greenhouse warming. *International Journal of Climatology*, **26**, 1133-1147.

Vergés, A., and 22 co-authors, 2014: The tropicalization of temperate marine ecosystems: climate mediated changes in herbivory and community phase shifts. *Proc. R. Soc. B.,* **281**, 20140846.

Wallace, J. M., and P. V. Hobbs, 1977: *Atmospheric Science, An Introductory Survey*. 1st Ed. Academic Press, 483 pp.

Walko, R. L., and C. A Tremback, cited 2001: Introduction to RAMS 4.3/4.4. [Available online at www.amet.com/html/docs/rams/ug44-rams.intro.pdf.]

Wang, H., E. Yu., and S. Yang, 2011: An exceptionally heavy snowfall in Northeast China: large-scale circulation anomalies and hindcast of the NCAR-WRF model., *Meteorol. Atmos. Phys.,* **113**, 11-25.

Wang, P.Y., J.E. Martin, J.D. Locatelli and P.V Hobbs, 1995: Structure and Evolution of Winter Cyclones in the United States and their Effects on the Distribution of Precipitation. Part II: Arctic Fronts. *Monthly Weather Review.,* **123**, 1328-1344.

Wang, W., W. D. Nowlin Jr., and R. O. Reid, 1998: Analyzed surface meteorological fields over the northwestern Gulf of Mexico for 1992-94: Mean, seasonal and monthly patterns, *Mon. Wea. Rev.,* **126**, 2864-2883.

Warrillow, M., and P. Mou, 1999: Ice storm damage to forest tree species in the

ridge and valley region of southwestern Virginia. *Journal of the Torrey Botanical Soc.,* **126,** 147-158.

White, E.D., L. L. Leslie, and P. J. Lamb, 2011: Winter storm simulations using WRF: identifying critical parameterizations. Presentation. *Atmospheric Systems Research, Fall Working Group Meeting, Annapolis, MD.*

WMO, 1996: *Measurement of Meteorological Variables. Part I, Guide to meteorological instruments and methods of observation*, 6th Ed., WMO Publication 8, World Meteorological Organization, 640 pp.

Yongning, S., 1996: A simulation of the effects of Gulf of Mexico sea surface temperature anomalies using the Canadian regional climate model, Masters Thesis, McGill University, Canada. Available at: [http://www.nlc-bnc.ca/obj/s4/f2/dsk2/ftp04/mq29784.pdf]

Zerr, R. J., 1997: Freezing rain: An observational and theoretical study. *J. Appl. Meteor., 36,* 1647–1661.

Zhang, G., S Luchs., A Ryzhkov., M Xue., L Ryzhkova., and Q Cao, 2010: Winter Precipitation Microphysics Characterized by Polarimetric Radar and Video Disdrometer Observations in Central Oklahoma. *Journal of Applied Meteorology and Climatology* **50**:7, 1558-1570.

Data and Resources

Atmospheric Radiation Measurement (ARM) online data archive: [http://archive.arm.gov]: Datasets used include: CMBE version 2, Microbase, Atmospheric soundings. Accessed periodically 2008-2014.

HYSPLIT (NOAA/Air Resources Lab) [http://arl.noaa.gov/HYSPLIT_info.php] Version 4.9.

Mesoscale and Microscale Meteorology Division (MMM), NCEP/UCAR Image Archive [http://locust.mmm.ucar.edu], accessed periodically 2010-2014.

Model Evaluation Toolkit (MET): [http:/www.dtcenter.org/met/users]: MET was developed at the National Centers for Environmental Research (NCAR) through grants from the United States Air Force Weather Agency (AFWA) and NOAA. NCAR is sponsored by the United States National Science Foundation (NSF). Accessed 06/2013.

NCAR Graphics Language (NCL) [http://ncl.ucar.edu] Version 5.2.0 Boulder, CO: UCAR/NCAR/CISL/VETS.

NCEP FNL Operational Model Global Tropospheric Analyses Final Analysis (GFS): Used as WRF input/boundary conditions [http://rda.ucar.edu/datasets/ds083.2/]

NCEP/NWS/NOAA/U.S Dept. Commerce. 2000, updated daily. Accessed 02/2012.

NCEP-NARR Reanalysis: Provided by NOAA/OAR/ERSL PSD, Boulder, CO [http://www.ersl.noaa.gov/psd/data/gridded/data.narr.html]. Accessed periodically 2009-2013.

NCEP Stage IV QPE Product [http://www.emc.noaa.gov/mmb/ylin/pcpanl/stage4] Data provided by NCAR/EOL under the sponsorship of the National Science Foundation http://data/eol/ucar.edu/. Accessed 2011.

National Climatic Data Center (NCDC): Climatological datasets included

- Storm Event/Storm Data [http://www.ncdc.noaa.gov/stormevents]
- Local climate summaries [http://www.ncdc.noaa.gov/IPS/lcd/lcd.html]

Accessed Periodically 2010-2014.

OSCER Supercomputing, University of Oklahoma [http://www.oscer.ou.edu/] OSCER (Oklahoma Supercomputing Center for Education and Research) is greatly appreciated in facilitating this work, including all the support staff.

Oklahoma Mesonet:
Obtained from the ARM archive: 5 Minute observations of surface temperature. Accessed 01/2013.

Optimal Interpolation (NOAA) Version 2 ¼ degree daily SST Analysis
Downloaded from: [ftp://eclipse.ncdc.noaa.gov/pub/OI-daily-v2/NetCDF]
Accessed periodically 2010-2013.

R Software for Statistical Computing [http://www.r-project.org/]

Real Time Global SST Analysis (RTG-SST) [http://polar.ncep.noaa.gov/sst/] Developed at the National Centers for Environmental Prediction/Marine Modeling and Analysis Branch (NCEP/MMAB), First accessed 2012.

University of Wyoming Sounding Archive
[http://weather.uwyo.edu/upperair/sounding/html/]
Accessed periodically 2010-2012.

Appendix

Section 2: Additional Material from Regional Climatology (Chapter 2)

Database Development

Chapter 2, section 2.2 introduces the methodology for establishing a winter storm database between 1993-2011. Fig. A2.1 below shows the format of the database, obtained primarily from *Storm Event/Storm Data* and companion sources discussed in the text.

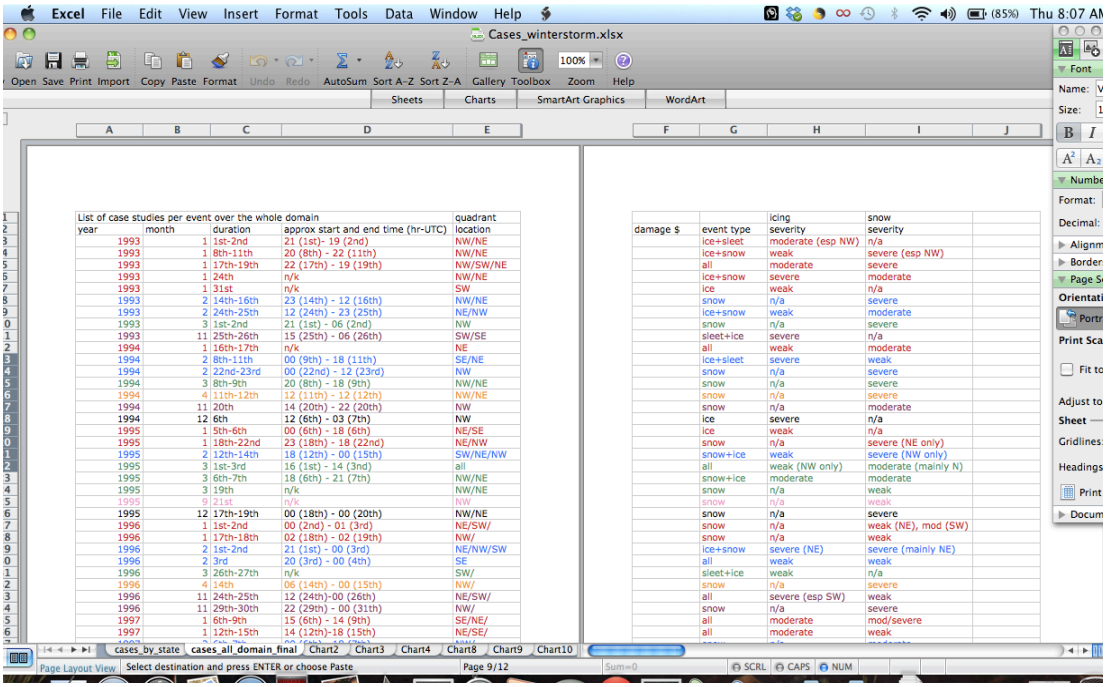

Figure A2.1. Screen-shot of winter storm database, which includes year and day, approximate durations, spatial location expressed as affected quadrant(s), and whether snow and/or ice occurred. Definitions of 'weak', 'moderate' and 'heavy' icing were quasi-subjective (especially in thresholds used) and based on event descriptions from *Storm Data/Storm Event,* included maximum reported accumulations (can be anywhere within the storm and not necessarily a widespread average). Weak is approximately < 0.25 ice and < 5 in snow, moderate 0.25-0.5 in ice, 5-8 in snow, and heavy > 0.5 in ice, >8 in snow.

Table A2.1 summarizes some basic information from the database by quadrant.

Quadrant	Number of evens with Ice	Number of events with Snow	Overlap event rate* (ice & snow). (% of total ice)	Number with weak ice (snow)$^{+}$	Number above moderate ice (snow)	Number impacting only stated quadrant (ice & snow)
Northwest	58	102	79.3	31 (34)	27 (68)	34
Southwest	33	48	75.6	17 (20)	16 (28)	10
Northeast	55	75	78.1	26 (22)	29 (53)	9
Southeast	24	26	79.2	7 (9)	17 (17)	2
Total storms	**156**					

*Where a snow event was accompanied by ice and vice versa. The locations of each phase type did not necessarily have to interest. We did not consider relative intensities of each phase type for this table. +Definitions of ice severity described above (Fig. A2.1).

Spatial Aggregation Methodology

Development of a spatial climatology (frequency by climate division) was discussed in section 2, and displayed in Fig. 2.3. Since the description in chapter 2 was brief, here we include the set of steps used to create this distribution:

1. List names of each county residing in each climate division (CD) used (Fig. 2.1 shows applicable CDs).
2. Using data sources in chapter 2 (especially *Storm Data/Storm Event*), manually count the number of days (24 hr period 00 UTC-00 UTC) that a report of freezing precipitation/snow was given. Match the described locations (e.g., counties, town names, spatial information from NARR, analysis charts, radar) with CDs. This step was performed for each month of each year and then summed to create a total for the 18-years. Figure A2.2 shows a couple of examples of how spatial -> CD information was derived.

3. Each CD has an area (in square miles). By calculating the mean CD area we can create a weighting (or normalization) factor that adjusts the total ice/snow frequency by area. Large (small) CDs are adjusted down (up) reflecting the fact that a smaller CD was likely to have observed less total events in part due to its size. Table A2.2 shows the values of each weighting factor, based on departures from a mean CD area of 11203.2 square miles.

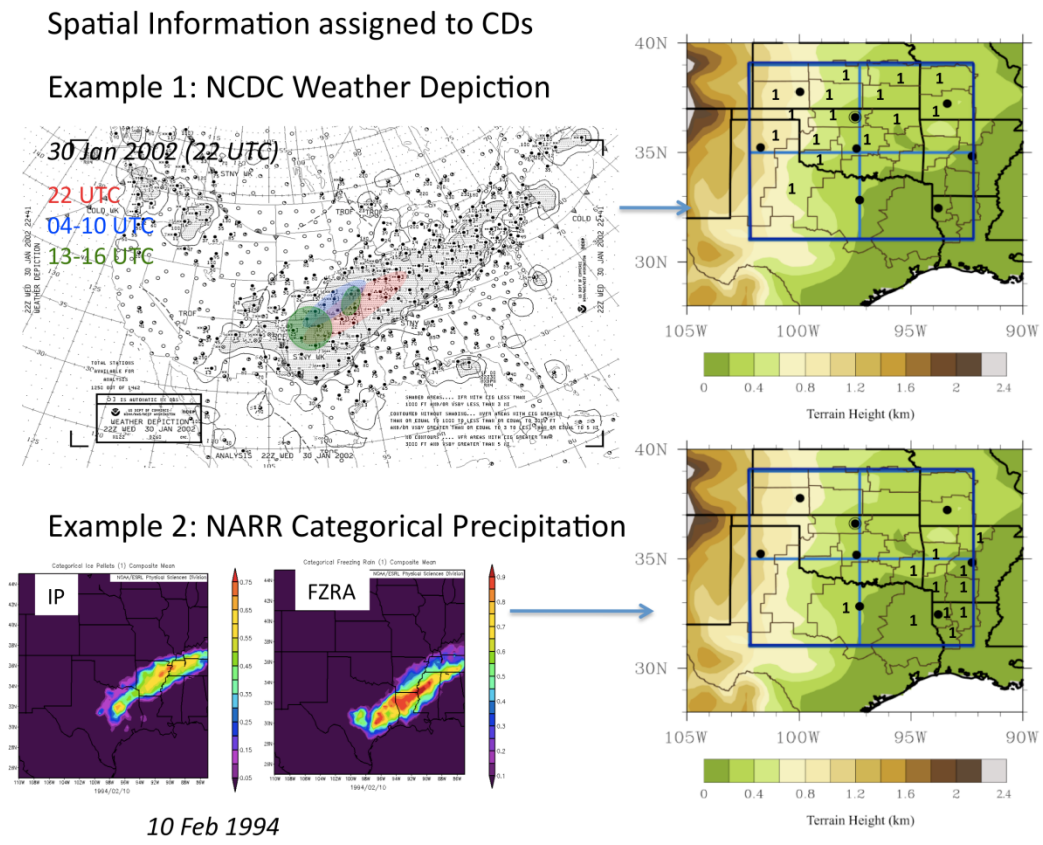

Figure A2.2: Example of methods used to derive spatial estimates of ice and snow by climate division. Top: Use of NCDC weather charts (3-hour interval) to assess locations for various times during a 24-hour period, Bottom: Use of NARR categorical precipitation type (both FZRA and IP). Right hand side shows how the spatial information is translated to a number (1 = 1-day observation). Where possible, these techniques were used in combination.

Table A2.2. Normalization factors and adjusted 18-year average event frequency (days per year) for each CD. Applicable CDs are shown by state abbreviation and number. Fig. A2.3 shows these visually, that image courtesy of http://www.esrl.noaa.gov/psd/data/usclimdivs/data/map.html. Note that these factors to not have a summation of 1, as is typically preferred when weighting. Normalization by the CD mean area, rather than its sum, is necessary to preserve the correct frequency magnitudes.

Climate Division (State and number)	Weighting factor	Ice	Snow
AR 1	1.57	3.06	5.42
AR 2	1.51	2.09	3.68
AR 4	1.40	2.10	3.03
AR 5	1.53	1.87	2.30
AR 7	1.55	1.37	1.72
AR 8	1.40	1.25	1.01
KS 4	1.29	0.14	7.00
KS 5	1.20	1.13	7.00
KS 6	1.22	2.03	7.31
KS 7	0.94	0.94	5.38
KS 8	1.00	1.77	5.49
KS 9	1.08	1.55	2.93
LA 1	1.65	1.92	0.46
LA 2	1.45	1.78	0.25
LA 4	1.65	1.46	0.64
MO 3	1.08	2.05	3.85
MO 4	0.97	1.62	1.57
OK 1	1.28	2.06	8.18
OK 2	1.27	2.54	4.90
OK 3	1.24	2.07	3.18
OK 4	1.46	2.03	4.39
OK 5	1.08	2.95	3.85
OK 6	1.36	2.42	3.03
OK 7	1.38	2.46	2.84
OK 8	1.25	2.36	1.73
OK 9	1.42	2.93	2.37
TX 1	0.40	0.80	3.33
TX 2	0.78	2.26	4.08
TX 3	0.40	1.21	1.03
TX 4	0.51	0.91	0.71

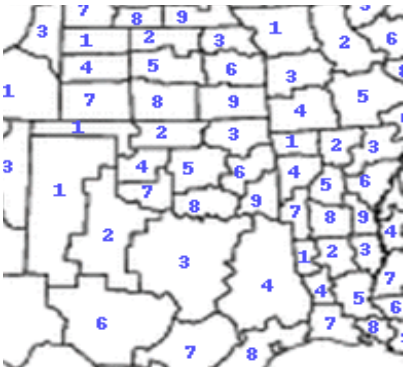

Figure A2.3: See Table A2.2.

Sounding Climatology

Here we provide further context for the methodology and results in Chapter 2, sec 2.3. Table A2.3 below shows the total number of soundings used from each of the eight station sites (Fig 2.1).

Table A2.3. Number of soundings used by station site for ice (*snow*). 51 profiles were from 12 UTC, 38 at 00 UTC, 5 at 18 UTC and 3 at 06 UTC.

Sounding Location (Site)	Number
Amarillo, TX	4 *(5)*
Dodge City, KS	8 *(4)*
Lamont, OK	11 *(5)*
Norman, OK	30 *(6)*
Little Rock, AR	10 *(0)*
Shreveport, LA	4 (*0*)
Springfield, MO	17 (*4)*
Dallas-Fort Worth, TX	8 *(0)*

A caveat from the text was that the number of profiles used (97 ice) was greater than the number of events from which those profiles were drawn (36). Table A2.4 lists the winter storms associated with ≥ 4 sounding profiles through their duration. Table A2.4 provides evidence supporting the statement on dissertation page 43 regarding the sounding bias toward long duration events and/or that producing significant icing. Co-location of observations with soundings generally meant that brief events must be well timed to the radiosonde launch. Chances of obtaining a temporal and spatial match was increased when the event temporal duration increased. Based on this, complete independence of sounding profiles cannot be assumed, albeit localized modifications to the thermal profile (terrain, precipitation intensity, strength of warm or cold advection, system movement) do produce observable distinctions between sites and times within a single storm.

Table A2.4. Case studies with ≥ 4 sounding profiles in the dataset. Rightmost column lists the locations, time and precipitation type for each.

Event	Number of Profiles	Locations, Time, Type
December 9-11 2007	8	Lamont 06 UTC 9 (FZRA), Springfield 00 UTC 10 (FZRA), 12 UTC 10 (FZRA), Lamont 18 UTC 10 (FZRA), Dodge City 00 UTC 11 (FZRA), OUN 12 UTC 9, 10 (FZDR), OUN 00 UTC 10 (IP).
December 24-27 2000	7	Little Rock, 00, 12 UTC 26 00 UTC 27 (FZRA), OUN 00 UTC 12 UTC 26 (FZRA), Dallas 00 UTC 26 (FZRA), Little Rock 12 UTC 27 (FZDR).
February 25-27 2003	6	Springfield 12 UTC 26 (FZRA), Little Rock 12 UTC 26, 00 UTC 27 (FZRA), OUN 12 UTC 26, 00 UTC 27 (FZDR), Dallas 12 UTC 26 (FZDR).
December 12-13 2000	6	Dallas 00 UTC 12 UTC 13 (FZRA), Shreveport 12 UTC 13 (FZRA), OUN 00 UTC, 12 UTC 13 (IP), Little Rock 12 UTC 13 (IP).
December 21-24 1998	5	Dallas 12 UTC 23 (FZRA), Shreveport 12 UTC 23, 24 (FZRA), OUN 12 UTC 21 (FZDR), Little Rock 12 UTC 23 (IP).
January 26-28 2009	5	Springfield 00 UTC 27 (FZRA), Little Rock 12 UTC 27 (FZRA), Lamont 18 UTC 26 (FZDR), OUN 00 UTC 27 (FZDR), OUN 12 UTC 27 (IP).
January 29-31 2002	4	OUN 12 UTC 30 (FZRA), Lamont 00 UTC 30 (FZRA), Amarillo 00 UTC 31 (FZRA), Amarillo 12 UTC 30 (IP).
January 28-30 2010	4	Amarillo 12 UTC 28 (FZDR), OUN 12 UTC 29 (FZDR), OUN 00 UTC 29 (IP), Little Rock 12 UTC 29 (IP).

Autocorrelations were calculated to check the degree of interdependence between profiles (for warm layer wetbulb maximum temperatures), shown in Fig. A2.4 overleaf. The values indicate reasonable independence of samples, although additional variables should also be tested. It may therefore be possible to examine the dataset using further statistical methods (e.g., bootstrapping), although such was outside of the scope of the dissertation.

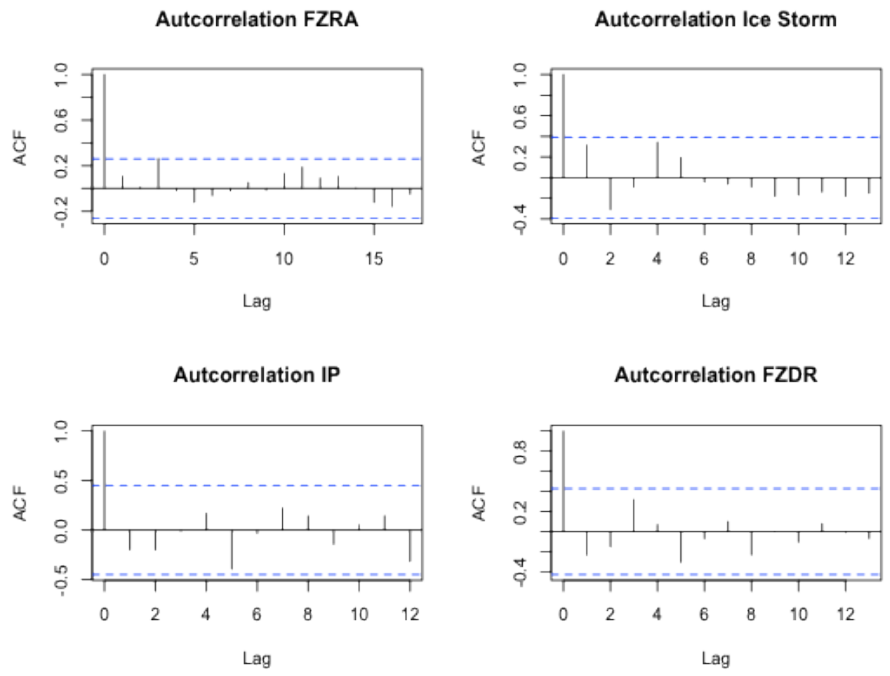

Figure A2.4. Autocorrelations computed from 'R' for each hydrometeor subcategory of freezing precipitation. Observation lag on x-axis (not strictly time as the samples were generally discrete), with magnitude of autocorrelation (ACF) on the y-axis. Range of statistical significance shown by the blue dashed lines.

Sounding Climatology: Linear Interpolation for MLD, FLD

When the 0°C level aloft bounding the warm layer and top of the refreezing layer do not fall on a measurement, level, the simple technique below is used to approximate these levels, for top of refreezing and warm layer respectively:

$$Z_{fz} = Z_{fz+1} - \left[\frac{|T_{fz+1}|}{(|T_{fz-1} + T_{fz+1}|)} \right] (Z_{fz+1} - Z_{fz-1}) \qquad \text{(A2.1)}$$

Where Z_{fz} is the height of the 0°C level, Z_{fz-1} and Z_{fz+1} the heights below and above this level respectively, and T_{fz-1} and T_{fz+1} their corresponding temperatures (°C).

Section 3: Additional Material from Synoptic Climatology (Chapter 3)

TABLE A3.1: List of events forming dataset for ice used in the rotated principal component analysis (PREOF). Table highlights time T_0, the patterns each case study was found to correspond with (where 0 indicates the event did not correlate with any of the resolved patterns from the PREOFs) and approximate locations impacted (state abbreviations). Using a combination of information, including *Storm Data*, and NCDC local climate summaries, durations and liquid precipitation equivalent (LPE) are estimated. LPE is evaluated from surface observations for several major stations over the impacted area, and the uppermost value is used, to provide an upper (recorded) threshold for each event. In cases where events are in two or more pattern groups, the highest correlated pattern is denoted by $^{+}$.

Event Date/Time (UTC) (T_0 ± 3 hr)	Type (Ice)	Areas Impacted	Approx. Duration of event (hours) from representative station	Approx maximum liquid equivalent precipitation (in) from representative station
2100 1 January 1993	4	S KS, W-C-E OK, N TX	24	0.25
1200 18 January 1993	7	N/C AR, N TX	30	0.70
1500 25 November 1993	0	E & S OK, N TX	15	0.22
0000 9 February 1994	5	SE OK, SW AR, NE TX	30	0.55
1200 6 January 1995	8	C AR	6	0.55
0000 2 February 1996	6	NE TX, NW LA, S AR	12	0.39
1800 24 November 1996	1 and 8^{+}	N TX, S OK	6	0.60
1500 8 January 1997	1	SE OK, N TX, S-C AR	24	0.45
0600 15 January 1997	7	S-SE OK, NE TX, S-C AR	30	0.56
1200 4 January 1998	4	S KS	12	1.10
1200 16 March 1998	1	N Panhandle, S KS	12	0.46
1800 20 December 1998	2	N OK, S KS, SW MO	38	0.35
0000 8 January 1999	6^{+} and 8	NW TX, SW OK, C OK, C AR	15	0.10
0000 13 December 2000	5	NC TX, S OK, SW AR	24	0.65
0000 26 December 2000	1^{+} and 7	N TX, S OK, SW/C AR	42	1.07
1800 28 January 2001	4	SC-NC OK, NE OK,	24	1.00
1200 27 February 2001	3^{+} and 7	C, SE KS	12	0.24
1800 28 November 2001	4 and 5^{+}	N TX	12	0.29
0000 30 January 2002	3	S/SE KS, N/C, W/C OK	36	1.10
0000 4 December 2002	7	C, NE OK, N AR	15	0.86
1200 26 February 2003	6	C TX, E OK, S AR	10	0.30
1800 4 January 2005	2^{+} and 4	N OK, S KS	18	1.82
1800 19 February 2006	2	C OK-NE OK, W-C AR	12	0.36
1200 19 December 2006	3^{+} and 7	SW KS, Panhandle	24	<0.5
1200 30 December 2006	1	C/E Panhandle (TX)	24	0.25
0000 13 January 2007	3	C, E/NE OK, SW MO	48	2.58
1200 9 December 2007	3	SW/C/NE OK, SW MO, NW AR	48	2.05
0600 22 January 2008	2^{+} and 6	SW, C-NE OK, NW AR	6	0.25
2100 15 February 2008	6	C & SE OK	24	<0.5
1200 23 December 2008	5	SE OK, E KS,C AR	10	<0.25
1800 26 January 2009	2	C/E OK, C/N AR	30	1.26
1500 28 January 2010	1	SW/C OK, E Panhandle (TX)	12	1.06

TABLE A3.2: As Table A1, but for snow events. Snow amounts are estimated in a similar fashion to the LPE estimates. When the estimate is uncertain (e.g. snowfall bands outside of measurement locations), measurement ranges from the *Storm Data* archive are used. As in Table A1, upper thresholds or ranges are shown below. Missing information is shown as a dash.

Event Date/Time (UTC) (T_0 ± 3 hr)	Type (Snow)	Locations Impacted	Approx. Duration of event (hours) from representative station	Approx maximum liquid equivalent precipitation (in) from representative station (max snowfall in inches)
0000 9 January 1993	3	Panhandle (OK/TX), NW OK, NC & C OK, S KS.	30	0.30 (6.3)
0600 15 February 1993	1^+ and 5	NW-NE OK, S/SW KS and S MO	48	0.77 (11.2)
1200 25 February 1993	3	N OK, SW-S KS, SW MO	24	0.69 (12.0)
1800 8 March 1994	0	N & Panhandle OK, E & C OK, C & N AR	24	1.75 (12.9)
0000 19 January 1995	2	S MO, SE KS,	18	0.57 (8.0)
1800 12 February 1995	1 and 3^+	SW-E Panhandle (OK, TX), NW & C OK, SW/SC KS	12	0.21 (5.1)
1200 1 March 1995	3	SW KS, NC OK	30	0.50 (9.2)
0600 7 March 1995	0	SW KS, N OK	24	0.22 (4-6)
0900 18 December 1995	2^+ and 5	NW OK, S KS, N Panhandle (OK, TX)	21	0.40 (5.0)
0900 2 January 1996	4	NE OK, N AR, SW MO	24	1.20 (8.2)
1200 18 January 1996	6	NW OK, C KS	12	1.27 (4)
0600 2 February 1996	1	C OK, C AR & N	18	0.15 (6-9)
1500 8 January 1997	4	W, C & E OK, SE KS, N AR, S MO	24	0.80 (9.0)
1200 8 January 1998	0	S/SE KS, SW MO	18	0.47 (4.2)
0000 8 March 1998	2	S KS/ SW KS, Panhandle (N TX)	18	0.66 (9.3)
1500 12 March 1999	2	Panhandle (OK/TX), NW OK, SW KS	24	1.81 (13.0)
2100 26 January 2000	0	W, C & E OK, S KS, N AR, N TX	21	0.80 (8.9)
0000 13 December 2000	1	N OK, N AR, SW MO	24	1.05 (7.3-14.2)
0900 31 December 2000	0	E OK, NW AR	21	0.13 (4-6)
0300 5 December 1999	2	S KS, N & C OK	9	0.63 (4.5)
1200 16 January 2001	5	NW OK, Panhandle, S KS	27	0.24 (4-10)
2100 28 November 2001	0	W & C OK, SW & C MO	15	-- (6.0-8.0)
1800 5 February 2002	2	SE Panhandle (TX), NW TX & C OK, N AR	18	0.24 (2-6)
0000 2 March 2002	1	N OK, C OK, NE & E OK	21	0.70 (6.4)
0000 4 December 2002	3			
0000 24 December 2002	5	N OK & S KS	24	0.80 (7.5)
1200 9 February 2003	1	N/C N N/E OK, S KS	10	0.20 (4-10)
1200 26 February 2003	3 and 5^+			
2100 12 December 2003	0	N OK, SW KS, N AR	15	0.37 (7.3)
1500 22 December 2004	1	C/S OK, C/N AR	12	0.15 (2-6)
1800 28 January 2005	3	C/N OK, S KS, TX Panhandle	18	0.35 (3.1)
1200 17 December 2005	5	SW-SE KS	24	0.52 (5.6)
1800 9 January 2006	0	TX panhandle W & C OK, SW-SE KS, NE OK	14	--- (3.0-8.0)
0000 30 November 2006	0	SW-SE KS, N & C OK,	21	1.14 (10.4)

		SW MO		
1500 20 January 2007	5	S KS, N & C OK	18	0.40 (5.2)
1800 31 January 2008	6	SE KS, N OK, N AR, S MO	18	0.28 (4.0-6.0)
1800 3 March 2008	4^{+} and 6	E OK, N & C AR, SW (Ozark) MO	12	--- (4.0-8.0)
1800 6 March 2008	4	E OK, C AR, N TX	12	0.93 (up to 12.0)
0000 25 December 2009	4	C OK, N/E OK & N AR	12	0.95 (13.5)
0300 1 February 2011	1^{+} and 4	C& N OK, NE OK & NW AR, SW MO	12	1.00 (13.2)
0000 9 February 2011	1	C & N OK, NE OK & NW AR, SW MO	15	0.40 (6.0)

Additional Figures

The figures overleaf display meteorological features of the remaining pattern types (6-8 for Ice, and 6 for Snow, see Tables A3.1 and A3.2). For each figure, plots were generated directly from NCEP-NARR online plotting tools, for T_{-24}, T_0 and T_{+24}. Fields include geopotential height at 500 hPa (gpm), sea level pressure (hPa), 250 hPa vector wind (and magnitude, ms^{-1}), precipitable water vapor (mm) and temperature at 850 hPa (^{o}C). Based on the constituent events, Ice Pattern 6 has a similar impact location for freezing rain as *Ice Pattern 5*, while Ice Pattern 7 was similar to *Ice Pattern 1*. Ice Pattern 8 only has three events, two of which also correspond with other pattern types, therefore this composite has too low of a sample size at this stage to be reliable, and is not shown. The same was true for Snow Pattern 6, also with three events (not shown). The evolution of this composite event was similar to *Snow Pattern 4.*

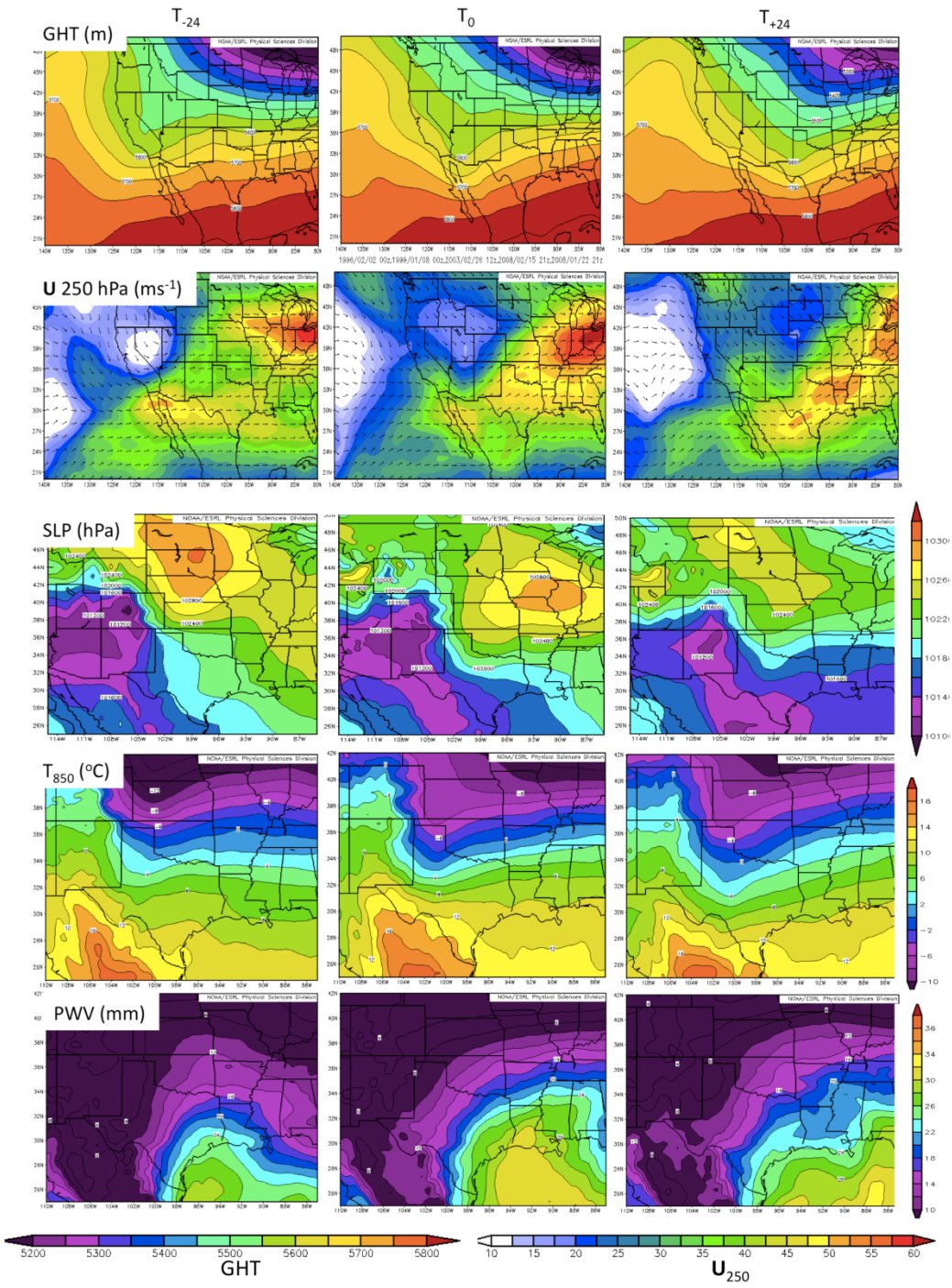

Figure A3.1: Ice Pattern 6 (n=5), variable descriptions shown above.

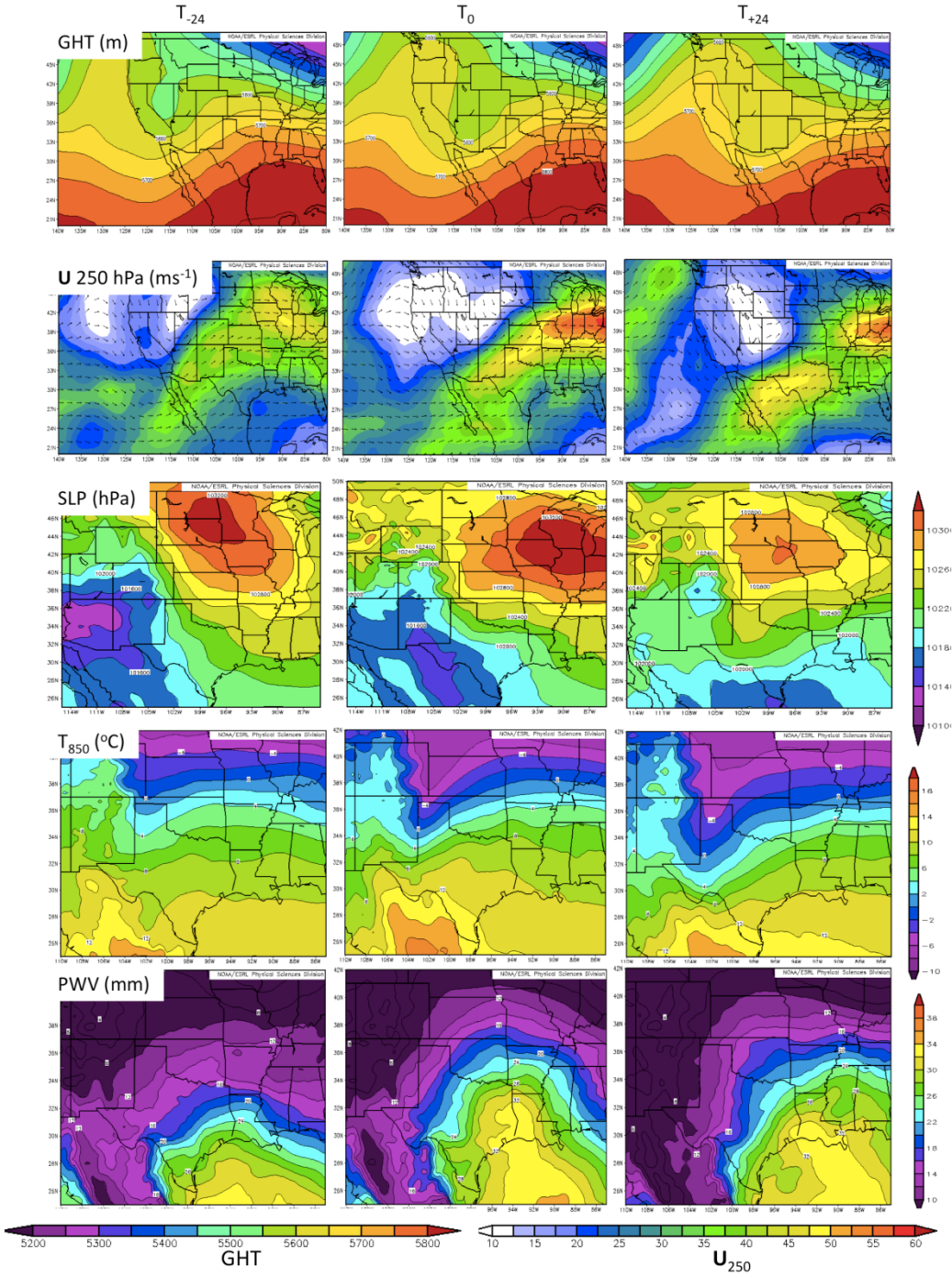

Figure A3.2: As Fig. A3.1 but for Ice Pattern 7 (n=6)

Section 4: SST Interpolation Uncertainty (Chapter 4)

This dissertation included a number of examples of regridding procedures, both for interpolation to a different grid (see section 5), or a different resolution. Chapter 4, sec 4.4 introduced the SST perturbations forming the sensitivity study. Daily climatological SST was most readily available at high ($1/12^{th}$ degree) resolution from the MMAB and was interpolated to 0.5^{o} for input to WRF. The interpolation was bilinear, using the NCL function 'linint2'. Bilinear techniques linearly interpolate from known to unknown points in the x and y directions separately, and are commonly used when data is already gridded and varies reasonably smoothly across a domain. To test error associated with this procedure, the $1/12^{o}$ field was interpolated to 0.5^{o} and then back to $1/12^{o}$. The difference between the original field and recovered field was then computed and halved to estimate error. Furthermore, the same technique was used to extract uncertainty for the interpolation of OIv2 0.25^{o} data to 0.5^{o}.

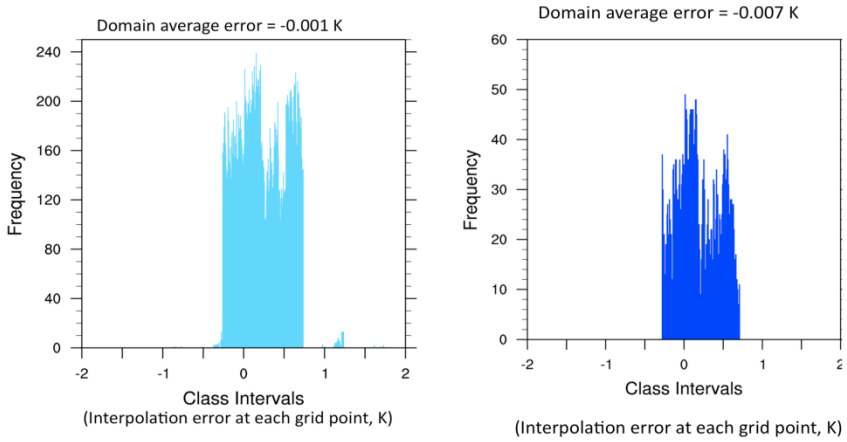

Figure A4.1. Interpolation errors (in Kelvin) expressed as a histogram for (left) $1/12^{o}$ to 0.5^{o}, and (right) 0.25^{o} to 0.5^{o} for the Gulf of Mexico region (100-78 ^{o}W, 14-30 ^{o}N). Total average domain error is the average over all grid points (top).

Interpolation uncertainty was generally between ±0.5 K, with a domain average 2-3 orders of magnitude smaller. This implies that regional SST structure may have experienced some larger error, however negligible bias appears for the basin as a whole. Since our sensitivity study does not require SST variations to be exact to a specific field, and was more concerned with the broad-scale anomaly (e.g., basin average SST), these errors are well within the tolerance of this study.

Section 5: Additional Interpretation of Methodology (Chapter 5)

Interpolation Uncertainty for Stage IV Precipitation using MET (sec. 5.3, 5.4,5.5)

In order to directly compare and perform verification of WRF model output against a user-specified dataset (in this case NCEP Stage IV), the two datasets must be on the same grid. Here we used the grid specifications of the WRF (projection, resolution) to regrid Stage IV. This procedure was performed in MET using the 'copygb' tool (see http://www.dtcenter.org/met/users/support/online_tutorial/METv3.1/copygb/index.php). Here the default bilinear regridding technique was used. The procedure to estimate error was similar to appendix section 4. The 48-hour Stage IV accumulated precipitation was regridded to the WRF grid, and then back to its original format. Figure A5.1 shows the magnitude of the uncertainty (in mm) for (a) December 9-11 2007, and (b) January 28-30 2010. No other sources of error were evaluated (e.g., Stage IV algorithms, instrumentation).

The resulting regridding error was on the order of ± 2 mm, with the December 2007 event (a) evidencing occasional larger negative departures (under-reproduced

precipitation). The morphology of precipitation was marked by a relatively narrow axis of heavy precipitation (e.g., Fig. 4.10), and therefore potentially sharp gradients in accumulation. The bilinear method can struggle in such cases due to the rapid rate of change underestimated from a linear slope formula. Alternate regridding/interpolation methods (e.g., bicubic, neighbor) were not considered.

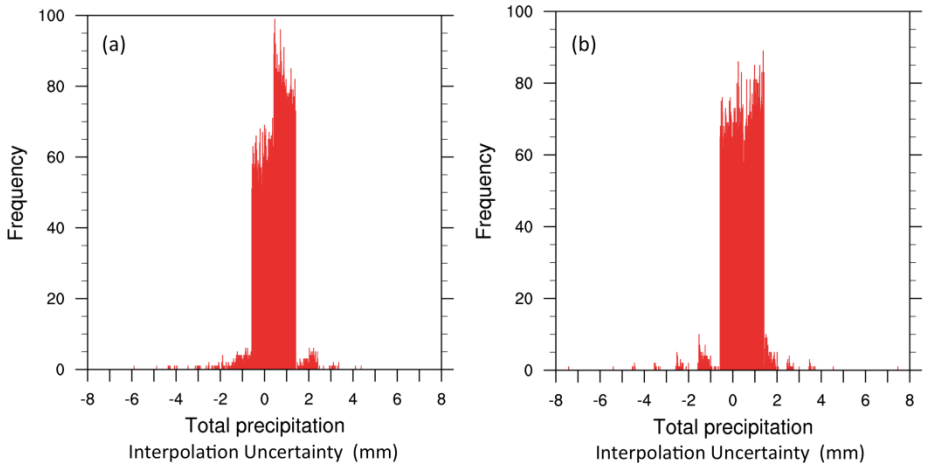

Figure A5.1. Histograms of regridding error (in mm) of 48-hour accumulated Stage IV precipitation using MET for (a) December 9-11 2007, (b) January 28-30 2010. Values calculated for WRF model domain 3.

Mesonet Regridding Error (sec 5.3, 5.4, 5.5)

Mesonet observations are ungridded and available at ~140 stations over Oklahoma. Validation of WRF surface air temperature used this data at 30-minute intervals, but for convenience the Mesonet information was gridded to a regular latitude/longitude 0.5x0.5^{o} grid using the NCL function 'cssgrid', which uses tension splines. This regularly spaced dataset then allowed for selection of specific points for both WRF and Mesonet, in the former by finding the nearest gridpoint to a user specified lat/lon. Tension splines are based on cubic splines but introduce a 'tension

factor', which adjusts to approach a cubic spline when the tension factor is zero, and a linear interpolation when the factor is large. The aim is to minimize the curvature of a surface (mathematically), and provide a smooth, spatially continuous field. The tension factor allows values to be more closely constrained by input data and does not permit values outside of the sample (raw Mesonet stations) range. Potential error was investigated by taking a raw station site in close proximity to an interpolated grid site and comparing the temperature time series. Figure A5.2 shows results from the January 2010 case study, from a site ~36°N, 96.5°W (Oilton, OK). Results indicated excellent agreement for the 48-hour time series at this location, with slightly warmer values (≤|0.3 K|) in the interpolated product.

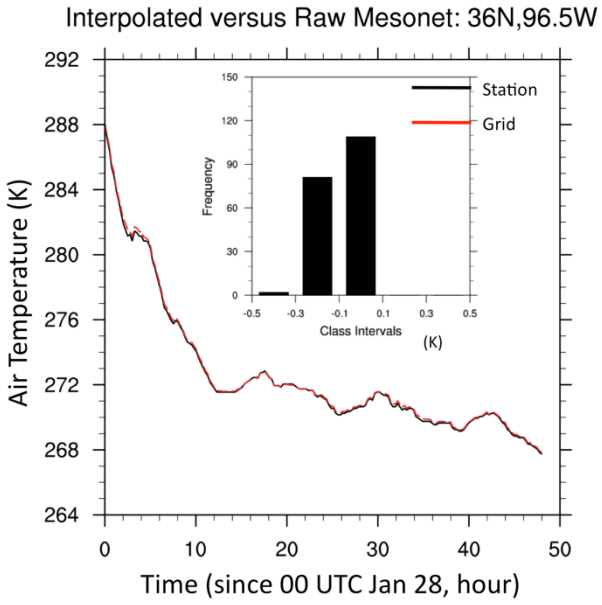

Figure A5.2. Air temperature time series for the January 2010 winter storm for the Mesonet station site at Oilton, OK (black), and a nearest interpolated grid (red). Inset histogram shows frequency of errors associated with this time series.

Verification Metrics (sec. 5.3, 5.4, 5.5)

When validating a forecast or simulation product against a corresponding observation, there is a suite of verification methods available. Forecasters commonly utilize 'skill scores', based on a 2x2 contingency matrix:

FORECAST	OBSERVATION Yes	No
Y	Hit (a)	False Alarm (b)
N	Miss (c)	Correct negative (d)

Equations for the metrics evaluated in Chapter 5 (e.g., Fig. 5.5, Table 5.2-5.6) are shown below, along with brief descriptions and/or advantages and disadvantages of each method (based on Richman, 2014 descriptive statistics class notes).

$$Accuracy = \frac{(a+d)}{(a+b+c+d)}$$

Accuracy is intuitive and simple (essentially, forecast 'hits' over all matrix categories), but can be heavily influenced by the most common category, which for rarer events is a 'no' observation (e.g., d).

$$Bias = \frac{(a+b)}{(a+c)}$$

Indicates whether an event is under (< 1) or over (>1) forecast, and measures only relative frequencies.

$$POD = \frac{a}{(a+c)}$$

Probability of detection (POD) measures the fraction of correct forecasts (e.g., match between observation and forecast amount for a given spatial point/domain). POD is

sensitive to 'hits', which for POD-yes (no) means events at or above (below) a given threshold.

$$FAR = \frac{b}{(a+b)}$$

The False Alarm Ratio (FAR) measures the number of times a forecasted event did not occur in the observation. *Con*: Ignores missed values.

$$POFD = \frac{b}{(b+d)}$$

Measure of inaccuracy of forecast compared with observations, especially focussed on false positive for an event.

$$CSI = \frac{a}{(a+b+c)}$$

The Critical Success Index (CSI) or 'threat score' is sensitive to hits, but penalizes false alarms and misses. *Con:* For rare events in a distribution, such as heavy precipitation, the CSI tends to yield a worse score.

$$GSS = \frac{(a - aref)}{(a - aref + b + c)} \quad \text{Where } aref = \frac{[(a+b)(a+c)]}{n}$$

n = number of events (e.g., number of domain 3 grid points).

The Gilbert Skill score (GSS), also known as 'equitable threat' measures the number of events that were correctly predicted, adjusted for an expected hit rate that may occur simply due to chance. *Con:* GSS penalizes both misses and false alarms equally and so the reason for error may not be distinguishable simply from this metric. *Pro:* Good for rare events.

$$HSS = \frac{2(ad - bc)}{(a+b)(b+d) + (a+c)(c+d)}$$

The Heidke Skill Score (HSS) uses all the measurements in the contingency table, and tends to work well for rare events.

$$FSS = 1 - \frac{1/n \sum (P_{fcst} - P_{obs})^2}{1/n \sum (P_{fcst})^2 + 1/n \sum (P_{obs})^2}$$

Where P_{fcst} (P_{obs}) is the fractional event frequency for the model (observation) within a defined neighborhood (we considered 3x3 and 5x5 grids ~10 and 15 km respectively), and the summation is over the number of points in the domain. The fractions skill score (FSS) (e.g., Roberts and Lean 2008) compares fractional coverage of observations and simulated quantities within a spatial sub-region. The score is sensitive to rare events.

Overview of the MET MODE tool (Chapter 5, sec. 5.4, 5.5, e.g., Fig. 5.8, 5.15)

MODE is an acronym for 'Method for Objected-based Evaluation' (Davis et al. 2006a,b, Brown et al. 2007), which can be used to verify data with coherent spatial structures, such as precipitation. In this dissertation, objects are precipitation areas above a threshold accumulation. Details of the calculation of skill attributes from MODE are provided in the MET users guide (version 3.1, see http://www.dtcenter.org/met/users/), although a basic overview is provided here. Firstly MODE needs a procedure to resolve spatial objects, which is termed 'convolution thresholding'.

$$C(x,y) = \sum \phi(u,v) f(x-u)(y-v)\,.$$

In this equation, C is the convolved field (object), ϕ the spatial filter function, and f the raw precipitation data. The filter function is calculated from

$$\phi(x,y) = H \text{ if } x^2 + y^2 \le R^2 \text{, and } \phi(x,y) = 0 \text{ otherwise.}$$

$$\pi R^2 H = 1.$$

R (radius of influence), and H (height-or 3D depiction of precipitation intensity, where higher precipitation = higher height) are interdependent and thus the user only need specify R to solve. MODE appeared quite sensitive to the choice of R, with larger values tending to overly smooth the data and eliminate localized intense precipitation, shown for December 2007 in Fig. A5.3. The convolved field (C) is then thresholded, using value T, creating a mask (M) that eliminates values < T.

$$M(x,y) = 1 \text{ if } C(x,y) \ge T \text{, and } M(x,y) = 0 \text{ otherwise.}$$

Raw data is subsequently restored to object interiors (F) via

$$F(x,y) = M(x,y) f(x,y).$$

Multiple attributes may be gathered from precipitation objects which help to later determine similarity between forecast and observed. Examples include area, moments (e.g., geographic centroid), axis angle (tilt, curvature), and aspect ratio. The degree of match is evaluated from user-defined weights placed on these attributes (for this dissertation, default weights were applied). For example, the centroid of the forecasted and observed objects has a higher weighting than some other variables, as the user would ideally like to see precipitation objects in a similar spatial location. The better these objects match, the higher their 'interest value', where ~0 = low or no

interest, and 1=high interest. MODE uses a default of 0.7 to keep or discard variables based on their interest value. 'Total interest' (T) is then summed as

$$T(\alpha) = \frac{\sum_i w_i C_i(\alpha) I_i(\alpha_i)}{\sum_i w_i C_i(\alpha)}$$

Where w_i are weighting factors, C_i the convolved field, and I_i interest value. The total interest is then thresholded and object pairs above the threshold are matched.

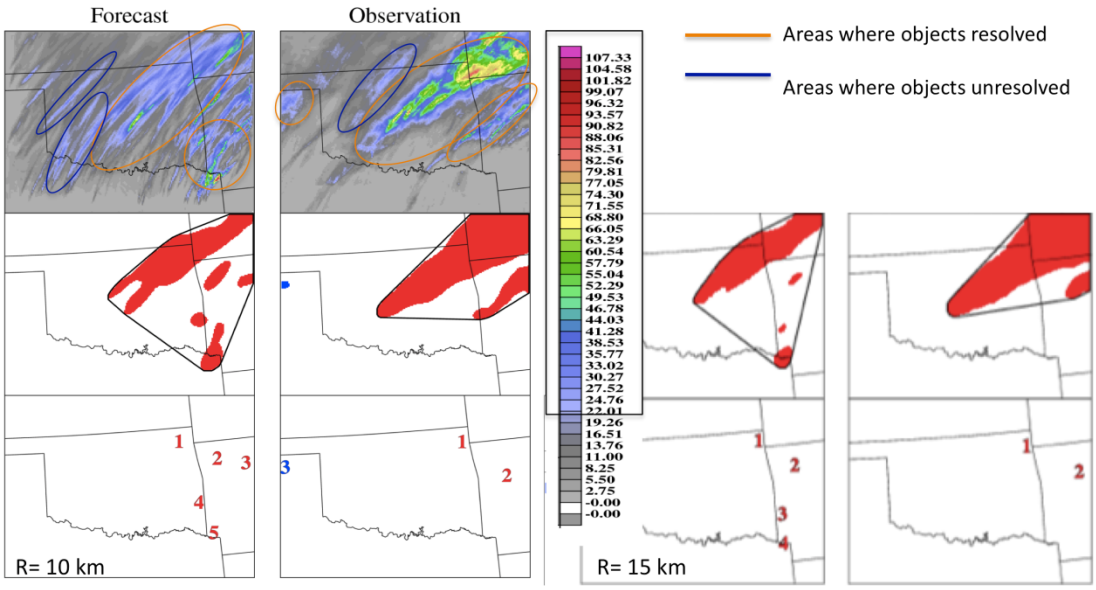

Figure A5.3. WRF simulated ('Forecast') and Stage IV ('observation') precipitation objects for 48-hour accumulations > 20 mm. Top panels show total precipitation (mm), center panels show precipitation objects for (left) radius R of 10 km, and (right) R=15 km. Areas of precipitation generally captured by the MODE process circled in orange, while regions with maximum precipitation above the threshold that were not resolved circled in dark blue. Use of a smaller radius of influence aids to better characterize spatial distribution for both WRF and observations, which are too smoothed on the right. Other parameters were altered, but their influence on the objects was much weaker (not shown). These changes included reducing area (merge) threshold to 10 mm (5 mm) on the left plot from 20 mm and 10 mm respectively.

Section 6: RIP 4 Ensemble Trajectories (Chapter 6, sec 6.5)

To briefly test the representativeness of the instantaneous trajectories analyzed in the text, an ensemble was generated from a grid of 10x10 points in x and y, each offset by half a grid cell, or 15 km, terminating over central Oklahoma at 850 hPa using REAL. Figure A6.1 demonstrates the results for (a) 12 UTC December 9, and (b) 12 UTC December 10. For (a), the ensemble confirmed the two diverse paths indicated in Fig. 6.21 (e.g., contrast CLIM to other perturbations), with reasonably low spatial spread. For (b) the vast majority of members showed anticyclonic flow from the Caribbean over the western GOM, although spread increased with southward extent (and therefore time).

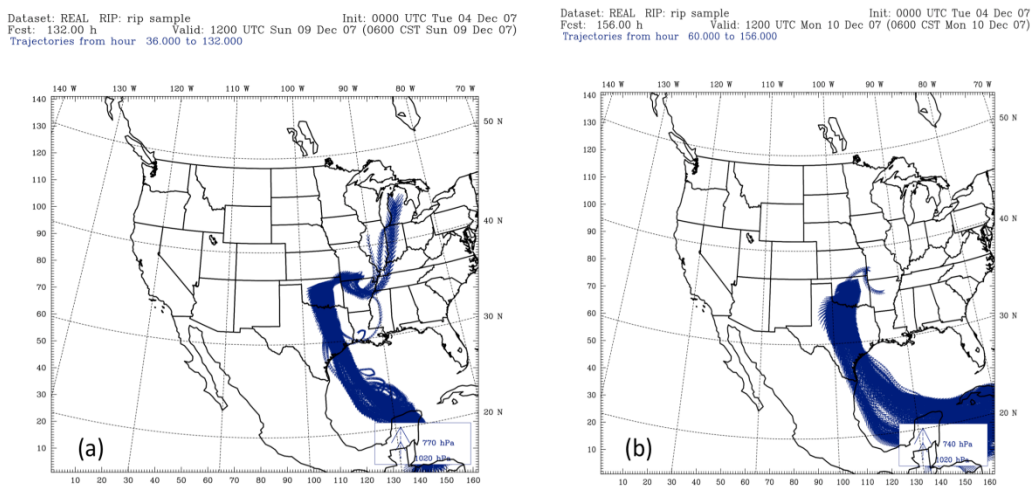

Figure A6.1. Air parcel ensemble trajectories initiated over a grid and interval described in above text valid (a) 12 UTC December 9, and (b) 12 UTC December 10. Trajectory altitude is accounted for by the width of the arrows but is not necessarily easy to pick out in the ensemble. Changes in altitude were not investigated.

Section 7: RIP 4 Ensemble Trajectories (Chapter 7, sec 7.5)

A test analogous to section 6, and with the same ensemble parameters was

performed for 21 UTC January 28 (Oklahoma) and 12 UTC January 29 (Arkansas) based on endpoint locations specified in the dissertation, and the levels near maximum warm layer temperature (~850 hPa and 800 hPa respectively). Results are shown in Fig. A7.1. Ensemble members showed more divergence compared with those of Chapter 6, especially with time. For (a) the dominant region of the GOM over which the members passed was similar to that of the instantaneous trajectory. For (b) a larger swath of the central and northern GOM was involved, with trajectory source regions varying from the northern states, to eastern Mexico, and some even from tropical Central America. This implies less certainty with respect to the representativeness of the trajectories analyzed in chapter 7. It also may be a consequence of the faster system progression such that grid points separated by 15, 30, 60 km experience more variable flow fields. Further work would be required to analyse this.

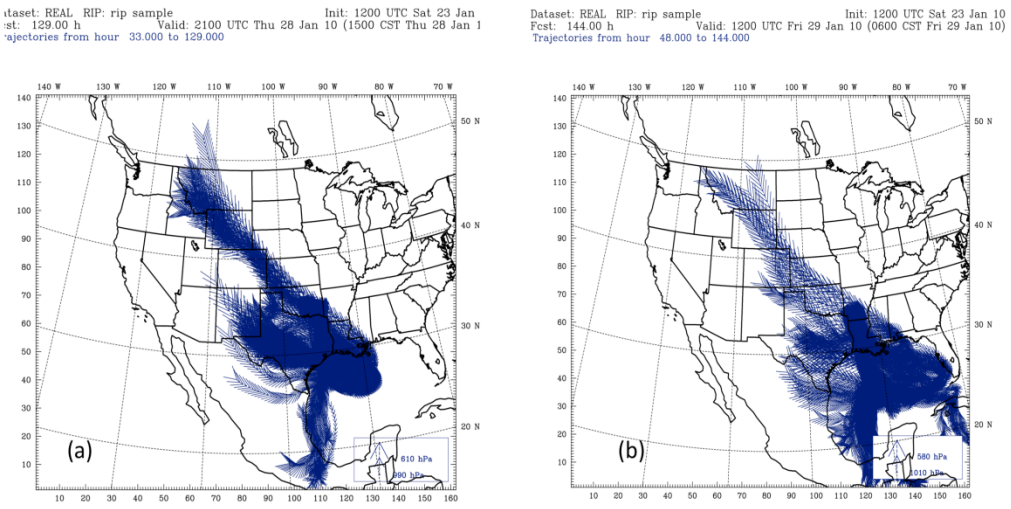

Figure A7.1. Air parcel ensemble trajectories as in Fig. A6.1, valid (a) 21 UTC January 28 (850 hPa) for west-central OK, and (b) 12 UTC January 29 (800 hPa) for western AR.

Section 8: Appendix References

Brown, B. G., R. Bullock, J. Halley Gotway, D. Ahijevych, C. Davis, E. Gilleland, and L. Holland, 2007: Application of the MODE object-based verification tool for the evaluation of model precipitation fields. Available at: http://ams.confex.com/ams/pdfpapers/124856.pdf.

Davis, C. A., B. G. Brown, and R. G. Bullock, 2006a: Object-based verification of precipitation forecasts, Part I: Methodology and application to mesoscale rain areas. *Mon. Wea. Rev.,* **134**, 1772-1784.

Davis, C. A., B. G. Brown, and R. G. Bullock, 2006b: Object-based verification of precipitation forecasts, Part II: Application to convective rain systems. *Mon. Wea. Rev.,* **134**, 1785-1795.

Roberts, N. M and H.W. Lean, 2008: Scale-selective verification of rainfall accumulations from high-resolution forecasts of convective events. *Mon. Wea. Rev.,* **136**, 78-97.